University of Southampton
Faculty of Engineering and the Environment
Institute of Sound and Vibration Research

Models for the prediction of rear-arc and forward-arc fan broadband noise in turbofan engines

by
Gareth Jenkins

Thesis for the degree of
Doctor of Philosophy

November 2013

UNIVERSITY OF SOUTHAMPTON

ABSTRACT

FACULTY OF ENGINEERING AND THE ENVIRONMENT
Institute of Sound and Vibration Research

Doctor of Philosophy

MODELS FOR THE PREDICTION OF REAR-ARC AND FORWARD-ARC FAN BROADBAND NOISE IN TURBOFAN ENGINES

by Gareth Jenkins

This thesis investigates three elements necessary for the prediction of the broadband noise from a turbofan engine due to the interaction between the turbulent rotor wakes with the Outlet Guide Vanes (OGVs). These are (i) the sound radiation from a cascade of closely spaced blades interacting with rotor wake turbulence, (ii) an analysis of the behaviour of hotwire velocity data from a Large Scale Fan Rig (LSFR), (iii) the development of a scheme for the prediction of the blockage due to the transmission of multi-mode sound across the rotor necessary for the prediction of noise in the forward-arc.

(i) Cascade noise model A noise model is presented for the prediction of rotor wake turbulence with a cascade of OGVs. Similar to other approaches of this kind, computation time becomes excessive at high frequencies as the number of modes required increases. This thesis shows that at sufficiently high frequencies, when at least two modes are cut-on between adjacent blades, the acoustic blade coupling is weak and the cascade sound radiation closely approximates to that of an isolated aerofoil whose radiation can be computed efficiently using single airfoil theory, thereby greatly reducing computation time.

(ii) Characteristics of rotor wake turbulence One factor currently limiting accurate fan broadband noise predictions is an understanding of rotor wake turbulence at the OGV leading edge. This thesis analyses in detail recent hotwire velocity data measured in the interstage of an LSFR. The focus here is on assessing the extent of self-preservation in the rotor wake, whereby the mean and turbulent wake characteristics can be deduced at any position downstream of the rotor and at any operating condition from a limited number of measurements. Unlike as previously assumed, this analysis demonstrates insufficient self-preserving behaviour to justify further pursuit of this approach. Rotor wake turbulence must therefore be measured or predicted at each operating condition separately.

An analysis procedure is developed by which the characteristics of individual wakes, necessary for broadband noise predictions, may be inferred from rotor wake velocity measurements in situations in which there is significant overlap between adjacent wakes.

(iii) Multi-mode rotor blockage Noise generated by the OGV propagates to the forward arc by passing upstream through the spinning rotor. This thesis presents a model for the sound power transmission loss associated with crossing the rotor that includes modal frequency scattering effects. It is shown that the results obtained using exact cascade scattering closely agree at low and high frequencies with the results from a relatively simple prediction scheme that assumes that only plane waves propagate through the cascade, thereby ignoring modal scattering effects. The advantage of making this approximation is that the computation is considerably more efficient than a full cascade calculation. At low frequencies, where only plane waves propagate in the gap, exact agreement is obtained between the exact and plane wave models. Close agreement is also observed in the high frequency limit where a large number of cascade modes are cut-on, most of which are well cut-on and hence whose behaviour tends that of the plane wave mode.

The three components of the prediction procedure outlined above are combined to perform a prediction of the rear-arc and forward-arc broadband noise from an LSFR. Comparison of the measured and predicted noise spectra are in reasonable agreement with variations with working line and fan speed being reasonably well captured.

Contents

List of Figures

List of Tables

Declaration Of Authorship

I, GARETH JENKINS declare that this thesis and the work presented in it are my own and has been generated by me as the result of my own original research.

Models for the prediction of rear-arc and forward-arc
fan broadband noise in turbofan engines

I confirm that:

1. This work was done wholly or mainly while in candidature for a research degree at this University;
2. Where any part of this thesis has previously been submitted for a degree or any other qualification at this University or any other institution, this has been clearly stated;
3. Where I have consulted the published work of others, this is always clearly attributed;
4. Where I have quoted from the work of others, the source is always given. With the exception of such quotations, this thesis is entirely my own work;
5. I have acknowledged all main sources of help;
6. Where the thesis is based on work done by myself jointly with others, I have made clear exactly what was done by others and what I have contributed myself;
7. Either none of this work has been published before submission, or parts of this work have been published as listed in Section 1.4.

Signed: .....

Date: .....

Acknowledgements

I would firstly like to thank my supervisor Professor Phillip Joseph for his continual guidance, support and persistent good humour. Phil has always made himself available to discuss new ideas or problems. His motivational speeches have helped me to persevere when progress seemed hard to find and he has made the time I have spent at the Institute for Sound and Vibration Research (ISVR) a real pleasure.

I am very grateful to my financial sponsors, Rolls-Royce and the Engineering and Physical Sciences Research Council (EPSRC), without whom these studies would not have been possible.

I have been very fortunate to have had the opportunity to collaborate with several people at the ISVR during my doctoral research, most notably Eugene Deane for his assistance with the LINSUB code, Vincent Blandeau for his work with the single airfoil noise model and Chris Powles for his methodical approach to the mathematics. I would also like to thank Gwénaël Gabard and Alan McAlpine for their valuable feedback during my review meetings. I have also had the pleasure of spending my time in the ISVR with many other researchers, too numerous to name. The countless discussions on matters technical, political and irrelevant have hugely enriched life in the office.

I have received much help and guidance from my contacts at the Rolls-Royce Noise Group. Particular thanks are due to Nick Humphreys, for his general guidance and assistance in preparation of my thesis, and to John Coupland, for his willingness to share his insights and for running RANS CFD predictions.

The research included in this thesis would not have been possible without the provision of data from the tests on the Large Scale Fan Rig (LSFR), that were organised by Rolls-Royce. The measurement and initial processing of the LSFR hotwire anemometry data were performed by DLR and the 28-vane OGV set used during these tests was provided by GKN.

I would also like to acknowledge the use of the IRIDIS High Performance Computing Facility, and associated support services at the University of Southampton, in the completion of the cascade simulations presented in this work.

Finally, I am deeply indebted to my family, in particular my wife Helen, for their perennial support and understanding over the duration of these studies. Thank you all for making all the work seem worthwhile and reminding me of the most important things in life.

List of symbols

Upper case Roman

A	$\sqrt{1 - M^2 \sin^2 \alpha}$
B	Number of rotor blades/vanes in OGV
$\mathcal{C}$	Cumulative density of incident sound power with respect to phase velocity angle
C_Λ	Coefficient for scaling RANS integral lengthscale
$\mathcal{D}$	Density of incident sound power with respect to phase velocity angle
$\mathrm{E}[\cdot]$	Expected value of $[\cdot]$
$F(\eta)$	Rotor mean wake profile function
$\mathcal{F}_r^{\pm}$	Non-dimensional cascade power function for turbulence interaction due to mode order r
$\mathcal{G}_{mn}^{\pm}$	Non-dimensional cascade pressure response for rotor transmission loss due to modes order m and n
H	Rotor wake turbulent profile function
$\mathcal{H}_{mn}^{\pm}$	Cascade power function for rotor transmission loss due to modes order m and n
$\mathbf{I}$	Acoustic intensity vector
I_1	Component of acoustic intensity resolved in axial (x_1) direction
$\mathbf{K}$	Kernel matrix
K_1	Wavenumber of convected frozen gust resolved in y_1 direction
L_τ	Rotor transmission loss level
L_0	Mean wake half-minimum half-width
$\mathcal{L}$	Effective unsteady loading in single airfoil theory
L_w	Mean-square velocity wake half-maximum half-width (w shown without loss of generality)
L_WW	Width of mean wake
$\mathbf{M}$	Mean flow Mach number vector
M	Component of $\mathbf{M}$ resolved in y_1 direction (magnitude of $\mathbf{M}$)
M_j	Component of $\mathbf{M}$ resolved in x_j direction
$M_{\Omega\mathrm{R}}$	Mach number associated with rotation of rotor at radius R
$\mathbb{N}$	Set of natural numbers, $\{1, 2, 3, \cdots\}$
$\mathcal{P}^{\pm}$	Power per unit span per unit angular frequency

$\mathcal{Q}_r^{\pm}$	Non-dimensional cascade power response for turbulence interaction due to mode order r
$\mathbf{R}$	Rotation matrix for resolving velocity components into streamwise-oriented coordinates
$\mathcal{R}_{\mathrm{ww}}$	Autocorrelation function (with respect to w component)
R	Medial radius of annular strip
$R_r^{\pm}$	Non-dimensional cascade pressure response function for mode order r
T	Blade passage period
T_{w}	Turbulence intensity (with respect to w component)
$\mathcal{T}_{mm}^{+}$	Power transmission coefficient of mode order m obtained using simplified rotor transmission model
$\mathbf{U}$	Mean flow velocity vector
U	Component of $\mathbf{U}$ resolved in y_1 direction (magnitude of $\mathbf{U}$)
U_j	Component of $\mathbf{U}$ resolved in x_j direction
$\overline{U}$	Circumferential average of mean flow velocity
U_∞	Free-stream value far from influence of wakes (U shown without loss of generality)
$\mathbb{Z}$	Set of integers, $\{\cdots, -2, -1, 0, 1, 2, \cdots\}$

Lower case Roman

c	Chord length
c_0	Speed of sound
$f(\eta)$	Individual mean wake profile function
$\hat{f}_m$	Order m Fourier coefficient of rotor mean wake profile function
h	Individual rotor blade wake turbulent profile function
$\hat{h}_l$	Order l Fourier coefficient of turbulent profile function
$\mathbf{k}$	Wavenumber of vortical perturbation
k	Free space wavenumber
k	Total kinetic energy in k-ω turbulence model
k_j	Wavenumber of vortical perturbation resolved in y_j direction
k_{x_j}	Wavenumber of vortical perturbation resolved in x_j direction
p	Pressure perturbation
$\mathbf{r}$	Skew coordinate transformation vector
s	Blade/vane separation distance in 'gap-wise' x_2 direction
t	Time
$\mathbf{w}$	Vortical velocity perturbation vector
w	Component of $\mathbf{w}$ resolved in vane-normal y_2 direction

w_j	Component of $\mathbf{w}$ resolved in x_j direction
w_{y_1}	Component of $\mathbf{w}$ resolved in vane-aligned y_1 direction
$\overline{w}$	Amplitude of harmonic gust
$\overline{w_0^2}$	Maximum mean-square turbulence velocity at the wake centreline
$\langle\overline{w^2}\rangle$	Circumferential average of mean-square velocity
$\mathcal{w}$	Fourier transform of upwash velocity w
$\mathbf{x}$	Duct-oriented coordinate system
$\tilde{\mathbf{x}}$	Fluid-fixed (and duct aligned) coordinate system
x_1	Axial component of $\mathbf{x}$
x_2	Transverse component of $\mathbf{x}$
$\hat{x}$	Non-dimensional distance downstream of rotor
x_h	Streamwise helical path length from rotor trailing edge
$\mathbf{y}$	Rotor/OGV-oriented coordinate system
y_1	Blade/vane-aligned component of $\mathbf{y}$
y_2	Blade/vane-normal component of $\mathbf{y}$
$\mathbf{z}$	Rotor-oriented coordinate system
z_1	Blade-aligned component of $\mathbf{z}$
z_2	Blade-normal component of $\mathbf{z}$

Upper case Greek

ΔU	Maximum mean wake deficit (U shown without loss of generality)
$\Delta\Omega_\pm$	Fundamental cut-off frequency for duct modes of positive and negative order
$\Delta\omega$	Fundamental cut-off frequency for cascade modes
Δ^2	Discriminant of axial acoustic wavenumber
Δk	Increment of change of vortical wavenumber
$\Delta\chi$	Change of stagger angle associated with camber
Λ	Turbulence integral lengthscale
Π	Total power per unit engine order
Φ	Dimensional wavenumber spectrum
Ω	Angular frequency of shaft rotation
Ω_m	Cut-off frequency of 'duct' mode of order m
$\aleph$	Factor used for scaling free stream velocity

Lower case Greek

α	Observer angle with respect to chord-oriented coordinate system
α'	Observer angle with respect to engine axis

β	Prandtl-Glauert number corresponding to M; $\beta = (1 - M^2)^{1/2}$
β_j	Prandtl-Glauert number corresponding to M_j: $\beta_j = (1 - M_j^2)^{1/2}$
γ	Azimuthal angle
δx	Spatial difference
ζ	Relative mean wake width
ζ_c	Critical value of mean wake width where wake overlap effects become significant
η	Non-dimensional circumferential distance
θ	Mean flow angle
θ_m	Momentum thickness
λ	Chordwise reduced frequency
μ	Acoustic wavenumber component in axial x_1 direction
μ_h	Hydrodynamic reduced frequency
μ_V	Wavenumber of vorticity component in Kaji formulation
$\mu_\mathrm{D}^{\pm}$	Wavenumber of upstream and downstream plane wave modes in Kaji formulation
ν	Acoustic wavenumber component in gap-wise x_2 direction
ξ	Vorticity
ξ	Separation angle between rotor stagger and duct flow
ρ_0	Average density of air
ρ	Perturbation of air density
ρ_ww	Normalised autocorrelation function (with respect to w component)
σ	Phase difference between adjacent vanes
τ	Temporal difference
ϕ	Normalised wavenumber spectrum
φ	Leading edge phase difference between cascade modes
χ	Stagger angle
ψ_p	Phase velocity angle
$\psi_\mathrm{p}^{\mathcal{D}}$	Phase velocity angle at which peak sound power is incident
$\psi_\mathrm{p}^{\mathcal{T}}$	Phase velocity angle at which peak rotor transmission occurs
ψ_g	Group velocity angle
ψ_w	Whirl angle of mean flow with respect to duct axis
ψ_r	Radial angle of mean flow with respect to duct axis
ω	Angular frequency
ω	Dissipation in k-ω turbulence model
ω_m	Frequency of incident mode order m as it appears in the rotor frame of reference
ω_{mn}	Frequency of incident mode order m, scattered into mode order n, as it appears in the stationary frame of reference

ω_n	Cut-off frequency of cascade mode of order n
$\omega_{\mathrm{int},m}$	Cascade mode interference peak or trough frequency of order m

Superscripts

LE	Value at leading edge
TE	Value at trailing edge
d	Components resolved in duct-aligned system
$+$	Upstream-propagating quantity
$-$	Downstream-propagating quantity
$\sim$	Vortical quantity
$*$	Complex conjugation

Subscripts

r	Value at rotor
s	Value at OGV
$\perp$	Perpendicular value

Accents and modifiers

$\hat{}$	Normalised quantity
$\hat{}$	Quantity in moving rotor frame of reference
$\hat{}$	Value derived from overlapped mean wake observation
$\langle\cdot\rangle$	Ensemble-averaged parameter

Chapter 1

Introduction

1.1 Broadband noise from turbofan engines

Aircraft noise pollution can be a source of annoyance for communities living close to airports and has become a major cause of conflict between those populations and the aeronautic community. Noise legislation has been strengthened resulting in restrictions to operations which have had an impact on logistical and economic concerns with capacity at many large European airports constrained by noise requirements [1]. It is therefore of great interest to airport and aircraft operators to reduce the noise exposure caused by their activities.

Since the widespread introduction of turbojet-powered flight technological advances have resulted in a reduction of around 20 dB to the noise produced by individual aircraft [1]. Despite this, the increase in air traffic has led to greater noise exposure in the population, with European air traffic projected to grow by approximately 17% over the period 2013–2019 [2] with faster growth predicted in the Middle East and Asia [1]. In order to avoid further restrictions to flight operations it will therefore be necessary to further reduce the noise produced by individual aircraft, with the target of 15 dB by 2050 relative to a 2000 baseline set by the Advisory Council for Aeronautics Research in Europe (ACARE). The changes in engine design needed to bring about the required noise reduction will require a detailed knowledge of the noise generation mechanisms.

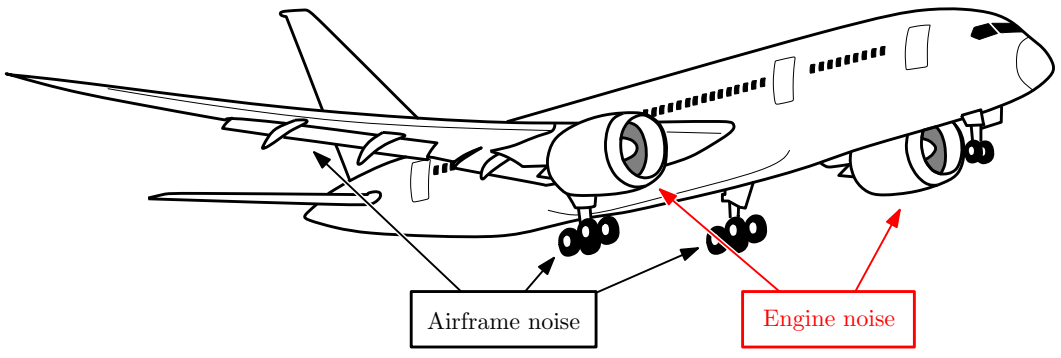

Figure 1.1 – Sources of aircraft noise.

Sources of aircraft noise

Many parts of an aircraft generate noise. The sources can be broadly divided into two categories, as illustrated in Figure 1.1. Airframe noise is caused by airflow over the surfaces and protuberances of the airframe such as the undercarriage, flaps and slats, nacelles, etc. Engine noise has contributions from; jet noise associated with the turbulent mixing of the engine exhaust with the relatively slow-moving ambient air, tones resulting from shocks formed at supersonic fan tips, tones due to the impingement of rotor velocity wakes on the Outlet Guide Vanes (OGVs), and noise due to interaction of engine components with turbulent flows within the engine.

Figure 1.2 shows a breakdown of the relative contributions of various aircraft noise sources to the overall aircraft noise. The data for sideline and approach certification conditions are shown in Figures 1.2a and 1.2b respectively. At both sideline and approach conditions the fan noise makes a significant contribution to the total engine noise and therefore the total aircraft noise. Note that the data in Figure 1.2 refer to airframes and engines from 1992 with bypass ratios of ∼5 and are taken from Kumasaka et al. [3]. More recent high bypass engine designs have bypass ratios of up to 11 in the case of the Rolls-Royce Trent 1000. The increase in bypass ratios has reduced jet exit velocity and hence the relative contribution of jet noise to total engine noise. Subsequently the contributions due to fan noise are more significant to total engine noise but are lower in absolute terms [4].

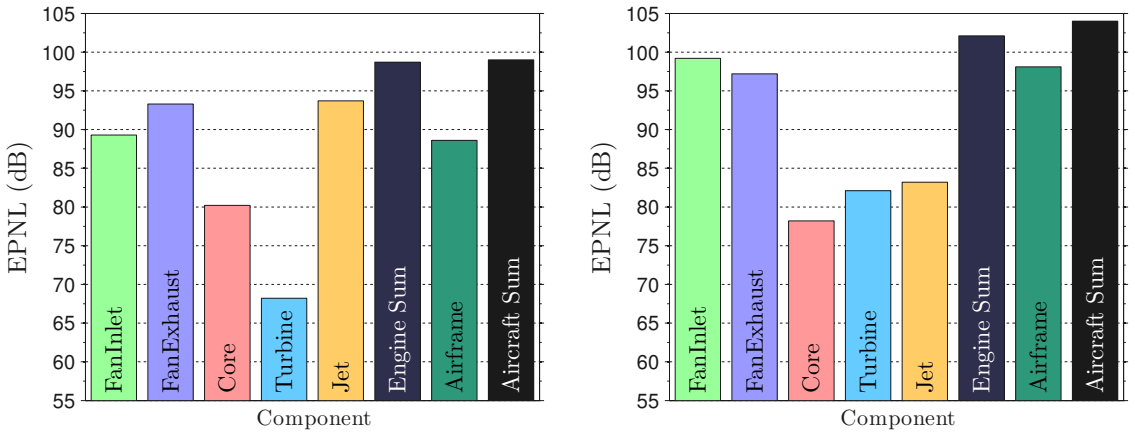

(a) Sideline (takeoff)

(b) Approach

Figure 1.2 – Relative importance of aircraft noise components at the sideline and approach certification conditions, 1992-level technology (bypass ratio ∼5) on a large 4-engine airframe (Boeing 747). Data taken from Kumasaka et al. [3].

1.2 Rotor wake-OGV interaction noise

Fan noise is a significant contribution to overall aircraft noise, as shown above. Four important noise generation mechanisms by which fan noise is generated are indicated in Figure 1.3. These four mechanisms are described in Sections 1.2.1–1.2.3.

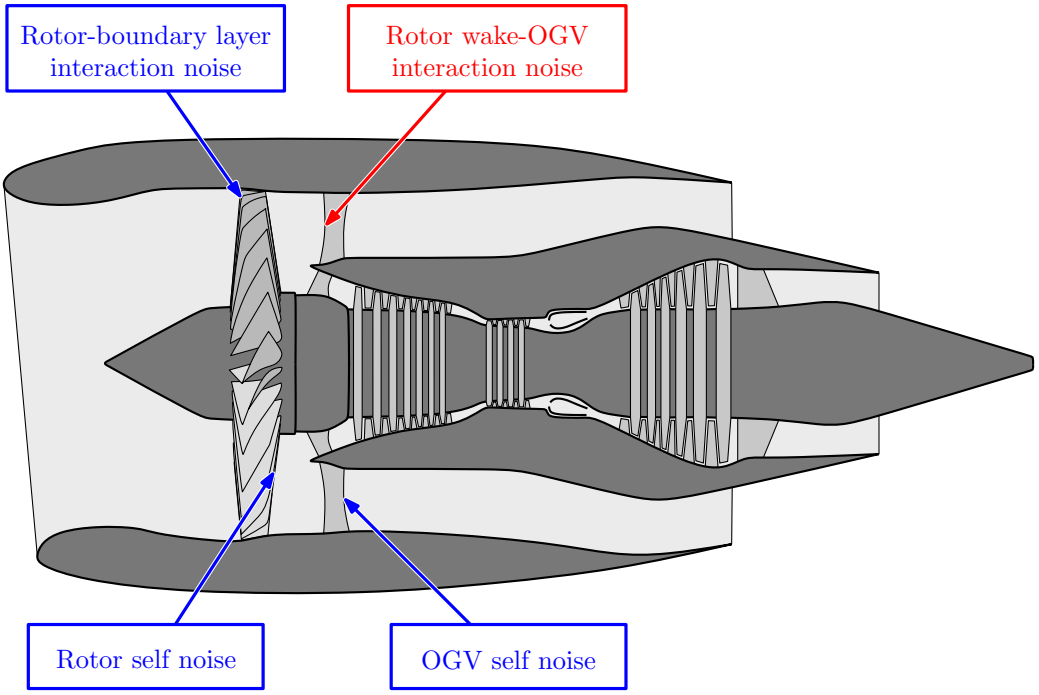

Figure 1.3 – Noise sources within a high bypass turbofan engine.

1.2.1 Rotor/OGV self noise

The noise generated by an airfoil in a smooth flow due to interaction between the airfoil and the turbulent boundary layer that forms on its surface is referred to as self noise. Both the rotor and OGV airfoil surfaces will generate self noise in this manner.

1.2.2 Rotor-boundary layer interaction noise

Turbulent boundary layers will build along the inlet surface. As the rotor cuts through this turbulent layer the surfaces are subject to unsteady loading which in turn leads to noise radiation.

1.2.3 Rotor-OGV interaction noise

The flow behind the rotor is complex, and can be decomposed into steady mean flow and unsteady turbulent velocity fields, which lead to tonal and broadband interactions with the OGV, as described below.

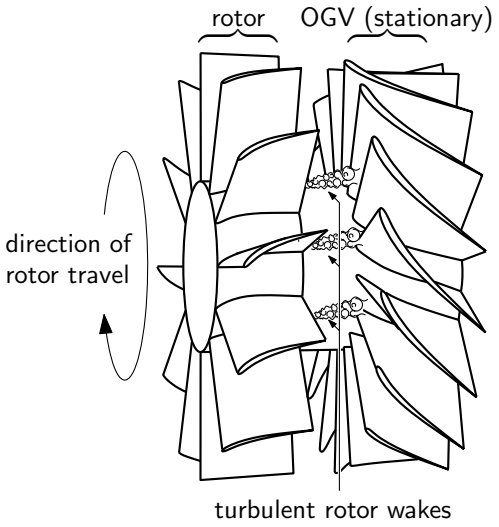

Figure 1.4 – Turbulent wakes of rotor blades convecting onto OGV and generating broadband noise.

Rotor-OGV interaction noise: tonal contribution

The flow velocity behind the rotor has mean velocity deficits in the 'shadow' of each of the rotor blades. These mean rotor wakes convect downstream onto the OGV and are periodically cut by the OGV leading edges resulting in tonal noise at the blade-passing frequency and its harmonics. Tonal fan noise contributions have been the subject of much interest and research has led to significant reductions of this noise source [5]. Consequently, the broadband noise due to rotor-OGV interactions have been exposed as significant contributors to overall fan noise.

Broadband rotor-OGV interaction noise

Measurements made on a low speed scale fan rig by Ganz et al. indicate that rotor-OGV interaction noise is a significant source of broadband noise at all frequencies and is the dominant source for frequencies above $\sim$5 kHz at rig scale [5, Page 128]. The importance of rotor-OGV interaction noise makes it crucial that this noise generation mechanism and the propagation of broadband noise generated on the OGV to the observer is well understood. For this reason rotor-OGV interaction noise is the focus of this thesis. Turbulence in the rotor wakes results in unsteady fluctuations in the rotor wake velocity. Broadband noise is generated by interactions between these turbulent flows and the Outlet Guide Vane (OGV or stator) as illustrated in Figure 1.4.

1.3 Literature review

In this thesis the problem of broadband rotor-OGV interaction noise has been divided into three parts:

- Prediction of the turbulence in the rotor wake at the OGV leading edge,

- Calculation of the noise generated on the OGV due to interaction with the turbulent rotor wakes,

- Prediction of the transmission loss due to the transmission through the rotor.

A survey of the literature relevant to these three areas is given in the following sections.

1.3.1 Rotor wake analysis and prediction of turbulence characteristics

This thesis focusses on the broadband noise generated by the interaction of the turbulent wakes behind a rotor with the vanes of the OGV. Predictions of broadband noise can be used to assess the changes to the radiated noise spectrum caused by changes in the design of engines or the modification of operating conditions. The noise calculations require the specification of the rotor wake turbulence at the OGV leading edge. For reasons of time and expense it will not generally be possible to measure rotor wakes for all desired configurations of geometry and flow conditions. Therefore, it becomes important that the wake development can be predicted in order to accurately specify the turbulence for input to the noise model.

One approach to the prediction of rotor wake turbulence is the identification of structure in turbulent wakes. Given that the wake structure was known it would be possible to predict the wake turbulence at some arbitrary point downstream of the rotor. One long-held view in the turbulence community is that turbulent plane wakes become 'self-preserving' at some point downstream of the wake generator. When in the self-preserving state the parameters describing the mean wake and turbulent wake characteristics scale with a single flow parameter, allowing the determination of the turbulence characteristics at the OGV from, say, a prediction of the pressure loss across the rotor. A review of the literature relevant to notions of self-preserving wakes and turbulent wake development is presented below.

1.3.1.1 Self-preserving plane wakes for rotor wake turbulence prediction

Self-preservation, or self-similarity, is a condition of a flow in which the velocity profile and other flow parameters scale with respect to a single flow parameter. Early work, defining these ideas, was conducted in 1907 by Blasius [6] where they were used in relation to laminar boundary layers. In 1937 self similarity was first applied to turbulent flows by Zel'dovich [7].

The book by Townsend [8] (1976) asserts that the self-preserving states in a turbulent flow occur as the flow characteristics become independent of the initial conditions, at some downstream location. According to this, the plane wakes due to bodies with different profiles should exhibit identical growth rates once the self-preserving condition is established. Experimental and theoretical investigations have provided evidence that, in some cases, appear to back this up (see, e.g. Sreenivasan and Narasimha [9] (1982) and Louchez et al.

[10] (1987)) and, in others, refute it (see, e.g. Bevilaqua and Lykoudis [11] (1978), Wygnanski et al. [12] (1986) and Marasli et al. [13] (1992)), leading to a division within the turbulence community.

Universality of self-preserving wakes

In their paper of 1982, Sreenivasan and Narasimha [9] argue that the wake due to any body will enter a universal self-preserving state when measured sufficiently far downstream. They contend that differences between wakes observed in experiment are the result long-lived transients that will dissipate given long enough.

Non-universal self-preserving states

A contrary view to that of Sreenivasan and Narasimha was presented in 1989 by George [14, 15], when he examined the historical assumptions surrounding self-preserving flows due to jets and wakes. George observed that earlier work relating to wake development assumed the wake generator to be a point source of drag and that the predicted flows therefore evolve into a particular self-preserving form in which the mean wake profile is independent of the characteristics of the wake generator. Furthermore, the dependency of the mean wake velocity deficit and half-maximum half-width of the mean wake would be universal, i.e. the wake due to, say, a cylinder is predicted to develop identically as that due to an airfoil. George argued that these earlier analyses, by ignoring the effects of the initial conditions at the wake generator, omitted the influence of the wake generator on subsequent wake development. In his analysis George found that the constants of proportionality that link the wake velocity deficit and half-maximum half-width of the mean wake to the downstream distance are not universal, but that the initial conditions dictate the rate of growth of the mean wake so that it is dependent on:

- The geometry of the wake generator,
- The velocity of the flow past the wake generator,
- The loading of the wake generator.

Despite these differences, George observed that the mean wake shapes should always be similar when normalised with local parameters.

George cited as evidence of non-universality recent experiments of two-dimensional plane wakes conducted by Wygnanski et al. [12]. In their measurement campaign, [12] analysed the wakes due to several bodies, including cylinders and a symmetric airfoil, all experiments being conducted in axial flows with no mean perpendicular loading. The published results showed that the mean wake shape was symmetric and similar to the Gaussian function but that the growth rates of the wake width and maximum velocity deficit were dependent on the geometry of the wake generating bodies, suggesting that

there was a lack of universality in the measured results. Wygnanski et al. found that the inflow turbulence in different test facilities greatly influenced the observed wake evolution.

Computational approaches to self-preserving wake research

Computational studies into wake self-preservation have also been conducted. In 1997 Ghosal and Rogers [16] Performed Large Eddy Simulations (LES) and found non-unique self-preserving states, characterized by different spreading rates and turbulent statistics that were maintained for significant time periods. Later, in 1998 Moser et al. [17] made a series of wake predictions using Direct Numerical Simulation (DNS) and demonstrated the sensitivity of the flows to the initial conditions. However, due to finite resources, their simulations were not able to show the final state of the wakes.

1.3.1.2 Rotor wake turbulent wake measurements

Few experimental studies have been conducted of the three-dimensional flow behind a rotor. In 1975 Evans [18] conducted a measurement campaign using an ensemble-averaging technique. Ganz et al. [5] (1998) performed an analysis of the flow in a low speed Boeing 18-inch fan rig subject to a variety of operating conditions. Comparison of the three-dimensional turbulence velocity with the homogeneous isotropic turbulence model due to von Kármán revealed weak evidence of anisotropy. However, despite the anisotropy, the turbulence integral lengthscale was found to scale with the wake width.

Gliebe et al. [19] (2000) performed a series of measurements and Reynolds-Averaged Navier-Stokes (RANS) predictions of the wakes behind the rotor stage of a low aspect ratio test rig. Hotwire probes were positioned at several radial and axial locations. RANS Results were shown to be in good agreement with experiment. Analysis of these results led to the definition of expressions defining the development of the mean and turbulent wake components with increasing distance downstream, all of which were related to the wake momentum thickness. These expressions allowed the definition of the wake turbulence spectrum using the velocity wavenumber spectra due to e.g. von Kármán or Liepmann, either of which require the specification of only two parameters; the root-mean-square velocity and an integral length scale. Gliebe et al. used their wake development rules to predict the broadband noise due to a turbofan-like test rig to within 5 dB at most frequencies. RANS solutions for the rotor wake have also been performed by Nallasamy et al. [20] (2002). In 2004 it was noted by Envia et al. [21] that most contemporary descriptions of the rotor turbulent wake were based on the results published by Ganz et al. [5], Gliebe et al. [19], Nallasamy et al. [20], as described above.

Cyclostationary analysis of rotor wakes

More recently, in 2009 Jurdic et al. [22] performed cyclostationary spectral analysis on rotor wakes measured on a low speed fan rig. This cyclostationary technique allowed

the separation of the turbulence in between the wakes from that in the rotor wakes with significantly greater frequency resolution than conventional spectral analysis. It is noted by Jurdic [23] that the Liepmann turbulence model for homogeneous isotropic turbulence is a good fit for the measured turbulence, even in hub and tip regions where secondary flows are significant.

The treatment of wake overlap phenomena

A consequence of the broadening of the wakes with increasing downstream distance is that at some point downstream of the rotor the wakes will become overlapped. Both Ganz et al. [5] and Gliebe et al. [19] acknowledge that wake overlap has occurred in some of their measurements of rotor wakes but in neither case was any attempt made to account for this phenomenon so that the values obtained for the maximum mean wake velocity deficit, free stream velocity or mean wake width are *not* the values associated with individual self-preserving mean wakes. The results of the mean wake overlap model presented in Chapter 6 of this thesis suggests that neglect of the mean wake overlap phenomena will have caused errors in the 'correlations' obtained by Gliebe et al. [19]. To the knowledge of the author, no attempt has been made elsewhere in the available literature to model the effects of mean wake overlap on measured mean wake parameters.

1.3.2 Noise due to interaction between OGV and convected turbulence

Developments relevant to the prediction of noise due to the interaction of turbulence with an OGV began in the 1930s with considerations of the unsteady lift on an airfoil due to a gust. Progress in this field has led to the inclusion of three-dimensional flow effects and compressibility and the interactions between adjacent vanes of the OGV. These developments are presented in approximately chronological order below.

1.3.2.1 Single airfoil interaction noise models

Early work on interaction noise concentrated on the response of an isolated airfoil subject to a sinusoidal vortical gust aligned perpendicularly to the airfoil surface. The unsteady lift on the airfoil is used to determine the strength of acoustic dipole sources that are assumed to replace the airfoil. Such interactions result in a single frequency, or tonal, response as the gust propagates past the airfoil leading edge in a steady mean flow.

Single airfoil models for the prediction of tonal noise

The foundations of the turbulence-OGV interaction problem lie in work performed in the field of aeronautics. In 1938 von Kármán and Sears [24] published work that aimed to simplify the contemporary body of airfoil theory (see, e.g. Theodorsen [25] and Küssner [26]). This work, subsequently summarised by Sears [27] in 1941, formulated expressions for the lift and moment on a two-dimensional flat plate airfoil of finite chord subject to

'translatory' and 'rotational' gust velocities, being respectively uniform along the chord and proportional to the location aft of the chord centre. Sears [27] extended the formulation to include the unsteady lift due to a sinusoidal gust.

In 1955 it was observed by Curle [28] that, through an extension of Lighthill's general theory of aerodynamic sound [29], the effect of a flat plate in a flow was equivalent to that of a distribution of dipoles in place of the solid boundary. Application of this theory to the sinusoidal gust formulation of Sears [27] led to the first flat-plate single airfoil noise model for prediction of the sound pressure due to a harmonic vortical gust. The formulation derived by Curle assumed that the flow was incompressible and was of limited accuracy at higher frequencies and Mach numbers, where compressibility effects become important.

Extension of single airfoil noise models to include three-dimensionality and compressibility effects

Much work has subsequently been undertaken in order to include the effects of three-dimensionality and compressibility. Formulations for three-dimensional incompressible flows were derived by Filotas [30] (1969) and Graham [31] (1970). Approximate solutions for the two-dimensional compressible flow were derived by Osborne [32] (1973) and Amiet [33] (1974), both valid at low frequency. The general three-dimensional compressible problem cannot be solved analytically but in 1970 Graham [34] deduced that the formulation for a three-dimensional gust in a compressible flow can be expressed in terms of the two-dimensional compressible and the three-dimensional incompressible results through the use of the so-called similarity conditions. Incident gusts are found to be either subcritical, with a subsonic phase speed along the leading edge of the blade, or supercritical, where the phase speed is supersonic along the blade leading edge. A subcritical case can be reduced to a case of oblique incidence in an incompressible fluid whereas a supercritical case is similar to compressible two-dimensional case where there is no span-wise wavenumber component.

Adamczyk [35] (1974) took an approximate approach to the three-dimensional compressible flow problem and derived a closed-form expression for the aerodynamic response of an infinite swept flat-plate airfoil in the form of a sum of two terms, representing the leading edge interaction and the subsequent trailing edge back-scattering.

Extension of single airfoil models to broadband noise

In 1975 Amiet [36] extended the earlier flat-plate theories to predict broadband noise emissions due to a stationary airfoil in a turbulent flow. The resulting formulation included the effects of non-zero span-wise wavenumber components of incident turbulence using the similarity rules of Graham [34]. Approximate solutions provided by Amiet divide the spectrum into low and high frequency regimes based on the reduced wavelength of the gust relative to a one-quarter airfoil chord and using the low frequency response function from Amiet [33] and the high frequency response function due to Adamczyk [35] as required.

The results of this model were subsequently validated in 1977 during a series of experiments conducted by Paterson and Amiet [37] who also showed that the effects of angle of attack on the radiated noise were small but that the noise from thick airfoils was under-predicted at high frequency due to the use of flat plate models. The single airfoil approach to interaction noise from rotors and stators has since been employed by many researchers (see, e.g. Roger et al. [38] (2006), Moreau and Roger [39] (2007) or Pagano et al. [40] (2010)).

In 2010 a frequency domain model for the broadband sound power radiated to the far-field from a single airfoil was developed by Blandeau et al. [41], where unsteady loading of the impinged blade row is modelled using classical isolated flat-plate airfoil theory of Amiet [33, 42] which predicts far-field pressure.

1.3.2.2 Cascade interaction noise models

In a typical turbofan engine the OGV has vanes that are closely spaced with chords that are long relative to the gaps separating them so that acoustic interactions between the vanes become a significant factor in the acoustic response to incident turbulence. The single airfoil approach clearly cannot account for interactions between the vanes of an OGV.

Cascade models for tonal noise prediction

In 1958 a two-dimensional unwrapped blade row was considered by Lane and Friedman [43] in an analysis of the unsteady lift and moment on compressor and turbine blades for the prediction of flutter rather than noise. Torsional flutter was also the subject of work by Whitehead [44] (1965) where a chord-wise distribution of bounded vorticity is described that is equivalent to the cascade surfaces. The reaction of the bounded vorticity and their shed vortices are combined to form a description of the blade forces.

Kaji and Okazaki [45] (1970) developed a model for the tonal noise generated due to the potential and velocity deficit interactions between a stator row and downstream rotor. Their formulation replaced the blade row with a distribution of pressure doublets, the strength of which was determined by the numerical solution of an integral equation.

In 1973 Smith [46] used a bounded vorticity approach, similar to that seen in Whitehead [44], in order to obtain an integral function for the unknown vorticity distribution along the cascade blades. Expressions were given for the calculation of the distribution of unsteady forces and moments and acoustic pressure due to blade torsion and translation and incident acoustic and vorticity waves. Solutions to the integral equation were obtained using a collocation technique. Further notes and a code based on this formulation, LINSUB, were presented in 1987 by Whitehead [47].

The analyses of Kaji and Okazaki [45], Smith [46], Whitehead [47] mentioned above all employ numerical schemes in order to obtain their solutions, introducing significant computational difficulties at high frequencies. Approximate analytic expressions for the

sound transmission through a two-dimensional cascade were presented in 1970 by Mani and Horvay [48]. Their approach was based on the Wiener-Hopf technique and neglected interaction between the leading and trailing edges by using semi-infinite blades for both the downstream-propagating waves from the leading edges and upstream-propagating waves from the trailing edge. These wave interactions were resolved in the vane overlap region, thus limiting this technique to overlapping configurations.

Since 1992 further developments have been undertaken by Peake and co-workers. The unsteady blade loading due to an incident vortical gust was calculated by Peake [49, 50]. The upstream radiation of sound waves where the angle of attack is non-zero was obtained using similar techniques by Peake and Kerschen [51] whilst the effects of small amounts of blade thickness and camber are considered by Evers and Peake [52].

Extension of cascade noise models to broadband

The numerical approach to the solution was extended to predictions of broadband noise in 1998 by Hanson and Horan [53]. Their paper utilised the formulation due to Glegg [54] with an incident gust that is generalised by the use of a Fourier transform, in a similar manner as had been adopted by Amiet [36] for the isolated airfoil case. The use of the Wiener-Hopf technique limits the application of this formulation to overlapped-blade configurations. Hanson [55, 56, 57, 58] later developed this broadband model to include transmission effects, which will be discussed in Section 1.3.3.

In 2006 Cheong et al. [59] developed a broadband model for turbulence-cascade interaction that employed the cascade formulation due to Smith [46], thus removing the limitation to overlapped-blade cascades imposed by the Wiener-Hopf technique. The broadband extension was developed using a Fourier transform approach similar to that of Hanson and Horan [53]. Cheong et al. observed that periodicity in the kernel function used to obtain the acoustic response of the cascade represented redundancy in the calculations and proposed a re-ordering of the formulation that has allowed a significant improvement in evaluation times.

Extension of cascade noise models to include three-dimensional effects

In 1976 Goldstein [60] proposed a solution for a rectilinear cascade to account for three-dimensional gusts with discrete span-wise wavenumbers due to rigid duct walls. This approach was adopted in 1981 by Atassi and Hamad [61] when considering the interaction of wakes and secondary flows with a cascade. This work extended the similarity rules established by Graham [34] to three-dimensional gusts impinging on a rectilinear cascade.

The Wiener-Hopf technique was employed by Glegg [54] (1999) to derive an exact analytical expression for the acoustic field radiated from a three-dimensional cascade of blades with finite chord subject to a three-dimensional gust. The result is obtained by observing that it is not necessary to derive expressions for the unsteady loadings on the blades in order to determine the acoustic potential outside the cascade.

In 2010 Posson et al. [62, 63] extended the formulation due to Glegg [54] in order to obtain a solution for the acoustic field that was also valid in the inter-vane space.

A semi-analytic model was developed in 2008 by Lloyd and Peake [64], extending the two-dimensional cascade model of Smith [46], Whitehead [47] and Hanson and Horan [53] to incorporate the effects of lean and sweep, further extending the similarity rules of Graham [34] and [61].

Noise models for three-dimensional geometries

A model for noise generated by an annular cascade of unloaded blades subject to swirling mean flows was developed by El Hadidi and Atassi [65] (2002) and Atassi et al. [66] (2004) which evaluated the pressure at the inlet and exit planes of an annular duct involved the matching of vortical and acoustic modes within an annular duct with radially variable swirling flow. Results of this model have shown that the span-wise variation of the swirl angle causes significant changes to the span-wise unsteady lift distribution and hence to the propagating acoustic pressure.

1.3.3 Calculation of rotor transmission loss

Semi-actuator disk modelling for transmission through a blade row

Early work on transmission through blade rows concentrated on discrete frequency (tonal) noise. The simplest formulation applicable to the rotor transmission problem was presented in 1970 by Kaji and Okazaki [67]. A semi-actuator disk method was adopted so that the flow field was divided into three regions: upstream of, downstream of, and within the blade row. The medium in the region within the blade row was assumed to support only plane-wave acoustic waves propagating upstream and downstream within notional ducts aligned with the stagger angle. Matching of the pressure, vorticity and enthalpy at the leading edge and trailing edge interfaces led to a system that was solved for the required acoustic parameters.

Cascade modelling of blade row transmission

Also in 1970, Kaji and Okazaki [68] took a more detailed approach to the cascade transmission problem. In this, the blades of a flat-plate cascade were replaced with acoustic doublets, subject to the boundary condition of zero velocity perpendicular to the blade surfaces. The resulting integral equation for the upwash velocity required numerical solution using the collocation technique.

The bounded vorticity formulation due to Smith [46], discussed in Section 1.3.2.2 for the interaction noise problem, included inputs for acoustic wave incidence and as such was applicable to the acoustic transmission problem. Here, as before, the collocation method was used to provide a solution for the upwash velocity.

Wiener-Hopf solution for cascade transmission

Mani and Horvay [48] (1970) took a different approach to the sound transmission problem. They split the transmission problem into two parts: the reflection and transmission by a cascade of semi-infinite plates and the radiation from the rectilinear ducts formed between the semi-infinite plates of a rectilinear cascade. The Wiener-Hopf technique was applied to obtain an approximate solution but the assumption of semi-infinite plates limited the application to cascades in which the adjacent blades are overlapped.

Koch [69] (1971) developed the work of Mani and Horvay [48] to provide an exact solution for the reflected and transmitted sound when a cascade of blades of finite chord is impinged upon by acoustic waves.

Application of models to broadband rotor transmission

In 1999 Hanson [55] adapted the cascade transmission model of Smith [46] by incorporating actuator disks to affect the flow turning due to steady loading and a formulation was derived for the sound pressure in a coupled rotor-OGV system. Later, in 2001 Hanson [56] adopted the cascade model due to Glegg [54] so that the effects of lean and sweep were treated but at the expense of the overlapped-cascade limitation of the Wiener-Hopf method. The resulting expressions were for tonal sound power. In later work Hanson [57, 58] extended the noise model to broadband sound power.

More recently, work on acoustic transmission loss through the rotor has been conducted by Posson and co-workers [70, 71, 72, 73, 74] (2007 onwards). In these papers the cascade formulation is that due to Glegg [54], with strip theory being used to treat the rotor geometry and the unsteady blade loading coupled to the duct modes to compute overall sound power transmitted along the duct.

1.4 Novel contributions of this thesis

The main contribution of this thesis is that it develops a comprehensive model for fan broadband noise prediction which addresses the issues of the behaviour of the turbulent wake convected onto the OGV, noise generation by the OGV cascade, and the subsequent blockage of sound by the rotor. A summary of the novel elements included in this work are given below:

- A model has been developed for the overlapping of self-preserving mean wakes due to a regular distribution of wake generating bodies that allows the properties of the individual mean wakes to be deduced from the characteristics of significantly overlapped mean wakes, as observed at downstream locations and permits the robust deduction of momentum thickness. These values are of fundamental importance in the prediction of turbulence parameters for the broadband noise calculations.

- Accurately describing the turbulence incident on the OGV is critical for making useful predictions of broadband interaction noise. Many noise prediction schemes use the results of rotor wake surveys undertaken by Gliebe et al. [19]; it is assumed that the rotor wake development observed in that study is applicable because of the universality of the individual wake self-preserving states. An analysis of fan test rig hotwire anemometry data has been undertaken which shows that the self-preservation states of rotor wakes are not universal, as the results exhibit sensitivity to working line and differ significantly from those recorded by [19].

- Observation that anisotropy in measured rotor wakes leads to underestimates of turbulence integral lengthscale when isotropy is assumed and that overestimates of the turbulence kinetic energy are observed when applying the inherently isotropic RANS CFD method to these anisotropic flows.

- Identification of frequency regimes, that are a function of mean flow Mach number, blade separation and stagger angle, in which the noise generated by a cascade of flat plate airfoils is insensitive to the interactions between blades. In these regimes single airfoil theory may be substituted for cascade theory, thus dramatically reducing the calculation time required for noise predictions.

- Presentation of a generalised formulation for noise scattering by a rotor. It is observed that the scattering predicted using the exact cascade model and the plane-wave assumption due to Kaji and Okazaki [67] are in very close agreement at low and high frequencies. A simplified frequency-averaged rotor transmission loss model is developed which indicates that rotor transmission loss is highest when broadband sound power incident on the rotor is concentrated on phase velocity angle bands that are poorly transmitted, which generally occurs when the power and transmission distributions are narrow at high mean flow Mach numbers.

The findings of this research have been published in The Journal of the Acoustical Society of America [75] and presented at the 17$^{\text{th}}$ and 18$^{\text{th}}$ AIAA/CEAS Aeroacoustics conferences [76, 77, 78].

1.5 Thesis overview

The significance of broadband rotor-OGV interaction noise means that it is important that accurate and practical methods are available for its prediction so that new engine designs and operating regimes can be assessed and refined prior to manufacture. This thesis concentrates on the broadband rotor-OGV interaction noise prediction methods, an approach that is divided as described below:

- A noise model to predict the sound power generated on an OGV impinged upon by a general spectrum of turbulence velocity is presented in Chapter 2. The model is

based on an exact cascade formulation that accounts for the interactions between the vanes of the OGV. The predicted spectral characteristics are explored in Chapter 3.

- Due to computational expense, evaluation of the exact cascade broadband noise model for rotor-OGV interaction noise is slow at high frequencies. An alternative analytical 'Single Airfoil' (SA) sound power model, which ignores the vane-to-vane interactions, is compared with the cascade model in Chapter 4 resulting in guidelines for the frequency regimes in which the SA noise model may be used instead of the exact cascade model.

- Noise generated on the OGV propagates to the forward arc by passing upstream through the rotor where some sound power will be reflected, resulting in a transmission loss. In Chapter 5 models are developed for the prediction and interpretation of the rotor transmission loss.

- The ability to predict the turbulence characteristics at the OGV, as required for performing noise predictions, depends on the presence of structure in the rotor wake and is in turn dependent on the onset of wake self-preservation. Self-preserving mean wakes behind a rotor will become overlapped when observed sufficiently far downstream. A method for the determination of the individual mean wake characteristics from overlapped mean wake observations is developed in Chapter 6. Application of the mean wake overlap model in Chapter 7 allows the robust calculation of the momentum thickness and in Chapter 8 allows the deduction of relations describing self-preserving wake development and hence prediction of the turbulence characteristics at the OGV leading edge locations as required for inputs to the noise model.

- In Chapter 9 the methods developed in earlier chapters are applied to the prediction of rear and forward arc noise from a fan test rig which are compared with experimental measurements.

Chapter 2

Model for the prediction of broadband noise radiated from a cascade interacting with velocity fluctuations

This chapter presents a model for the prediction of the sound power radiated from a two-dimensional cascade of flat plate airfoils interacting with arbitrary velocity perturbations. In Chapter 9 this model will be used to predict the broadband noise due to the interaction between rotor wake turbulence and downstream OGVs.

This radiated sound power model and the rotor sound power transmission loss model of Chapter 5 are both extensions of a general formulation for the acoustic pressure response of a cascade, derived by Smith [46] and Whitehead [47]. Due to the complex fan and flow geometries inherent to turbofan designs a number of simplifying assumptions are made which are presented in the following section. These assumptions are common to both the noise model and the rotor transmission model.

2.1 Assumptions for the cascade model

The fan blades and stator vanes within a turbofan engine have complex geometry where the stagger angle, lean angle, sweep angle, camber, thickness and shape of the blades vary across the radial span. Such complications make it necessary to adopt simplifying assumptions in order to develop broadband noise and multi-mode transmission models base on analytic and semi-analytic models rather than computationally expensive CFD methods. The assumptions and simplifications are listed below.

1. The rotor/stator is divided into annular strips. Each strip is unwrapped at its medial radius to form a two-dimensional blade row or 'cascade' of flat plate airfoils, as illustrated in Figures 2.1 and 2.2. Broadband noise contributions of overall noise sound power due to each strip are calculated and the total broadband noise prediction for the three-dimensional rotor/stator is obtained from the incoherent summation of the sound power from each strip. Further detail of the derivation of the cascade-defining parameters is given in Section 2.2.

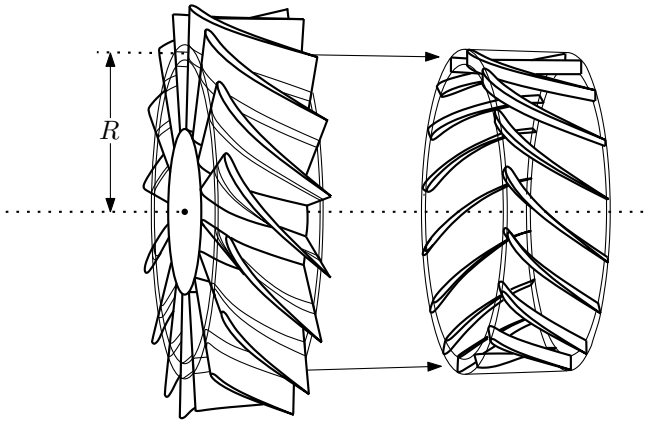

Figure 2.1 – Illustration of single annular strip taken from an OGV.

2. Turbulence impinging on the rotor/stator is assumed to be two-dimensional, i.e. the span-wise wavenumber component is assumed to be zero.

3. Broadband noise is assumed to be radiated from the rotor/stator into free field: the effects of the duct on radiated sound are ignored.

4. The blades of the rotor/stator in each strip are represented as flat plates of zero thickness (see Figure 2.2).

5. The blades/vanes of the rotor/stator are assumed to be identical and evenly spaced around its circumference.

6. The rotor/stator is assumed to have no steady loading so that the mean flow is assumed to impinge on the blades with zero angle of incidence (see Figure 2.3).

7. The Kutta condition is imposed, i.e. the pressure jump is continuous at the vane trailing edges [47].

8. Unsteady flow perturbations are assumed to be very small compared to the mean flow velocity so that linear theory may be employed.

9. Turbulence vorticity is assumed to be convected by the mean flow as a 'frozen gust pattern'. This assumption is representative of a case where the time taken for a vortex to sweep past the cascade is short compared to the turbulence decay timescale.

10. The flow is assumed to be subsonic and isentropic.

11. The medium is assumed to be inviscid so that boundary layers on vane surfaces are neglected.

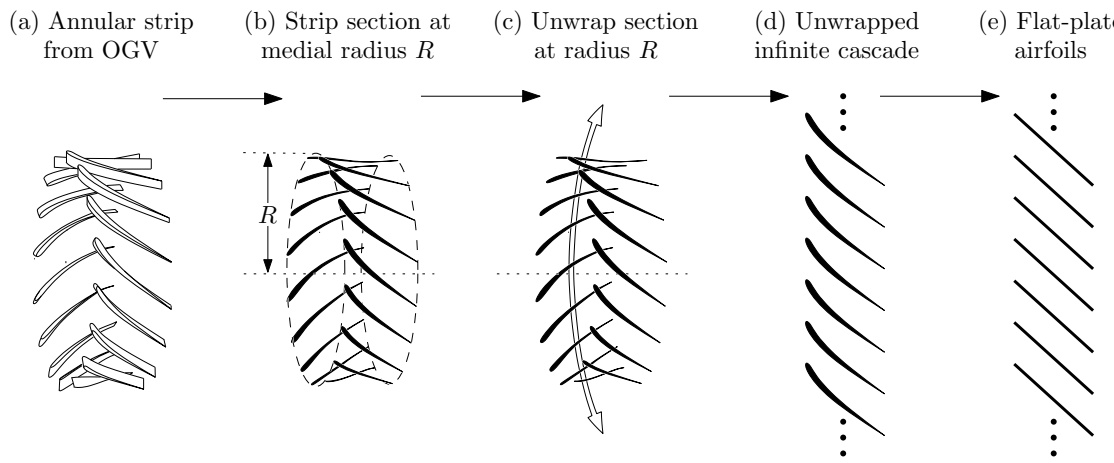

Figure 2.2 – OGV 'unwrapped' at strip medial radius R to form an infinite cascade of two-dimensional blades which are in turn modelled as flat-plate airfoils.

2.2 Cascade geometry

2.2.1 Defining annular strips

Consider an OGV with B_s evenly spaced vanes. The OGV is divided into a number of annular strips covering the entire span, as illustrated in Figure 2.1. The stagger angle, chord and aerodynamic behaviour of the vanes at each strip's medial radius, R, is assumed to be representative of the characteristics over the whole strip.

2.2.2 Unwrapping strip to define an infinite rectilinear cascade

Each strip is 'unwrapped' at its medial radius to form a two-dimensional vane row or 'cascade' as illustrated in Figure 2.2. The cascade is assumed to be of infinite extent in the gap-wise direction. Due to the spatial periodicity of the annular strip the vane pattern is assumed to repeat every B_s vanes. Finally the vanes are assumed to be flat-plate airfoils of zero thickness (Assumption 4 in Section 2.1). The flat-plate airfoils of the cascade are assumed to have identical stagger angle χ_s, chord c_s and inter-blade spacing $s_\mathrm{s} = 2\pi R/B_\mathrm{s}$.

A representation of the two-dimensional cascade is shown in Figure 2.3 indicating the coordinate systems used in the noise model. The unwrapped duct coordinate system has components $\mathbf{x} = (x_1, x_2)$ in the axial and gap-wise directions respectively with its origin at the leading edge of a cascade reference vane. The OGV-aligned $\mathbf{y}$ coordinate system

$$\begin{Bmatrix} y_1 \\ y_2 \end{Bmatrix} = \begin{bmatrix} \cos\theta_\mathrm{s} & \sin\theta_\mathrm{s} \\ -\sin\theta_\mathrm{s} & \cos\theta_\mathrm{s} \end{bmatrix} \begin{Bmatrix} x_1 \\ x_2 \end{Bmatrix} \tag{2.1}$$

also has its origin at the leading edge of the reference vane with y_1 lying along its chord and y_2 perpendicular to it.

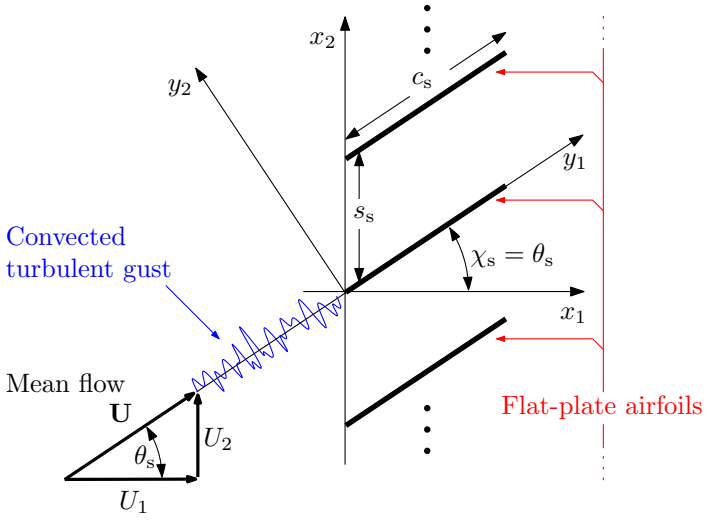

Figure 2.3 – Geometry of the infinite cascade of flat-plate airfoils representing stator vanes in a given annular strip. The mean flow **U** is aligned with the cascade vanes so that the stagger angle matches the whirl angle, $\chi_s = \theta_s$.

2.2.3 Velocity field

The velocity field associated with the turbulence is decomposed into a steady mean velocity vector **U** oriented parallel to the airfoil chords ($\theta_s = \chi_s$) plus an unsteady velocity fluctuation vector **w** due to the turbulent wakes shed by the upstream rotor.

U : The steady mean velocity has components (U_1, U_2) with respect to **x** that are assumed to be subsonic. In this model the radial component is assumed to be insignificant. By definition the **y** coordinate system is aligned with the mean flow so that its resolved components with respect to **y** are $(U, 0)$.

w : The unsteady velocity fluctuation vector **w** has resolved components (w_1, w_2) with respect to the **x** coordinate system and (w_{y_1}, w) with respect to **y**. The unsteady velocity component normal to the blade surface w is referred to as the upwash velocity.

2.3 Pressure radiated from cascade due to velocity perturbation

Several methods exist for the solution of the acoustic pressure field that is generated due to the interaction of a single-frequency harmonic gust with a flat-plate cascade, as discussed in Chapter 1. The results presented in this thesis have been obtained using the method due to Whitehead [47] and Smith [46], key features of which are summarised below.

1. The upwash velocity distribution on the vanes of the flat plate cascade is represented by a chord-wise distribution of bounded vortices. The fixed vane spacing s_s results in a constant inter-vane phase angle given by

$$\sigma = (k_1 \sin\theta_s + k_2 \cos\theta_s) s_s, \tag{2.2}$$

where k_1 and k_2 are the wavenumber components of the incident vortical gust with respect to the cascade-aligned $\mathbf{y}$ coordinate system.

2. The periodic nature of the bounded vortices allows the resulting vorticity field to be decomposed into continuous wave-like sheets of vorticity of order r which are referred to as 'cascade waves'. The rth cascade wave has wavenumber component ν_r in the x_2 direction given by

$$\nu_r = \frac{\sigma - 2\pi r}{s_\mathrm{s}} = \frac{(k_1 \sin\theta_\mathrm{s} + k_2 \cos\theta_\mathrm{s}) s_\mathrm{s} - 2\pi r}{s_\mathrm{s}}. \tag{2.3}$$

Wave solutions to the linearised Euler equations, shown in Equation (2.8), predict upstream and downstream-propagating acoustic waves equivalent to azimuthal modes of order r, hereafter indicated by superscript symbols + and − respectively. The axial wavenumber components corresponding to ν_r at some angular frequency ω are given by

$$\mu_r^{\pm} = -\frac{M_1(k - M_2\nu_r) \pm \sqrt{(k - M_2\nu_r)^2 - \beta_1^2\nu_r^2}}{\beta_1^2}, \tag{2.4}$$

where M_1 and M_2 are the Mach number components of the mean flow with respect to the $\mathbf{x}$ coordinate system, $\beta_1 = (1 - M_1^2)^{1/2}$ is the Prandtl-Glauert number corresponding to M_1 and $k = \omega/c_0$ is the free space acoustic wavenumber where c_0 is the sound speed.

3. The interaction of a single frequency harmonic gust of amplitude $\overline{w}$ with a flat-plate cascade results in upstream-propagating and downstream-propagating acoustic pressure fluctuations. An expression for $p^{\pm}$ at some location $\mathbf{x}$ at time t can be written as the sum of contributions due to cascade waves of order r

$$p^{\pm}(\mathbf{x}, t) = \rho_0 \overline{w} U \sum_{r=-\infty}^{\infty} R_r^{\pm}(\mathbf{k}, \omega) \exp\left\{\mathrm{i}(\omega t - \mu_r^{\pm} x_1 - \nu_r x_2)\right\}, \tag{2.5}$$

where $R_r^{\pm}$ represents the single-frequency cascade response function specifying the non-dimensional pressure amplitude due to the rth cascade wave and turbulence with wavenumber components $\mathbf{k} = (k_1, k_2)$. ρ_0 is the density of air.

2.4 Extension of single-frequency pressure formulation to broadband sound power

The preceding section summarised the main features of a model for the prediction of sound pressure due to the interaction of a single harmonic vortical gust with a cascade of flat-plate airfoils, culminating in Equation (2.5). In Chapter 5 this cascade pressure response will be extended to the case of incident acoustical waves in order to calculate the sound power transmitted through a rotor. However, the focus of the current chapter is to formulate an expression for the sound power radiated from an OGV due to turbulence comprised of a

continuum of wavenumber components, enabling the calculation of broadband rotor-stator interaction noise. The following section describes the generalisation of the incident gust.

2.4.1 Generalisation of upwash velocity using Fourier transform

The instantaneous acoustic pressure due to a two-dimensional turbulence gust with a continuum of wavenumber components k_1 and k_2 can be expressed by generalisation of Equation (2.5) formed by integrating over all frequency components and two-dimensional wavenumber components k_1 and k_2 as [56]

$$p^{\pm}(\mathbf{x},t) = \rho_0 U \iiint_{-\infty}^{\infty} \mathit{w}(\mathbf{k},\omega) \sum_{r=-\infty}^{\infty} R_r^{\pm}(\mathbf{k},\omega) \exp\left\{\mathrm{i}(\omega t - \mu_r^{\pm} x_1 - \nu_r x_2)\right\} \, \mathrm{d}^2\mathbf{k} \, \mathrm{d}\omega, \quad (2.6)$$

where $\mathit{w}(\mathbf{k},\omega)$ is the frequency-wavenumber upwash velocity spectrum given by the Fourier transform of the incident upwash velocity $w(\mathbf{x},t)$

$$\mathit{w}(\mathbf{k},\omega) = \left(\frac{1}{2\pi}\right)^3 \iiint_{-\infty}^{\infty} w(\mathbf{x},t) \exp\left\{-\mathrm{i}(\omega t - k_1 x_1 - k_2 x_2)\right\} \, \mathrm{d}^2\mathbf{x} \, \mathrm{d}t. \quad (2.7)$$

The frequency-wavenumber upwash velocity spectrum $\mathit{w}(\mathbf{k},\omega)$ is an averaged spectrum and as such is a statistical description of the non-deterministic upwash velocity w.

Velocity perturbations in the flow are assumed to be very small (Assumption 8 in Section 2.1). The flow can therefore be described in terms of the two-dimensional linearised momentum equations [46], expressed with respect to $\mathbf{x}$ as

$$\frac{\partial w_1}{\partial t} + U_1 \frac{\partial w_1}{\partial x_1} + U_2 \frac{\partial w_1}{\partial x_2} + \frac{1}{\rho_0} \frac{\partial p}{\partial x_1} = 0, \quad (2.8a)$$

$$\frac{\partial w_2}{\partial t} + U_1 \frac{\partial w_2}{\partial x_1} + U_2 \frac{\partial w_2}{\partial x_2} + \frac{1}{\rho_0} \frac{\partial p}{\partial x_2} = 0. \quad (2.8b)$$

In order to compute the sound intensity, and hence sound power, radiated from the cascade, we require the particle velocity components in the x_1 and x_2 directions. These may be deduced from Equations (2.6) and (2.8)

$$w_1^{\pm}(\mathbf{x},t) = \rho_0 U \iiint_{-\infty}^{\infty} \mathit{w}(\mathbf{k},\omega) \sum_{r=-\infty}^{\infty} \frac{\mu_r^{\pm}}{\rho_0(\omega - U_1\mu_r^{\pm} - U_2\nu_r)} R_r^{\pm}(\mathbf{k},\omega) \times \exp\left\{\mathrm{i}(\omega t - \mu_r^{\pm} x_1 - \nu_r x_2)\right\} \, \mathrm{d}^2\mathbf{k} \, \mathrm{d}\omega, \quad (2.9a)$$

$$w_2^{\pm}(\mathbf{x},t) = \rho_0 U \iiint_{-\infty}^{\infty} \mathit{w}(\mathbf{k},\omega) \sum_{r=-\infty}^{\infty} \frac{\nu_r}{\rho_0(\omega - U_1\mu_r^{\pm} - U_2\nu_r)} R_r^{\pm}(\mathbf{k},\omega) \times \exp\left\{\mathrm{i}(\omega t - \mu_r^{\pm} x_1 - \nu_r x_2)\right\} \, \mathrm{d}^2\mathbf{k} \, \mathrm{d}\omega. \quad (2.9b)$$

2.4.2 Acoustic intensity

The sound power generated by the cascade is obtained by spatial integration of the axial component of acoustic intensity over the duct cross-section. The axial component of the

instantaneous acoustic intensity in a uniform steady isentropic flow $\mathbf{U}$ is given by [60]

$$I_1^{\pm}(\mathbf{x},t) = \left(\frac{p^{\pm}(\mathbf{x},t)}{\rho_0} + \mathbf{U}\cdot\mathbf{w}^{\pm}(\mathbf{x},t)\right)\left(\rho_0 w_1^{\pm *}(\mathbf{x},t) + U_1\frac{p^{\pm *}(\mathbf{x},t)}{c_0^2}\right), \tag{2.10}$$

where the superscript $*$ denotes complex conjugation.

The pressure and velocity terms in Equation (2.10) are dependent on the frequency-wavenumber upwash velocity spectrum $\mathcal{w}(\mathbf{k},\omega)$, as described in Section 2.4.1. Their values are therefore not knowable at a given instant in time but are characterised in an average sense. Assuming identical blades, and therefore identical blade wake turbulence statistics, we may assume that the turbulent wake statistics, and therefore the statistics of the generated noise, are identical over a single blade passage T, suggesting the use of ensemble-averaging. The expected value operator $\mathrm{E}[\cdot]$ is used to indicate the ensemble-average value at $\mathbf{x}$ as a function of time, so that

$$\mathrm{E}\left[I_1^{\pm}(\mathbf{x},t)\right] = \frac{1}{K}\sum_{k=1}^{K} I(\mathbf{x},t+kT), \tag{2.11}$$

where T is the period of blade passage, $k\in\mathbb{N}$ is the cycle index where there are K cycles in the average. Thus Equation (2.10) is expanded by substitution of Equations (2.6) and (2.9), yielding

$$\begin{aligned}\mathrm{E}\left[I_1^{\pm}(\mathbf{x},t)\right] = \mathrm{Re}\Bigg\{&\frac{\rho_0}{c_0}U^2\iiiint_{-\infty}^{\infty}\mathrm{E}\left[\mathcal{w}(\mathbf{k},\omega)\mathcal{w}^*(\mathbf{k}',\omega')\right]\\
&\times\sum_{r=-\infty}^{\infty}\sum_{r'=-\infty}^{\infty}\frac{\omega/c_0\left[\mu_{r'}^{\pm *}+M_1(\omega'/c_0-M_1\mu_{r'}^{\pm *}-M_2\nu_{r'})\right]}{\left(\omega/c_0-M_1\mu_r^{\pm}-M_2\nu_r\right)\left(\omega'/c_0-M_1\mu_{r'}^{\pm *}-M_2\nu_{r'}\right)}\\
&\times R_r^{\pm}(\mathbf{k},\omega)\,R_{r'}^{\pm *}(\mathbf{k}',\omega')\exp\left\{\mathrm{i}(\omega-\omega')t\right\}\\
&\times\exp\left\{-\mathrm{i}\left[\left(\mu_r^{\pm}-\mu_{r'}^{\pm *}\right)x_1+(\nu_r-\nu_{r'})\,x_2\right]\right\}\,\mathrm{d}^2\mathbf{k}\,\mathrm{d}^2\mathbf{k}'\,\mathrm{d}\omega\,\mathrm{d}\omega'\Bigg\}.\end{aligned} \tag{2.12}$$

2.4.3 General form of the velocity wavenumber-frequency cross spectrum $\mathrm{E}\left[\mathcal{w}(\mathbf{k},\omega)\mathcal{w}^*(\mathbf{k}',\omega')\right]$

The definition of $\mathcal{w}(\mathbf{k},\omega)$ is given in Equation (2.7) so that the expected value of the upwash velocity wavenumber-frequency cross spectrum can be written

$$\begin{aligned}\mathrm{E}\left[\mathcal{w}(\mathbf{k},\omega)\mathcal{w}^*(\mathbf{k}',\omega')\right] = \frac{1}{(2\pi)^6}&\iiiint_{-\infty}^{\infty}\mathrm{E}\left[w(\mathbf{x},t)w^*(\mathbf{x}',t')\right]\\
&\times\exp\left\{-\mathrm{i}(\omega t-\omega' t'-\mathbf{k}\cdot\mathbf{x}+\mathbf{k}'\cdot\mathbf{x}')\right\}\,\mathrm{d}^2\mathbf{x}\,\mathrm{d}^2\mathbf{x}'\,\mathrm{d}t\,\mathrm{d}t'.\end{aligned} \tag{2.13}$$

where it is understood that $\mathrm{E}[\cdot]$ represents the expectation over numerous blade passages in the sense of Equation (2.11).

For a typical rotor wake the perturbation velocities $\mathbf{w}$ are very much smaller than the mean flow velocity $\mathbf{U}$ and hence the gust pattern changes only slightly as it convects

past the cascade leading edge (Assumption 9 in Section 2.1). The velocity disturbance is therefore assumed to be independent of time in the flow-fixed frame of reference $\tilde{\mathbf{x}} = \mathbf{x} - \mathbf{U}t$. Writing

$$\tilde{\mathbf{x}}' = \tilde{\mathbf{x}} + \delta\tilde{\mathbf{x}}, \tag{2.14a}$$

$$t' = t + \tau, \tag{2.14b}$$

Equation (2.13) can be rewritten as*

$$\begin{aligned} \mathrm{E}\left[w(\mathbf{k},\omega)w^*(\mathbf{k}',\omega')\right] = \frac{1}{(2\pi)^4} \iiiint_{-\infty}^{\infty} & \mathrm{E}\left[w(\tilde{\mathbf{x}})w^*(\tilde{\mathbf{x}}+\delta\tilde{\mathbf{x}})\right] \\ & \times \exp\left\{-\mathrm{i}(\mathbf{k}'-\mathbf{k})\cdot\tilde{\mathbf{x}}\right\} \exp\left\{-\mathrm{i}\mathbf{k}'\cdot\delta\tilde{\mathbf{x}}\right\}\ \mathrm{d}^2\tilde{\mathbf{x}}\,\mathrm{d}^2\delta\tilde{\mathbf{x}} \\ & \times \frac{1}{2\pi}\int_{-\infty}^{\infty} \exp\left\{-\mathrm{i}[(\omega-\mathbf{k}\cdot\mathbf{U})-(\omega'-\mathbf{k}'\cdot\mathbf{U})]t\right\}\ \mathrm{d}t \\ & \times \frac{1}{2\pi}\int_{-\infty}^{\infty} \exp\left\{\mathrm{i}(\omega'-\mathbf{k}'\cdot\mathbf{U})\tau\right\}\ \mathrm{d}\tau, \end{aligned} \tag{2.15}$$

where $\mathrm{E}\left[w(\tilde{\mathbf{x}})w^*(\tilde{\mathbf{x}}+\delta\tilde{\mathbf{x}})\right]$ corresponds to the general definition of an autocorrelation function $\mathcal{R}_{\mathrm{ww}}(\tilde{\mathbf{x}},\delta\tilde{\mathbf{x}})$ while the t and τ integrations are recognised as the Fourier transform representation of the Dirac delta function so Equation (2.15) may be simplified to

$$\begin{aligned} \mathrm{E}\left[w(\mathbf{k},\omega)w^*(\mathbf{k}',\omega')\right] = \frac{1}{(2\pi)^4} \iiiint_{-\infty}^{\infty} & \mathcal{R}_{\mathrm{ww}}(\tilde{\mathbf{x}},\delta\tilde{\mathbf{x}}) \\ & \times \exp\left\{-\mathrm{i}(\mathbf{k}'-\mathbf{k})\cdot\tilde{\mathbf{x}}\right\} \exp\left\{-\mathrm{i}\mathbf{k}'\cdot\delta\tilde{\mathbf{x}}\right\}\ \mathrm{d}^2\tilde{\mathbf{x}}\,\mathrm{d}^2\delta\tilde{\mathbf{x}} \\ & \times \delta(\omega-\mathbf{k}\cdot\mathbf{U})\ \delta(\omega'-\mathbf{k}'\cdot\mathbf{U}). \end{aligned} \tag{2.16}$$

2.4.4 Simplification of wake turbulence autocorrelation function

The description of the wake developed by Ventres et al. [79] and subsequently employed by, e.g. Hanson [56], Nallasamy and Envia [80], Jurdic et al. [81], Lloyd and Peake [64], and Posson et al. [82] modulates the velocity and not the correlation. Where wake widths are large with respect to the rotor blade spacing s_{r} the adjacent wakes become correlated, leading to unrealistic scaling of the mean-square acoustic pressure as B_{s}^2. It will be shown in Chapter 8 that adjacent wake overlap is a common phenomenon in rotor wakes.

The analysis of the hotwire turbulence velocity behind a rotor by Jurdic et al. [22] has shown that its correlation structure is consistent with that of isotropic turbulence $\boldsymbol{\rho}_{\mathrm{ww}}(\delta\tilde{\mathbf{x}})$ which is assumed to be homogeneous, and therefore a function of only the separation distance $\delta\tilde{\mathbf{x}}$, modulated by a periodic wake profile which is a function of position $\mathbf{x}$ in the wake. This representation of the turbulence autocorrelation yields adjacent wakes that are uncorrelated, regardless of the width of the wake relative to the rotor blade spacing s_{r}.

The rotor wake is separated into terms that are purely dependent on $\tilde{\mathbf{x}} = \mathbf{x} - \mathbf{U}t$ and

*The change of variables given by Equations (2.14) has the property that its Jacobian $|\mathbf{J}| = 1$.

the 'separation' vector $\delta\tilde{\mathbf{x}}$ in the form

$$\mathcal{R}_{\mathrm{ww}}(\tilde{\mathbf{x}}, \delta\tilde{\mathbf{x}}) = \overline{w_0^2} H(\tilde{\mathbf{x}}) \boldsymbol{\rho}_{\mathrm{ww}}(\delta\tilde{\mathbf{x}}), \tag{2.17}$$

where $\overline{w_0^2}$ is the maximum mean-square turbulence velocity at the wake centreline, $\boldsymbol{\rho}_{\mathrm{ww}}(\delta\tilde{\mathbf{x}})$ is the autocorrelation function of homogeneous isotropic turbulence velocity, normalised such that $\boldsymbol{\rho}_{\mathrm{ww}}(0) = 1$, and $H(\tilde{\mathbf{x}})$ is a non-dimensional turbulent wake velocity correlation profile, the properties of which are developed in the following section. The advantages of this turbulent wake description compared to that of Ventres et al. will be made clear in Section 2.4.9.

2.4.5 Properties of the turbulent wake profile function $H(\tilde{\mathbf{x}})$

1. In the stationary duct-aligned frame of reference, $\mathbf{x}$, a reference point on H moves in the azimuthal direction with velocity $R\Omega$.

2. H is time-independent when viewed in the frame of reference moving with and aligned to the rotor $\mathbf{z} = (x_1, x_2 - R\Omega t)$.

3. For the sake of simplicity H is assumed to be time-independent with respect to the fluid-fixed frame of reference $\tilde{\mathbf{x}} = \mathbf{x} - \mathbf{U}t$. The turbulence model shall be applied to noise calculations at discrete downstream locations. In this context the turbulent wake development is of little concern.

4. At any given instant H shall be assumed to be invariant along vectors aligned with $\mathbf{U}_{\mathrm{r}}$, the mean flow as seen in the rotor-fixed frame of reference $\mathbf{z}$.

5. Wake statistics are assumed to be identical for all rotor blades so that H is spatially periodic in the x_2 direction over $s_{\mathrm{r}} = 2\pi R/B_{\mathrm{r}}$ and time-periodic over $T = s_{\mathrm{r}}/R\Omega$.

The turbulent wake velocity correlation modulation function H is an infinite train of individual wake correlation profiles, $h(\mathbf{x}, t, n)$, and is of the form

$$H(\mathbf{x}, t) = \sum_{n=-\infty}^{\infty} h(\mathbf{x}, t, n). \tag{2.18}$$

The characteristics of $h(\mathbf{x}, t, n)$ are defined in the following section.

2.4.6 Characteristics of individual wake profile functions $h(\mathbf{x}, t, n)$

Consider the wake due to an isolated 'reference' wake generator ($n = 0$) located at (0,0) in a mean flow with $\theta_{\mathrm{r}} = 0$ at time $t = 0$. The corresponding wake profile h is defined so that its centreline is at $x_2 = 0$ for all x_1

$$h(\mathbf{x}, t = 0, n = 0) = h(x_2). \tag{2.19}$$

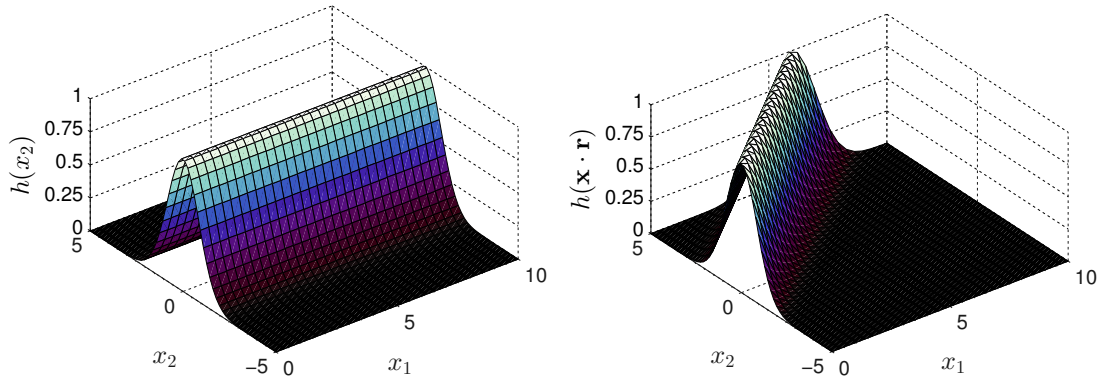

(a) $h(x_2)$, equivalent to $\theta_\mathrm{r} = 0$ and $t = 0$ **(b)** $h(\mathbf{x}\cdot\mathbf{r})$, equivalent to $\theta_\mathrm{r} = 40°$ and $t = 0$

Figure 2.4 – Individual turbulent wake correlation modulation function defined as function of x_2 and as a function of the skew coordinate transformation $\mathbf{x}\cdot\mathbf{r}$.

Figure 2.4a shows an example of Equation (2.19) evaluated using a Gaussian wake function for $h(x_2)$.

For a wake generated in a mean flow with arbitrary whirl angle θ_r the same wake profile function can be used but its argument must be zero along the line parallel to $\mathbf{U}_\mathrm{r}$ that passes through (0,0). The skew coordinate transformation vector $\mathbf{r}$ is defined

$$\mathbf{r} = (-\tan\theta_\mathrm{r}, 1). \tag{2.20}$$

Taking the scalar product of this with $\mathbf{x}$ yields the appropriate argument, so that

$$h(\mathbf{x}, t = 0, n = 0) = h(\mathbf{x}\cdot\mathbf{r}), \tag{2.21}$$

and the individual wake correlation modulation function is correctly aligned. Figure 2.4b shows the example Gaussian wake profile generated with Equation (2.21) for $\theta_\mathrm{r} = 40°$. Note that the x_2 profile at $x_1 = 0$ is identical to that seen in Figure 2.4a.

For arbitrary t the expression shown in Equation (2.21) is valid for arbitrary t if the frame of reference moves with the fluid. This is achieved by substitution of $\tilde{\mathbf{x}}$ in place of $\mathbf{x}$ (see Item 3 in Section 2.4.5). The nth wake is described by the addition of ns_r to the argument so that

$$h(\mathbf{x}, t, n) = h(\tilde{\mathbf{x}}\cdot\mathbf{r} + ns_\mathrm{r}), \tag{2.22}$$

and so the wake correlation modulation function of Equation (2.18) becomes

$$H(\mathbf{x}, t) = H(\tilde{\mathbf{x}}). \tag{2.23}$$

2.4.7 Fourier decomposition of turbulent wake function $H(\tilde{\mathbf{x}})$

The wake function defined by Equations (2.18) and (2.22) is periodic in the $\hat{x}_2$ direction and may be expressed using the Poisson summation formula as

$$H(\tilde{\mathbf{x}}) = \frac{1}{s_\mathrm{r}} \sum_{l=-\infty}^{\infty} \hat{h}_l \exp\left\{-\mathrm{i}\Delta k_l\, \tilde{\mathbf{x}} \cdot \mathbf{r}\right\}, \tag{2.24}$$

where Δk_l is the lth harmonic of the azimuthal wavenumber

$$\Delta k_l = \frac{2\pi l}{s_\mathrm{r}}, \tag{2.25}$$

and $\hat{h}_l$ is the lth Fourier coefficient of h

$$\hat{h}_l = \int_{-\infty}^{\infty} h(\tilde{\mathbf{x}} \cdot \mathbf{r}) \exp\left\{\mathrm{i}\Delta k_l\, \tilde{\mathbf{x}} \cdot \mathbf{r}\right\}\, \mathrm{d}\tilde{x}_2. \tag{2.26}$$

Substitution of Equations (2.17) and (2.24) into Equation (2.15) and separation of $\tilde{\mathbf{x}}$ and $\delta\tilde{\mathbf{x}}$ integrals yields

$$\begin{aligned}
\mathrm{E}\left[w(\mathbf{k},\omega)w^*(\mathbf{k}',\omega')\right] = \sum_{l=-\infty}^{\infty} \frac{\hat{h}_l\, \overline{w_0^2}}{s_\mathrm{r}}\, \delta(\omega - \mathbf{k}\cdot\mathbf{U})\, \delta(\omega' - \mathbf{k}'\cdot\mathbf{U}) \\
\times \frac{1}{(2\pi)^2} \iint_{-\infty}^{\infty} \boldsymbol{\rho}_\mathrm{ww}(\delta\tilde{\mathbf{x}})\, \exp\left\{-\mathrm{i}\mathbf{k}'\cdot\delta\tilde{\mathbf{x}}\right\}\, \mathrm{d}^2\delta\tilde{\mathbf{x}} \\
\times \frac{1}{(2\pi)^2} \iint_{-\infty}^{\infty} \exp\left\{-\mathrm{i}(\mathbf{k}' - \mathbf{k} + \Delta k_l\, \mathbf{r})\cdot\tilde{\mathbf{x}}\right\}\, \mathrm{d}^2\tilde{\mathbf{x}}.
\end{aligned} \tag{2.27}$$

The second line of Equation (2.27) represents the definition of the normalised two-dimensional wavenumber spectrum of homogeneous wake turbulence

$$\phi(\mathbf{k}) = \frac{1}{(2\pi)^2} \iint_{-\infty}^{\infty} \boldsymbol{\rho}_\mathrm{ww}(\delta\tilde{\mathbf{x}}) \exp\left\{-\mathrm{i}\mathbf{k}\cdot\delta\tilde{\mathbf{x}}\right\}\, \mathrm{d}^2\delta\tilde{\mathbf{x}}. \tag{2.28}$$

The $\mathrm{d}\tilde{\mathbf{x}}$ integrations in Equation (2.27) are Fourier transform representations of Dirac delta functions so that Equation (2.27) reduces to

$$\mathrm{E}\left[w(\mathbf{k},\omega)w^*(\mathbf{k}',\omega')\right] = \sum_{l=-\infty}^{\infty} \frac{\hat{h}_l\, \overline{w_0^2}}{s_\mathrm{r}}\, \phi(\mathbf{k}')\, \delta(\mathbf{k}' - \mathbf{k} + \Delta k_l\, \mathbf{r})\, \delta(\omega - \mathbf{k}\cdot\mathbf{U})\, \delta(\omega' - \mathbf{k}'\cdot\mathbf{U}). \tag{2.29}$$

Combining Equation (2.20) with Equation (2.1) it is possible to write expressions for the components of $\Delta k_l\, \mathbf{r}$ resolved in the flow-aligned $\mathbf{y}$ coordinate directions

$$\Delta k_l\, \mathbf{r}\cdot\hat{\mathbf{y}}_1 = \Delta k_l \frac{\sin(\theta_\mathrm{s} - \theta_\mathrm{r})}{\cos\theta_\mathrm{r}} \equiv \Delta k_{1,l}, \tag{2.30a}$$

$$\Delta k_l\, \mathbf{r}\cdot\hat{\mathbf{y}}_2 = \Delta k_l \frac{\cos(\theta_\mathrm{s} - \theta_\mathrm{r})}{\cos\theta_\mathrm{r}} \equiv \Delta k_{2,l}, \tag{2.30b}$$

whilst, by definition

$$\mathbf{k} \cdot \mathbf{U} = k_1 U. \tag{2.30c}$$

Substituting Equation (2.29) and Equations (2.30) into Equation (2.12) gives

$$\begin{aligned}
\mathrm{E}\left[I_1^{\pm}(\mathbf{x},t)\right] = \mathrm{Re}\Bigg\{ & \frac{\rho_0}{c_0} \iiiint\limits_{-\infty}^{\infty} \sum_{l=-\infty}^{\infty} \frac{\hat{h}_l \, \overline{w_0^2}}{s_\mathrm{r}} \, \phi(k_1', k_2') \\
& \times \delta(k_1' - k_1 + \Delta k_{1,l}) \, \delta(k_2' - k_2 + \Delta k_{2,l}) \\
& \times U\delta(\omega - k_1 U) \, U\delta(\omega' - k_1' U) \\
& \times \sum_{r=-\infty}^{\infty} \sum_{r'=-\infty}^{\infty} R_r^{\pm}(k_1, k_2, \omega) \, R_{r'}^{\pm *}(k_1', k_2', \omega') \\
& \times \frac{\omega/c_0 \left[\mu_{r'}^{\pm *} + M_1(\omega'/c_0 - M_1 \mu_{r'}^{\pm *} - M_2 \nu_{r'})\right]}{\left(\omega/c_0 - M_1 \mu_r^{\pm} - M_2 \nu_r\right)\left(\omega'/c_0 - M_1 \mu_{r'}^{\pm *} - M_2 \nu_{r'}\right)} \\
& \times \exp\left\{\mathrm{i}\left[(\omega - \omega')\, t - \left(\mu_r^{\pm} - \mu_{r'}^{\pm *}\right) x_1 - (\nu_r - \nu_{r'})\, x_2\right]\right\} \, \mathrm{d}k_1 \, \mathrm{d}k_1' \, \mathrm{d}k_2 \, \mathrm{d}k_2' \, \mathrm{d}\omega \, \mathrm{d}\omega' \Bigg\}.
\end{aligned} \tag{2.31}$$

Recalling the property of the Dirac delta function $\delta(ax) = \delta(x)/|a|$ and performing the integrations over k_1, k_1' and k_2' , the terms $U\delta(\omega - k_1 U)$ and $U\delta(\omega' - k_1' U)$ arising from the frozen gust assumption in Equation (2.16) imply that k_1 and k_1' at any frequency ω take the values

$$k_1 = \omega/U \equiv K_1, \qquad k_1' = \omega'/U \equiv K_1', \tag{2.32a}$$

whilst, from the k_2' integral

$$k_2' = k_2 - \Delta k_{2,l}, \tag{2.32b}$$

so that Equation (2.31) reduces to

$$\begin{aligned}
\mathrm{E}\left[I_1^{\pm}(\mathbf{x},t)\right] = \mathrm{Re}\Bigg\{ & \frac{\rho_0}{c_0} \iiint\limits_{-\infty}^{\infty} \sum_{l=-\infty}^{\infty} \frac{\hat{h}_l \, \overline{w_0^2}}{s_\mathrm{r}} \, \phi(K_1', k_2 - \Delta k_{2,l}) \\
& \times U \, \delta(\omega' - \omega + U\Delta k_{1,l}) \\
& \times \sum_{r=-\infty}^{\infty} \sum_{r'=-\infty}^{\infty} R_r^{\pm}(k_2, \omega) \, R_{r'}^{\pm *}(k_2 - \Delta k_{2,l}, \omega') \\
& \times \frac{MK_1 \left[\mu_{r'}^{\pm *} + M_1(MK_1' - M_1 \mu_{r'}^{\pm *} - M_2 \nu_{r'})\right]}{\left(MK_1 - M_1 \mu_r^{\pm} - M_2 \nu_r\right)\left(MK_1' - M_1 \mu_{r'}^{\pm *} - M_2 \nu_{r'}\right)} \\
& \times \exp\left\{\mathrm{i}\left[(\omega - \omega')\, t - \left(\mu_r^{\pm} - \mu_{r'}^{\pm *}\right) x_1 - (\nu_r - \nu_{r'})\, x_2\right]\right\} \, \mathrm{d}k_2 \, \mathrm{d}\omega \, \mathrm{d}\omega' \Bigg\}.
\end{aligned} \tag{2.33}$$

The delta function term under the ω' integration will give

$$\omega' = \omega - U\Delta k_{1,l}. \tag{2.34}$$

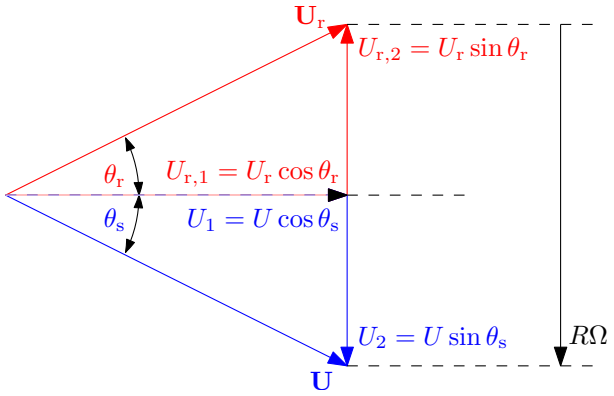

Figure 2.5 – Relation between whirl angles and velocity components of mean flow as seen in stationary and rotor-fixed frames of reference.

The relation between the x_2 component of the mean flow as seen in the stationary and rotor-fixed frames of reference, illustrated in Figure 2.5 is

$$U_2 = U_{\mathrm{r},2} + R\Omega. \tag{2.35}$$

The axial component of the mean flow velocity is invariant when seen from the rotor-fixed or the stationary frame of reference so that $U_{\mathrm{r},1} = U_1$ (see Figure 2.5) and so Equation (2.35) can be rearranged to yield

$$R\Omega = U\frac{\sin(\theta_\mathrm{s} - \theta_\mathrm{r})}{\cos\theta_\mathrm{r}}. \tag{2.36}$$

Combining Equations (2.25), (2.30a) and (2.36) allows simplification of the last term of Equation (2.34)

$$U\Delta k_{1,l} = lB_\mathrm{r}\Omega. \tag{2.37}$$

Performing the integration over ω' in Equation (2.33) and using Equation (2.37) yields

$$\begin{aligned}
\mathrm{E}\left[I_1^{\pm}(\mathbf{x},t)\right] = \mathrm{Re}\Bigg\{ & \rho_0 M \iint_{-\infty}^{\infty} \sum_{l=-\infty}^{\infty} \frac{\hat{h}_l\,\overline{w_0^2}}{s_\mathrm{r}}\,\phi(K_1 - \Delta k_{1,l}, k_2 - \Delta k_{2,l}) \\
& \times \sum_{r=-\infty}^{\infty}\sum_{r'=-\infty}^{\infty} R_r^{\pm}(k_2,\omega)\,R_{r'}^{\pm *}(k_2 - \Delta k_{2,l}, \omega - lB_\mathrm{r}\Omega) \\
& \times \frac{MK_1\left[\mu_{r'}^{\pm *} + M_1(M(K_1 - \Delta k_{1,l}) - M_1\mu_{r'}^{\pm *} - M_2\nu_{r'})\right]}{\left(MK_1 - M_1\mu_r^{\pm} - M_2\nu_r\right)\left(M(K_1 - \Delta k_{1,l}) - M_1\mu_{r'}^{\pm *} - M_2\nu_{r'}\right)} \\
& \times \exp\left\{\mathrm{i}\left[mB_\mathrm{r}\Omega t - \left(\mu_r^{\pm} - \mu_{r'}^{\pm *}\right)x_1 - (\nu_r - \nu_{r'})\,x_2\right]\right\}\,\mathrm{d}k_2\,\mathrm{d}\omega\Bigg\}.
\end{aligned} \tag{2.38}$$

This expression represents the instantaneous ensemble-averaged time-dependent axial component of upstream and downstream acoustic intensity due to wake turbulence periodically interacting with the OGVs. Equation (2.38) is in the form of the sum of intensity contri-

butions over all frequencies, such that

$$\mathrm{E}\left[I_1^{\pm}(\mathbf{x},t)\right] = \int_{-\infty}^{\infty} \mathrm{E}\left[I_1^{\pm}(\mathbf{x},t,\omega)\right]\ \mathrm{d}\omega. \tag{2.39}$$

Comparison of Equation (2.39) with Equation (2.38) defines the ensemble-averaged time-dependent acoustic intensity spectrum in the form of a Fourier series

$$\mathrm{E}\left[I_1^{\pm}(\mathbf{x},t,\omega)\right] = \mathrm{Re}\Big\{ \sum_{l=-\infty}^{\infty} I_{1,l}^{\pm}(\omega,\mathbf{x}) \exp\left\{\mathrm{i}lB_\mathrm{r}\Omega t\right\} \Big\}, \tag{2.40}$$

where $I_{1,l}^{\pm}(\omega,\mathbf{x})$ are the time-independent axial intensity spectra associated with the lth harmonic of the response to the periodic rotor blade passage, given by

$$\begin{aligned} I_{1,l}^{\pm}(\omega,\mathbf{x}) = \rho_0 M \int_{-\infty}^{\infty} & \frac{\hat{h}_l\,\overline{w_0^2}}{s_\mathrm{r}}\ \phi(K_1-\Delta k_{1,l}, k_2-\Delta k_{2,l}) \\ & \times \sum_{r=-\infty}^{\infty}\sum_{r'=-\infty}^{\infty} R_r^{\pm}(k_2,\omega)\ R_{r'}^{\pm *}(k_2-\Delta k_{2,l}, \omega - lB_\mathrm{r}\Omega) \\ & \times \frac{MK_1\left[\mu_{r'}^{\pm *} + M_1(M(K_1-\Delta k_{1,l}) - M_1\mu_{r'}^{\pm *} - M_2\nu_{r'})\right]}{\left(MK_1 - M_1\mu_r^{\pm} - M_2\nu_r\right)\left(M(K_1-\Delta k_{1,l}) - M_1\mu_{r'}^{\pm *} - M_2\nu_{r'}\right)} \\ & \times \exp\left\{-\mathrm{i}\left[\left(\mu_r^{\pm} - \mu_{r'}^{\pm *}\right)x_1 + \left(\nu_r - \nu_{r'}\right)x_2\right]\right\}\ \mathrm{d}k_2, \end{aligned} \tag{2.41}$$

in which the acoustic wavenumbers $\mu_r^{\pm}$, $\mu_{r'}^{\pm *}$, ν_r and $\nu_{r'}$ defined in Equations (2.3) and (2.4) are given by

$$\mu_r^{\pm} = -\frac{M_1[MK_1 - M_{s,2}\nu_r] \pm \sqrt{[MK_1 - M_{s,2}\nu_r]^2 - \beta_1^2\nu_r^2}}{\beta_1^2}, \tag{2.42a}$$

$$\nu_r = \frac{[K_1\sin\theta_\mathrm{s} + k_2\cos\theta_\mathrm{s}]s_\mathrm{s} - 2\pi r}{s_\mathrm{s}}, \tag{2.42b}$$

$$\mu_{r'}^{\pm *} = -\frac{M_1[M(K_1-\Delta k_{1,l}) - M_{s,2}\nu_{r'}] \pm \sqrt{[M(K_1-\Delta k_{1,l}) - M_{s,2}\nu_{r'}]^2 - \beta_1^2\nu_{r'}^2}}{\beta_1^2}, \tag{2.42c}$$

$$\nu_{r'} = \frac{[(K_1-\Delta k_{1,l})\sin\theta_\mathrm{s} + k_2\cos\theta_\mathrm{s}]s_\mathrm{s} - 2\pi r}{s_\mathrm{s}} + \Delta k_l. \tag{2.42d}$$

Equation (2.40) defines the instantaneous intensity spectrum. Owing to the periodicity assumptions made about the turbulence statistics the intensity spectrum is predicted to vary periodically with a fundamental frequency equal to the blade passing frequency (BPF). The concept of the time-frequency (Wigner-Ville) representation for rotor-OGV broadband interaction noise does not appear to be well recognised in the literature. A more detailed discussion of this property can be found in Jurdic et al. [22].

2.4.8 Broadband power spectrum $\mathcal{P}^{\pm}(\omega)$

The previous section develops an expression for the time-dependent axial acoustic intensity spectrum due to the periodically varying ensemble-averaged turbulence velocity in the

wake of a rotor in the form of a Fourier series (see Equations (2.40) and (2.41)). This formulation reveals that the intensity spectrum varies periodically in time as a result of periodic modulation of assumed homogeneous turbulence that impinges upon the stator vanes.

In Chapter 9 the results of the sound power model are compared with experimental measurements of sound power. Experimental sound power spectra are inferred from time-averaged records of acoustic pressure measurements made over time durations much longer than the blade passage period T. These measured spectra therefore represent *equivalent* spectra with stationarity assumed. To allow valid comparison between predictions and measurements it is therefore necessary to compute the time-average spectra from Equation (2.40).

The time-average of the ensemble-average axial acoustic intensity is given by

$$\left\langle I_1^{\pm}(\omega,\mathbf{x})\right\rangle = \lim_{T\to\infty}\frac{1}{T}\int_0^T \mathrm{E}\left[I_1^{\pm}(\mathbf{x},t,\omega)\right]\,\mathrm{d}t. \tag{2.43}$$

Applying this to the Fourier series expression in Equation (2.40) will result in a cancellation of all higher order contributions ($|l|>0$) in the limit $T\to\infty$ so that only the $l=0$ term contributes to the sound intensity in the long-term average. This term refers to axisymmetric intensity because it is constant with respect to x_2. The time-averaged axial intensity spectrum is now expressed as

$$\begin{aligned}\left\langle I_1^{\pm}(\omega,\mathbf{x})\right\rangle = \mathrm{Re}\Bigg\{&\rho_0 M\int_{-\infty}^{\infty}\langle\overline{w^2}\rangle\,\phi(K_1,k_2)\sum_{r=-\infty}^{\infty}\sum_{r'=-\infty}^{\infty}R_r^{\pm}(k_2,\omega)\,R_{r'}^{\pm *}(k_2,\omega)\\ &\times\frac{MK_1\left[\mu_{r'}^{\pm *}+M_1(MK_1-M_1\mu_{r'}^{\pm *}-M_2\nu_{r'})\right]}{\left(MK_1-M_1\mu_r^{\pm}-M_2\nu_r\right)\left(MK_1-M_1\mu_{r'}^{\pm *}-M_2\nu_{r'}\right)}\\ &\times\exp\left\{-\mathrm{i}\left[\left(\mu_r^{\pm}-\mu_{r'}^{\pm *}\right)x_1+\left(\nu_r-\nu_{r'}\right)x_2\right]\right\}\,\mathrm{d}k_2\Bigg\},\end{aligned} \tag{2.44}$$

where $\langle\overline{w^2}\rangle$ is the mean-square turbulence velocity averaged over a complete blade passage $\gamma=2\pi/B_\mathrm{r}$ given by

$$\langle\overline{w^2}\rangle=\frac{B_\mathrm{r}}{2\pi}\int_0^{2\pi/B_\mathrm{r}}\overline{w_0^2}\,\mathrm{d}\gamma=\frac{\hat{h}_0\overline{w_0^2}}{s_\mathrm{r}}, \tag{2.45}$$

since $\hat{h}_0/s_\mathrm{r}$ is the mean value of the normalised unsteady mean-square velocity profile H over a blade passage.

The sound power spectral density per unit span is now found by gap-wise integration of this time-averaged ensemble-averaged axial acoustic intensity over a distance corresponding to a single complete circumference $2\pi R=B_\mathrm{s}s_\mathrm{s}$

$$\mathcal{P}^{\pm}(\omega)=\int_0^{B_\mathrm{s}s_\mathrm{s}}\left\langle I_1^{\pm}(\omega,\mathbf{x})\right\rangle\,\mathrm{d}x_2. \tag{2.46}$$

In Equation (2.43) the gap-wise wavenumber components ν_r and $\nu_{r'}$ that are defined in

Equations (2.42b) and (2.42d) are now both purely functions of K_1, k_2, s_s and θ_s with no dependence on modal order m. Their values are periodic over the circumferential distance $B_\mathrm{s}s_\mathrm{s}$. Under the x_2 integration, therefore, the orthogonality of the resulting complex exponentials gives

$$\int_0^{B_\mathrm{s}s_\mathrm{s}} \exp\left\{-\mathrm{i}(\nu_r - \nu_{r'})x_2\right\}\,\mathrm{d}x_2 = B_\mathrm{s}s_\mathrm{s}\delta_{rr'}, \tag{2.47}$$

where $\delta_{rr'}$ is the Kroneker delta function. The application of Equation (2.47) to Equation (2.44) gives an expression which is non-zero only for purely real values of the axial wavenumber component $\mu_r^\pm$. Equations (2.43) and (2.46) for the total time-averaged sound power now yield

$$\mathcal{P}^\pm(\omega) = \rho_0 M B_\mathrm{s}s_\mathrm{s} \int_{-\infty}^{\infty} \Phi(K_1, k_2) \sum_{r=-\infty}^{\infty} \left|R_r^\pm(K_1, k_2)\right|^2 \mathcal{F}_r^\pm(\mu_r^\pm, \nu_r)\,\mathrm{d}k_2, \tag{2.48}$$

where $\mathcal{F}_r^\pm$ is the non-dimensional power factor

$$\mathcal{F}_r^\pm(\mu_r^\pm, \nu_r) = \frac{MK_1\left[(MK_1 - M_2\nu_r)^2 - \beta_1^2\nu_r^2\right]^{1/2}}{\left|MK_1 - M_1\mu_r^\pm - M_2\nu_r\right|^2}, \tag{2.49}$$

and Φ is the turbulence velocity wavenumber spectrum

$$\Phi(K_1, k_2) = \langle\overline{w^2}\rangle\ \phi(K_1, k_2). \tag{2.50}$$

2.4.9 Re-ordering of the sound power expression for computational efficiency

The previous section develops the formulation for sound power spectral density per unit span. Evaluation of the expression shown in Equation (2.48) is difficult as the cascade response terms $R_r^\pm$ are time consuming to compute. Following the approach due to Cheong et al. [59] a change of order is introduced that substantially reduces the required number of calculations of the blade response function $R_r^\pm$.

The annulus of fan geometry that is represented by the rectilinear cascade has spatial periodicity over a distance $2\pi R = B_\mathrm{s}s_\mathrm{s}$ corresponding to the circumference at the medial radius R. The acoustic wavenumber in the x_2 direction must therefore satisfy

$$\nu_m = \frac{2\pi m}{B_\mathrm{s}s_\mathrm{s}}. \tag{2.51}$$

where $m \in \mathbb{Z}$ denotes the order of the acoustic mode, equivalent to the azimuthal mode index. These acoustic modes shall be referred to as 'duct modes' and their influence on the sound power spectra produced by this model shall be demonstrated in Chapter 3. Combining Equations (2.32a) and (2.51) with the definition of the x_2 wavenumber component of the rth cascade wave given in Equation (2.3) the turbulence wavenumber component in the y_2 direction may be defined as a function of the acoustic modal order m and the

index r that is now interpreted as a scattering index; describing the scattering of acoustic modes into cascade waves

$$k_{2,m+B_\mathrm{s}r} = \frac{2\pi}{B_\mathrm{s}s_\mathrm{s}\cos\theta_\mathrm{s}}(m + B_\mathrm{s}r) - K_1\tan\theta_\mathrm{s}. \tag{2.52}$$

The discrete nature of this wavenumber for fixed values of ω and scattering index r means that the integration over k_2 in Equation (2.48) is replaced by a summation over m with

$$\mathrm{d}k_2 = \frac{2\pi}{B_\mathrm{s}s_\mathrm{s}\cos\theta_\mathrm{s}}, \tag{2.53}$$

so that

$$\mathcal{P}^{\pm}(\omega) = \frac{2\pi\rho_0 M}{\cos\theta_\mathrm{s}} \sum_{m=-\infty}^{\infty}\sum_{r=-\infty}^{\infty} \Phi(K_1, k_{2,m+B_\mathrm{s}r}) \ \left|R_r^{\pm}(K_1,k_2)\right|^2 \mathcal{F}_r^{\pm}(\mu_r^{\pm},\nu_r). \tag{2.54}$$

Evaluation of the non-dimensional cascade response function $R_r^{\pm}(K_1,k_2)$ relies on a numerical step which involves the calculation and inversion of kernel matrices $\mathbf{K}$, full details of which can be found in Smith [46]. A considerable simplification of Equation (2.54) is possible by noting that the kernel matrices $\mathbf{K}$ are periodic so that they exhibit the behaviour (in the matrix notation of Equation (51) in Smith [46])

$$\mathbf{K}^{-1}(\sigma_{m+B_\mathrm{s}r}) = \mathbf{K}^{-1}(\sigma_{\mathrm{mod}\ (m,B_\mathrm{s})}), \tag{2.55}$$

where the function mod (m, B_s) denotes the remainder when dividing m by B_s [59]. Therefore, the relation in Equation (2.52) allows Equation (2.54) to be rearranged to

$$\mathcal{P}^{\pm}(\omega) = \frac{2\pi\rho_0 M}{\cos\theta_\mathrm{s}} \sum_{m=-\infty}^{\infty} \mathcal{Q}_m^{\pm}(K_1, k_{2,\ \mathrm{mod}\ (m,B_\mathrm{s})}) \sum_{r=-\infty}^{\infty} \Phi(K_1, k_{2,m+B_\mathrm{s}r}) \ . \tag{2.56}$$

where

$$\mathcal{Q}_m^{\pm}(K_1, k_{2,\ \mathrm{mod}\ (m,B_\mathrm{s})}) = \left|R_m^{\pm}(K_1, k_{2,\ \mathrm{mod}\ (m,B_\mathrm{s})})\right|^2 \mathcal{F}_m^{\pm}(\mu_m^{\pm},\nu_m), \tag{2.57}$$

is the non-dimensional power radiated by the mth cascade wave due to a harmonic vortical gust of the form $\exp\{-\mathrm{i}(\omega t - K_1 x_1 - k_{2,\ \mathrm{mod}\ (m,B_\mathrm{s})}x_2)\}$.

The definition of the non-dimensional power factor $\mathcal{F}_m^{\pm}$ given in Equation (2.49) ensures that $\mathcal{P}^{\pm}$ has contributions only from modes m having strictly real-valued axial wavenumber components $\mu_m^{\pm}$. Solving the discriminant of Equation (2.4) gives the limits of m to be

$$m_{\min} = \left\lceil \frac{B_\mathrm{s}s_\mathrm{s}}{2\pi}k\frac{M_2-\beta_1}{\beta^2} \right\rceil, \tag{2.58a}$$

and

$$m_{\max} = \left\lfloor \frac{B_\mathrm{s}s_\mathrm{s}}{2\pi}k\frac{M_2+\beta_1}{\beta^2} \right\rfloor, \tag{2.58b}$$

where $\lceil\cdot\rceil$ and $\lfloor\cdot\rfloor$ denote ceiling and floor functions respectively. Equation (2.56) may now

be written as

$$\mathcal{P}^{\pm}(\omega) = \frac{2\pi\rho_0 M}{\cos\theta_{\mathrm{s}}} \sum_{m_{\min}}^{m_{\max}} \mathcal{Q}_m^{\pm}(K_1, k_{2,\,\mathrm{mod}\,(m,B_{\mathrm{s}})}) \sum_{r=-\infty}^{\infty} \Phi(K_1, k_{2,m+B_{\mathrm{s}}r}) \;, \tag{2.59}$$

where $\Phi(K_1, k_{2,m+B_{\mathrm{s}}r})$ is modelled by a two-dimensional Liepmann spectrum for homogeneous isotropic turbulence given by

$$\Phi(K_1, k_{2,m+B_{\mathrm{s}}r}) = \frac{\langle\overline{w^2}\rangle\Lambda^2}{4\pi} \frac{1 + \Lambda^2(4k_1^2 + k_{2,m+B_{\mathrm{s}}r}^2)}{[1 + \Lambda^2(k_1^2 + k_{2,m+B_{\mathrm{s}}r}^2)]^{5/2}}, \tag{2.60}$$

where Λ is the integral lengthscale of the turbulence.

Equation (2.59) is identical to that for the broadband power spectrum proposed by Cheong et al. [59] despite the fact that Cheong et al. assume axisymmetric turbulence rather than the formulation presented in this chapter where the turbulence correlation function is assumed to be modulated by the wake profile. This indicates that only circumferentially-averaged values of wake turbulence velocity and lengthscale are needed as inputs for the broadband noise model due to the cancellation of the higher order Fourier coefficients of the unsteady wake profile (see Equation (2.44)). The use of Equation (2.60) for the turbulence statistics is therefore preferable to that of Ventres et al. [79] because the resulting noise predictions are relatively insensitive to the shape of the wake profile, unlike those due to the noise model due to Ventres et al. which retains the dependency on the higher order unsteady wake profile Fourier coefficients.

Chapter 3

Characteristics of the cascade sound power spectrum

This chapter describes the characteristics of the sound power spectra obtained using the radiation model developed in Chapter 2. This will include an investigation of the spectral characteristics associated with the cut-on frequencies of duct modes Ω_m and cascade modes ω_n, both of which are defined in Section 3.1. The relation between these frequencies and the cascade geometry will be explained and the spectral effects due to changing flow conditions presented.

3.1 Effects of mode cut-on frequencies on a cascade sound power spectrum

In this section the characteristics of the sound power spectrum shall be described with a particular emphasis on the phenomena associated with the cut-on frequencies of duct modes Ω_m and cascade modes ω_n.

Figure 3.1 shows upstream-propagating and downstream-propagating sound power spectra (blue and red, respectively) generated using the model described in Chapter 3 for a cascade with $B_\mathrm{s} = 20$, $s_\mathrm{s}/c_\mathrm{s} = 0.7$ and $\chi_\mathrm{s} = 30^\circ$ in a mean flow with $M = 0.5$ and normalised turbulence lengthscale $\Lambda/s_\mathrm{s} = 0.2$. The downstream level is greater than upstream, largely as a result of convective amplification. Various other features shall be explained in the following paragraphs.

3.1.1 Duct modes

In Section 2.4.9 it was noted that the expression for the sound power in Equation (2.59) is the sum over a finite number of acoustic duct modes m that are cut-on at a given frequency ω, as defined in Equation (2.58). These duct modes are equivalent to azimuthal modes in

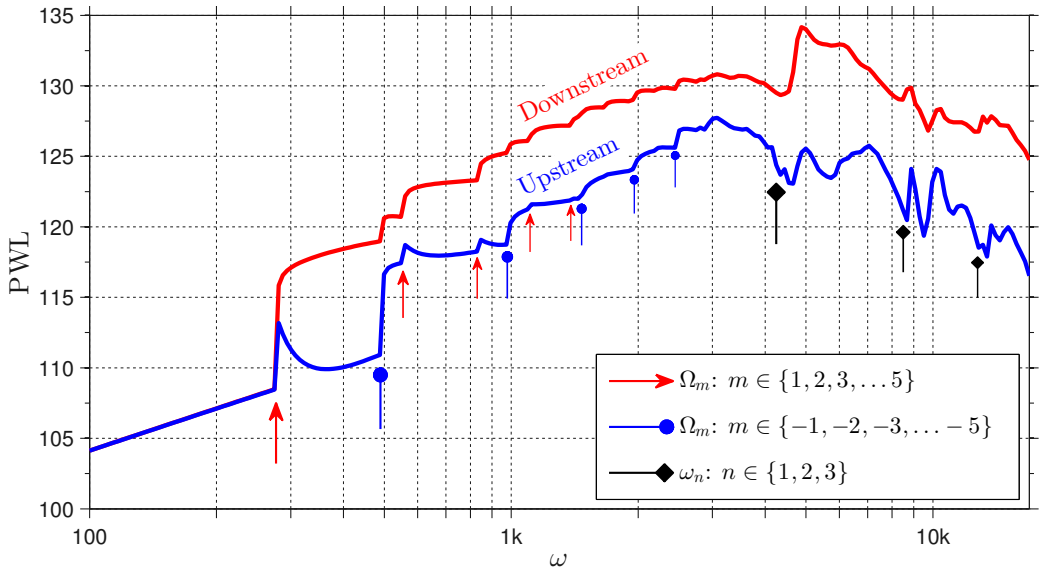

Figure 3.1 – Upstream and downstream one-third octave equivalent sound power spectra obtained using the broadband radiation model for a cascade with $B_s = 20$, $s_s/c_s = 0.7$ and $\chi_s = 30°$ in a mean flow with $M = 0.5$ and normalised turbulence lengthscale $\Lambda/s_s = 0.2$. Power radiated upstream and downstream is represented by blue and red lines respectively. Arrows indicate the frequencies at which various modes cut-on, as explained in the text.

a cylindrical duct. The cut-on frequency of duct mode m is expressed as

$$\Omega_m = \begin{cases} m\Delta\Omega_- : & m < 0, \\ m\Delta\Omega_+ : & m > 0, \end{cases} \tag{3.1}$$

where $\Delta\Omega_\pm$ is the fundamental cut-on frequency for upstream and downstream propagating modes m that is obtained from the discriminant of Equation (2.4)

$$\Delta\Omega_\pm = \frac{\beta^2}{M_2 \pm \beta_1} \frac{2\pi c_0}{B_s s_s}. \tag{3.2}$$

In Figure 3.1 the cut-on frequencies for the first 5 positive m are indicated with red arrows. Blue circle-headed pointers indicate the cut-on frequencies for the first 5 negative m. The difference in fundamental cut-on frequency for upstream and downstream propagating modes (positive and negative m) is due to the presence of whirling flow and hence non-zero M_2 in Equation (3.2). For axial flow with $\theta = 0$ Equation (3.2) reduces to the expression

$$\Delta\Omega_\pm = \pm\beta \frac{2\pi c_0}{B_s s_s}. \tag{3.3}$$

The response of the upstream and downstream spectra differ as the frequency moves upwards through duct mode cut-on frequencies. For the upstream spectrum (blue line), counter-rotating modes ($m > 0$, red arrow pointers) are associated with 'spikes' such that the sound power rapidly falls back to levels similar to those seen prior to modal cut-on. Co-rotating modes ($m < 0$, blue circle pointers) are associated with 'steps' in the spectrum:

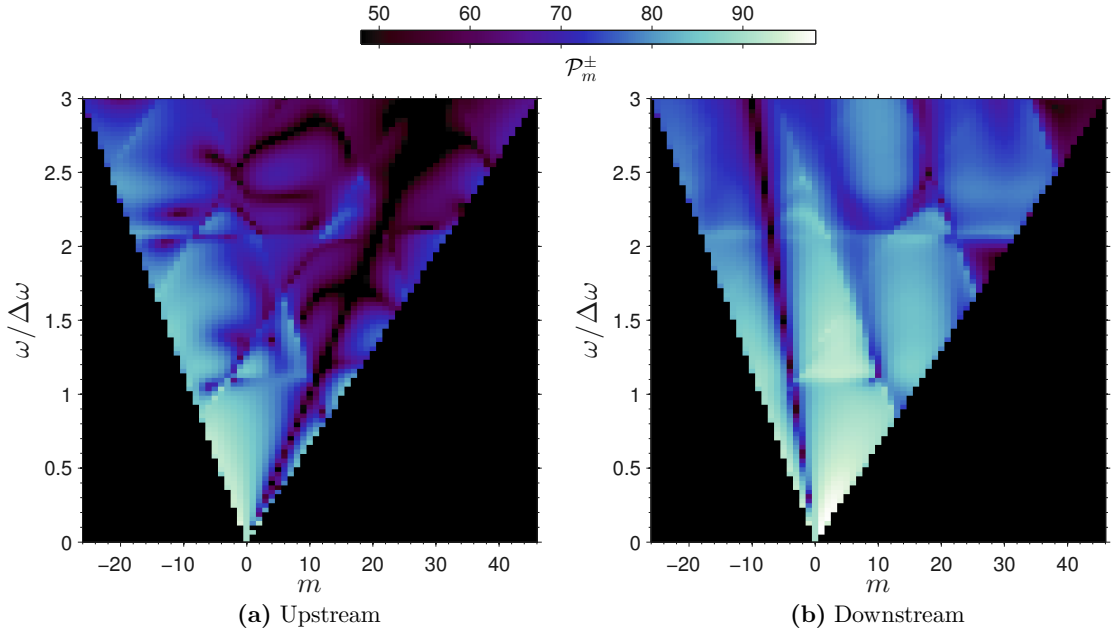

(a) Upstream **(b)** Downstream

Figure 3.2 – Upstream and downstream modal sound power for the spectra shown in Figure 3.1.

the new level is maintained as frequency increases. In the downstream spectrum (red line) the cut-on frequencies of both co- and counter-rotating modes are associated with steps in the spectral level.

Figure 3.2 shows the modal power $\mathcal{P}_m^{\pm}$ for cut-on modes m plotted against the normalised frequency $\omega/\Delta\omega$. The cut-on triangles are skewed because of the asymmetry of the cut-on frequencies of co-rotating and counter-rotating modes shown in Equation (3.2). Upstream (Figure 3.2a), co-rotating modes ($m < 0$) carry most sound power and the distribution of modal power changes slowly with both modal order and frequency. The right hand edge of the cut-on triangle in Figure 3.2a shows the cut-on of counter-rotating modes. The power contribution of each counter-rotating mode decreases rapidly with increasing frequency following cut-on leading to the observed spectral 'spike' features. The sound power distribution for downstream propagation (Figure 3.2b) is generally more even and slower varying than that upstream. This accounts for the more 'step-like' behaviour observed in the downstream sound power spectrum of Figure 3.1.

Both upstream and downstream modal power maps have distinct diagonal lines along which modal sound power approaches zero. Upstream (Figure 3.2a) this line corresponds to modes for which the group velocity angle $\psi_{\mathrm{g},m} = \pi/2$ so that no sound power propagates axially. The diagonal line in Figure 3.2b for downstream propagation corresponds to modes for which the phase velocity angle $\psi_{\mathrm{p},m}$ is aligned with the stator stagger angle. The phase velocity angle $\psi_{\mathrm{p},m}$ of a mode order m is given by

$$\psi_{\mathrm{p},m}^{\pm} = \arctan\left(\frac{\nu_m}{\mu_m^{\pm}}\right), \tag{3.4}$$

where ν_m and $\mu_m^{\pm}$ are the gap-wise and axial acoustic wavenumber components as defined

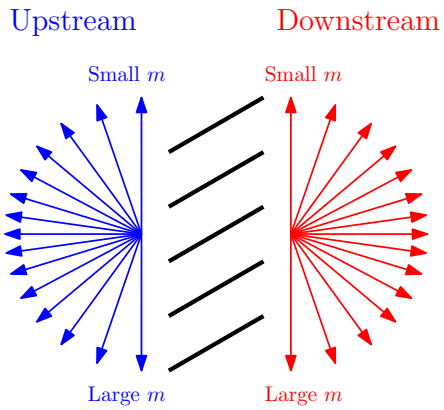

Figure 3.3 – Trend of phase velocity angle $\psi_{\mathrm{p},m}$ with increasing modal order m. The distribution is relatively sparse for large and small m.

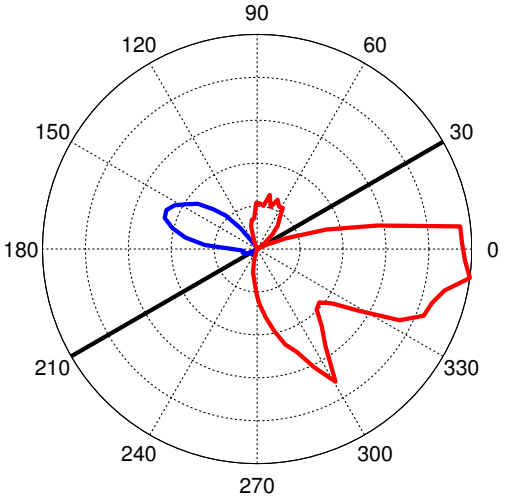

Figure 3.4 – Phase velocity angle sound power density obtained using the broadband radiation model for a cascade with $B_\mathrm{s} = 20$, $s_\mathrm{s}/c_\mathrm{s} = 0.7$ and $\chi_\mathrm{s} = 30^\circ$ in a mean flow with $M = 0.5$ and normalised turbulence lengthscale $\Lambda/s_\mathrm{s} = 0.2$ over the octave-band $1.5 < \omega/\Delta\omega < 3$. The values are normalised with respect to the peak value shown. Upstream propagating power is shown in blue and downstream in red. The stagger angle of the cascade is indicated by the black line.

in Equations (2.3) and (2.4) respectively. Clearly for upstream-propagating modes the axial component of the phase velocity must be opposite to that of the mean flow. It is suggested that this explains the 'spike' behaviour in upstream counter-rotating modes that must 'work against' the mean flow while downstream propagation is relatively insensitive to this effect.

In Chapter 5 it shall be shown that the strength of interaction between a mode order m and the rotor is strongly influenced by the relation between the stagger angle of the rotor and $\psi_{\mathrm{p},m}$ obtained using Equation (3.4). It is therefore important to understand the 'directivity' of the modal sound power distribution in terms of $\psi_{\mathrm{p},m}$. When applying Equation (3.4) to all propagating modes at a particular frequency, the modal distribution is not even with respect to $\psi_{\mathrm{p},m}$, tending to be relatively sparsely populated at the extremes of the cut-on range of m as defined in Equation (2.58). The distribution of modes in terms of m and $\psi_{\mathrm{p},m}$ is sketched in Figure 3.3 to illustrate the sparsity for very large and very small m. The directivity of the sound power is therefore assessed by summing the sound power radiated into discrete phase angle bands, thus obtaining the approximate sound power density with respect to phase velocity angle.

Figure 3.4 shows the sound power density with respect to phase velocity angle calculated from the data shown in Figure 3.2, aggregating the sound power over the octave frequency band $1.5 < \omega/\Delta\omega < 3$ in order to smooth the results. The upstream-propagating power is shown in blue and downstream in red. The stagger angle of the cascade is indicated by the black line. Observations about Figure 3.4 are listed below.

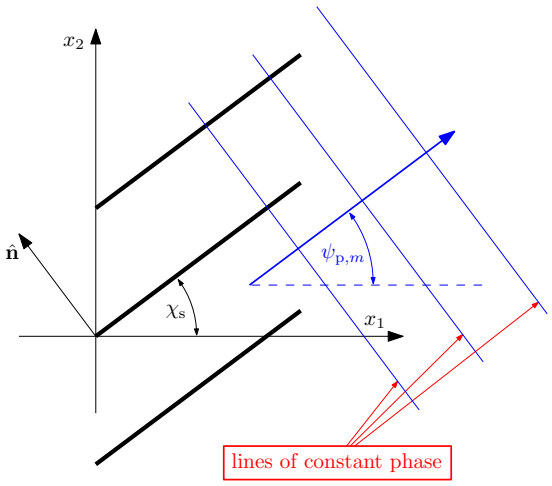

Figure 3.5 – Plane wave representing acoustic mode with phase velocity angle $\psi_{\mathrm{p},m} = \chi_\mathrm{s}$ cannot be excited by upwash normal to blade surfaces due to orthogonality.

1. The upstream radiation pattern (blue) has a principal lobe corresponding to the range of angles over which most of the acoustic energy is radiated.

2. The upstream radiation pattern is significantly narrower than downstream (red). This is explained by the effects of convection on the group velocity angle, as discussed by Jurdic and Joseph [83].

3. The downstream radiation pattern has a gap at the cascade stagger angle (30°). This is due to the orthogonality of the upwash velocity on the blade surfaces with modes having $\psi_{\mathrm{p},m} = \chi_\mathrm{s}$, as illustrated in Figure 3.5. Any such modes cannot be excited.

4. The upstream radiation pattern is directed away from the line of the cascade stagger and the downstream radiation has a peak at 300°, perpendicular to the cascade airfoils, suggesting 'beaming' of the sound power in blade-perpendicular directions, due to alignment of $\psi_{\mathrm{p},m}$ with the blade normal.

3.1.2 Cascade modes

The PWL spectra in Figure 3.1 show relatively large oscillations in both upstream and downstream spectra at the frequencies marked with black diamond-headed pointers. These frequencies correspond to the cut-on frequencies of the higher-order modes in the ducts formed between adjacent blades in the cascade. These modes shall be referred to as 'cascade modes' and it will be shown that they are an important feature in many aspects of the cascade response to impinging turbulence. The cut-on frequency of the cascade mode of order n is given by

$$\omega_n = n\Delta\omega, \tag{3.5}$$

where

$$\Delta\omega = \frac{\pi\beta c_0}{s_\mathrm{s}\cos\chi_\mathrm{s}}. \tag{3.6}$$

A full derivation of Equation (3.6) is given in Appendix A. In Section 4.2.2.1 it will be shown that the existence of several cut-on cascade modes fundamentally changes the interactions between adjacent blades.

In the following section the results of a parameter study shall be presented showing the influence of cascade geometry and flow on the sound power radiated by the cascade.

3.2 Cascade spectral power parameter study

In the previous section the spectrum of upstream and downstream sound power radiated from a cascade was shown and its main features described. In this section a study is conducted to show the effects of parameter changes on upstream and downstream sound power spectra.

3.2.1 Parameter study design

A reference set of parameters is defined, as listed in Table 3.1. A parameter sweep is conducted for each of these as the others are held at the reference value. In each case the turbulence intensity is constant at 2% so that the mean-square turbulence velocity $\langle\overline{w^2}\rangle = 4 \times 10^{-4}\, U^2$.

Table 3.1 – Reference cascade parameters for cascade geometry parameter study.

Parameter	B_s	$s_\mathrm{s}/c_\mathrm{s}$	M	θ (°)	Λ (m)
Value	6	0.1	0.4	40	0.1

In Section 4.2.2.1 it shall be shown that cascade behaviour is fundamentally different at frequencies below and above $\approx \omega_2$ as defined in Equation (3.5). In this parameter study two frequency bands are defined for each parameter sweep so that, as far as possible, they fall either side of ω_2. The total sound power in these low frequency (LF) and high frequency (HF) bands shall be shown as a function of the parameter under investigation.

3.2.2 Spectral power changes due to variation of vane count B_s

Figures 3.6a and 3.6c show the variation in upstream and downstream sound power spectra generated as the number of stator vanes B_s is changed while keeping all other parameters listed in Table 3.1 fixed. Note that fixing the value of $s_\mathrm{s}/c_\mathrm{s}$ requires the variation in chord c_s as s_s is inversely proportional to B_s. The values of B_s and corresponding values of $\Delta\omega$ are listed in Table 3.2.

Table 3.2 – B_s and corresponding values of $\Delta\omega$.

B_s	6	12	24	48
$\Delta\omega$	1.53e3	3.05e3	6.10e3	1.22e4

The total sound power in frequency bands

$$\begin{aligned} \text{LF}: &\quad 300\,\text{rad/s} < \omega < 600\,\text{rad/s}, \\ \text{HF}: &\quad 5000\,\text{rad/s} < \omega < 10000\,\text{rad/s}. \end{aligned}$$

is shown as a function of B_s in Figures 3.6b and 3.6d. Note that the HF band is not above ω_2 for $B_\text{s} > 6$.

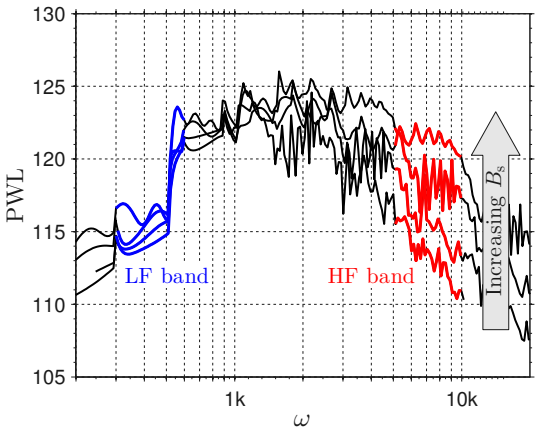

(a) Upstream-propagating sound power spectra

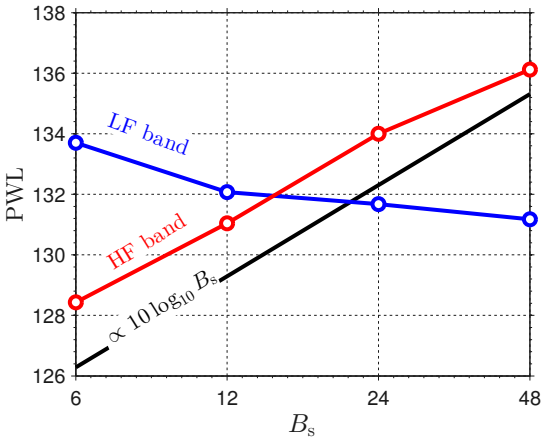

(b) Total upstream sound power in low and high normalised frequency bands plotted against stator vane count B_s

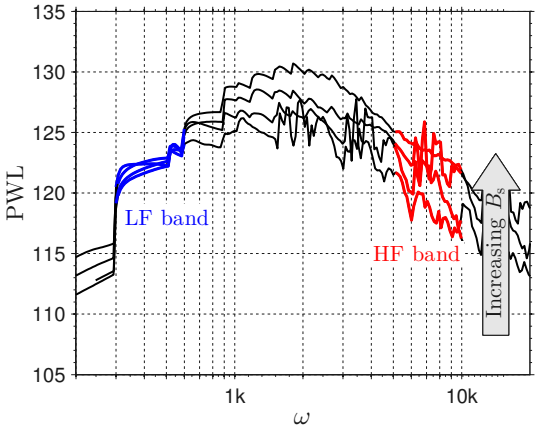

(c) Downstream-propagating sound power spectra

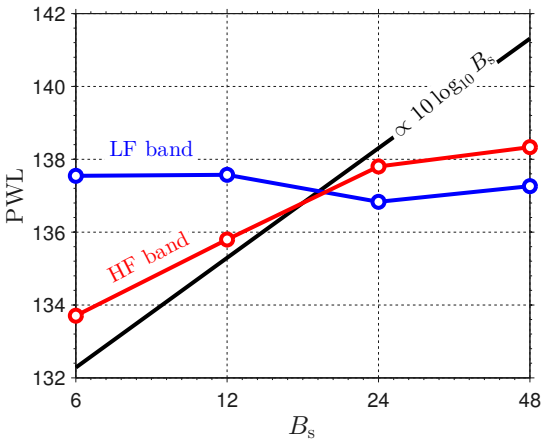

(d) Total downstream sound power in low and high normalised frequency bands plotted against stator vane count B_s

Figure 3.6 – Effect of changing number of stator vanes B_s on the predicted sound power spectrum plotted against angular frequency ω. Frequency bands 'LF' and 'HF' are indicated by coloured sections in left hand plots with corresponding band total power plotted against B_s in right hand plots.

1. Sound power in the HF band is seen to increase with the number of stator vanes despite the inverse relationship between B_s and chord length c_s. It shall be shown in the following section that sound power is insensitive to the chord length for sufficiently large c_s. Upstream sound power is seen to increase in proportion to the

number of stator vanes, as shown by the black line. The downstream sound power in the HF band increases at a slower rate. This may be influenced by the high values of $\Delta\omega$ seen for large B_s.

2. Little change is seen in the LF band. In the low frequency regime the low radiation efficiency of the cascade limits the sound power. Increasing the number of vanes decreases the spacing between vanes s_s and consequently reduces the radiation efficiency (see Section 4.2.2.1).

3.2.3 Spectral power changes due to variation of cascade space-chord ratio $s_\mathrm{s}/c_\mathrm{s}$

In this section the parameter $s_\mathrm{s}/c_\mathrm{s}$ is changed by means of the variation of the chord length c_s. Figure 3.7 shows the resulting sound power spectra and corresponding band total sound powers in the frequency bands

$$\begin{aligned} \text{LF}: &\quad 300\,\text{rad/s} < \omega < 600\,\text{rad/s}, \\ \text{HF}: &\quad 3000\,\text{rad/s} < \omega < 6000\,\text{rad/s}. \end{aligned}$$

The chord length does not influence $\Delta\omega$ which has the same value as shown for $B_\mathrm{s} = 6$ in Table 3.2.

1. Sound power in LF and HF bands is insensitive to chord length c_s for small values of $s_\mathrm{s}/c_\mathrm{s}$. In this regime the acoustic reduced frequency $\mu_\mathrm{a} = \omega c_\mathrm{s}/c_0\beta^2 > 1$ and the cascade chord is significantly longer than the acoustic wavelength so that leading-edge noise sources are decoupled from the trailing edge.

2. Sound power decreases as with chord length c_s as $s_\mathrm{s}/c_\mathrm{s}$ increases. The slope approaches proportionality with c_s^2, which is consistent with a chord-wise distribution of coherently radiating compact dipole sources.

3.2.4 Spectral power changes due to variation of mean flow Mach number M

Sound power spectra obtained for several values of the mean flow mach number M are shown in Figures 3.8a and 3.8c. The total sound power in the frequency bands

$$\begin{aligned} \text{LF}: &\quad 300\,\text{rad/s} < \omega < 600\,\text{rad/s}, \\ \text{HF}: &\quad 3000\,\text{rad/s} < \omega < 6000\,\text{rad/s}, \end{aligned}$$

are shown in Figures 3.8b and 3.8d plotted against M. Table 3.3 shows the effect of M on the values of $\Delta\omega$ and confirms that LF and HF bands are always either side of ω_2.

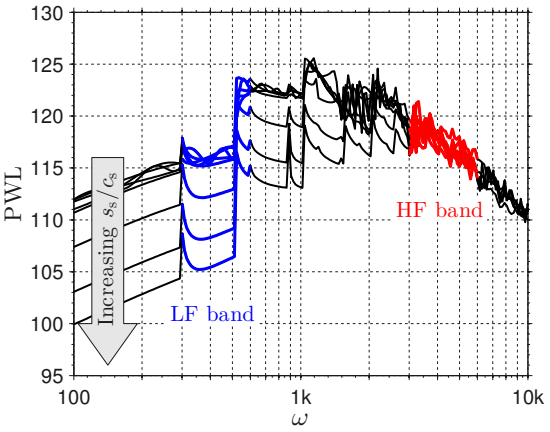

(a) Upstream-propagating sound power spectra

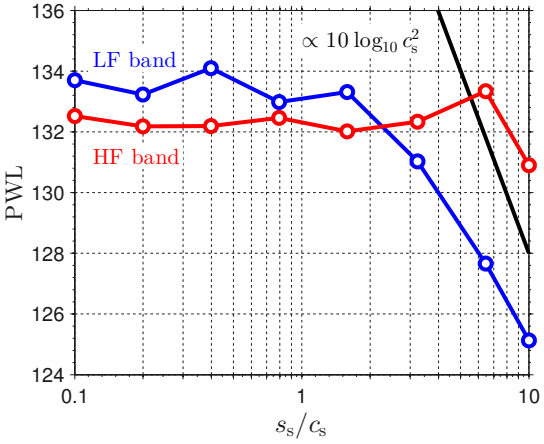

(b) Total upstream sound power in low and high normalised frequency bands plotted against space-chord ratio s_s/c_s

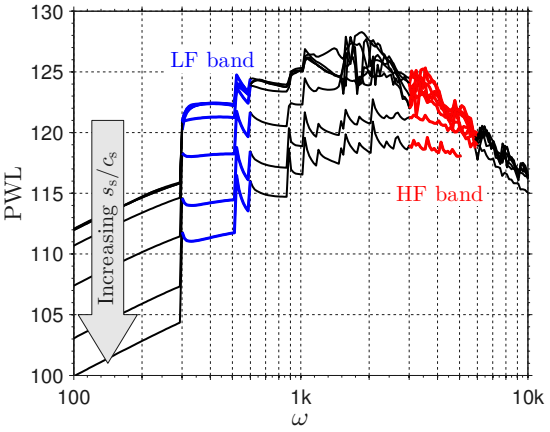

(c) Downstream-propagating sound power spectra

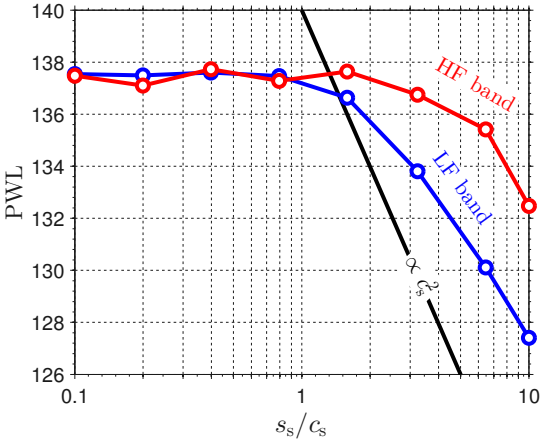

(d) Total downstream sound power in low and high normalised frequency bands plotted against space-chord ratio s_s/c_s

Figure 3.7 – Effect of changing chord c_s, and hence space-chord ratio s_s/c_s, on the predicted sound power spectrum plotted against angular frequency ω. Frequency bands 'LF' and 'HF' are indicated by coloured sections in left hand plots with corresponding band total power plotted against s_s/c_s in right hand plots.

Table 3.3 – Mean flow mach number M and corresponding values of $\Delta\omega$.

M	0.1	0.2	0.3	0.4	0.5	0.6	0.7	0.8	0.9
$\Delta\omega$	1.66e3	1.63e3	1.59e3	1.53e3	1.44e3	1.33e3	1.19e3	9.99e2	7.25e2

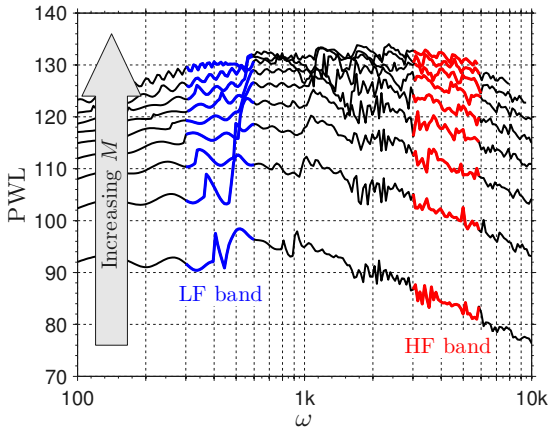

(a) Upstream-propagating sound power spectra

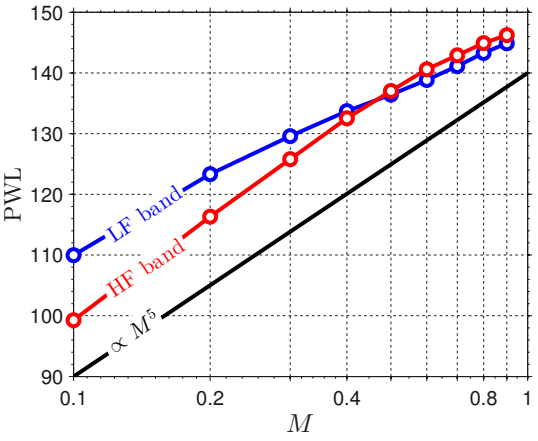

(b) Total upstream sound power in low and high normalised frequency bands plotted against Mach number M

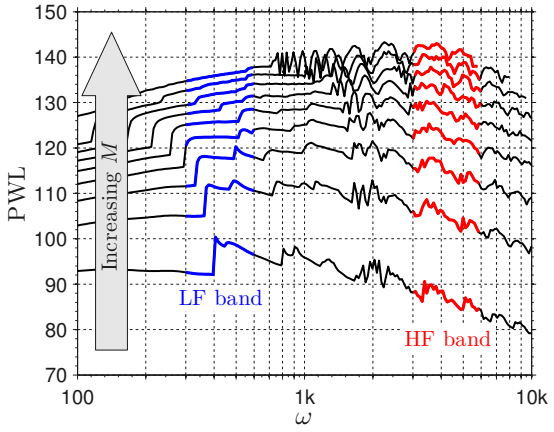

(c) Downstream-propagating sound power spectra

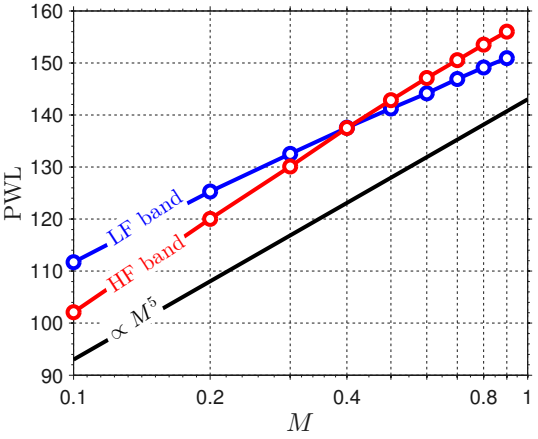

(d) Total downstream sound power in low and high normalised frequency bands plotted against Mach number M

Figure 3.8 – Effect of changing mean flow Mach number M on the predicted sound power spectrum plotted against frequency normalised with cascade mode frequency step $\Delta\omega$. Frequency bands 'LF' and 'HF' are indicated by coloured sections in left hand plots with corresponding band total power plotted against M in right hand plots.

1. The total power in both LF and HF bands increases faster than the classical M^5 power law indicated by the black lines in Figures 3.8b and 3.8d. The sensitivity for small M is approximately M^6.

2. The sensitivity reduces as M increases, more rapidly for the LF bands. Similar observations with respect to frequency sensitivity of the sound power response to mean flow Mach number have been made by Atassi and Logue [84]. Glegg and Jochault [85] found sensitivity increasing from M^5 to M^6 at higher Mach numbers for rotor self noise.

3. As the turbulence intensity is constant and $\langle\overline{w^2}\rangle \propto U^2$ the observed near-M^5 power law can be interpreted as being due to $\langle\overline{w^2}\rangle U^3$ which shall be used when assessing the impact of turbulence parameter prediction errors on sound power estimates in Section 8.12.

3.2.5 Spectral power changes due to variation of mean flow whirl angle θ

Figure 3.9 shows the effect on sound power of changing stagger angle χ_s and hence mean flow angle θ. In this case the frequency bands are defined

$$\begin{aligned} \text{LF}: &\quad 300\,\text{rad/s} < \omega < 600\,\text{rad/s}, \\ \text{HF}: &\quad 5000\,\text{rad/s} < \omega < 10000\,\text{rad/s}. \end{aligned}$$

The range of θ for which sound power has been calculated and corresponding values of $\Delta\omega$ are listed in Table 3.4. Note that the largest values of θ result in large values of $\Delta\omega$ such that the HF band is not above ω_2 for $\theta = 80°$.

Table 3.4 – Mean flow whirl angle θ and corresponding values of $\Delta\omega$.

θ (°)	0	20	30	35	40	45	50	60	80
$\Delta\omega$	1.17e3	1.24e3	1.35e3	1.43e3	1.53e3	1.65e3	1.82e3	2.34e3	6.73e3

1. Upstream sound power increases with stagger angle. This may be explained by convection effects due to the reduction of the axial component of the mean flow that occurs as θ increases with constant mach number onto the cascade M. In Figure 3.9b the sensitivity is slightly greater in the LF band with approximately 9 dB increase over the range $0 < \theta < 80$ versus 6 dB in the HF band.

2. Downstream, a clockwise 'rotation' of the sound power spectrum is observed as θ increases. The LF band shows a 5 dB increase over the range of angles whilst the HF band decreases by 3.5 dB over the same range.

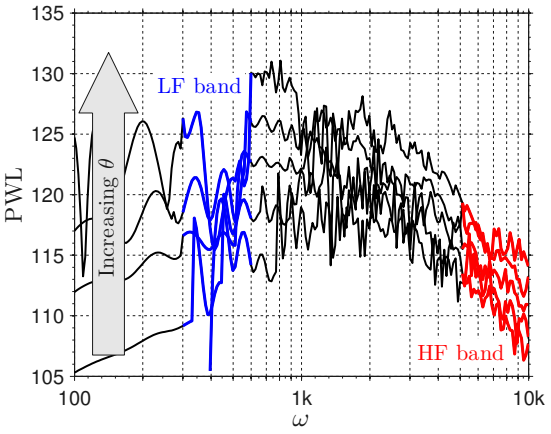

(a) Upstream-propagating sound power spectra

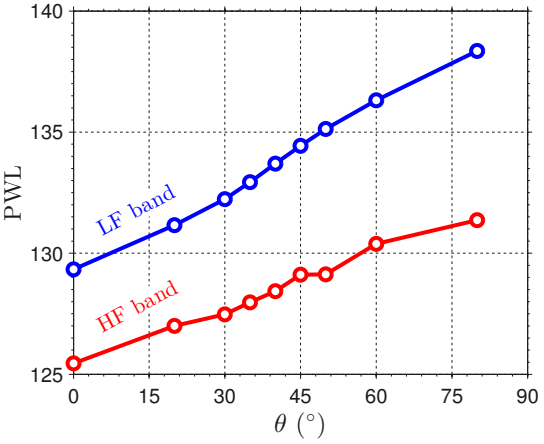

(b) Total upstream sound power in low and high normalised frequency bands plotted against whirl angle θ

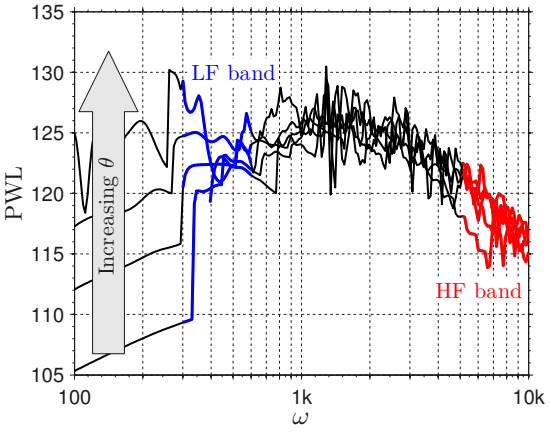

(c) Downstream-propagating sound power spectra

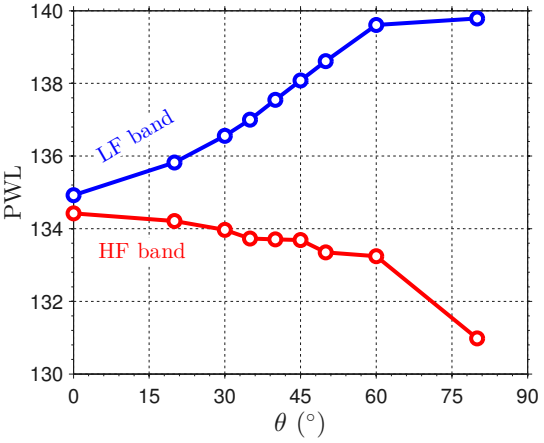

(d) Total downstream sound power in low and high normalised frequency bands plotted against whirl angle θ

Figure 3.9 – Effect of changing mean flow whirl angle θ on the predicted sound power spectrum plotted against frequency normalised with cascade mode frequency step $\Delta\omega$. Frequency bands 'LF' and 'HF' are indicated by coloured sections in left hand plots with corresponding band total power plotted against θ in right hand plots.

3. Note that due to symmetry the upstream and downstream sound power spectra must converge as $\theta \to 90°$.

3.2.6 Spectral power changes due to variation of turbulence integral lengthscale Λ

Figure 3.10 shows the results on sound power spectra of variation of turbulence integral lengthscale Λ. Frequency bands either side of $\omega_2 = 3050\,\text{rad/s}$ are given by

$$\text{LF}: \quad 300\,\text{rad/s} < \omega < 600\,\text{rad/s},$$
$$\text{HF}: \quad 5000\,\text{rad/s} < \omega < 10000\,\text{rad/s}.$$

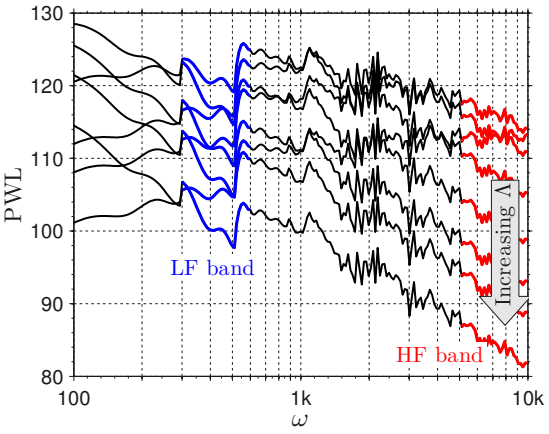

(a) Upstream-propagating sound power spectra

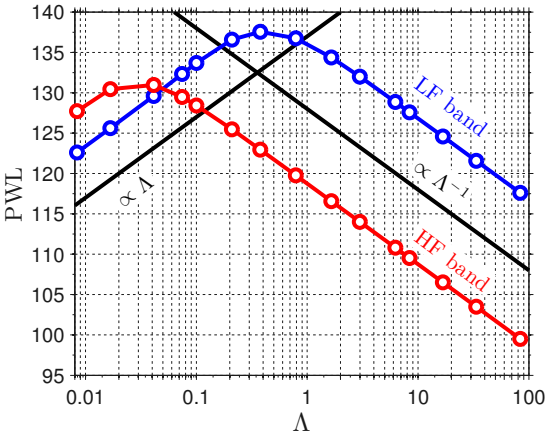

(b) Total upstream sound power in low and high normalised frequency bands plotted against turbulence integral lengthscale Λ

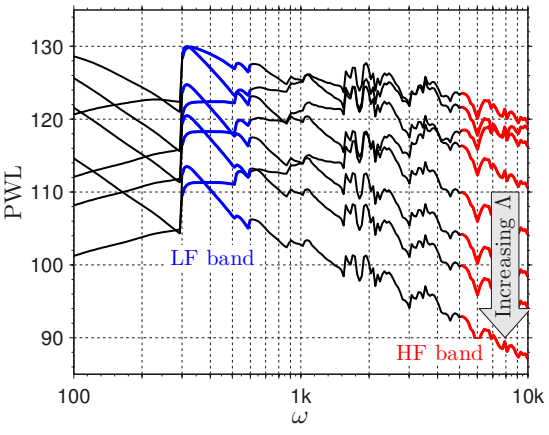

(c) Downstream-propagating sound power spectra

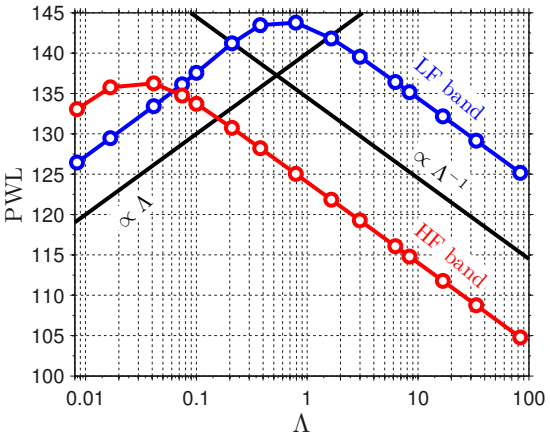

(d) Total downstream sound power in low and high normalised frequency bands plotted against turbulence integral lengthscale Λ

Figure 3.10 – Effect of changing turbulence integral lengthscale Λ on the predicted sound power spectrum plotted against angular frequency ω. Frequency bands 'LF' and 'HF' are indicated by coloured sections in left hand plots with corresponding band total power plotted against Λ in right hand plots.

1. Sound power in LF and HF bands increases in proportion to Λ before falling in inverse proportion to Λ. The location peak of the band power is almost independent of the direction of sound propagation but is clearly sensitive to the location of the frequency band. These effects are due to the changing shape of the Liepmann turbulence velocity spectrum.

Chapter 4

Comparison of sound power radiation from cascades and single airfoils

The noise model described in Chapter 2 allows the prediction of the broadband sound power radiated from an OGV due to the interaction with turbulence from an upstream rotor. The model takes into account the acoustic interactions between the vanes of the OGV. Calculations using this 'exact' cascade noise model rely on a numerical procedure. At high frequencies this numerical step is computationally expensive and time consuming.

Alternative models are sought which offer computational benefits over the exact cascade model without sacrificing the accuracy of noise prediction. One model that has been investigated for this purpose is the semi-analytical single-airfoil sound power model (SA-model) developed by Blandeau et al. [41]. The SA-model uses the classical isolated flat-plate airfoil theory of Amiet [33, 42] to model the unsteady loading of a blade.

In this chapter, predictions of the radiated sound power made using the SA-model and the exact cascade model are compared. This will lead to insight into the behaviour of the cascade and allow the definition of circumstances under which the SA-model may be used in place of the exact cascade model, i.e. when the blade-to-blade interaction effects can be ignored. The chapter commences with a brief description of the SA-model.

4.1 General formulation for single airfoil sound power radiation

An isolated flat plate airfoil of chord c_s is assumed to interact with homogeneous isotropic two-dimensional turbulence convected in a mean flow parallel to the chord with mean flow velocity U at an angle θ_s relative to an observer axis, which shall be used to define upstream and downstream directions in Section 4.1.1. The flow is defined identically to that for the cascade problem in Chapter 2, having mean-square upwash velocity $\langle\overline{w^2}\rangle$ and integral lengthscale Λ. The turbulent upwash velocity is represented by the Liepmann velocity frequency spectrum denoted Φ_{ww} as defined in Equation (2.60).

The single airfoil geometry is illustrated in Figure 4.1a. For comparison a cascade with identical chord and flow is shown in Figure 4.1b. The cascade has leading edge spacing s_s, stagger angle χ_s aligned with the flow angle θ_s and gap-wise periodicity $B_\mathrm{s}s_\mathrm{s}$.

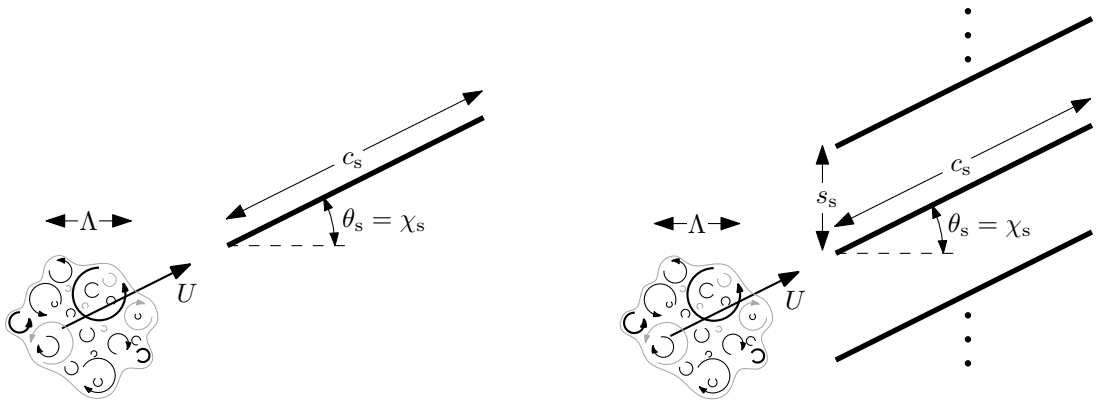

(a) Single airfoil **(b)** Cascade

Figure 4.1 – Diagram of single airfoil and cascade geometries.

4.1.1 Expression for the sound power radiated from a single airfoil

For the sake of brevity only the final expression for the sound power due to B_s isolated airfoils is shown here. A full derivation and discussion of the single airfoil sound power radiation model can be found in Blandeau et al. [41].

As noted above, the mean flow U is assumed to be at an angle θ_s to the observer axis, which can be considered equivalent to the duct axis. The SA-model formulation defines the far-field intensity at observer angles α relative to the duct axis, as illustrated in Figure 4.2. The upstream and downstream sound power are the half-circuit integrals of this directional sound power given by [41]

$$\mathcal{P}^{\pm}_{\mathrm{SA}}(\omega) = \frac{\pi}{4}\beta^4 M_s k \rho_0 \left(\frac{c_s}{2}\right)^2 \Phi_{ww}(K_1) \oint_{\mp\pi/2}^{\pm\pi/2} \frac{|\mathcal{L}(\alpha', K_1)|^2 \sin^2\alpha'}{A(\alpha', M_s)^2 \left[A(\alpha', M_s) - M_s \cos\alpha'\right]^2} \, \mathrm{d}\alpha, \tag{4.1}$$

where $\alpha' = \alpha - \chi_s$ is the effective observer angle with respect to the blade stagger angle, as illustrated in Figure 4.2. The term $\mathcal{L}$ in Equation (4.1) represents the effective acoustically weighted unsteady loading across the chord of the flat plate defined by Equation (2) in Blandeau et al. [75] while $A(\alpha, M_s) = \sqrt{1 - M_s^2 \sin^2\alpha}$.

For the purposes of direct comparison with the sound power radiated by the cascade given by Equation (2.56) the SA-model result is multiplied by the number of vanes in the OGV B_s so that

$$\mathcal{P}^{\pm}(\omega) = B_s \mathcal{P}^{\pm}_{\mathrm{SA}}(\omega). \tag{4.2}$$

Despite the differences between the exact cascade formulation of Equation (2.56) and the single-airfoil formulation of Equation (4.1) it will be shown that the results of these two sound power models are in close agreement at sufficiently high frequencies. The frequencies above which close agreement is assured will be identified during the course of this chapter.

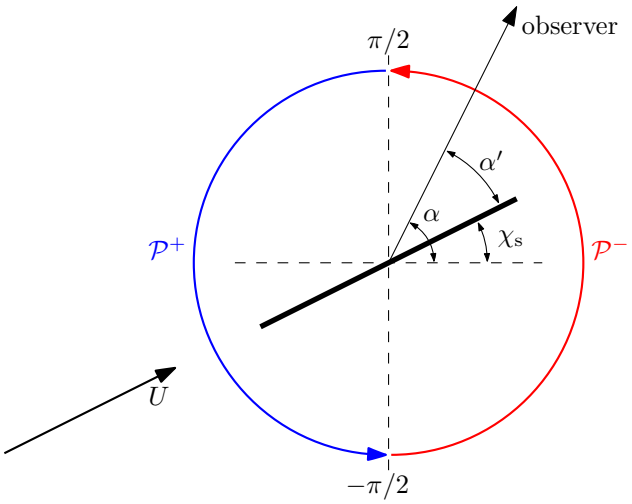

Figure 4.2 – Observer angles relative to single airfoil stagger angle.

4.2 Comparison of single airfoil and cascade sound power spectra

Single airfoil and cascade sound power spectra obtained using Equations (2.56) and (4.1) will be compared in this section. It will be seen that above a certain frequency the predicted sound power spectra are in close agreement. This observation will lead to criteria, and in turn to the definition of minimum frequencies, above which single airfoil theory may be substituted for cascade theory without significant loss of accuracy. We begin by comparing sound power spectra for a typical turbofan geometry, allowing the identification of some important differences in spectral characteristics.

4.2.1 Characteristics of single airfoil and cascade power spectra

Predicted upstream and downstream power spectra of the sound power level per unit span are shown in Figure 4.3. The parameters chosen for these simulations are typical of a turbofan bypass stator, having $B_s = 40$ with space-chord ratio $s_s/c_s = 0.5$ at radius $R = 0.8\,\mathrm{m}$ and stagger angle $\chi_s = 40°$. The mean flow onto the stator vanes has Mach number $M_s = 0.4$ and the turbulence has normalised lengthscale $\Lambda/s_s = 0.2$ and turbulence intensity $T_w = \langle\overline{w^2}\rangle^{1/2}/U = 0.02$. Arrows indicate the cut-on frequencies of the duct modes and cascade modes identified in Chapter 3. The sound power level plotted in Figure 4.3 represents the contributions from all blades, the single airfoil sound power being multiplied by B_s as defined in Equation (4.2). These spectra are plotted against frequency normalised by $\Delta\omega$, the fundamental cut-on frequency of the cascade modes as defined in Equation (3.6). Some important features of these sound power level spectra are summarised below:

- In both upstream and downstream figures there is a frequency above which there is negligible difference between the single airfoil and cascade sound power spectra.
- The frequencies above which agreement occurs are different for upstream-propagating and downstream propagating noise.

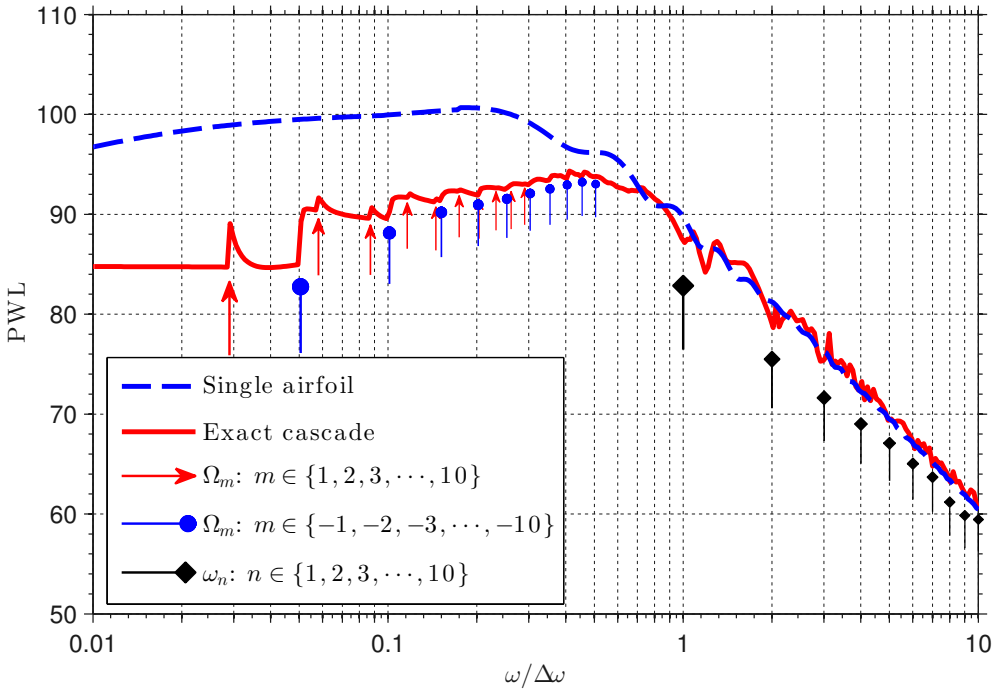

(a) Upstream.

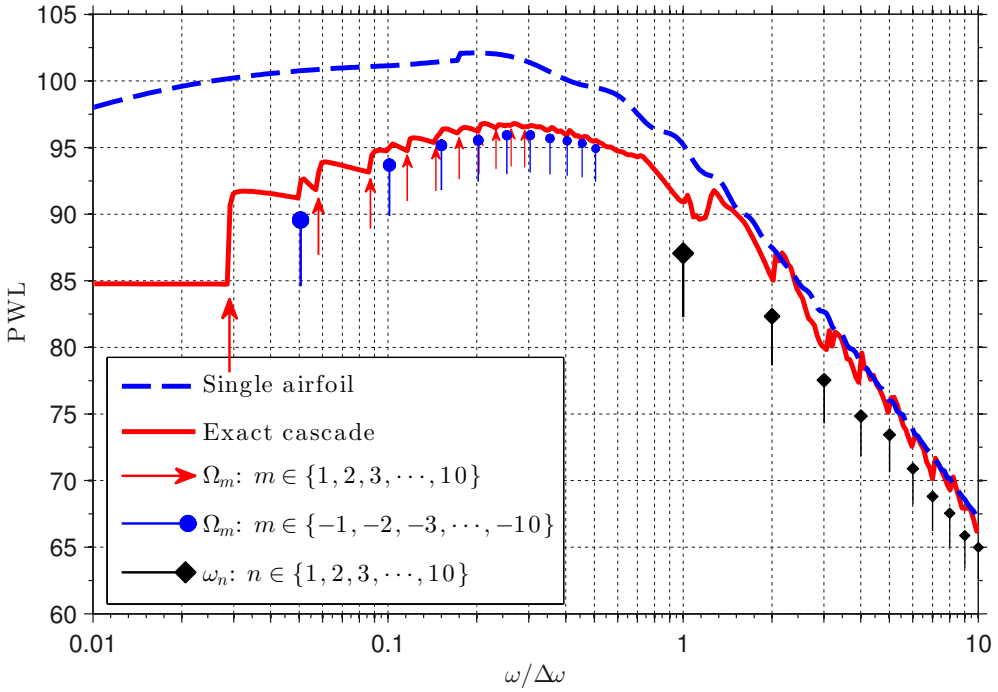

(b) Downstream.

Figure 4.3 – Spectra of upstream-propagating and downstream-propagating sound power per unit span obtained using single airfoil model and cascade model. Red and blue arrows indicate cut-off frequencies of circumferential modes Ω_m of positive and negative order respectively. Black arrows indicate the cut-off frequencies of the inter-blade cascade modes ω_n. The nature of these modes was discussed in Chapter 3.

- The single airfoil spectrum is generally smooth compared to the cascade spectrum which is oscillatory due to the cut-on of various modes. Duct modes Ω_m dominate the response at low frequencies while inter-blade cascade modes ω_n dominate at high frequencies (see Chapter 3).

- Variations in the spectra at frequencies between successive cascade cut-on frequencies ω_n are due to the interference between all modes cut-on in this frequency band. This behaviour will be explored in detail in Section 4.2.4.

- Ripples are evident in the single airfoil spectra due to interactions between leading and trailing edges. The identical phenomenon is present in the cascade spectra but is generally obscured by cascade mode interference. This will be seen more clearly in Section 4.2.3. These ripples are deeper in the upstream direction due to the stronger directivity of the trailing edge noise in the upstream direction.

It will be argued that the reasons for the differing behaviour between the single airfoil and cascade sound power predictions are due to the following main physical processes:

1. A difference in radiation efficiency: the single airfoil radiates into free field whereas radiation from a cascade is via duct *exits* that may or may not be efficient depending on their size compared with the acoustic wavelength.

2. The cut-on of cascade modes within the inter-blade gaps which are clearly not present for an isolated airfoil.

3. Differing behaviour in the oscillations in upstream and downstream sound power spectra arising from interactions between the leading and trailing edges.

In the next section the characteristics of the sound power radiated from cascades with overlapping blades will be compared with those of non-overlapping cascades. This will lead to the definition of low and high $s_\mathrm{s}/c_\mathrm{s}$ regimes in which distinct behaviours in the power spectra are seen in the cascade results.

4.2.2 Effect blade overlap on the strength of cascade interaction

In this section the effect of blade overlap on the strength of cascade interactions are explored by comparison of exact cascade and equivalent single airfoil spectra for geometries with differing degrees of cascade blade overlap. Clearly, a pre-requisite for strong modal interactions between adjacent blades is that a substantial section of adjacent blades must overlap in the sense of Figures 4.4(a),(b) and (c) which show overlapping $(s_\mathrm{s}/c_\mathrm{s})\sin\chi_\mathrm{s} < 1$, just-overlapping $(s_\mathrm{s}/c_\mathrm{s})\sin\chi_\mathrm{s} = 1$ and non-overlapping blades $(s_\mathrm{s}/c_\mathrm{s})\sin\chi_\mathrm{s} > 1$ respectively. Note that this study could not have been performed using the Wiener-Hopf solution for the cascade blade response as it is restricted to overlapping blades.

In order to illustrate the effect of blade overlap on blade-to-blade interaction consider three examples of cascade geometries with $B_\mathrm{s} = 48$, $\chi_\mathrm{s} = 40°$, $M_\mathrm{s} = 0.4$, $\Lambda/s_\mathrm{s} = 0.2$

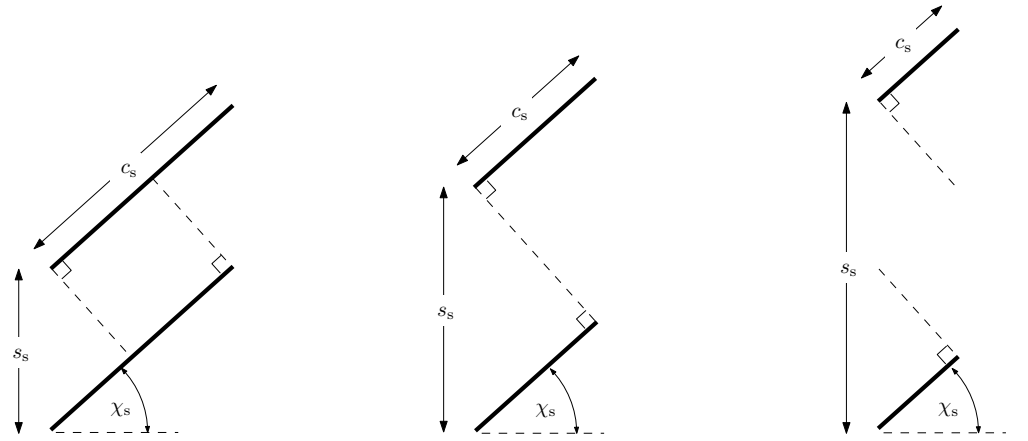

(a) $(s_s/c_s)\sin\chi_s < 1$ — Overlap forms rectilinear duct

(b) $(s_s/c_s)\sin\chi_s = 1$ — Leading-edge and trailing-edge perpendiculars coincide

(c) $(s_s/c_s)\sin\chi_s > 1$ — No overlap

Figure 4.4 – Illustration of perpendicular overlap forming between blades of a non-zero stagger cascade for $(s_s/c_s)\sin\chi_s < 1$.

and $T_w = 0.02$ but with varying degrees of blade overlap. The first has significantly overlapping blades $(s_s/c_s)\sin\chi_s \ll 1$, the second has significantly non-overlapping blades $(s_s/c_s)\sin\chi_s \gg 1$ while the third is a transition geometry in which the blades are neither significantly overlapped or significantly non-overlapped $(s_s/c_s)\sin\chi_s \approx 1$. A comparison of their 'exact' spectra and corresponding single airfoil sound power spectra are plotted in Figure 4.5 against frequency normalised with the fundamental cascade mode cut-on frequency $\Delta\omega$. The values of $(s_s/c_s)\sin\chi_s$ used are listed in the figure caption. Observations regarding the results shown in Figure 4.5 are listed below, grouped according to their overlap condition. Note that a 20 dB offset has been added to these spectra in order to clearly see each example clearly.

4.2.2.1 Differences between exact cascade and SA-model for substantially overlapping blades, $(s_s/c_s)\sin\chi_s \ll 1$

In this case the overlaps between adjacent blades form well defined ducts. Effects due to cascade interactions are therefore strong, as can be seen by the depth of the oscillations in the spectra due to cascade mode interference for $\omega/\Delta\omega > 1$. Nevertheless, single airfoil theory is observed to be in good agreement with the cascade solution above a certain frequency.

In this example, the cascade prediction for $\omega/\Delta\omega \lesssim 1$ is significantly lower than for the single airfoil calculation. In this frequency range the only cascade mode to be cut-on is the plane-wave mode $n = 0$.

Note that close agreement is *generally* seen for $\omega > \Delta\omega$ although the frequency of agreement is appreciably lower for upstream rather than downstream radiation. It will be shown in Section 4.3 that this condition does not always ensure agreement and further refinements to this criterion will be proposed.

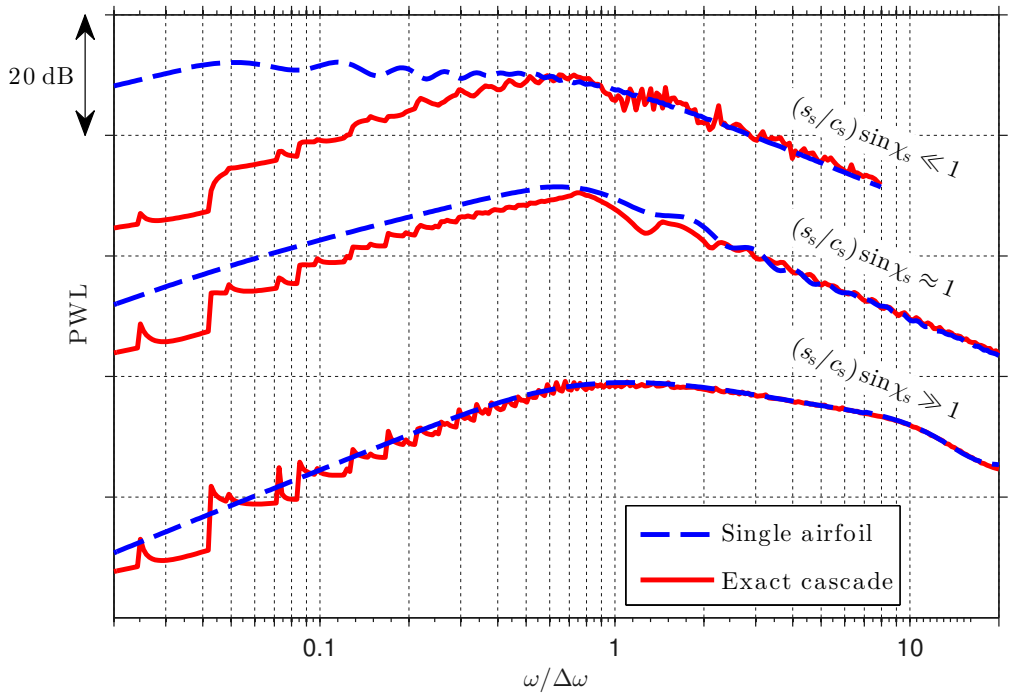

(a) Upstream.

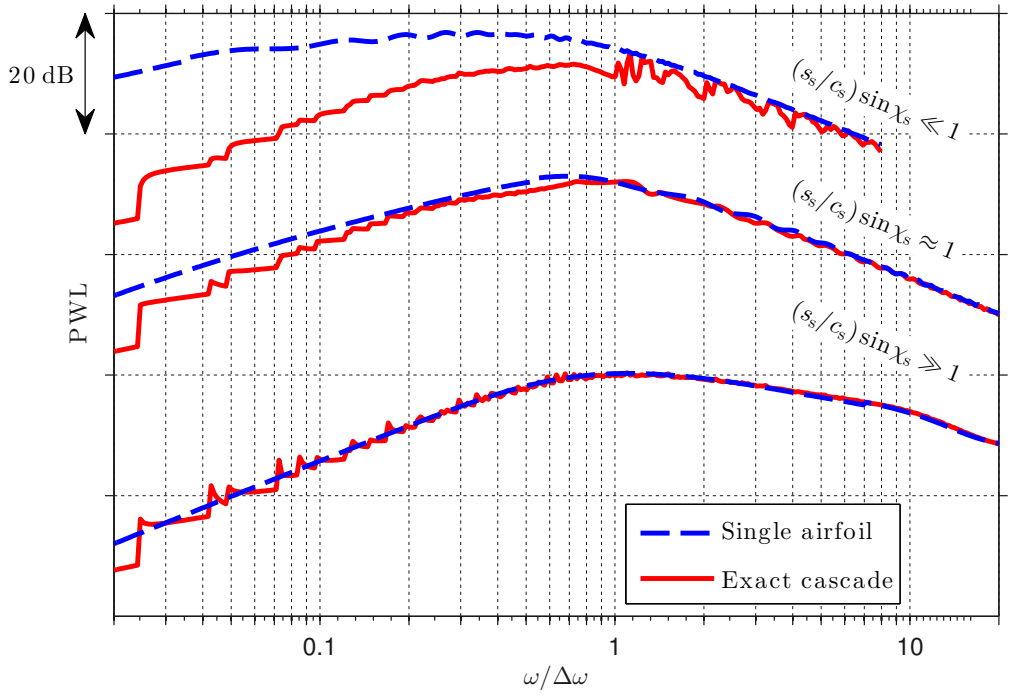

(b) Downstream.

Figure 4.5 – Cascade sound power spectra for three values of $(s_s/c_s)\sin\chi_s = [0.06, 1, 13]$ demonstrating the effect of blade overlap. Equivalent single airfoil sound power spectra shown for comparison. All flow and geometry parameters held constant, $B_s = 48$, $\chi_s = 40°$, $M_s = 0.4$, $\Lambda/s_s = 0.2$ and $T_w = 0.02$. Note that a 20 dB offset has been added to these spectra in order to clearly see each example clearly.

4.2.2.2 Differences between exact cascade and SA-model for substantially non-overlapping blades, $(s_s/c_s)\sin\chi_s \gg 1$

This is the case of most interest in open rotor applications where solidity is low. Close agreement is obtained over all frequencies above a certain, but generally low, frequency in both upstream and downstream directions. The reason for their departure at low frequency is simply that periodicity is imposed on the cascade solution while none is imposed on the single airfoil prediction.

In the following section the changes of behaviour due to changes in s_s/c_s are presented, allowing the identification of cascade mode interference effects which are critical to establishing agreement criteria for substantially overlapping blades.

4.2.2.3 Differences between exact cascade and SA-model for partially overlapping blades, $(s_s/c_s)\sin\chi_s \approx 1$

In this case, there is only partial overlap between neighbouring blades. This is the case of most interest in turbofan applications. Single airfoil theory is still observed to have good agreement with the cascade solution above a certain frequency. The factors that influence the frequency at which agreement occurs differ in the upstream and downstream cases. Note that no abrupt change in behaviour is observed as the blades become non-overlapped.

Upstream radiation for partially overlapping blades, $(s_s/c_s)\sin\chi_s \approx 1$. When the blades are only partially overlapped the oscillations in the power spectra arising from the interference between cascade modes become significantly lower in amplitude. These effects are not present in the single airfoil calculation. Reduced blade overlap also results in a reduction of the difference in sound power radiation seen at low frequencies, suggesting a reduction of the plane wave radiation efficiency effect observed in for significantly overlapped blades. Both of these effects imply that duct radiation effects are reduced as the inter-blade ducts become shorter.

For upstream radiation the main distinctions between the spectra predicted by the two models arise due to the small differences in the manner in which the leading and trailing edge interactions occur. This leads to significant, but slowly varying, oscillations that are present in both power spectra but with their peaks and troughs in slightly different positions. However, unlike for substantially overlapping blades, when the overlap is only partial the influence of the trailing edge becomes a significant factor in determining the degree of agreement between the two spectral predictions. The magnitude of these oscillations for upstream radiation are greater than in the downstream spectra. This is because of interference between the downstream propagation modes with the reflected upstream propagating modes which requires at least two reflections in the downstream case, as depicted in Figure 4.6. The combined effect of these phenomena is that the frequency of agreement is now appreciably higher than when substantially overlapped.

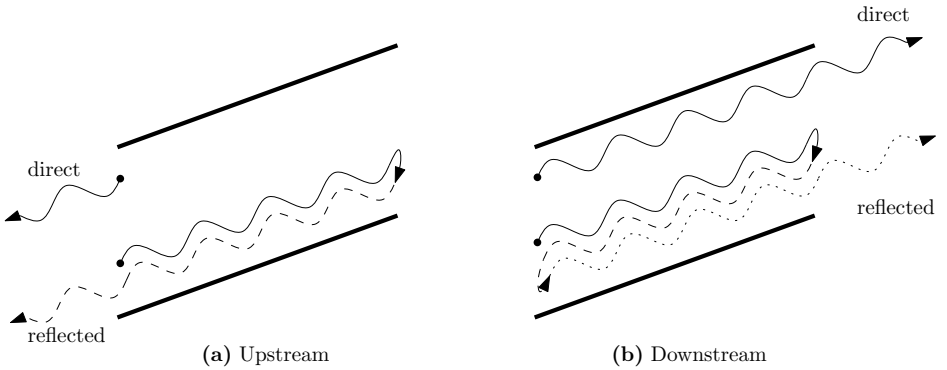

(a) Upstream **(b)** Downstream

Figure 4.6 – Illustration of waves reflecting in duct formed between overlapped blades.

Downstream radiation for partially overlapping blades, $(s_\mathrm{s}/c_\mathrm{s})\sin\chi_\mathrm{s} \approx 1$. Qualitative agreement between the single airfoil and cascade spectra are different for downstream radiation compared to that upstream. Good agreement is obtained for downstream radiation over a much wider range of frequencies. In particular it may be noted that the oscillations in the power spectra arising from the cut-on of the cascade modes are negligible. It will be shown in Section 4.2.4 that the character of the interference between cascade modes that cause these oscillations leads to their disappearance at lower values of $s_\mathrm{s}/c_\mathrm{s}$ for downstream radiation compared with upstream radiation.

4.2.3 Effect of '$s_\mathrm{s}/c_\mathrm{s}$' on fine structure of cascade interaction power spectra

The effect of changes to s_s and c_s on the upstream and downstream of both single airfoil and cascade spectra are now investigated in greater detail. The leading-edge spacing s_s controls the number of cascade modes that will be cut-on at a given frequency and is therefore only of concern to the cascade. The chord c_s is linked with reduced-frequency effects, particularly those associated with leading-trailing edge interactions. The ratio of these two parameters $s_\mathrm{s}/c_\mathrm{s}$ forms the independent parameter in controlling the cascade response [59] while it was also shown to be critical in the determination of blade overlap in the preceding section. In order to identify the detailed behaviour of the variation in sound power spectra, they are presented on two-dimensional 'maps' in which the cascade-equivalent PWL is plotted against $\omega/\Delta\omega$ and $s_\mathrm{s}/c_\mathrm{s}$. The frequency normalisation factor $\Delta\omega$ has been chosen to reveal the precise frequencies at which the cascade modes cut-on.

Figures 4.7 and 4.8 show respectively the upstream and downstream maps for single airfoils and cascades with common parameters: $B_\mathrm{s} = 48$, $\chi_\mathrm{s} = 40°$, $M_\mathrm{s} = 0.4$, $\Lambda/s_\mathrm{s} = 0.2$ and $T_\mathrm{w} = 0.02$. Significant interference due to cascade effects are seen in the upstream and downstream plots for $s_\mathrm{s}/c_\mathrm{s} \lesssim 1.5$ and $\omega/\Delta\omega > 1$. Moreover, distinct regions of behaviour can be observed corresponding to the different frequency bands $\omega_n < \omega < \omega_{n+1}$. In these regions, complex interference patterns are visible, which in Section 4.2.4 are demonstrated to be due to interference between cascade modes. Note also that significant cascade mode

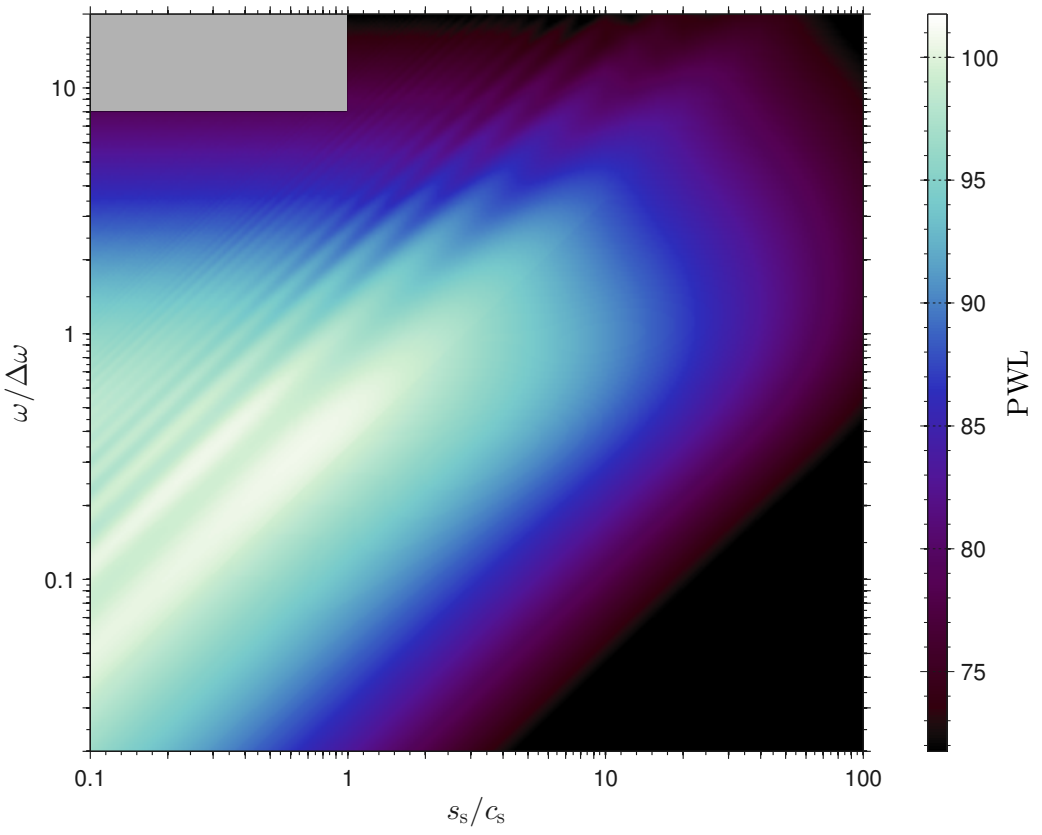

(a) Single airfoil

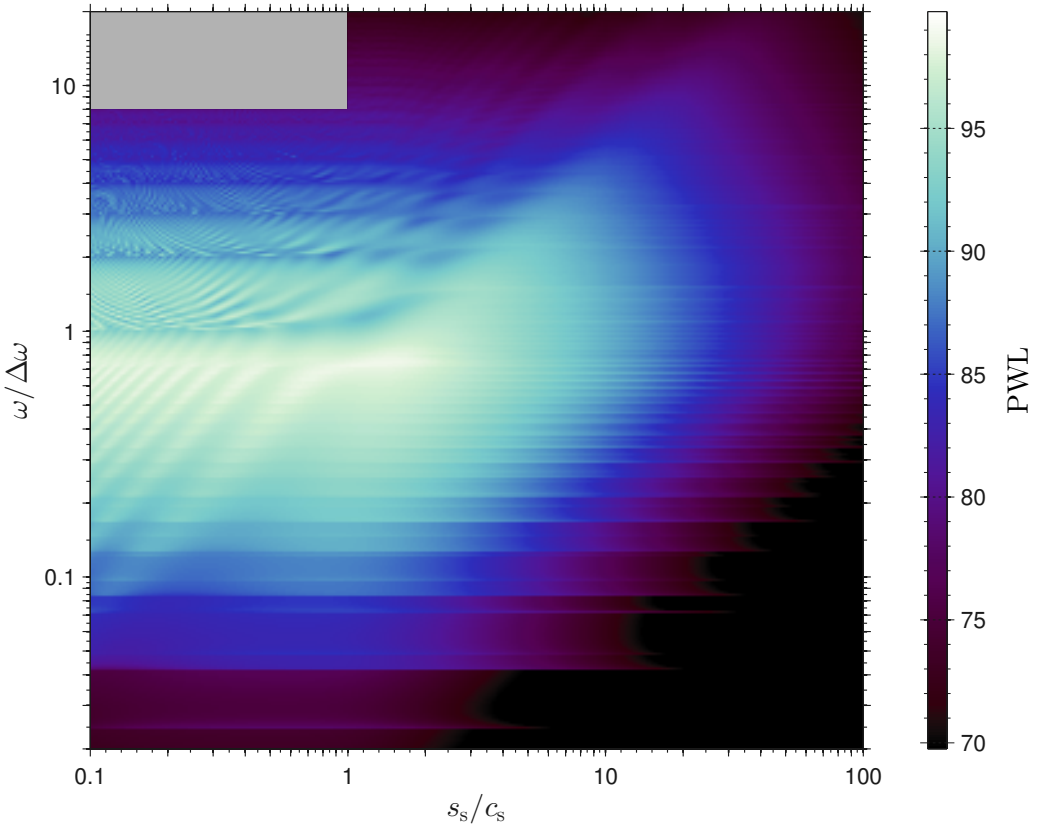

(b) Cascade

Figure 4.7 – 'Maps' of upstream sound power level per unit span plotted against s_s/c_s and $\omega/\Delta\omega$. Other geometry and flow parameters held constant, $B_s = 48$, $\chi_s = 40°$, $M_s = 0.4$, $\Lambda/s_s = 0.2$ and $T_w = 0.02$. Calculations not performed for $s_s/c_s < 1$ AND $\omega/\Delta\omega > 8$ for computational reasons.

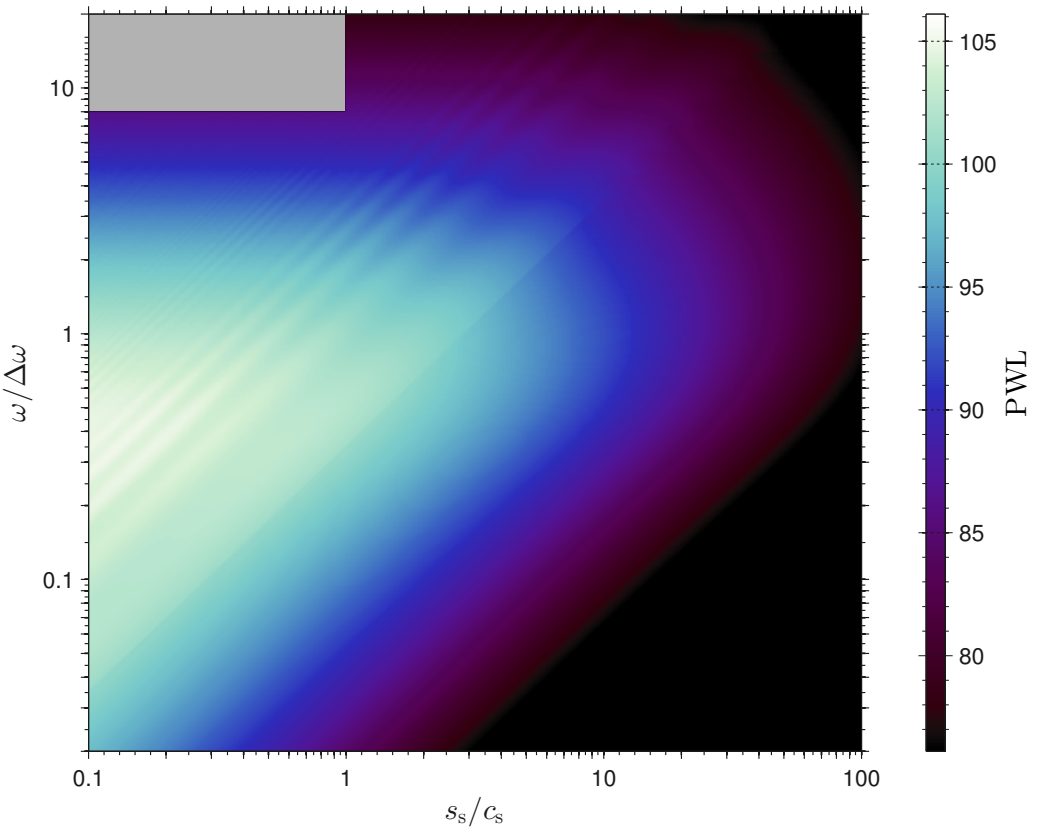

(a) Single airfoil

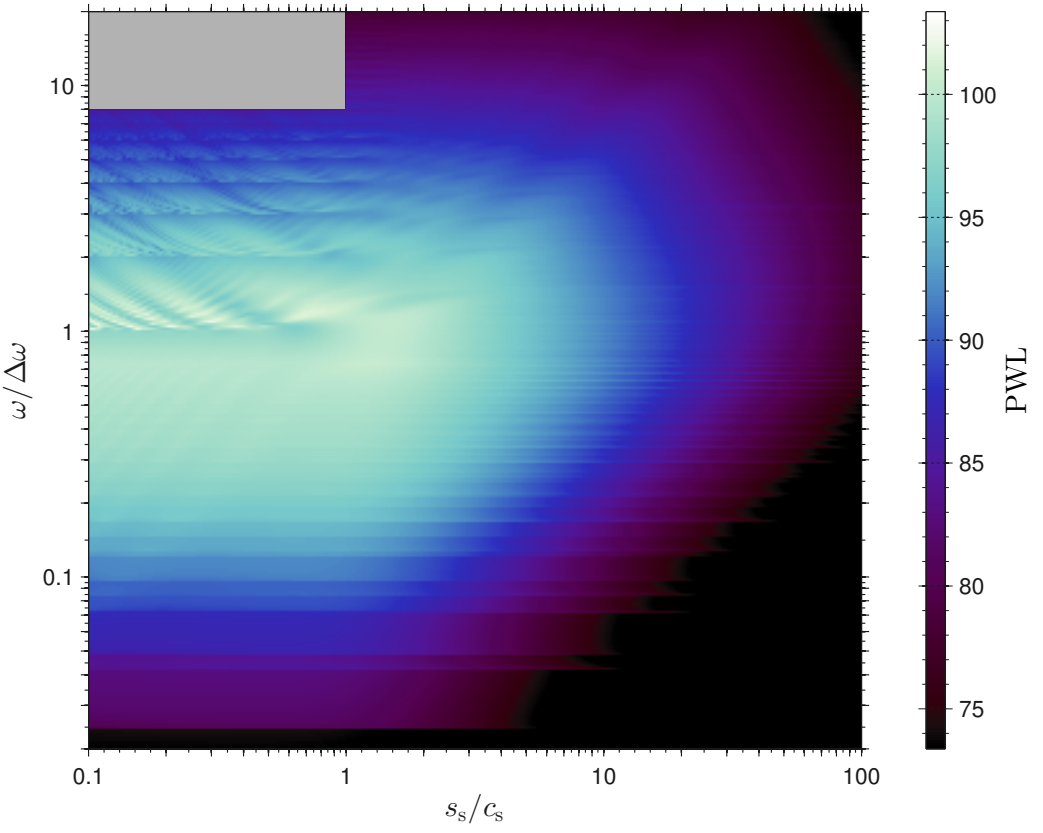

(b) Cascade

Figure 4.8 – 'Maps' of downstream sound power level per unit span plotted against s_s/c_s and $\omega/\Delta\omega$. Other geometry and flow parameters held constant, $B_s = 48$, $\chi_s = 40°$, $M_s = 0.4$, $\Lambda/s_s = 0.2$ and $T_w = 0.02$. Calculations not performed for $s_s/c_s < 1$ AND $\omega/\Delta\omega > 8$ for computational reasons.

interactions are still visible for non-overlapping blades, corresponding to $s_s/c_s > 1.5$ in this example. However, their intensity falls off rapidly for s_s/c_s values above this.

Also clearly visible in the single airfoil and cascade spectral map are distinct diagonal features. These correspond directly to lines of constant reduced-frequency and are related to the peaks and troughs of ripples associated with waves repeatedly interacting between the trailing edge and leading edge. It is noteworthy that these features are appreciably stronger in the single airfoil spectra, suggesting that ducting of the radiated sound by adjacent blades causes a weakening of this behaviour. As s_s/c_s increases and cascade effects weaken the frequencies at which the peaks and troughs of these ripples appear become closer in single airfoil and cascade calculations so that the spectral differences are reduced.

4.2.4 Cascade mode interference

It will now be demonstrated by simple analysis that the interference patterns seen for $(s_s/c_s) < 1.5$ in the cascade power maps of Figures 4.7b and 4.8b are due to interference between cascade modes.

For simplicity, consider the frequency range in which only the cascade modes of orders $n = 0$ and $n = 1$ are cut-on: $\omega_1 < \omega < \omega_2$ (Equation (3.5)). First consider the behaviour of the downstream sound power spectra. It is assumed that the downstream radiated sound power is related to the mean-square pressure at the trailing edge plane. The pressure at the trailing edge due to the two cascade modes of orders $n = 0$ and $n = 1$, each of unit amplitude and with phase difference φ, generated at the leading edge is given by

$$p\left(c_s\right) = e^{-i\varphi}e^{-ik_{1,0}c_s} + e^{-ik_{1,1}c_s}, \tag{4.3}$$

where $k_{1,n}$ is the axial wavenumber of the cascade mode of order n given by

$$k_{1,n} = \frac{kM_s \pm \sqrt{k^2 - \beta^2 k_{2,n}^2}}{\beta^2}, \tag{4.4}$$

and from Equation (3.5)

$$k_{2,n} = \frac{n\pi}{s_s \cos\chi_s}, \tag{4.5}$$

is the corresponding gap-wise wavenumber component. The mean-square pressure at the trailing edge is given by

$$\overline{p^2}\left(c_s\right) = \frac{1}{2}pp^* = 1 + \cos\left(\varphi + k_{1,0}c_s - k_{1,1}c_s\right), \tag{4.6}$$

where * denotes complex conjugation. The peaks and troughs of $\overline{p^2}\left(c_s\right)$ will occur when

$$\left(k_{1,0} - k_{1,1}\right)c_s = m\pi - \varphi, \text{ for } m \in \mathbb{N}. \tag{4.7}$$

Even values of m result in peaks, associated with constructive interference. Destructive interference troughs occur at odd values of m. It is now assumed for the sake of simplicity that the phase difference $\varphi = 0$. Equation (4.4) is solved for $n = 0$ and $n = 1$ and the resulting expressions are substituted into Equation (4.7), giving the following expression for the frequency at which the peak or trough of order m is located

$$\omega_{\mathrm{int},m} = \pm \frac{\pi \beta c_0}{2 s_\mathrm{s} \cos \chi_\mathrm{s}} \left\{ \beta m \left(s_\mathrm{s}/c_\mathrm{s} \right) \cos \chi_\mathrm{s} + \left[\beta m \left(s_\mathrm{s}/c_\mathrm{s} \right) \cos \chi_\mathrm{s} \right]^{-1} \right\}. \tag{4.8}$$

Figure 4.9 shows a set of curves obtained using Equation (4.8) overlaid on a map of downstream PWL plotted against $s_\mathrm{s}/c_\mathrm{s}$ and $\omega/\Delta\omega$.

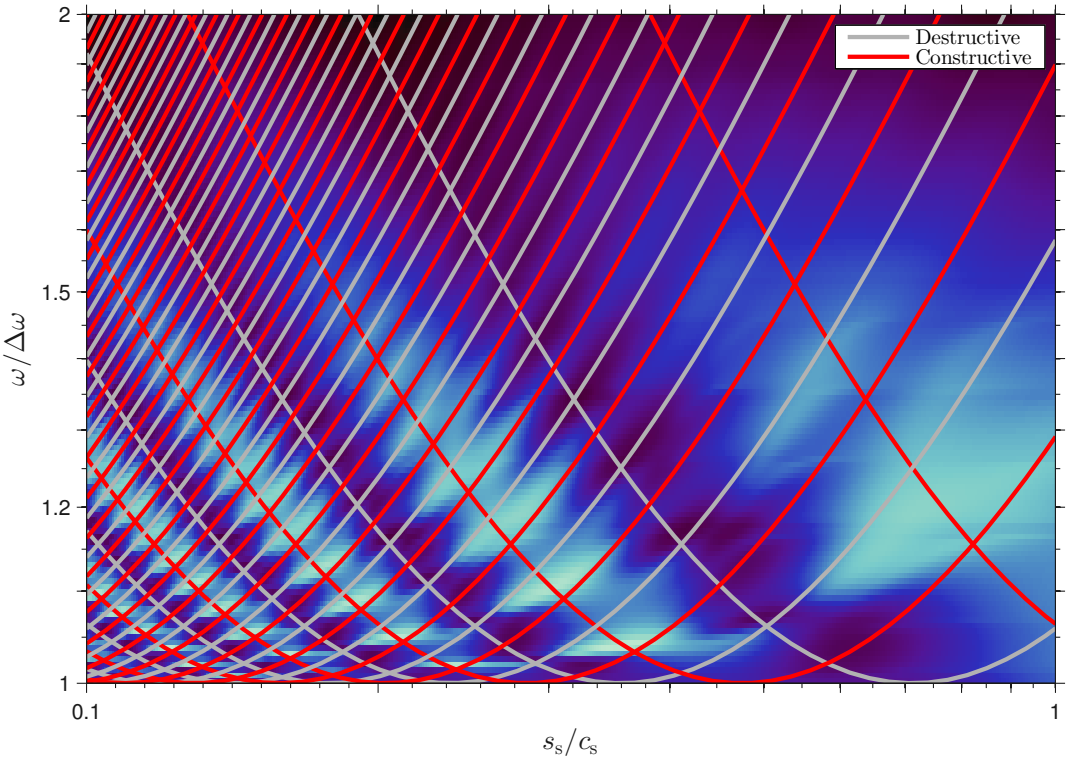

Figure 4.9 – Peak and trough lines overlaid on a cascade sound power level map showing modal interference for $\omega_1 < \omega < \omega_2$, $0.1 < s_\mathrm{s}/c_\mathrm{s} < 1$ obtained using parameters: $\varphi = 0$, $B_\mathrm{s} = 12$, $\chi_\mathrm{s} = 40°$, $M_\mathrm{s} = 0.4$, $\Lambda/s_\mathrm{s} = 0.01$ and $T_\mathrm{w} = 0.02$.

4.3 Criteria for agreement between single airfoil and cascade theory

The purpose of this chapter is to identify the frequencies above which close agreement is seen between the PWL spectra obtained using the exact cascade and single airfoil noise models using Equations (2.56) and (4.1) allowing improvements to the efficiency of sound power calculations for broadband noise. The main differences between exact cascade and single airfoil sound power spectra have been demonstrated and the physical causes behind these differences discussed in the preceding section. In this section criteria will be established that allow the identification of frequencies above which agreement at a desired level is obtained.

4.3.1 Definition of agreement criteria

A method shall now be described that allows the identification of frequencies above which agreement between two PWL spectra is obtained to within a given threshold. The concept of close agreement is somewhat arbitrary and hence has proved difficult to define in precise terms. However, the following method has produced results that appear to be acceptable.

Having chosen a desired level of agreement (in dB) the objective of the new method is to ensure that at all frequencies above the resulting minimum agreement frequency:

"The difference in PWL exceeds the threshold for no more than one-third octave bandwidth."

This definition ignores small-bandwidth excursions of sound power level difference, assuming that these are of little importance to band-average behaviour (tending to become 'averaged-out').

The level difference between two spectra is calculated ΔPWL. The analysis of the difference spectrum is conducted one frequency point at a time from high frequencies to low. A one-third octave band is identified below the current frequency point. If any part of the one-third octave band is within the prescribed threshold then the current frequency point is regarded as being in agreement. This process is repeated until the first band is encountered which has no part within the prescribed threshold. This process is illustrated in Figure 4.10.

Figure 4.10a shows PWL spectra obtained for a cascade and the equivalent single airfoil spectrum while Figure 4.10b shows the level difference between these two spectra ΔPWL. Overlaid on Figure 4.10b are horizontal blue lines indicating the threshold values (± 1 dB in this case) and a vertical green line showing the minimum agreement frequency. The spectra at higher frequencies are in agreement within the specified threshold, this area being shaded in green. The one-third octave band corresponding to the agreement frequency is shown as the pink area. Note that throughout this entire band ΔPWL is outside the threshold.

4.3.2 Example of cascade-single airfoil agreement frequencies obtained using agreement criteria

Using the agreement criteria defined in Section 4.3.1 the variation of the minimum agreement frequencies are investigated for changing $s_\mathrm{s}/c_\mathrm{s}$ using the geometry $B_\mathrm{s} = 48$, $M_\mathrm{s} = 0.4$, $\Lambda/s_\mathrm{s} = 0.2$ and $T_\mathrm{w} = 0.02$ which are the same selection of parameters as used for the examples presented in Sections 4.2.2 and 4.2.3. This study is restricted to the case when $\Lambda/s_\mathrm{s} < 0.25$ for non-overlapped wakes. Different behaviour is observed at larger normalised length scales, particularly at low frequencies. These effects will not be discussed further in this thesis. Upstream and downstream results are presented separately.

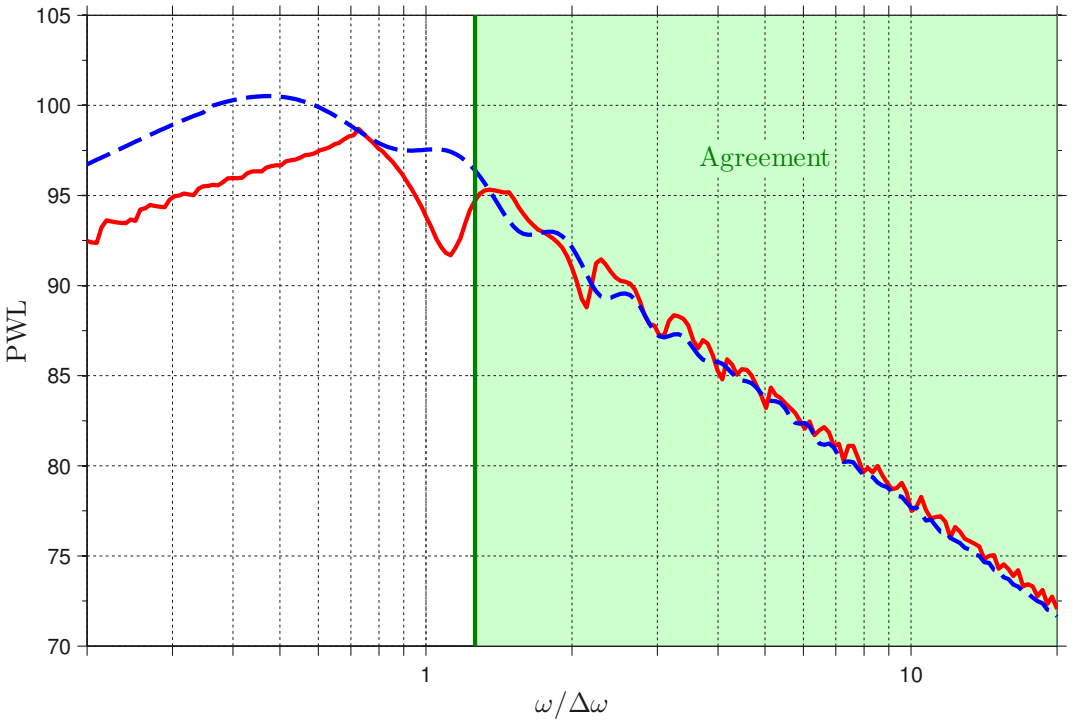

(a) Sound power spectra

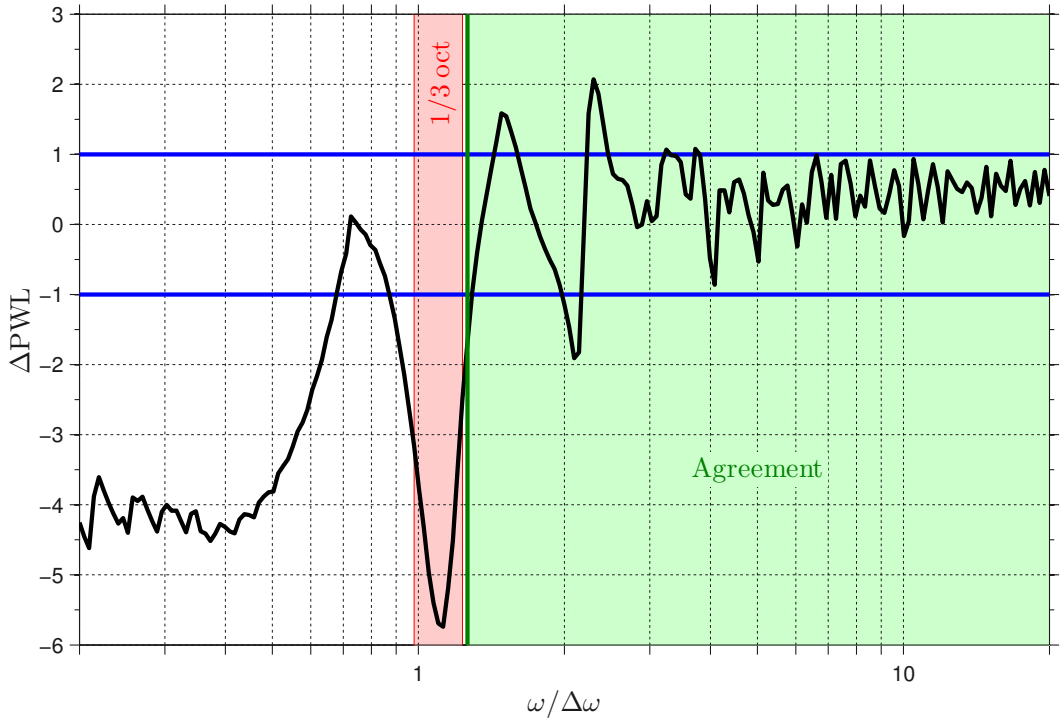

(b) Level difference spectrum

Figure 4.10 – Cascade and SA-model PWL spectra and corresponding level difference plotted on separate axes to illustrate agreement at 1 dB. Also shown are horizontal blue lines indicating the threshold (±1 dB) and a vertical green line indicating the corresponding minimum agreement frequency. The green shaded areas indicate frequencies where agreement is seen. The pink shaded area in the lower plot is of one-third octave bandwidth and shows that the level difference is outside the threshold over its entire width. These spectra obtained using the parameters: $s_s/c_s = 1$, $B_s = 48$, $\chi_s = 40°$, $M_s = 0.4$, $\Lambda/s_s = 0.2$ and $T_w = 0.02$.

4.3.2.1 Upstream agreement frequencies

Figure 4.11 shows the 1 dB and 3 dB upstream minimum agreement frequencies versus s_s/c_s. These frequencies are normalised with $\Delta\omega$, the fundamental frequency for cascade modes defined in Equation (3.6). Also shown is Ω_{-1}, the cut-on frequency of the duct mode of order -1 (see Equation (3.2)). The vertical dash-dotted line represents the value of s_s/c_s for which the blades cease to overlap as s_s/c_s increases from below.

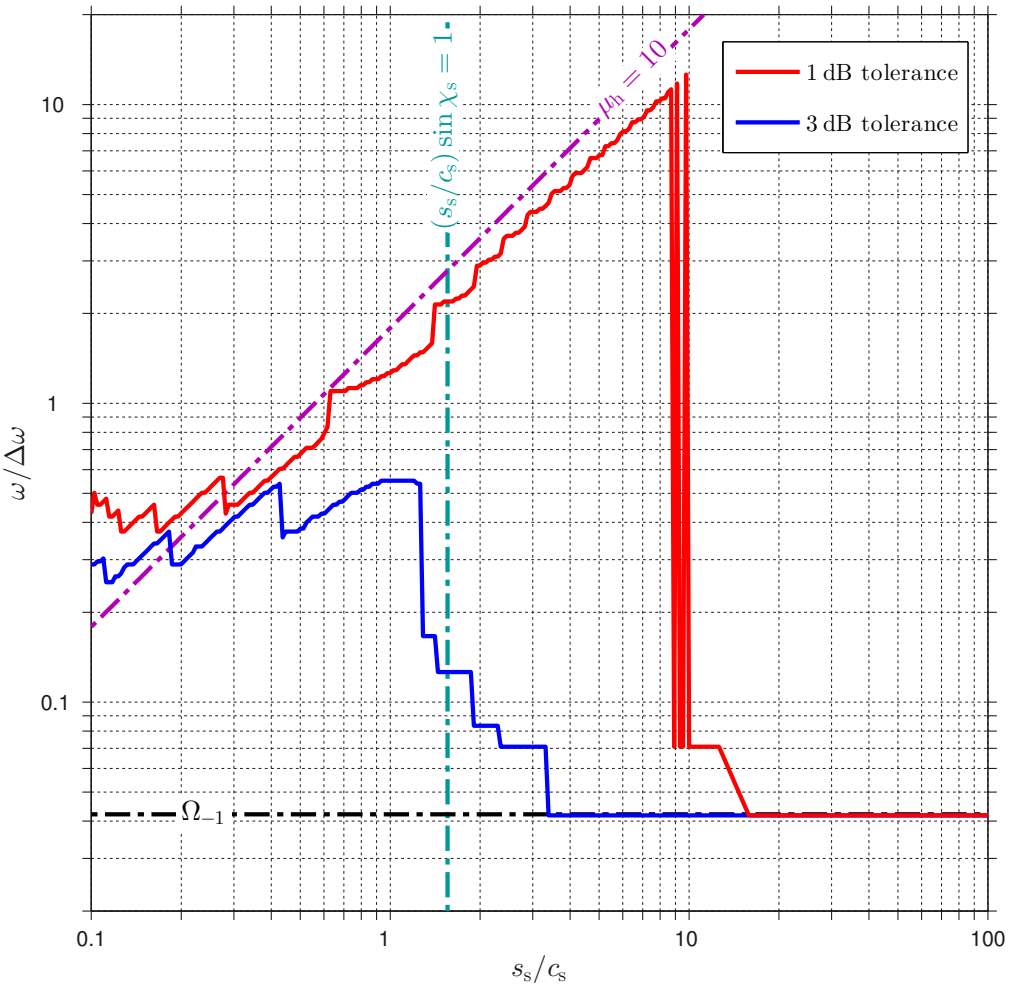

Figure 4.11 – Upstream minimum agreement frequencies obtained at 1 dB and 3 dB levels for cascade and equivalent single airfoil predictions with $B_s = 48$, $M_s = 0.4$, $\Lambda/s_s = 0.2$ and $T_w = 0.02$ over a range of s_s/c_s. The frequencies Ω_{-1} and the constant hydrodynamic reduced-frequency $\mu_h = 10$ are indicated, as is the overlap condition $(s_s/c_s)\sin\chi_s = 1$. All frequencies are normalised with $\Delta\omega$.

The most striking feature of this figure is that the minimum agreement frequencies appear to follow the line of constant reduced-frequency, $\mu_h = \omega c_s/2\beta^2 U = 10$ at small values of s_s/c_s. As the tolerance is reduced from 3 dB to 1 dB the minimum agreement frequencies deviate from this straight line at increasing values of s_s/c_s. The reason for this behaviour can be found by inspection of Figure 4.5a showing comparisons between single airfoil and cascade spectra at very small, moderate and very large $(s_s/c_s)\sin\chi_s$ values. It can be seen that the main differences between the cascade and single airfoil spectra as they converge result from their slightly differing responses due to leading-trailing edge

interactions. Peaks and troughs are present in both spectra but appear at slightly different frequencies. These oscillations generally become smaller as s_s/c_s is increased, eventually becoming unimportant.

For high values of s_s/c_s, where the differences in leading-trailing edge interactions are insignificant for model agreement, the agreement frequency becomes equal to the cut-off frequency of the duct mode of order $m = -1$. This mode is co-rotating and carries significant power unlike the counter-rotating $m = +1$, as observed in Section 3.1.1. The duct modes, absent from the single airfoil radiation model, cause a fundamental difference in low-frequency spectral behaviour.

For small s_s/c_s, where cascade interaction effects are important, good agreement is obtained well below $\Delta\,\omega$, the frequency at which the first higher-order cascade mode cuts on. This suggests that upstream radiation is predominantly generated by direct radiation from the leading edges to the upstream observer with only a minor influence by the rectilinear inter-blade duct.

4.3.2.2 Downstream agreement frequencies

Figure 4.12 shows the 1 dB and 3 dB downstream minimum agreement frequencies versus s_s/c_s. These frequencies are normalised by $\Delta\omega$. A horizontal dash-dotted line indicates the frequency Ω_{+1} defined in Equation (3.2). Also shown as a vertical dash-dotted line is the value of s_s/c_s for which the blades cease to overlap as s_s/c_s increases from below.

The behaviour of the minimum agreement frequencies with s_s/c_s is markedly different from that obtained for upstream radiation, as shown in Figure 4.11. These minimum agreement frequencies are observed to largely independent of s_s/c_s for $(s_s/c_s)\sin\chi_s \lesssim 0.8$. This suggests that for downstream radiation a reasonable degree of blade overlap is necessary for cascade effects to become significant. Unsurprisingly, the minimum agreement frequencies increase as the tolerance is reduced.

In this downstream case, for overlapped blades, the agreement frequencies correspond closely to the cut-off frequencies of the cascade modes of order $n = 1$ and $n = 2$. Thus, it would appear that cascade effects can be neglected when at least one higher-order cascade mode is cut-on (for agreement at 3 dB). Figure 4.12 indicates that if better agreement is sought using single airfoil theory then at least 2 or 3 higher-order cascade modes are required to be cut-on.

For high values of s_s/c_s, where the blades are non-overlapped, the agreement frequency becomes equal to the cut-off frequency of the duct mode of order $m = +1$. This mode is counter-rotating but carries significant power since the axial component of the downstream modal phase angle is aligned with that of the mean flow.

4.3.3 Summary or agreement criteria

It has been demonstrated that the sound power spectra for upstream and downstream radiation obtained using single airfoil and cascade theory are in close agreement above

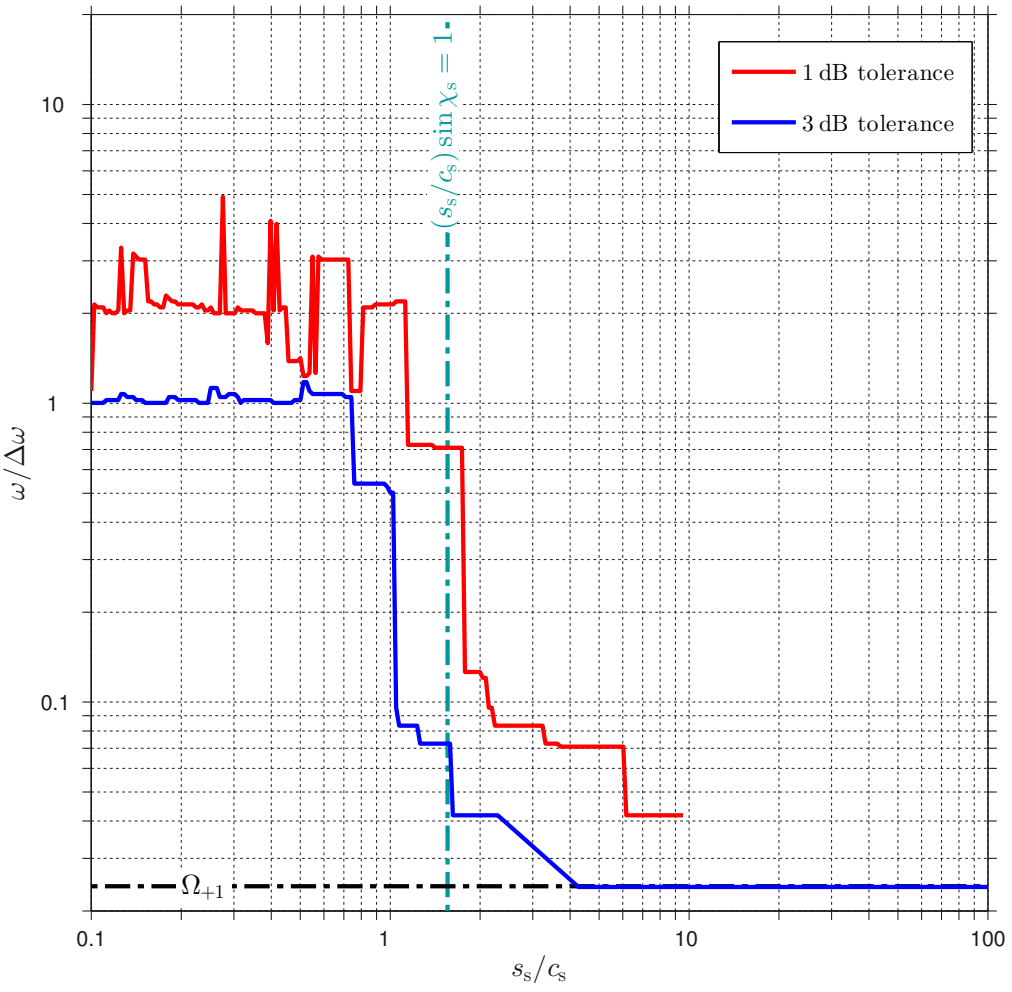

Figure 4.12 – Downstream minimum agreement frequencies obtained at 1 dB and 3 dB levels for cascade and equivalent single airfoil predictions with $B_s = 48$, $M_s = 0.4$, $\Lambda/s_s = 0.2$ and $T_w = 0.02$ over a range of s_s/c_s. The frequency Ω_{+1} is indicated, as is the overlap condition $(s_s/c_s)\sin\chi_s = 1$. All frequencies are normalised with $\Delta\omega$.

certain minimum agreement frequencies that are influenced by the extent of blade overlap and other geometrical and flow parameters. In general, where there is substantial blade overlap the upstream and downstream agreement frequencies are approximately $\Delta\omega$, the fundamental cut-on frequency of cascade modes as defined in Equation (3.5).

In the partially overlapping regime, $(s_\mathrm{s}/c_\mathrm{s})\sin\chi_\mathrm{s} \approx 1$, it is likely that around $\Delta\omega$ there will be differences between the cascade and single airfoil sound power spectra of a few decibels. In the upstream case the spectra diverge because of differences in the nature of the leading-trailing edge interactions. In downstream propagation spectral differences occur because of large-bandwidth excursions due to cascade mode interference that are absent in the single airfoil calculations. However, agreement between cascade and single airfoil spectra is improved considerably at ω_2.

Where the blades are substantially non-overlapping, $(s_\mathrm{s}/c_\mathrm{s})\sin\chi_\mathrm{s} \gg 1$, the minimum frequency required to see close agreement between the sound power spectra obtained using cascade theory and single airfoil theory is $\Omega_{\pm1}$ as defined in Equation (3.1) the cut-on frequency for the first co-rotating duct mode associated with the periodicity imposed on sound power radiation in the cascade formulation (Equation (2.56)).

The agreement frequencies are summarised in Table 4.1 and sketched in Figure 4.13.

Table 4.1 – Summary of the criteria for agreement between sound power spectra using single airfoil and cascade.

	Substantially overlapped	Substantially non-overlapped
Upstream	$\omega > \Delta\omega$	$\omega > \Omega_{-1}$
Downstream	$\omega > \Delta\omega$	$\omega > \Omega_{+1}$

4.4 Concluding remarks

This chapter makes the following main contributions to the understanding of cascades and how they relate to isolated airfoils:

1. It is observed that upstream and downstream sound power radiation spectra are in close agreement above certain frequencies, which can be calculated for a given geometry and turbulent subsonic flow.

2. Significant cascade interactions occur for cascade geometries where adjacent blades have a substantial perpendicular overlap, forming inter-blade ducts. The resulting phenomena – duct radiation efficiency and cascade mode interference – dominate the agreement in this overlapped regime.

3. In the partially-overlapping case the upstream agreement frequencies are relatively high due to differences in the manner of leading-trailing edge interactions seen in single airfoil and cascade calculations.

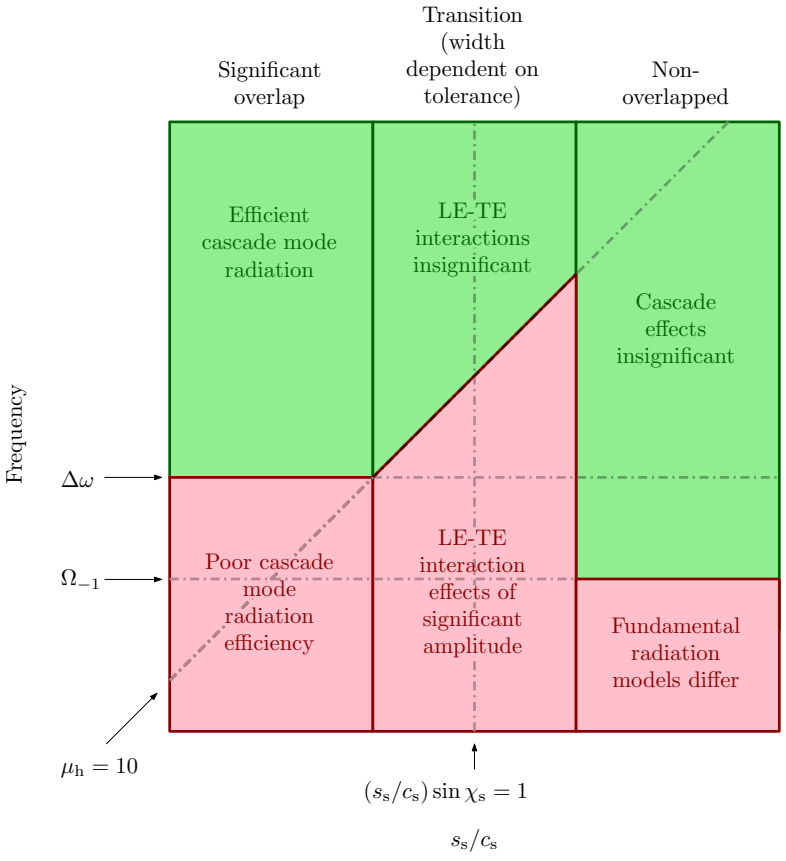

(a) Upstream

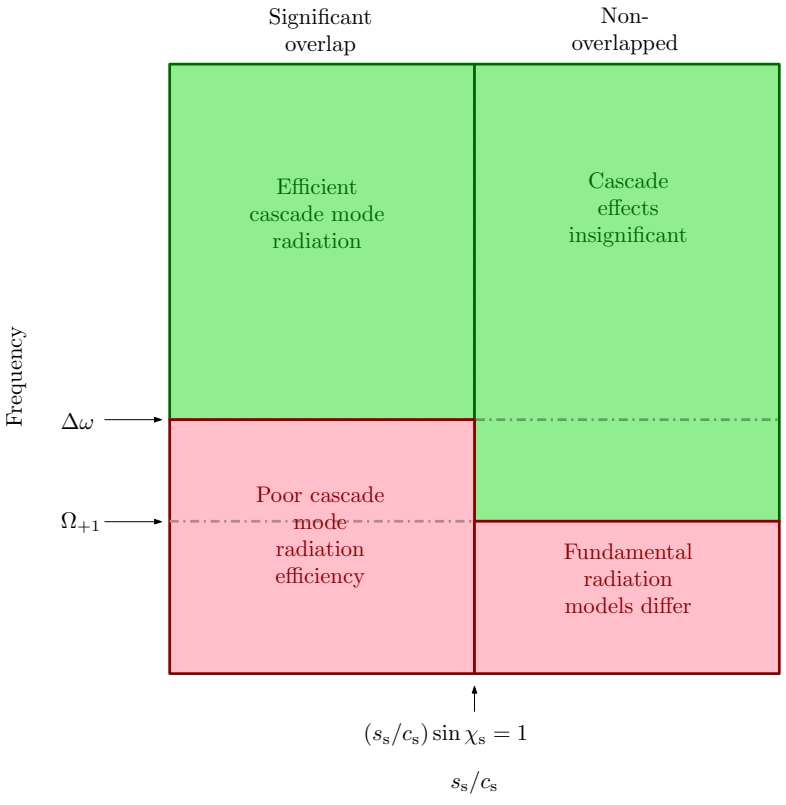

(b) Downstream

Figure 4.13 – Sketch indicating the areas of agreement between cascade and single airfoil predicted sound power levels.

4. Where cascade blades are substantially non-overlapped the lower limit of agreement is controlled only by the periodicity condition imposed on cascade radiation.

Chapter 5

Sound power transmission loss across the rotor

Broadband rotor-stator interaction noise has been shown to be a major contributor to the noise generated by a turbofan engine. Noise generated in this manner will propagate to the far-field observer both downstream and upstream. The upstream path, indicated in Figure 5.1, must pass through the rotor which will both reflect some of the incident power and scatter energy between frequencies. It is this upstream path and the scattering of sound by the spinning fan that is the primary concern of this chapter.

In this chapter a general modal power scattering model is developed which is expressed in terms of non-dimensional modal pressure scattering coefficients. The model is used to perform simulations of rotor sound power transmission loss where the scattering is calculated using the acoustic scattering model due to Smith [46] and Whitehead [47]. A series of blockage results are presented to show trends with Mach number, stagger angle, rotor pitch-chord ratio and rotation speed. The analytical rotor transmission model due to Kaji and Okazaki [67] is used to derive a rotor sound power transmission loss model which provides a simple interpretation of the blockage mechanism.

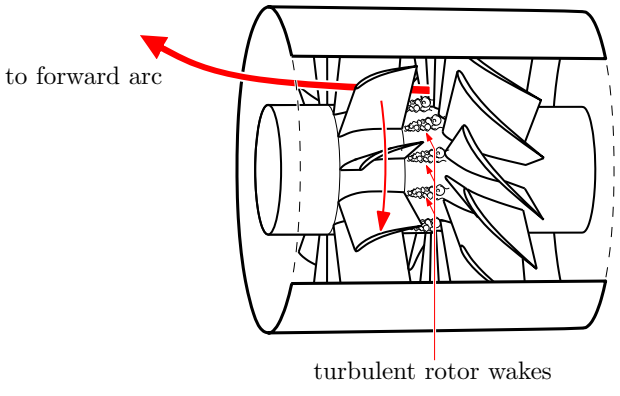

Figure 5.1 – Noise generated on the OGV surface propagates to the forward arc through the rotor.

5.1 Scattering theory

In this section a general scattering model is presented that is expressed in terms of modal pressure scattering coefficients. This begins by outlining the basic modelling assumptions.

5.1.1 Modelling assumptions

The following series of assumptions are employed in the modelling approach

1. The rotor is divided into annular strips, as for the noise model in Chapter 2. The sound power in each strip is summed incoherently. This 'strip theory' approach is common in solutions to the vortical impingement problem where coherence between adjacent strips is low due to the random nature of the incident field. However, in the current problem of impingement by deterministic acoustical modes the radial coherence of each incident mode is assured. We assert that due to the broadband multi-modal character of the incident field there will, in fact, be low coherence between adjacent strips at sufficiently high frequency.

2. The broadband noise is assumed to be radiated from the OGV in free field. The effects of the duct on radiated sound are ignored.

3. The blades of the rotor in each strip are represented as flat plates of zero thickness.

4. The rotor is assumed to have no steady loading so that the mean flow can be modelled as uniform. The mean flow is assumed to impinge with zero angle of incidence.

5. The annular duct is assumed to have a constant cross section. This, combined with the steady mean flow (see item 4), leads to an assumption that there is a constant range of cut-on acoustic modes at any axial location for a given frequency.

6. The finite unsteady blade loading assumption is satisfied and the Kutta condition is imposed, i.e. the pressure is continuous at the blade trailing edges (see e.g. Whitehead [47]).

7. The unsteady flow perturbations are assumed to be very small compared to the mean flow velocity so that linear theory may be employed.

8. The flow is assumed to be subsonic and isentropic.

9. The medium is assumed to be inviscid and hence boundary layers on vane surfaces are neglected.

5.1.2 Incident acoustic field

In a circular or annular duct, a system of cylindrical coordinates (x, ϕ, R) can be defined such that the x-axis points along the duct centreline, R is a radial coordinate from the

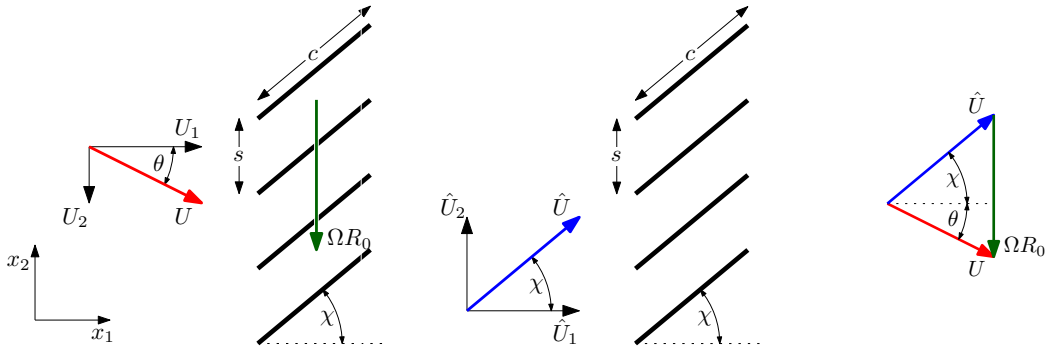

(a) Static 'duct' **x** frame. **(b)** Rotor-fixed $\hat{\mathbf{x}}$ frame. **(c)** Velocity vector triangle.

Figure 5.2 – Illustration of the geometry of flat plate airfoils with stagger angle χ translating in the duct **x** reference frame with velocity ΩR_0. The mean flow is assumed to be unchanged by its passage through the rotor so that the **x** frame velocity U and whirl angle θ are identical upstream and downstream of the blade row. In the $\hat{\mathbf{x}}$ frame, moving with the blade row, the mean flow appears to have velocity $\hat{U}$ and is aligned with the blades so that the whirl angle is χ.

duct centreline, and ϕ is the azimuthal angle. At a single frequency acoustic modes of azimuthal order m in the duct are of the form

$$p_m(\mathbf{x}, t) = f(R)\mathrm{e}^{\mathrm{i}(\omega_0 t + \mu_m^{\pm} x + m\phi)},$$

where $f(R)$ is a radially dependent function (usually involving Bessel functions), ω_0 is the acoustic frequency and $\mu_m^{\pm}$ is the associated axial wavenumber, with $+$ denoting a wave travelling upstream, and $-$ denoting a wave travelling downstream.

Consider a thin annular section of the duct, about medial radius R_0, and suppose that within this section the pressure is independent of R, so $f(R) = \textit{constant}$. The duct section is 'unwrapped', with the ϕ coordinate mapping to the new 'gap-wise' coordinate $x_2 = \phi R_0$. Then $\phi = 2\pi x_2/Bs$, where B is the number of fan blades and $s = 2\pi R_0/B$ is the blade pitch, as illustrated in Figure 5.2a. The pressure in this strip can be written as

$$p_m(\mathbf{x}, t) = P_m \mathrm{e}^{\mathrm{i}(\omega_0 t + \mu_m^{\pm} x_1 + \nu_m x_2)}, \tag{5.1}$$

where P_m is the complex pressure magnitude and $\mu_m^{\pm}$ and ν_m are the wavenumber components resolved in the axial and gap-wise directions respectively.

The mode order m incident upon the rotor is constrained by the periodic nature of the cylindrical duct so that the gap-wise wavenumber component is given by

$$\nu_m = \frac{2\pi m}{Bs}. \tag{5.2}$$

Substitution of Equation (5.1) into the convected wave equation results in the acoustic dispersion relation

$$\left(\tfrac{\omega_0}{c_0} + M_1\mu_m + M_2\nu_m\right)^2 - \left(\mu_m^2 + \nu_m^2\right) = 0, \tag{5.3}$$

where M_1 and M_2 are the axial and gap-wise components of the mean flow Mach number. Solving for the axial wavenumber component yields

$$\mu_m^{\pm} = \frac{M_1(\frac{\omega_0}{c_0} + M_2\nu_m) \pm \left((\frac{\omega_0}{c_0} + M_2\nu_m)^2 - \beta_1^2\nu_m^2\right)^{1/2}}{\beta_1^2}, \tag{5.4}$$

where the two solutions describe upstream and downstream propagating modes, denoted by $+$ and $-$ respectively. The model will be restricted to the cut-on modes so that

$$(\tfrac{\omega_0}{c_0} + M_2\nu_m)^2 - \beta_1^2\nu_m^2 \geq 0,$$

and $\mu_m^{\pm} \in \mathbb{R}$. This can be used to specify a pair of numbers m_{min} and m_{max} which give the lowest and highest cut-on values of m, defined by

$$m_{\text{min}} = \left\lceil \frac{Bs\omega_0}{2\pi c_0\beta^2}\left(M_2 - \beta_1\right)\right\rceil, \tag{5.5a}$$

$$m_{\text{max}} = \left\lfloor \frac{Bs\omega_0}{2\pi c_0\beta^2}\left(M_2 + \beta_1\right)\right\rfloor, \tag{5.5b}$$

where $\lfloor\rfloor$ denotes a floor function (rounding down to the nearest integer) and $\lceil\rceil$ denotes a ceiling function (rounding up).

The following section considers the mode scattering implications of the periodicity imposed by the unwrapping of the cylindrical duct.

5.1.3 Scattering between modes

Consider an incident mode of order m, as described in Section 5.1.2. The gap-wise wavenumber component is 'sampled' by the blades, so that the phase difference between adjacent blades can be seen to be

$$\sigma_m = s\nu_m = \frac{2\pi m}{B}. \tag{5.6}$$

In Figure 5.3 the mode order m is sketched alongside two higher order modes which share the same phase difference, mod (2π). In this situation there will be an aliasing of these modes and an exchange of sound pressure, or scattering between them. This will occur for any mode order n that satisfies

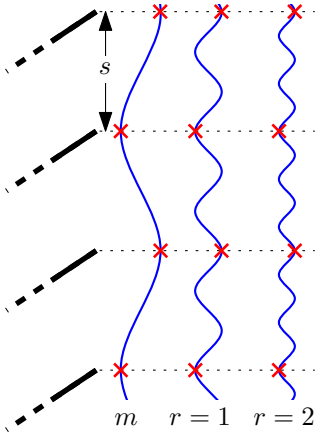

Figure 5.3 – Aliasing of incident mode order m: phase of each modal order $n = m + rB$ is identical when sampled at blades.

$$s\nu_n = \sigma_m + 2\pi r, \tag{5.7}$$

where the scattering index $r \in \mathbb{Z}$. The gap-wise wavenumber component of mode n is given by

$$\nu_n = \frac{\sigma_m + 2\pi r}{s} = \frac{2\pi}{Bs}\left(m + rB\right). \tag{5.8}$$

Comparison of this expression with Equation (5.2) shows that the modal order of n is given by the scattering rule

$$n = m + rB. \tag{5.9}$$

In the following section the inter-mode scattering is combined with the frequency scattering effects that result from translation of the blade row.

5.1.4 Scattering by a translating row of flat plates

Consider the case where the fan rotates clockwise (i.e. in the negative ϕ direction) with angular velocity Ω. The equivalent blade row is seen to move in the negative x_2 direction in the 'unwrapped' duct geometry, with velocity $\Omega R_0 = \Omega Bs/2\pi$. In this unwrapped geometry, we shall require two coordinate systems: $\mathbf{x}$, in which the duct is stationary and the blades move, and $\hat{\mathbf{x}}$, in which the blade row is stationary and the duct moves. These are sketched in Figures 5.2a and 5.2b. The assumption that the blades are unloaded (item 4 in Section 5.1.1) implies that the mean flow is unchanged as it passes through the blade row.

The coordinate systems are related by

$$\hat{x}_1 = x_1; \qquad \hat{x}_2 = x_2 + \Omega\frac{Bs}{2\pi}t. \tag{5.10}$$

Mean-flow velocity components are related by

$$\hat{U}_1 = U_1; \qquad \hat{U}_2 = U_2 + \Omega\frac{Bs}{2\pi}, \tag{5.11}$$

and total velocities are given by the Pythagorean theorem. Note that

$$\hat{U}_1 = \hat{U}\cos\chi \qquad \text{and} \qquad \hat{U}_2 = \hat{U}\sin\chi. \tag{5.12}$$

Note also that $U_1 \neq U\cos\chi$, as the flow in the $\mathbf{x}$ reference frame is not in the χ direction. Figure 5.2c illustrates the relation between the flow velocity magnitudes as seen in the $\mathbf{x}$ and $\hat{\mathbf{x}}$ frames. A closed velocity vector triangle is formed from the two flow velocities and the frame translation velocity ΩR_0.

In the fixed-duct reference frame $\mathbf{x}$, consider an incident mode of order m, as defined by Equations (5.1)–(5.4) in Section 5.1.2. This mode is expressed in the fixed-blade reference frame $\hat{\mathbf{x}}$ by substitution of Equations (5.2) and (5.10) into Equation (5.1) to yield

$$p_m(\hat{\mathbf{x}}, t) = P_m \mathrm{e}^{\mathrm{i}\left((\omega_0 - m\Omega)t + \mu_m^{\pm}\hat{x}_1 + \nu_m\hat{x}_2\right)}. \tag{5.13}$$

In shifting between reference frames, the mode is perceived to have undergone a Doppler shift to the frequency ω_m defined by

$$\omega_m = \omega_0 - m\Omega. \tag{5.14}$$

Note that the dispersion relation in the $\hat{\mathbf{x}}$ frame (see Equation (5.3)) requires an $\hat{x}_1$ wavenumber component $\hat{\mu}_m^{\pm}(\omega_m)$ defined by

$$\hat{\mu}_m^{\pm}(\omega_m) = \frac{\hat{M}_1(\frac{\omega_m}{c_0} + \hat{M}_2\nu_m) \pm \left((\frac{\omega_m}{c_0} + \hat{M}_2\nu_m)^2 - \hat{\beta}_1^2\nu_m^2\right)^{1/2}}{\hat{\beta}_1^2}. \tag{5.15}$$

Since $\hat{M}_1 = M_1$, $\hat{\beta}_1 = \beta_1$, and $\hat{M}_2 = M_2 + \frac{\Omega Bs}{2\pi c_0} = M_2 + \frac{\Omega m}{\nu_m c_0}$, therefore

$$\tfrac{\omega_m}{c_0} + \hat{M}_2\nu_m = \tfrac{\omega_0}{c_0} + M_2\nu_m,$$

and so the axial wavenumber components in the $\hat{\mathbf{x}}$ and $\mathbf{x}$ frames are unchanged

$$\hat{\mu}_m^{\pm}(\omega_m) = \mu_m^{\pm}(\omega_0). \tag{5.16}$$

The incident mode may thus be written in terms of $\hat{\mathbf{x}}$ frame values as

$$p_m(\hat{\mathbf{x}}, t) = P_m \mathrm{e}^{\mathrm{i}\left(\omega_m t + \hat{\mu}_m^{\pm}(\omega_m)\hat{x}_1 + \nu_m \hat{x}_2\right)}. \tag{5.17}$$

When the incident mode $p_m(\hat{\mathbf{x}}, t)$ interacts with a blade row a scattered field is generated which is composed of a superposition of all possible duct modes $n(r) = m + rB$ defined by the scattering rule shown in Equation (5.9). Henceforth the dependency of n on r shall not be explicitly noted for the sake of brevity. We denote the upstream and downstream scattered pressure field by $p^{\pm}(\mathbf{x}, t)$, where $\pm$ indicates the direction of propagation, as described earlier. The scattered field due to all cut-on modes m incident at frequency ω_0 can be written as the modal superposition

$$p^{\pm}(\hat{\mathbf{x}}, t) = \sum_{m=m_{\min}}^{m_{\max}} \sum_{r=r_{\min}}^{r_{\max}} P_m \mathcal{G}_{mn}^{\pm} \mathrm{e}^{\mathrm{i}(\omega_m t + \hat{\mu}_n^{\pm}(\omega_m)\hat{x}_1 + \nu_n \hat{x}_2)}. \tag{5.18}$$

Here $\mathcal{G}_{mn}^{\pm}$ are a set of non-dimensional pressure scattering coefficients which may be evaluated using a scattering model such as the exact cascade model due to Smith [46] and Whitehead [47]. It is shown by Smith and Whitehead that each $\mathcal{G}_{mn}^{\pm}$ is dependent on the incident and scattered mode numbers, m and n respectively, the fan geometry, the $\hat{\mathbf{x}}$ frame flow Mach number $\hat{M}$ and the direction and frequency of the incident field, so that

$$\mathcal{G}_{mn}^{\pm} = \mathcal{G}_{mn}^{\pm}(s/c, \theta, \hat{M}, \omega_m, \mathrm{sgn}(\hat{\mu}_m^{\pm})), \tag{5.19}$$

where $\mathrm{sgn}(\hat{\mu}_m^{\pm})$ gives the direction of the incident field, and the superscript on $\mathcal{G}_{mn}^{\pm}$ gives the direction of the scattered field. For brevity of notation, we shall subsequently write only the $\hat{M}$ and ω_m arguments of the $\mathcal{G}$ functions, the first to represent the coordinate system, the second to note the Doppler-shifted frequency.

In the rotor-fixed $\hat{\mathbf{x}}$ frame the minimum and maximum scattering indices are

$$r_{\min}(\omega_m) = \left\lceil \frac{s\omega_m}{2\pi c_0 \hat{\beta}^2} \left(\hat{M}_2 - \hat{\beta}_1 \right) - \frac{m}{B} \right\rceil, \tag{5.20a}$$

$$r_{\max}(\omega_m) = \left\lfloor \frac{s\omega_m}{2\pi c_0 \hat{\beta}^2} \left(\hat{M}_2 + \hat{\beta}_1 \right) - \frac{m}{B} \right\rfloor. \tag{5.20b}$$

The scattered field (Equation (5.18)) can be converted back into the fixed-duct ($\mathbf{x}$) observer reference frame using Equations (5.10) and (5.2), to give

$$p^{\pm}(\mathbf{x}, t) = \sum_{m=m_{\min}}^{m_{\max}} \sum_{r=r_{\min}(\omega_m)}^{r_{\max}(\omega_m)} P_m \mathcal{G}^{\pm}_{mn}(\hat{M}, \omega_m) \mathrm{e}^{\mathrm{i}((\omega_m + n\Omega)t + \hat{\mu}^{\pm}_n(\omega_m)x_1 + \nu_n x_2)}. \tag{5.21}$$

Here again it is noted that a Doppler shift has occurred so that, using Equation (5.14), the observer fixed-duct frame radiation frequency is defined as

$$\omega_{mn} = \omega_0 - (m - n)\Omega = \omega_0 + rB\Omega. \tag{5.22}$$

Hence the incident frequency is scattered into frequencies separated by integer multiples of the blade passing frequency $B\Omega$.

The frequency scattering effect is illustrated in Figure 5.4. This figure shows the scattering into modes n of all cut-on modes m incident at frequency $\omega_0 = 15\Omega$ for the case; $B = 5$, $\hat{M} = 0.7$, $\chi = 40°$, $\theta = -30°$, $M_{\Omega R} = 0.45$, $R_0 = 0.5\,\mathrm{m}$. Here the modes m incident at the 'source' frequency $\omega_0/\Omega = 15\,\mathrm{EO}$ are marked with blue squares. Note that these occupy the entire width of the dark grey duct frame cut-on triangle at this frequency. These modes appear in the rotor-fixed frame at the frequencies ω_m, which are marked by the large green circles. Note that while the incident modes at higher orders ($m = [6, 7]$) fall outside the dark grey duct frame cut-on triangle at their rotor frame frequencies ω_m, all of them fall within the rotor frame cut on 'triangle' overlaid as the light grey region. The scattering rule (Equation (5.9)) allows these to be scattered (horizontally here) into modes $n = m + rB$, represented by small green circles. Each of these scattered modes radiates into the duct-fixed frame at frequencies ω_{mn} as defined in Equation (5.22), marked by red stars. Note that these stars all fall within the original duct cut-on triangle and the different scattering orders r result in emission at $\omega_{mn} = \omega_0 + rB\Omega$ (offset step of 5 EO in this case).

Considering the axial wavenumber components as in Equation (5.16), these are again found to be equal in their respective frames of reference

$$\hat{\mu}^{\pm}_n(\omega_m) = \mu^{\pm}_n(\omega_{mn}). \tag{5.23}$$

The scattered pressure field observed in the fixed-duct frame can thus finally be written

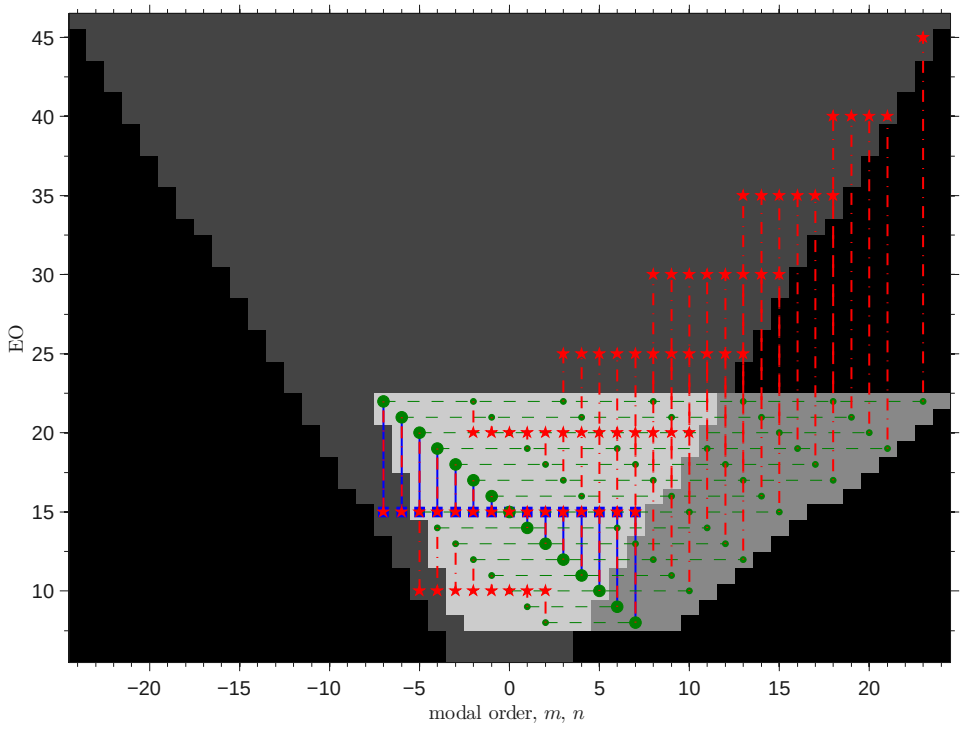

Figure 5.4 – The scattering into modes n of all cut-on modes m incident at frequency $\omega_0 = 15\Omega$ for the case $B = 5$, $\hat{M} = 0.7$, $\chi = 40°$, $\theta = -30°$, $M_{\Omega R} = 0.45$ and $R_0 = 0.5\,\mathrm{m}$. The modes m incident at the 'source' frequency $\omega_0/\Omega = 15\,\mathrm{EO}$, marked with blue squares are scattered into modes $n = m + rB$ which are radiated at frequencies $(\omega_{mn} = \omega_0 + rB\Omega)/\Omega\,\mathrm{EO}$ (offset step of $B = 5\,\mathrm{EO}$ in this case).

in the form

$$p^{\pm}(\mathbf{x},t) = \sum_{m=m_{\min}}^{m_{\max}} \sum_{r=r_{\min}(\omega_m)}^{r_{\max}(\omega_m)} P_m \mathcal{G}^{\pm}_{mn}(\hat{M},\omega_m) \mathrm{e}^{\mathrm{i}(\omega_{mn}t + \mu^{\pm}_n(\omega_{mn})x_1 + \nu_n x_2)}. \tag{5.24}$$

This chapter is primarily concerned with the transmitted acoustic power across the rotor. Substitution of Equation (5.24) into the linearised momentum equation gives the acoustic particle velocity components of the scattered field:

$$u^{\pm}_1(\mathbf{x},t) = -\frac{1}{\rho_0} \sum_{m=m_{\min}}^{m_{\max}} \sum_{r=r_{\min}(\omega_m)}^{r_{\max}(\omega_m)} P_m \mathcal{G}^{\pm}_{mn} \times \frac{\mu^{\pm}_n(\omega_{mn})}{\omega_{mn} + U_1\mu^{\pm}_n(\omega_{mn}) + U_2\nu_n} \mathrm{e}^{\mathrm{i}(\omega_{mn}t + \mu^{\pm}_n(\omega_{mn})x_1 + \nu_n x_2)}, \tag{5.25a}$$

$$u^{\pm}_2(\mathbf{x},t) = -\frac{1}{\rho_0} \sum_{m=m_{\min}}^{m_{\max}} \sum_{r=r_{\min}(\omega_m)}^{r_{\max}(\omega_m)} P_m \mathcal{G}^{\pm}_{mn} \times \frac{\nu_n}{\omega_{mn} + U_1\mu^{\pm}_n(\omega_{mn}) + U_2\nu_n} \mathrm{e}^{\mathrm{i}(\omega_{mn}t + \mu^{\pm}_n(\omega_{mn})x_1 + \nu_n x_2)}. \tag{5.25b}$$

The axial component of the time-averaged acoustic intensity is given by Goldstein [60] as

$$I_1 = \lim_{T\to\infty} \mathrm{Re}\left[\left(\frac{p^{\pm}}{\rho_0} + U_1 u_1 + U_2 u_2\right)\left(\rho_0 u_1^* + \frac{U_1 p^*}{c_0^2}\right)\right]. \tag{5.26}$$

Substitution of Equations (5.25a) and (5.25b) into Equation (5.26) (with a new dummy variables r' and corresponding $n' = m' + r'B$) and treating the broadband incident field as uncorrelated gives

$$\begin{aligned} I_1^{\pm}(\mathbf{x}) = \lim_{T\to\infty} \mathrm{Re}\Bigg[\frac{1}{\rho_0} \sum_{m=m_{\min}}^{m_{\max}} \sum_{m'=m_{\min}}^{m_{\max}} \sum_{r=r_{\min}(\omega_m)}^{r_{\max}(\omega_m)} \sum_{r'=r_{\min}(\omega_m)}^{r_{\max}(\omega_m)} E\left[P_m P_{m'}^*\right] \\ \times \mathcal{G}_{mn}^{\pm} \mathcal{G}_{m'n'}^{\pm *} \mathrm{e}^{\mathrm{i}(\mu_n^{\pm}(\omega_{mn}) - \mu_{n'}^{\pm *}(\omega_{m'n'}))x_1} \mathrm{e}^{\mathrm{i}(\nu_n - \nu_{n'})x_2} \\ \times \omega_{mn} \frac{\left(-\mu_{n'}^{\pm *}(\omega_{m'n'}) + M_1(\frac{\omega_{m'n'}}{c_0} + M_1 \mu_{n'}^{\pm *}(\omega_{m'n'}) + M_2 \nu_{n'})\right)}{(\omega_{mn} + U_1 \mu_n^{\pm}(\omega_{mn}) + U_2 \nu_n)(\omega_{m'n'} + U_1 \mu_{n'}^{\pm *}(\omega_{m'n'}) + U_2 \nu_{n'})}\Bigg], \end{aligned} \tag{5.27}$$

where $E[\cdot]$ denotes the expected value, or ensemble average value. Assuming that P_m is a statistically random variable then

$$\lim_{T\to\infty} \sum_{m=m_{\min}}^{m_{\max}} \sum_{m'=m_{\min}}^{m_{\max}} E\left[P_m P_{m'}^*\right] = \sum_{m=m_{\min}}^{m_{\max}} \sum_{m'=m_{\min}}^{m_{\max}} |P_{m'}|^2 \delta_{m,m'}, \tag{5.28}$$

where $\delta_{m,m'}$ is a Kronecker delta function.

The acoustic power per unit span is calculated by integrating the acoustic intensity around the circumference of the duct strip

$$\mathcal{P}^{\pm} = \int_0^{2\pi} I_1^{\pm}(\mathbf{x}) R_0 \, \mathrm{d}\phi = \int_0^{Bs} I_1^{\pm}(\mathbf{x}) \, \mathrm{d}x_2. \tag{5.29}$$

The only x_2 dependence in the intensity expression shown in Equation (5.27) is in a complex exponential, so it can be evaluated using an orthogonality condition

$$\int_0^{Bs} \mathrm{e}^{\mathrm{i}(\nu_n - \nu_{n'})x_2} \, \mathrm{d}x_2 = \int_0^{Bs} \mathrm{e}^{\mathrm{i}(n-n')2\pi x_2/Bs} \, \mathrm{d}x_2 = Bs \, \delta_{n,n'}, \tag{5.30}$$

Using Equations (5.28) and (5.30), the m' and r' summations in Equation (5.27) can be performed to give

$$\begin{aligned} \mathcal{P}^{\pm} = \frac{Bs}{\rho_0} \sum_{m=m_{\min}}^{m_{\max}} \sum_{r=r_{\min}(\omega_m)}^{r_{\max}(\omega_m)} \frac{\omega_{mn} |P_m|^2 |\mathcal{G}_{mn}^{\pm}(\hat{M}, \omega_m)|^2}{|\omega_{mn} + U_1 \mu_n^{\pm}(\omega_{mn}) + U_2 \nu_n|^2} \\ \times \mathrm{Re}\left[\left(-\mu_n^{\pm *} + M_1(\tfrac{\omega_{mn}}{c_0} + M_1 \mu_n^{\pm *} + M_2 \nu_n)\right) \mathrm{e}^{\mathrm{i}(\mu_n^{\pm} - \mu_n^{\pm *})x_1}\right]. \end{aligned} \tag{5.31}$$

Noting that the term in brackets is non-zero only for purely real values of the axial

wavenumber component $\mu_r^{\pm}$, this expression can be further simplified to

$$\mathcal{P}^{\pm} = \mp\frac{Bs}{\rho_0}\sum_{m=m_{\min}}^{m_{\max}}\sum_{r=r_{\min}(\omega_m)}^{r_{\max}(\omega_m)}|P_m|^2|\mathcal{G}_{mn}^{\pm}(\hat{M},\omega_m)|^2\mathcal{H}^{\pm}(\omega_{mn},M,\theta,n). \tag{5.32}$$

where $\mathcal{H}^{\pm}$ are the upstream and downstream power factors:

$$\mathcal{H}^{\pm}(\omega,M,\theta,m) = \frac{\omega_{mn}\left[(\frac{\omega}{c_0}+M_2\nu_m)^2-\beta_1^2\nu_m^2\right]^{1/2}}{|\omega+U_1\mu_m^{\pm}(\omega)+U_2\nu_m|^2}. \tag{5.33}$$

5.1.5 Effect of rotor diffusion on flow modelling

The base flow described in Section 5.1.2 abides by the modelling assumptions listed in Section 5.1.1 but is not typical of the flows seen in a real turbofan application. Instead, the inlet flow is typically axial whilst steady loading of the rotors leads to a turning of the mean flow, inducing whirl. Additionally, the blades of a rotor are typically cambered, with stagger angle decreasing from leading to trailing edges. Such an arrangement presents a divergent duct to the rotor-relative flow, leading to diffusion and deceleration of the flow through the inter-blade space. Figure 5.5 shows a sketch of a typical rotor blade geometry, indicating the leading and trailing edge stagger angles χ^{LE} and χ^{TE} respectively.

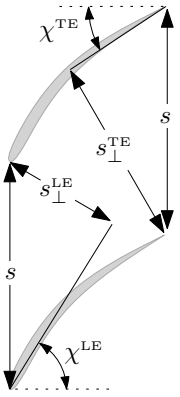

Figure 5.5 – Leading edge and trailing edge dimensions and parameters.

5.1.5.1 Incompressible flow model for diffusion in the blade passage

The cambered rotor blade passage presents a divergent passage to the mean flow and therefore acts as a diffuser in the rotor frame of reference. The $\hat{\mathbf{x}}$ rotor frame Mach number of the mean flow at the leading edge of the rotor $\hat{M}^{\mathrm{LE}}$ is now used in conjunction with the geometry to define all other flow parameters.

An incompressible diffusion model is employed in order to provide an approximation for the trailing edge Mach number $\hat{M}^{\mathrm{TE}}$. A generalised model for diffusion is adopted in which the medium is assumed to have constant density ρ. As the medium flows with velocity V_1 through an area A_1, as shown in the left hand side of Figure 5.6 the mass flow is given by the product $\rho V_1 A_1$. Continuity of mass flow leads to the expression

$$V_2 = V_1\frac{A_1}{A_2}. \tag{5.34}$$

In the case of the rotor, the cross-sectional area of the blade passage at the leading and trailing edges is proportional to the perpendicular separation of the blades at each location $s_{\perp}^{\mathrm{LE}} \approx s\cos\chi^{\mathrm{LE}}$ and $s_{\perp}^{\mathrm{TE}} \approx s\cos\chi^{\mathrm{TE}}$, as illustrated in Figure 5.5. Therefore Equation (5.34)

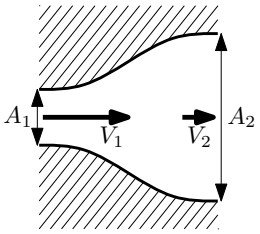

Figure 5.6 – Definitions of the parameters defining the incompressible diffusion model.

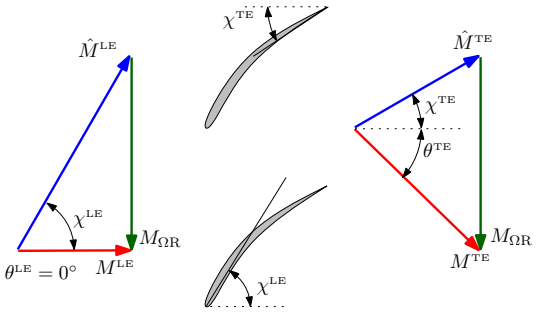

Figure 5.7 – Mach number vector triangles for the mean flow at leading and trailing edges.

is extended to give the following relation in terms of the defining parameters

$$\hat{M}^{\mathrm{TE}} = \hat{M}^{\mathrm{LE}} \frac{\cos(\chi^{\mathrm{TE}} + \Delta\chi)}{\cos \chi^{\mathrm{TE}}}, \tag{5.35}$$

where $\Delta\chi = \chi^{\mathrm{LE}} - \chi^{\mathrm{TE}}$ is the flow turning angle associated with the rotor blade camber.

5.1.5.2 Mach number vector triangles at leading and trailing edges.

In order to calculate the input parameters for the scattering model developed in Section 5.1 the relation between the mean flows as seen in the $\mathbf{x}$ duct frame and the $\hat{\mathbf{x}}$ rotor frame must be known. The left hand side of Figure 5.7 shows a vector triangle for the mean flow Mach number at the rotor leading edge. The inlet flow is assumed to be axial with respect to the static frame of reference, having whirl angle $\theta^{\mathrm{LE}} = 0$. In the $\hat{\mathbf{x}}$ frame of reference the flow is assumed to be perfectly aligned with the rotor leading edge 'metal angle' χ^{LE}. The magnitude of the incident flow Mach number is derived using

$$M^{\mathrm{LE}} = \hat{M}^{\mathrm{LE}} \cos(\chi^{\mathrm{TE}} + \Delta\chi). \tag{5.36}$$

At the rotor trailing edge, shown on the right hand side of Figure 5.7, the flow is also assumed to be aligned with the blade. This is consistent with the assumption of zero steady loading (item 4), however Cumpsty [4] observes that the flow deviation at the rotor trailing edge is typically of order 10°.

The flow in the 'duct' behind the rotor is assumed to adopt a constant defined whirl angle θ^{TE} that is independent of the fan speed. Thus, for a given trailing edge stagger angle χ^{TE} the rotation Mach number $M_{\Omega\mathrm{R}}$ and duct mean flow Mach number M^{TE} will scale linearly with $\hat{M}^{\mathrm{LE}}$, forming a family of similar triangles. In terms of the defining parameters these Mach number relations are

$$M^{\mathrm{TE}} = \hat{M}^{\mathrm{LE}} \frac{\cos(\chi^{\mathrm{TE}} + \Delta\chi)}{\cos \theta^{\mathrm{TE}}}, \tag{5.37}$$

$$M_{\Omega\mathrm{R}} = \hat{M}^{\mathrm{LE}} \cos(\chi^{\mathrm{TE}} + \Delta\chi) \left[\tan \chi^{\mathrm{TE}} - \tan \theta^{\mathrm{TE}}\right]. \tag{5.38}$$

5.1.5.3 Choice of model input parameters

There are two components to the blockage presented by a rotor as illustrated in Figure 5.8:

1. The scattering of incident acoustic field that occurs at the trailing edge.

2. Scattering by regions of transonic and supersonic flow in between the rotor blades.

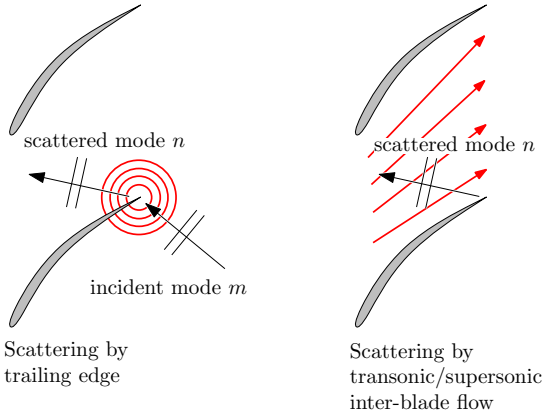

Figure 5.8 – Illustration of blockage of a mode m propagating upstream and incident on rotor trailing edge. The mode is scattered into modes n. These must propagate through inter-blade flow which is faster towards the leading edge for typical cambered rotor blades.

In order to best capture these two effects in simulations the model inputs have been chosen to be $\chi = \chi^{\mathrm{TE}}$ and $\hat{M} = \hat{M}^{\mathrm{LE}}$. The flow parameters $\theta = \theta^{\mathrm{TE}}$ and $M = \hat{M}^{\mathrm{TE}}$ are used to describe flow for the incident modes, while $\theta = \theta^{\mathrm{LE}}$ and $M = \hat{M}^{\mathrm{LE}}$ are used for the radiation of scattered modes.

The attempt to include diffusion by the rotor using the flat plate incompressible flow model described above is at the expense of introducing discontinuities in the flow speed and angle at the rotor leading and trailing edges. Simulations have shown that, in some cases, this discontinuity causes the modal sound power transmission coefficient across the rotor to exceed unity, which is clearly non-physical.

5.2 Simulated rotor transmission results

A series of parameter studies have been conducted using the acoustic scattering model presented in Section 5.1. The scattering coefficients $\mathcal{G}^{\pm}_{mn}$ have been calculated using both the exact cascade model due to Smith [46] and Whitehead [47] and semi-actuator disk model due to Kaji and Okazaki [67], that will be discussed in Section 5.3.2.1.

5.2.1 Characteristics of blockage spectra

Figure 5.9 shows a typical rotor blockage spectrum obtained using the exact cascade scattering model due to Smith [46] and Whitehead [47]. The upstream-propagating sound power radiated upstream of the rotor $\mathcal{P}^{\mathrm{r}+}(\omega)$ is compared with that incident upon it

$\mathcal{P}^{\mathrm{inc}}(\omega)$, such that the rotor transmission loss level in dB is given by

$$L_\tau(\omega) = 10\log_{10}\frac{\mathcal{P}^{\mathrm{r}+}(\omega)}{\mathcal{P}^{\mathrm{inc}}(\omega)}. \tag{5.39}$$

Negative values of L_τ indicate a reduction of sound power transmitted through the rotor. Note that in this and other results shown in this chapter, unit power is assumed to be incident on the rotor at all frequencies, divided equally between the cut-on modes. Thus the values plotted in Figure 5.9 are $L_\tau(\omega) = 10\log_{10}\mathcal{P}^{\mathrm{r}+}(\omega)(\omega)$. The thick red line shows the blockage spectrum, which is the sum of contributions from the scattered modes $n = m + rB$ in accordance with Equation (5.9). The contributions due to each value of the scattering index r are shown individually in Figure 5.9 as thin blue lines. The spectra are plotted against ω/Ω, the normalised frequency referred to as engine order (EO).

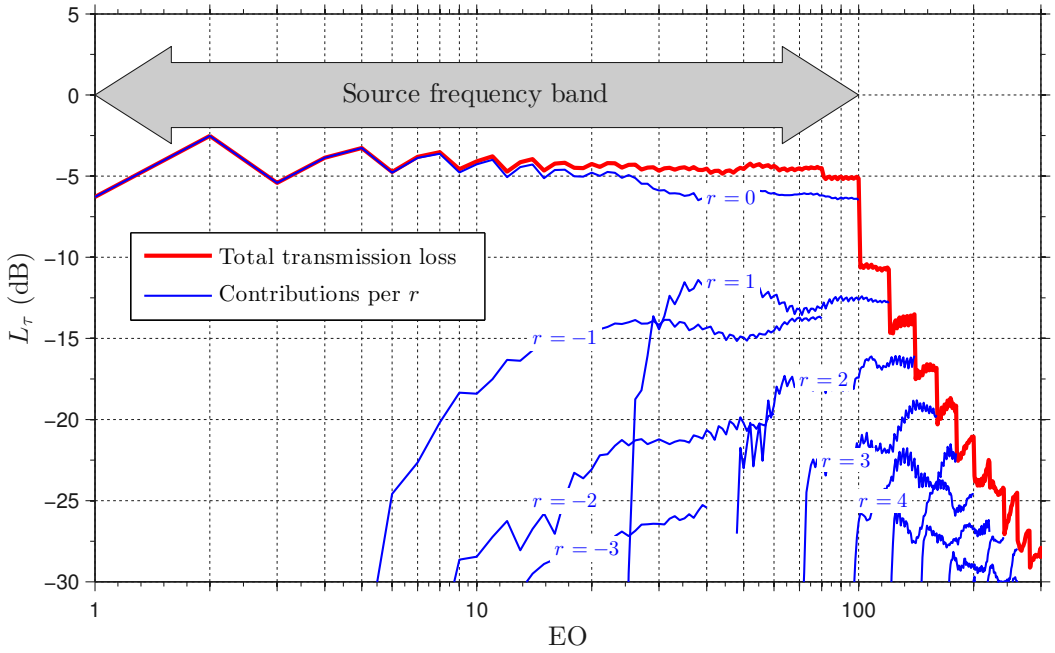

Figure 5.9 – Typical blockage spectrum (red line) plotted with the scattered contributions due to scattering indices r (blue lines) for the 'control' configuration $B = 20$, $s/c = 0.7$, $\chi = 40°$, $\theta = -30°$, $\hat{M} = 0.7$. Frequency scattering causes the offset of the contributions due to $r \neq 0$. The band limiting of the source frequency range (0 EO–100 EO) results in a discontinuity where the $r = -1$ contribution ceases (80 EO).

The 'source' in this case and those seen subsequently is band limited to the range 0 EO–100 EO. The set of source frequencies shall be denoted by $\boldsymbol{\omega}$. It can be seen that the individual scattered modal contributions are offset by the blade passing frequency (20 EO) multiplied by the scattering index r. The overall level of the contributions decreases with increasing $|r|$. The contribution for $|r| = 1$ is significant in the superposition, resulting in a discontinuity at 80 EO where the $r = -1$ contribution ceases.

Ideally the contributions from all possible 'source' frequencies would be evaluated in order to obtain the true scattered spectrum, the evidence shown here suggests that only a few values of r are needed in order to obtain a converged blockage estimate. Further work

is required to identify the range of contributions required for a given rotor configuration, although it is suggested that the product rB is an important factor.

A common feature of the rotor transmission loss level spectrum shown in Figure 5.9 is that, aside from the noted discontinuities, is exhibits only weak frequency dependency. The ripples seen at low frequency are due to the cut-on of the incident modes m. In order to simplify the results of the parameter study shown in Section 5.2.3 they shall be presented as frequency band averaged values.

In the following section the results obtained using the exact scattering model will be compared the with those obtained using the semi-actuator disk model due to Kaji and Okazaki [67].

5.2.2 Equivalence of exact cascade and Kaji-Okazaki scattering coefficient models

Figure 5.10 shows rotor transmission loss spectra obtained using the semi-actuator disk model due to Kaji and Okazaki [67] (blue line) with those using the exact cascade scattering coefficients (red dashed line with circle markers) for the stationary blade case $B = 20$, $\hat{M} = 0.7$, $s/c = 0.7$, $\chi = 40°$. The normalising frequency $\Delta\omega$ used in Figure 5.10 is that at which the first higher order mode cuts on in the inter-blade region, as defined in Equation (3.6).

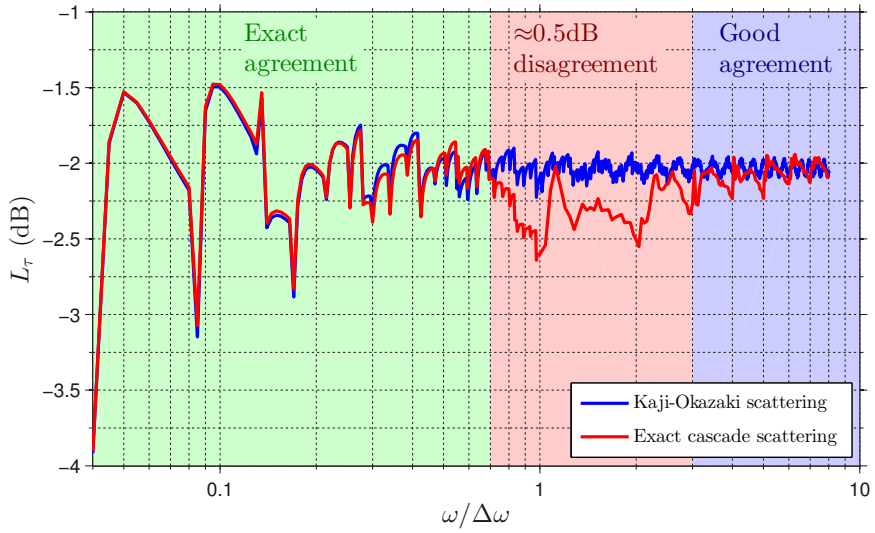

Figure 5.10 – Equivalence of blockage calculated using Kaji-Okazaki and exact cascade scattering coefficients. Blockage spectra calculated for static case $B = 20$, $\hat{M} = 0.7$, $s/c = 0.7$, $\chi = 40°$.

5.2.2.1 Low frequency equivalence of scattering models

The Kaji-Okazaki rotor transmission loss spectrum is more finely resolved than that using the exact cascade model, but the points at which the exact cascade results are calculated (the marker locations) are in exact agreement for $\omega/\Delta\omega \lesssim 0.7$, indicated by the green

region in Figure 5.10. The limitation to plane waves in the inter-blade space assumed in the scattering model of Kaji and Okazaki limits its application to $\omega/\Delta\omega \lesssim 1$.

5.2.2.2 High frequency equivalence of scattering models

Given that the highest frequency of validity for the Kaji-Okazaki scattering model is $\omega/\Delta\omega \lesssim 1$ it is surprising to see that there is agreement in the overall rotor transmission loss seen for $\omega/\Delta\omega \gtrsim 3$. In the high frequency regime $\omega/\Delta\omega \gtrsim 3$ the acoustic field in the inter-blade region is dominated by several well cut-on modes. The chord-wise component of the wavenumbers associated with well cut-on modes is approximately equal to that of the plane-wave mode of order $n = 0$ so that the overall behaviour becomes increasingly dominated by plane wave-like behaviour as frequency increases.

Figure 5.11 illustrates the convergence of the values of the chord-wise wavenumber components k_1 associated with the order $n = 0$ and $n = 1$ modes as frequency increases above $\Delta\omega$, the fundamental cascade mode cut-on frequency. These values of k_1 have been calculated using the negative (upstream) branch of

$$k_{1,n} = \frac{kM \pm \sqrt{k^2 - \beta^2 k_{2,n}^2}}{\beta^2}, \qquad k_{2,n} = \frac{n\pi}{s\cos\theta}, \tag{5.40}$$

where $k = \omega/c_0$ is the free-space acoustic wavenumber and $\beta = (1-M^2)^{1/2}$ is the Prandtl-Glauert number. The expressions in Equation (5.40) are derived in Appendix A. The values of k_1 in Figure 5.11 are normalised with $\Delta\omega/c_0$.

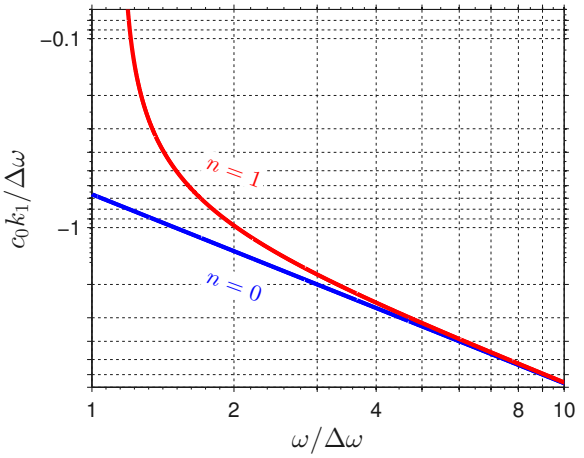

Figure 5.11 – Normalised chord-wise wavenumber component for cascade modes of orders $n = 0$ and $n = 1$ plotted against normalised frequency. The chord-wise component of the acoustic wavenumber of a cascade mode $n = 1$ approaches that of the plane wave mode $n = 0$ as frequency increases above the fundamental cascade mode cut-on frequency $\Delta\omega$.

5.2.3 Frequency-averaged rotor transmission loss coefficients

In Figure 5.10 it is observed that the rotor transmission loss coefficients obtained using both the exact cascade and Kaji-Okazaki scattering models are only weakly frequency

dependent. This suggests that the rotor transmission loss behaviour can be presented in terms of a single frequency-averaged rotor transmission loss coefficient L_τ , defined as

$$L_\tau = \frac{\sum_{\omega\in\boldsymbol{\omega}} \mathcal{P}^{\mathrm{r}+}(\omega)}{\sum_{\omega\in\boldsymbol{\omega}} \mathcal{P}^{\mathrm{inc}}(\omega)}, \tag{5.41}$$

where $\boldsymbol{\omega}$ is the set of source frequencies. Sound power scattered outside the source frequency band is not included.

The changes to frequency-averaged rotor blockage that occur as the rotor geometry and flow parameters are changed are now explored. A 'control' geometry and flow configuration is defined using the values listed in Table 5.1. Each of these parameters is swept through a range of values while the others are held constant at their control values and the radius is held constant at $R_0 = 0.5\,\mathrm{m}$. For the rotating cases a fixed $\mathbf{x}$ frame flow whirl angle $\theta = -30°$ is used.

Table 5.1 – Control configuration for rotor transmission loss coefficient parameter study.

B	s/c	χ	$\hat{M}$
20	0.71	40 °	0.7

The rotor transmission loss has been calculated using four combinations of flow model and modal scattering model:

1. Stationary flat-plate blade row, exact modal scattering model,
2. Stationary flat-plate blade row, Kaji-Okazaki scattering model,
3. Rotating flat-plate blade row, exact modal scattering model,
4. Rotating 'cambered' blade row, exact modal scattering model.

The flat-plate flows (items 1–3) are calculated using flow model described in Section 5.1.2, while in the case of item 4 the flow model of Section 5.1.5 has been applied to derive the scattering model inputs. The two modal pressure scattering models used are the same as are compared in Section 5.2.2. The corresponding band-averaged rotor transmission loss coefficients obtained using Equation (5.41) are shown in Figure 5.12. Observations are listed below.

- Figure 5.12a shows that the rotor transmission loss is independent of the number of blades.
- Figure 5.12b shows that the rotor transmission loss associated with overlapping cascades ($(s/c)\sin\chi < 1$) is independent of the pitch-chord ratio. For $(s/c)\sin\chi > 1$ the exact cascade results all show significant increases in transmission: the cascade

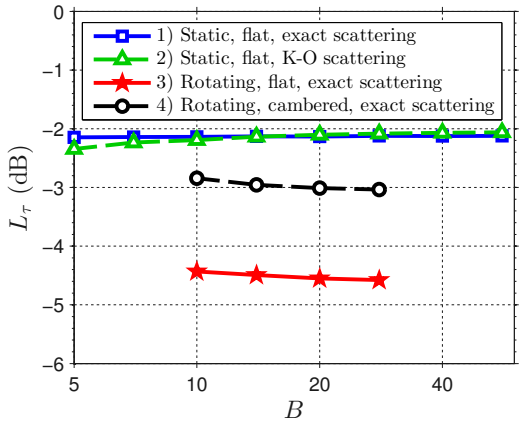

(a) Variation of rotor blade count B.

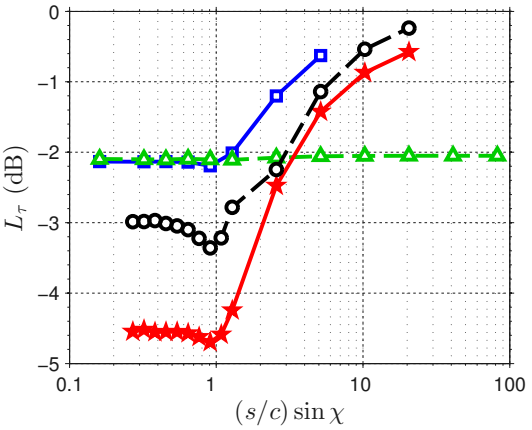

(b) Variation of rotor pitch-chord ratio (s/c), plotted against $(s/c)\sin\chi$. The blades are non-overlapping for $(s/c)\sin\chi > 1$.

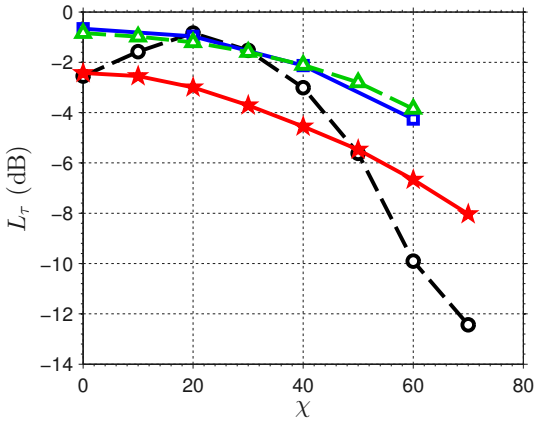

(c) Variation of rotor stagger angle χ.

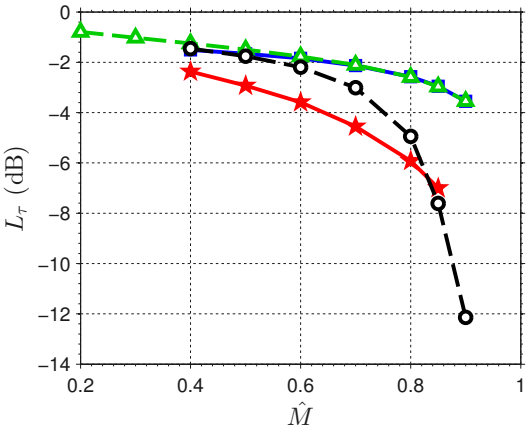

(d) Variation of relative Mach number $\hat{M}$.

Figure 5.12 – Plots of band-averaged rotor transmission loss coefficients showing changes due to single parameter variation. Power scattered upstream in the source frequency band is compared with incident power calculations for four different flow model and scattering model combinations as described in the text.

scattering effects become weak when there is no overlap, as was shown by Jenkins et al. [77]. The result obtained using the Kaji-Okazaki scattering model is insensitive to $(s/c)\sin\chi$ because it effectively assumes an infinite blade density so that it is ignorant of s/c and hence is always 'overlapped'.

- Figure 5.12c shows the changes to the rotor transmission loss as the stagger angle χ is changed. Generally there is an increase in blockage as χ increases, although the diffused flow model result (black dashed line with circle markers) shows an increase from $\chi = 0°$ to $\chi = 40°$.

- Figure 5.12d shows the effect of changing rotor-frame Mach number $\hat{M}$. A monotonic increase in the rotor transmission loss with rotor-relative Mach number $\hat{M}$ is observed for all flow and scattering models.

In the following section, the analytic model of Kaji and Okazaki [67] shall be adapted in order to create a simplified blockage model which will allow an intuitive interpretation of the blockage effect based on power transmission coefficients as a function of incident mode phase angle ψ_p and the distribution of power in the incident field.

5.3 Interpretation of rotor transmission using simplified power transmission model

In this section, explanations will be sought for the rotor transmission loss behaviour observed in the parameter study shown in Section 5.2. The blockage problem will be broken down into two parts; the power distribution of the incident field and the transmission of sound power, both as functions of the phase velocity angle ψ_p. It will be shown that it is the interaction of these two functions that controls the overall blockage behaviour.

5.3.1 Phase velocity angle distribution of incident sound power

The results shown in Section 5.2 have been obtained using an equal power per mode model for the incident sound field. This assumption is not typical of the sound field upstream of an OGV (see Section 3.1.1) but is relatively simple and provides expressions that permit analysis. In this section, an equal power per mode distribution is used to derive an expression for the phase velocity sound power density $\mathcal{D}$ as a function of the phase velocity angle ψ_p. This density function $\mathcal{D}(\psi_\mathrm{p})$ is identical in form to a probability density function (PDF), the theory for which shall be reviewed in Section 5.3.1.1.

5.3.1.1 Probability density functions and cumulative distribution functions

A PDF $p(x)$ defines the likelihood that a random variable adopts a particular value. The probability that the variable has a value within the range $a \leq x \leq b$ is given by the integral

of the probability density function over that range

$$P(a \leq x \leq b) = \int_a^b p(x)\ \mathrm{d}x. \tag{5.42}$$

Being a probability, the solution for an infinite range of values is unity

$$\int_{-\infty}^{\infty} p(x)\ \mathrm{d}x = 1. \tag{5.43}$$

For a given PDF of a random variable X, there exists a cumulative distribution function (CDF) defined as $F(x_0) = P(X < x_0)$. Thus using Equation (5.42), $F(x_0)$ is related to $p(x)$ by

$$F(x_0) = \int_{-\infty}^{x_0} p(x)\ \mathrm{d}x. \tag{5.44}$$

The CDF is non-decreasing and has the properties

$$\lim_{x_0 \to -\infty} F(x_0) = 0, \quad \lim_{x_0 \to \infty} F(x_0) = 1. \tag{5.45}$$

Furthermore, any non-decreasing function with the limiting characteristics defined in Equations (5.45) can be used as a CDF with a corresponding PDF $p(x)$ that is obtained by taking the partial derivative of F with respect to x. This will be used in Section 5.3.1.4 in order to define the phase velocity sound power density $\mathcal{D}(\psi_\mathrm{p})$.

5.3.1.2 Normalised circumferential wavenumber component as a cumulative distribution function

It is observed that the equal power per mode assumption means that the sound power over a given range of phase velocity angle ψ_p is proportional to the number of modes present over that range. Equation (5.2) defines a linear relationship between the gap-wise component of the wavenumber ν and the modal order m which will be used in this section to relate the sound power over a range of phase velocity angle ψ_p to ν.

At a given frequency, the range of cut-on modes m is limited to lie between the limits m_min and m_max by the expressions in Equations (2.58). Thus it is possible to define the normalised value of ν

$$\mathcal{C}(m) = \begin{cases} 0 & : m < m_\mathrm{min}, \\ \dfrac{\nu(m) - \nu(m_\mathrm{min})}{\nu(m_\mathrm{max}) - \nu(m_\mathrm{max})} & : m_\mathrm{min} \leq m \leq m_\mathrm{max}, \\ 1 & : m > m_\mathrm{max}. \end{cases} \tag{5.46}$$

$\mathcal{C}(m)$ as defined in Equation (5.46) is non-decreasing and behaves according to the limits defined in Equations (5.45) and is therefore of the form of a CDF. Because the value of ν is proportional to the modal order and the sound power is proportional to the number of modes $\mathcal{C}(m)$ represents a CDF for the sound power.

5.3.1.3 CDF for sound power as a function of phase velocity angle ψ_p

Equation (5.46) gives a definition of the CDF for sound power as a function of modal order m. In this section Equation (5.46) will be used to define the CDF for sound power in terms of phase velocity angle ψ_p.

The phase velocity angle of a wave propagating in the duct is given by Equation (3.4), which can be rearranged to give

$$\nu = \mu \tan \psi_\mathrm{p}, \tag{5.47}$$

where the axial and circumferential wavenumbers μ and ν satisfy the acoustic dispersion relation shown in Equation (5.3). Substituting Equation (5.47) into Equation (5.3) and solving for the upstream-going axial wavenumber component μ^+ gives

$$\mu^+(k, M, \theta, \psi_\mathrm{p}) = \frac{-k}{M_1 + M_2 \tan \psi_\mathrm{p} - \sqrt{1 + \tan^2 \psi_\mathrm{p}}}. \tag{5.48}$$

Substitution of Equation (5.48) into Equation (5.47) now gives

$$\nu(k, M, \theta, \psi_\mathrm{p}) = \frac{-k \tan \psi_\mathrm{p}}{M_1 + M_2 \tan \psi_\mathrm{p} - \sqrt{1 + \tan^2 \psi_\mathrm{p}}}. \tag{5.49}$$

It is now assumed that at an arbitrarily high frequency the circumferential wavenumber ν is continuous rather than the discrete modal model so far employed. Cut-on waves will have circumferential wavenumber component that falls in the range $\nu_\mathrm{min} \leq \nu \leq \nu_\mathrm{max}$ defined by substitution of Equations (2.58) into Equation (5.2)

$$\nu_\mathrm{min}(k, M, \theta) = k \frac{M_2 - \beta_1}{\beta^2}, \tag{5.50a}$$

$$\nu_\mathrm{max}(k, M, \theta) = k \frac{M_2 + \beta_1}{\beta^2}. \tag{5.50b}$$

This range of ν corresponds to the range of phase angles bounded by

$$\psi_\mathrm{p,min} = -\arccos M_1, \tag{5.51a}$$

$$\psi_\mathrm{p,max} = \arccos M_1. \tag{5.51b}$$

The relation between M_1 and the range of ψ_p is sketched in Figure 5.13.

Equation (5.49) and the values for ν_min and ν_max given by Equations (5.50) are now substituted into Equation (5.46), hence defining the frequency-independent cumulative ray density valid for $\nu_\mathrm{min} \leq \nu \leq \nu_\mathrm{max}$

$$\mathcal{C}(M, \theta, \psi_\mathrm{p}) = -\frac{1}{2\beta_1} \left(\frac{\beta^2 \tan \psi_\mathrm{p}}{M_1 + M_2 \tan \psi_\mathrm{p} - \sqrt{1 + \tan^2 \psi_\mathrm{p}}} + (M_2 - \beta_1) \right). \tag{5.52}$$

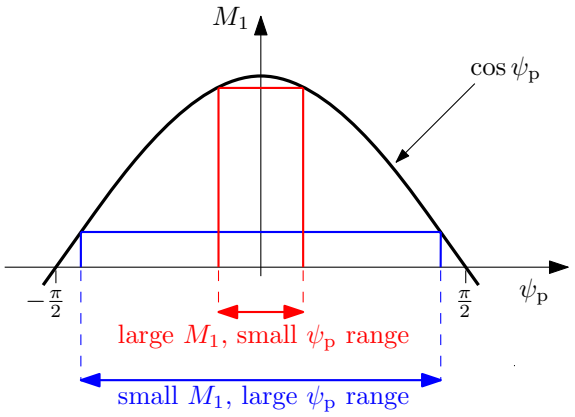

Figure 5.13 – Illustration of the range of phase velocity angles ψ_p valid for a given axial Mach number component M_1.

5.3.1.4 Ray angle density function

Using the relation between a cumulative distribution function and the corresponding density function defined in Section 5.3.1.1, the ray angle density is now obtained by differentiating Equation (5.52) with respect to the phase velocity angle ψ_p

$$\mathcal{D}(M,\theta,\psi_\mathrm{p}) = \frac{\partial \mathcal{C}}{\partial \psi_\mathrm{p}} = \frac{-\beta^2}{2\beta_1}\frac{M_1 - \cos\psi_\mathrm{p}}{\left(M_1\cos\psi_\mathrm{p} + M_2\sin\psi_\mathrm{p} - 1\right)^2}. \tag{5.53}$$

In the case where each mode (corresponding to a duct spinning mode) has equal sound power, Equation (5.53) represents the sound power angular distribution function.

An example power density function is shown in Figure 5.14 where it is compared with an equivalent distribution obtained numerically, both for the case $M = 0.7$, $\theta = 40°$. Here it can be seen that the two methods produce practically identical results, however the numerical version requires the calculation and sorting into phase angle 'bins' of all cut-on wavenumbers at a frequency high enough that the distribution has converged. The analytic result is quicker and more flexible to implement.

Figure 5.15 shows the variations of the power density function $\mathcal{D}$ due to changes to the flow parameters M and θ. In the left hand plot (Figure 5.15a) M is changed whilst the whirl angle is maintained at $\theta = 40°$. The distribution becomes increasingly offset as M increases. Defining the angle at which the peak in $\mathcal{D}$ occurs $\psi_\mathrm{p}^{\mathcal{D}}$, it can be shown that $\psi_\mathrm{p}^{\mathcal{D}} \to 0$ as $M \to 0$ and that $\psi_\mathrm{p}^{\mathcal{D}} \to \theta$ as $M \to 1$, so that in all cases $\psi_\mathrm{p}^{\mathcal{D}}$ falls between θ and 0. Also worthy of note is the fact that as M increases the width of the base of the distribution narrows in accordance with Equation (5.51).

The right hand plot (Figure 5.15b) shows the effect of changing flow whirl angle θ. It can be seen that the power distribution broadens and becomes increasingly offset as θ increases. Note also that larger values of θ increase the cut-on range as $M_1 = M\cos\theta$ decreases.

Having identified the power distribution due to a given flow the following section con-

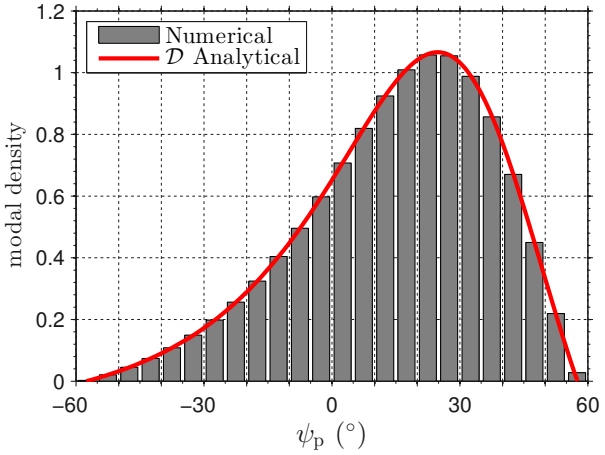

Figure 5.14 – Power density function $\mathcal{D}$ compared with numerically obtained ray density for the case $M = 0.7$, $\theta = 40°$.

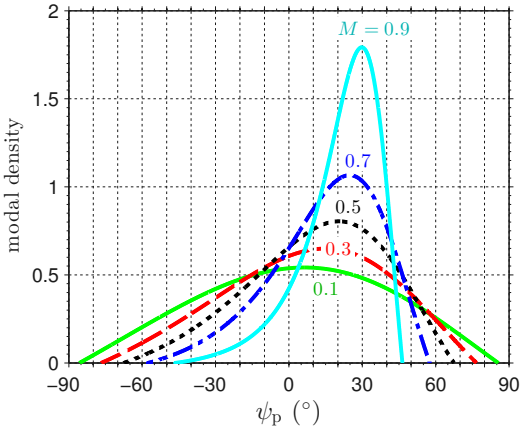

(a) Family of curves associated with changing flow Mach number M. In all cases the flow whirl angle is $\theta = 40°$.

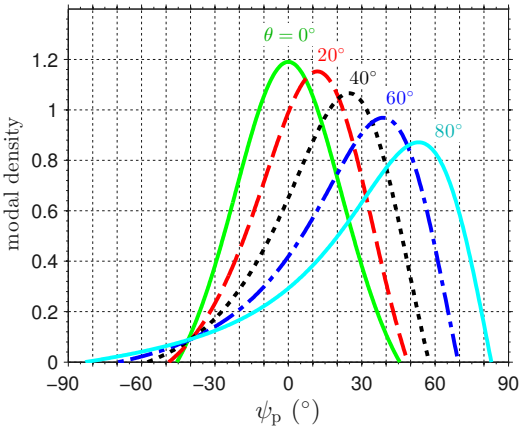

(b) Family of curves associated with changing whirl angle θ. In all cases the flow Mach number is $M = 0.7$.

Figure 5.15 – Curves showing the ray angle density $\mathcal{D}$ for a range of Mach numbers $M = [0.1, 0.3, 0.5, 0.7, 0.9]$ and whirl angles $\theta = [-80°, -60°, -40°, -20°, 0°]$.

siders the transmission of the incident power through the blade row.

5.3.2 Power transmission coefficients

In Section 5.2 it was observed that there was good agreement in the band-averaged rotor transmission loss coefficients obtained using the exact cascade scattering model due to Smith [46] and the semi-actuator disk model of Kaji and Okazaki [67]. In this section, the simpler Kaji-Okazaki scattering model will be adapted in order to interpret the Section 5.2 results. This analysis commences by showing the formulation for calculation of the scattering coefficients.

5.3.2.1 Scattering model due to Kaji and Okazaki

The semi-actuator disk model due to Kaji and Okazaki [67] assumes that the blade row is replaced by a medium which supports only plane waves, propagating upstream and downstream aligned with the stagger angle χ as a one dimensional sound field. This assumption ensures that the ν wavenumber component of a transmitted mode must match that of the incident mode so that $\mathcal{G}^{+}_{mn} = \mathcal{G}^{+}_{mm}\delta_{mn}$.

Kaji and Okazaki describe a method for matching the mass flow and enthalpy at the cascade leading and trailing edges whilst imposing the Kutta condition at the trailing edge [67]. In so doing, it can be shown that the relation between the scattering coefficients $\mathcal{G}^{\pm}_{mm}$ and an acoustic mode incident from the downstream side of a blade row with amplitude I is given by the system:

$$\frac{c_0}{2\omega_m \Lambda^{+}_{m}}\left(1+\frac{\nu_m}{\mu_V}\tan\theta\right)\left(\left(\Psi_m + k_m\cos\theta\right)\mu^{+}_{D}\mathrm{e}^{\mathrm{i}\mu^{+}_{D}c} - \left(\Psi_m - k_m\cos\theta\right)\mu^{-}_{D}\mathrm{e}^{\mathrm{i}\mu^{-}_{D}c}\right)\mathcal{G}^{+}_{mm} - \frac{1}{\Lambda^{-}_{m}}\left(\mu^{-}_{m}+\frac{\nu^2_m}{\mu_V}\right)\mathrm{e}^{\mathrm{i}\mu^{-}_{m}L}\mathcal{G}^{-}_{mm} = \frac{1}{\Lambda^{+}_{m}}\left(\mu^{+}_{m}+\frac{\nu^2_m}{\mu_V}\right)\mathrm{e}^{\mathrm{i}\mu^{+}_{m}L}I, \quad (5.54a)$$

$$\frac{c^2_0}{2\omega_m \Lambda^{+}_{m}\cos\theta}\left(\left(\Psi_m + k_m\cos\theta\right)\mu^{+}_{D}\mathrm{e}^{\mathrm{i}\mu^{+}_{D}c} + \left(\Psi_m - k_m\cos\theta\right)\mu^{-}_{D}\mathrm{e}^{\mathrm{i}\mu^{-}_{D}c}\right)\mathcal{G}^{+}_{mm} - \mathrm{e}^{\mathrm{i}\mu^{-}_{m}L}\mathcal{G}^{-}_{mm} = \mathrm{e}^{\mathrm{i}\mu^{+}_{m}L}I, \quad (5.54b)$$

where $k_m = \omega_m/c_0$ is the free-space acoustic wavenumber, μ_V is the axial wavenumber component of shed vorticity defined by

$$\mu_V = -\frac{\omega_m + \hat{U}_2\nu_m}{\hat{U}_1}, \quad (5.55)$$

while the wavenumbers of the one-dimensional inter-blade sound field are given by

$$\mu^{\pm}_{D} = \frac{k_m(\hat{M}\pm 1)}{1-\hat{M}^2}, \quad (5.56)$$

and the functions

$$\Lambda_m^{\pm} = \omega_m + \hat{U}_1\mu_m^{\pm} + \hat{U}_2\nu_m, \tag{5.57}$$

$$\Psi_m = \left[(k_m + \hat{M}_2\nu_m)^2 - \beta_1^2\nu_m^2\right]^{1/2}, \tag{5.58}$$

which have units of frequency and wavenumber respectively. The system (5.54) may be solved for $\mathcal{G}_{mm}^{+}$ to give the modal pressure transmission coefficients.

5.3.3 Phase angle dependency of power transmission coefficients

Kaji and Okazaki present plots of pressure transmission versus the phase angle of incident waves [67]. In the same spirit we shall now present the transmission of sound power. Using the solution to the system shown in Equation (5.54) and assuming a continuum of wavenumbers the power transmission may be calculated for arbitrary values of ψ_{p}.

Recalling the final expression for sound power shown in Equation (5.32), it is noted that $\mathcal{P}^{\pm}$ is expressed in terms of the pressure amplitude of incident modes m. Now assuming an incident field in which each incident mode m carries equal sound power, Equation (5.33) is employed to calculate the pressure magnitudes. The resulting ratio of power factors $\mathcal{H}^{+}$ will be unity when $n = m$, and hence $\omega_{mn} = \omega_0$, as must be the case when using Kaji-Okazaki scattering. Hence in this case the power transmission coefficient is given by

$$\mathcal{T}_{mm}^{+} = |\mathcal{G}_{mm}^{+}|^2. \tag{5.59}$$

Consider the frequency dependency of $\mathcal{T}_{mm}^{+}$ at low and high values of $\hat{M}$. Figure 5.16 shows $\mathcal{T}_{mm}^{+}$ plotted against ψ_{p} for a range of values of the reduced frequency kc. At $\hat{M} = 0.7$ (Figure 5.16b) very little difference can be seen between the plotted cases, this is in agreement with the results given by Kaji and Okazaki [67]. A single peak in $\mathcal{T}_{mm}^{+}$ is seen at $\psi_{\mathrm{p}}^{\mathcal{T}} = \chi = 40°$. This is a nil-shielding angle: incident modes with phase angle $\psi_{\mathrm{p}}^{\mathcal{T}}$ do not interact with the blade row and hence are not scattered.

At $\hat{M} = 0.1$ (Figure 5.16b) it is observed that $\psi_{\mathrm{p}}^{\mathcal{T}} = \chi = 40°$. However, there is now considerable variation in the shape of $\mathcal{T}_{mm}^{+}$ as kc changes. Kaji and Okazaki explain these variations by observing that kc is the phase change of a transmitted wave across the blade row. We shall perform an averaging of $\mathcal{T}_{mm}^{+}$ over the period $\pi/100 \leq kc \leq \pi$ for all further cases in order to deal with this frequency variation.

5.3.3.1 Effect of rotor-relative Mach number on $\mathcal{T}_{mm}^{+}$

Figure 5.17a shows the variation of $\mathcal{T}_{mm}^{+}$ with rotor-relative flow Mach number $\hat{M}$. In all cases the stagger angle is $\chi = 40°$. The nil-shielding effect is seen to be independent of $\hat{M}$ in that for all cases $\psi_{\mathrm{p}}^{\mathcal{T}} = \chi$ and $\mathcal{T}_{mm}^{+}(\chi) = 1$. The width of the transmission band narrows as $\hat{M}$ increases.

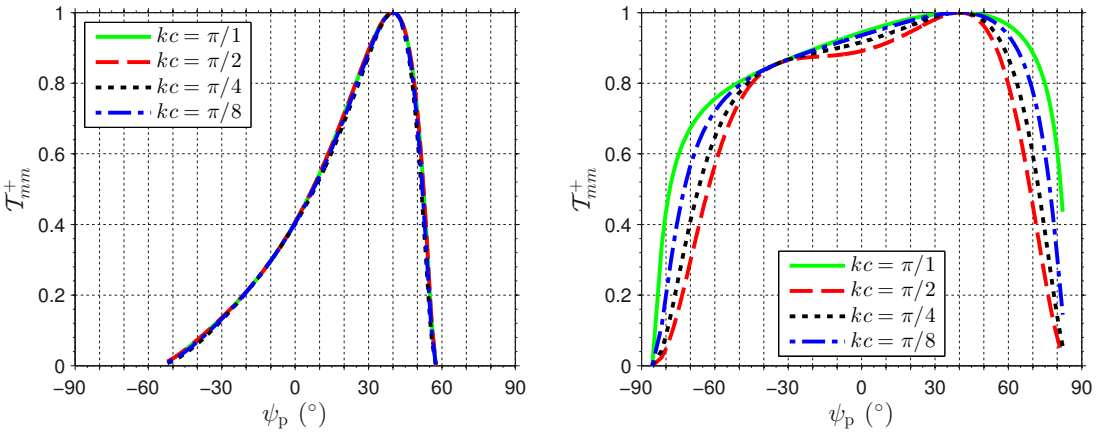

(a) $\hat{M} = 0.7$ **(b)** $\hat{M} = 0.1$

Figure 5.16 – Power transmission coefficients plotted against phase angle showing frequency dependency for low and high $\hat{M}$. In both cases $\chi = 40°$, $s/c = 0.71$.

5.3.3.2 Effect of rotor stagger angle on $\mathcal{T}^+_{mm}$

Figure 5.17b shows the variation of $\mathcal{T}^+_{mm}$ due to changing stagger angle χ. Only positive values are shown here as the symmetry of the problem would otherwise lead to duplication. For all cases $\psi^{\mathcal{T}}_\mathrm{p} = \chi$ and $\mathcal{T}^+_{mm}(\chi) = 1$. Finite transmission is seen over a wider range of ψ for larger values of χ but the width over which appreciable transmission occurs narrows at larger values of χ.

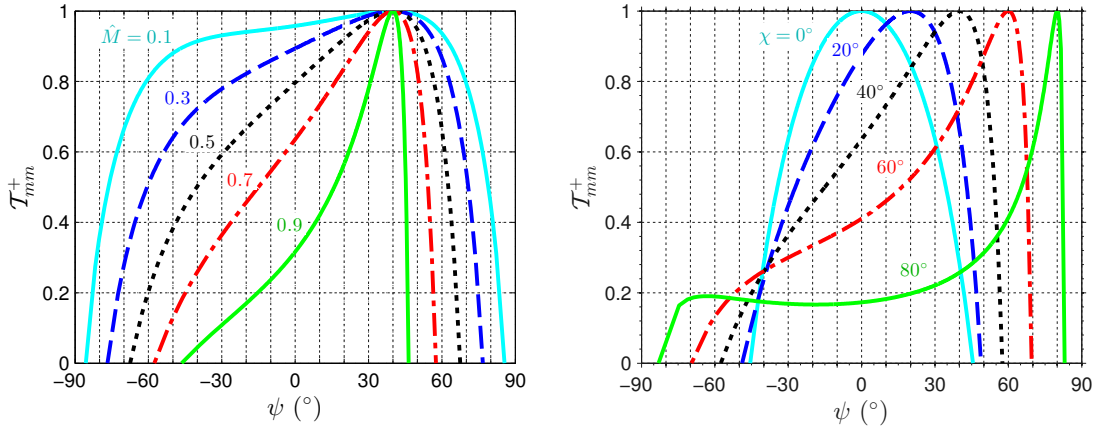

(a) Variation of $\hat{M}$ for case $\chi = 40°$, $s/c = 0.71$. **(b)** Variation of χ, for case $\hat{M} = 0.7$, $s/c = 0.71$.

Figure 5.17 – Power transmission coefficients, frequency averaged over interval $\pi/100 \leq kc \leq \pi$, plotted against phase angle showing dependency on $\hat{M}$ and χ.

In the following section the power transmission function will be combined with the incident power density function to show the effects of stagger angle and flow Mach number on the power transmitted through a stationary blade row.

5.3.4 Blockage results using simplified sound power transmission model

This section provides a validation of the simplified sound power transmission model developed in Sections 5.3.1 and 5.3.2 by comparing its rotor transmission loss predictions with the exact cascade scattering results presented in Section 5.2.

Noting that, by the definitions given in Equations (5.52) and (5.53), $\int_{-\pi/2}^{\pi/2} \mathcal{D}(\psi_\mathrm{p})\,\mathrm{d}\psi_\mathrm{p} = 1$, the sound power transmission loss coefficient may be estimated using the simplified sound power transmission model by evaluating

$$L_\tau = 10\log_{10}\int_{-\pi/2}^{\pi/2} \mathcal{T}^+_{mm}(\psi_\mathrm{p})\mathcal{D}(\psi_\mathrm{p})\,\mathrm{d}\psi_\mathrm{p}, \tag{5.60}$$

where $\mathcal{D}$ and $\mathcal{T}^+_{mm}$ are obtained using Equations (5.53) and (5.59) respectively.

Figure 5.18 shows a comparison of the rotor transmission loss coefficients obtained using Equation (5.60) and (5.41) evaluated for exact cascade scattering over a range of M and χ values. Agreement to within 0.5 dB is observed in all cases.

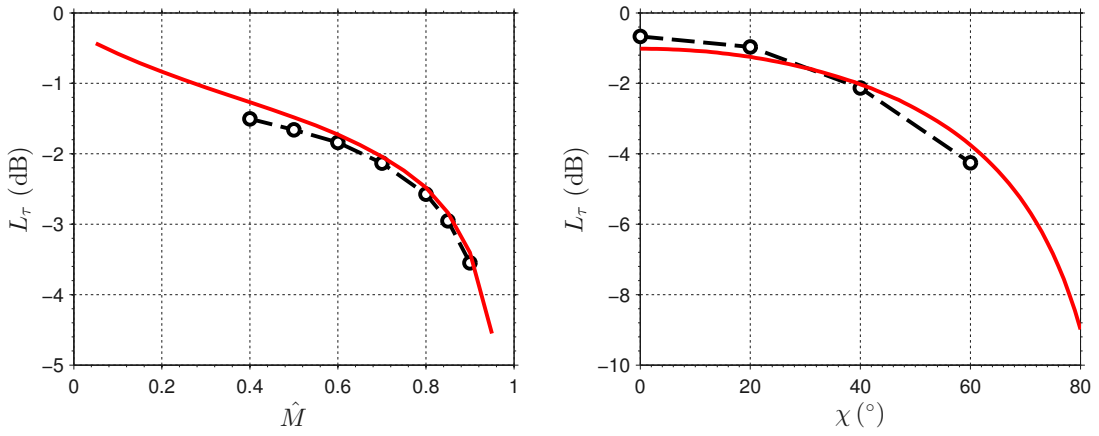

(a) Changing flow Mach number $\hat{M}$. In all cases the flow whirl angle is $\theta = \chi = 40°$.

(b) Changing flow whirl angle $\theta = \chi$. In all cases the flow Mach number is $\hat{M} = 0.7$.

Figure 5.18 – Comparison of mean blockage for simplified model (—) and exact cascade scattering (− ∘ −) for static blade row with $B = 20$ and $s/c = 0.71$.

The relation between the ψ_p dependency of $\mathcal{D}$ and $\mathcal{T}^+_{mm}$ is now explored in order to explain the observed behaviour. An array of results are shown in Figure 5.19. Each sub-figure plots against ψ_p the power density function $\mathcal{D}$ (red dash-dotted), the power transmission coefficient $\mathcal{T}^+_{mm}$ (blue dashed) and the product $\mathcal{T}^+_{mm}\mathcal{D}$ (red solid) for a particular combination of $\hat{M}$ and χ. The blade row is stationary and so the flow whirl angle $\theta = \chi$ and flow Mach numbers are equal $M = \hat{M}$. Note that as the power density values $\mathcal{D}$ and $\mathcal{T}^+_{mm}\mathcal{D}$ are plotted relative to the left hand (red) axis, whilst the dimensionless transmission coefficients $\mathcal{T}^+_{mm}$ are plotted relative to the right hand (blue) axis. The area under the incident power density function $\mathcal{D}$ represents the total incident power, whilst the area under $\mathcal{T}^+_{mm}\mathcal{D}$ (shown in cyan) represents the total transmitted power, thus the difference between these two areas (shaded in dark grey) represents the incident power

that is either reflected or shed as vorticity.

The four subplots Figures 5.19b, 5.19e, 5.19h and 5.19k show the results for $\chi = 40°$ and as such represent 'snapshots' of the detailed behaviour at different points of Figure 5.18a. At $\hat{M} = 0.1$ (Figure 5.19b) the distribution of $\mathcal{T}^{+}_{mm}$ is nearly symmetrical and $\mathcal{T}^{+}_{mm} > 0.8$ for $\approx 75\%$ of the cut-on range of ψ_{p}. Moreover, the tails of $\mathcal{D}$ extending outside this 'window' of transmission are relatively small. This combination results in the grey area representing non-transmitted power being small relative to the (cyan) transmitted power region, the predicted transmission loss is -0.6 dB. Moving down through the higher values of $\hat{M}$, both $\mathcal{T}^{+}_{mm}$ and $\mathcal{D}$ distributions become increasingly skewed and narrow. The value of peak of $\psi^{\mathcal{D}}_{\mathrm{p}}$ approaches χ as observed in Section 5.3.1 but the selectivity of the two distributions results in increasing transmission loss (larger grey area) as $\hat{M}$ increases.

Now considering the results associated with changing χ, the detailed behaviour underlying the curve shown in Figure 5.18b at the points $\chi = [0°, 40°, 80°]$ is shown in Figures 5.19g, 5.19h and 5.19i. At $\chi = 0°$ (Figure 5.19g) both $\mathcal{T}^{+}_{mm}$ and $\mathcal{D}$ distributions are symmetric and $\mathcal{T}^{+}_{mm} > 0.8$ for $\approx 50\%$ of the cut-on range of ψ_{p}. While this is considerably narrower than the $\mathcal{T}^{+}_{mm}$ distributions shown in Figure 5.19b the comparative narrowness of the power distribution $\mathcal{D}$ results in an overall blockage of -1 dB. Moving to larger values of χ, (Figures 5.19h and 5.19i) the distribution of $\mathcal{T}^{+}_{mm}$ becomes narrower while the power distribution becomes broader, and hence more thinly spread, leading to greater loss.

For $\chi = 0°$, the proportion of power lost to reflection and vorticity appears to be largely independent of $\hat{M}$, as $\psi_{\mathrm{T}} = \psi_{\mathrm{D}}$ (see Figures 5.19a, 5.19d, 5.19g and 5.19j).

5.3.5 Effects of rotation on rotor transmission loss

It has been shown that the alignment of the peaks in the incident power distribution $\mathcal{D}$ and the sound power transmission coefficient $\mathcal{T}^{+}_{mm}$ is the dominant factor in determining the overall rotor transmission loss. The effects of changes to the rotor geometry and flow conditions on the locations of the peaks of these distributions are considered in this section.

In Section 5.1.2 a model for the base flow corresponding to a translating flat plate blade row was defined. Using this definition, the duct whirl angle is related to the rotor stagger angle χ, flow Mach number in the $\hat{\mathbf{x}}$ frame $\hat{M}$ and the rotor spin Mach number $M_{\Omega\mathrm{R}} = \Omega R_0/c_0$ by

$$\theta = \arctan\left(\tan\chi - \frac{M_{\Omega\mathrm{R}}}{\hat{M}\cos\chi}\right), \tag{5.61}$$

so that $\theta \to \chi$ as $M_{\Omega\mathrm{R}} \to 0$. Figure 5.20 shows the dependency of the 'difference' angle $\xi = \chi - \theta$ on the rotor stagger angle χ and the Mach number ratio $M_{\Omega\mathrm{R}}/\hat{M}$.

These curves may be readily interpreted by considering the vector triangles that define them, as originally illustrated in Figure 5.2c. Figure 5.21 illustrates the changes to the vector triangles for large and small values of χ with $M_{\Omega\mathrm{R}}/\hat{M}$ at extremal values. Here it may be seen that a small stagger angle results in a slow change of the difference angle,

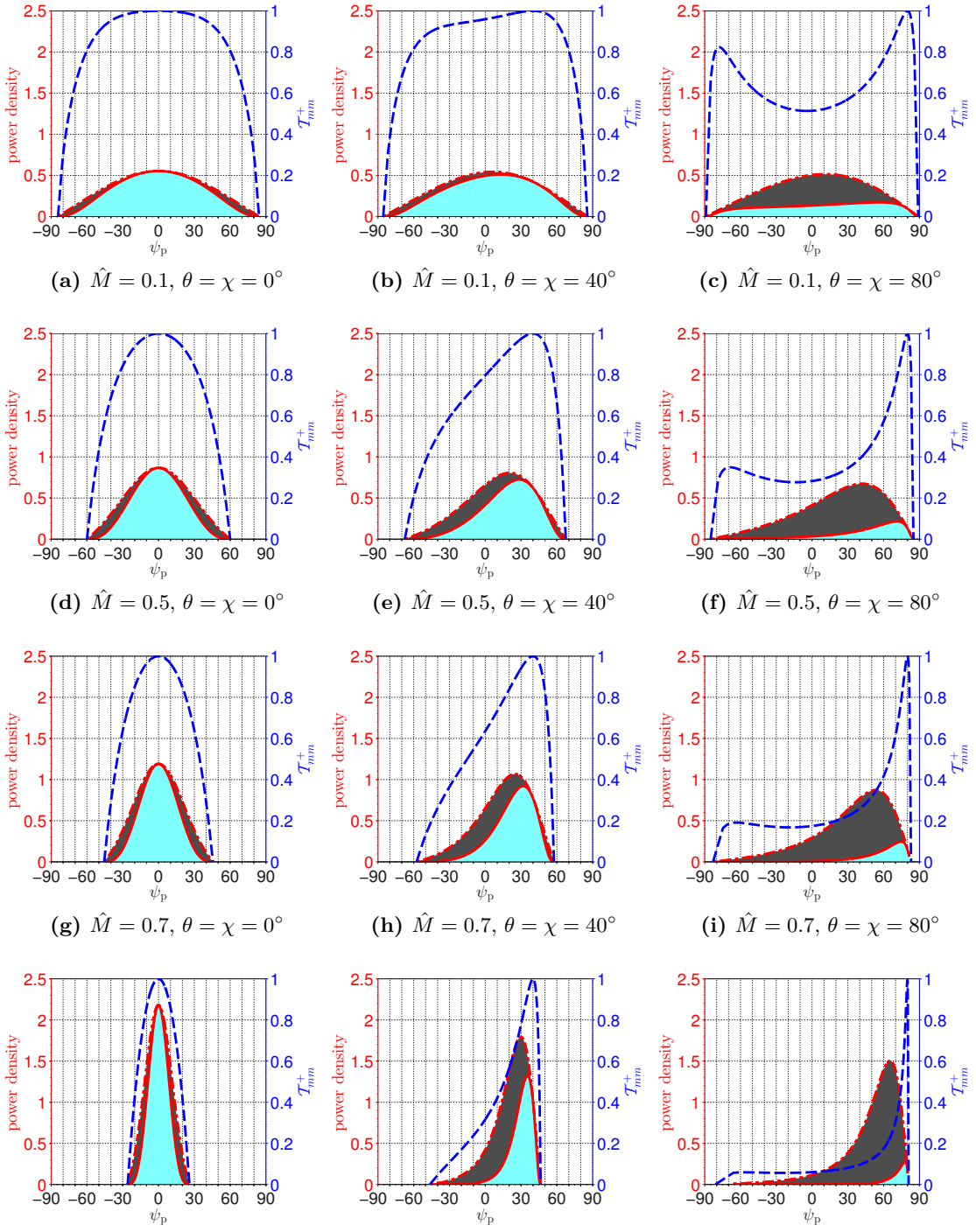

(a) $\hat{M} = 0.1$, $\theta = \chi = 0°$ **(b)** $\hat{M} = 0.1$, $\theta = \chi = 40°$ **(c)** $\hat{M} = 0.1$, $\theta = \chi = 80°$

(d) $\hat{M} = 0.5$, $\theta = \chi = 0°$ **(e)** $\hat{M} = 0.5$, $\theta = \chi = 40°$ **(f)** $\hat{M} = 0.5$, $\theta = \chi = 80°$

(g) $\hat{M} = 0.7$, $\theta = \chi = 0°$ **(h)** $\hat{M} = 0.7$, $\theta = \chi = 40°$ **(i)** $\hat{M} = 0.7$, $\theta = \chi = 80°$

(j) $\hat{M} = 0.9$, $\theta = \chi = 0°$ **(k)** $\hat{M} = 0.9$, $\theta = \chi = 40°$ **(l)** $\hat{M} = 0.9$, $\theta = \chi = 80°$

Figure 5.19 – Comparison of power density function $\mathcal{D}$ (– · –), the power transmission coefficient $\mathcal{T}^+_{mm}$ (– – –) and $\mathcal{T}^+_{mm}\mathcal{D}$ (—) for combinations of $\hat{M}$ and χ calculated for a stationary blade row.

while at a large values of χ the difference angle changes rapidly as the Mach number ratio passes through unity.

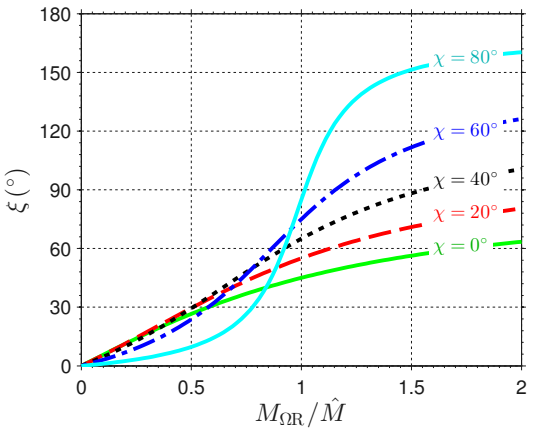

Figure 5.20 – Dependence of difference angle ξ on stagger angle χ and Mach number ratio $M_{\Omega R}/\hat{M}$.

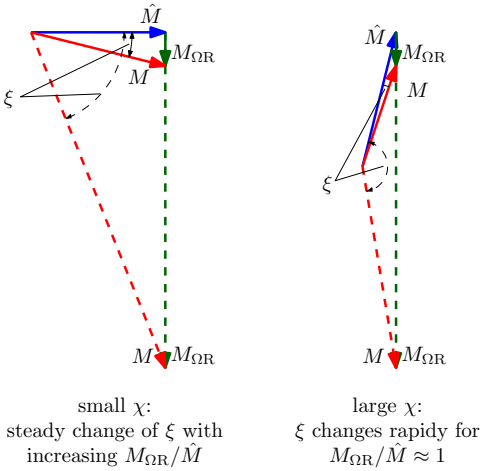

Figure 5.21 – Illustration of difference angle ξ dependence on Mach number ratio $M_{\Omega R}/\hat{M}$.

The implication of Equation (5.61) is that for any non-zero value of $M_{\Omega R}/\hat{M}$ the rotor stagger angle and flow whirl angles will be separated. Low sound power transmission is observed when $\psi_p^{\mathcal{D}} \neq \psi_p^{\mathcal{T}}$ but as $\psi_p^{\mathcal{D}}$ always lies between 0 and θ the changes predicted can only move $\psi_p^{\mathcal{D}}$ and $\psi_p^{\mathcal{T}}$ further apart, hence the rotor transmission loss increases as $M_{\Omega R}$ increases.

Figure 5.22 shows a comparison between the frequency-averaged blockage values calculated using the exact cascade model and the simplified model for spinning rotor with the 'control' geometry at different rotation speeds, and hence different values of ξ. These two sets of results are in agreement to within 0.5 dB at all points.

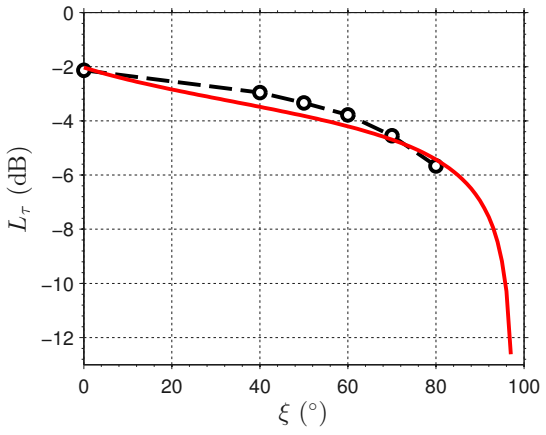

Figure 5.22 – Band-averaged blockage for flat-plate flow over a range of ξ, calculated using exact cascade and simplified model. The blade row geometry is $B = 20$, $\chi = 40°$, $s/c = 0.7$ while relative Mach number is $\hat{M} = 0.7$.

Figure 5.23 shows three 'snapshots' from the Figure 5.22 results to show the ψ_p dependence of the power density function $\mathcal{D}$, the power transmission coefficient $\mathcal{T}^+_{mm}$ and

$\mathcal{T}^+_{mm}\mathcal{D}$ as the blade row spins progressively faster. The lines and transmitted and 'lost' power regions are indicated as in Figure 5.19. Figure 5.23a for $\xi = 0°$ has no rotation but moving to the right the rotation increases, shifting the duct whirl angle θ further from the stagger angle χ and causing a reduction in transmitted power.

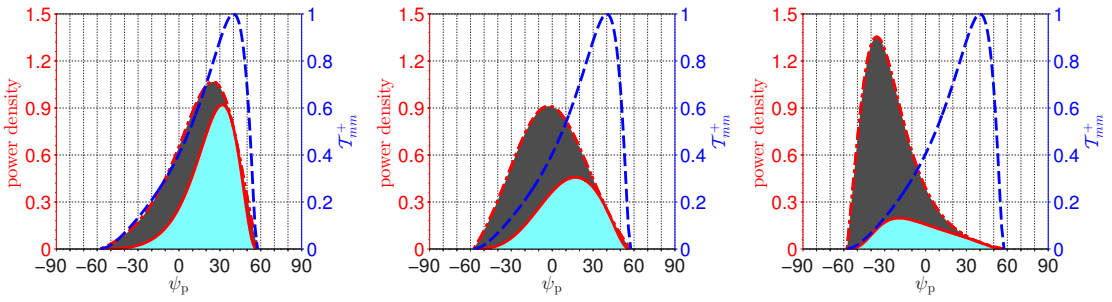

(a) $\xi = 0°$ **(b)** $\xi = 45°$ **(c)** $\xi = 90°$

Figure 5.23 – Comparison of power density function $\mathcal{D}$ (– · –), the power transmission coefficient $\mathcal{T}^+_{mm}$ (– – –) and $\mathcal{T}^+_{mm}\mathcal{D}$ (—) for blade row with $\hat{M} = 0.7$, $\chi = 40°$ and a range of values for the difference angle ξ.

5.3.6 Effects of rotor blade 'camber' on rotor transmission loss

This section explores the effects on rotor transmission loss of application of the diffused rotor flow model described in Section 5.1.5.

Figure 5.24 shows the frequency-averaged rotor transmission loss calculated for the case $B = 20$, $\chi = 40°$, $s/c = 0.7$ while relative Mach number is $\hat{M} = 0.7$ and difference angle $\xi = 70°$. This has been evaluated over a range of 'camber' angles $\Delta\chi$ using the exact cascade model (black dashed lines with circle markers) and the simplified model described earlier in this section (red line).

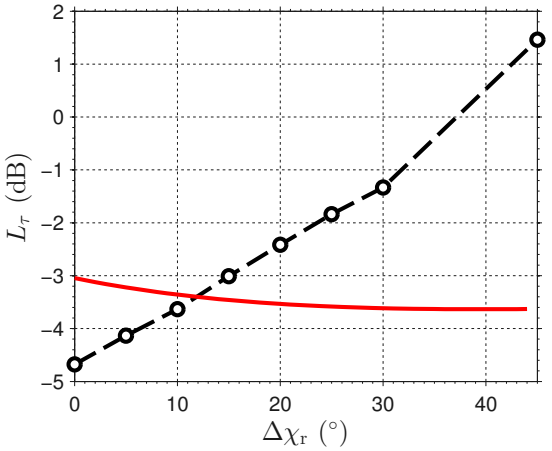

Figure 5.24 – Band-averaged rotor transmission loss for diffused flow over a range of $\Delta\chi$, calculated using exact cascade and simplified model. The blade row geometry is $B = 20$, $\chi = 40°$, $s/c = 0.7$ while relative Mach number is $\hat{M} = 0.7$ and difference angle $\xi = 70°$.

Note that in Figure 5.24 the flow at the leading edge of the rotor is assumed to be axial, it shall be shown in Section 9.3.1 that the flow discontinuity caused by this assumption

leads to non-physical rotor transmission loss calculations. The results shown in Figure 5.22 assume flow that is not turned at the leading edge: the difference in leading edge flow between these two cases accounts for differences in the predictions made for $\xi = 70°$ in Figure 5.22 and the result for $\Delta\chi = 0°$ in Figure 5.24.

The simplified rotor transmission loss model does not exhibit the same behaviour as the exact cascade scattering model and therefore no insight into the camber effects can be obtained by its use. This result highlights the difficulties associated with the use of flat-plate models when modelling real-world problems such as steady loading and cambered blade effects.

5.4 Concluding remarks

In this chapter, a general model has been developed to describe the scattering of sound power incident on a rotating fan. This model has been used to calculate the loss of sound power incident from the downstream direction, as if for rotor-stator interaction noise passing through the rotor of a turbofan engine.

Two flow models are used: an unloaded flat plate model where the flow is undisturbed by the rotor and a new model that estimates the diffusion of the flow through the divergent duct formed by cambered rotor blades and the change of flow whirl angle across the rotor. Application of the new flow model imposes a flow discontinuity at the rotor trailing edge due to the flat plates used to model the rotor blades and it has been found that transmission coefficients in excess of unity are possible when employing this flow model, which is physically unrealistic.

The results obtained when using the exact cascade scattering model due to Smith [46] and Whitehead [47] to evaluate the unloaded flat plate flow model shows that the rotor transmission loss increases as the relative Mach number of the flow is increased and as the rotor stagger angle is increased. The blockage effect is found to be largely frequency independent and is not influenced by either the number of rotor blades or, for overlapped fan blades, by the pitch-chord ratio s/c.

Good agreement with the results of the exact cascade scattering model has been observed when evaluating the modal scattering with the semi-actuator disk model due to Kaji and Okazaki [67]. This analytic modal scattering model has been adapted to create a simplified sound power transmission model based on the interaction between the incident sound power distribution $\mathcal{D}(\psi_\mathrm{p})$ and the transmission coefficient of the blade row $\mathcal{T}^+_{mm}(\psi_\mathrm{p})$. The power distribution $\mathcal{D}(\psi)$ has one distinct peak which falls between $\psi_\mathrm{p} = 0$ and $\psi_\mathrm{p} = \theta$. At low M the peak is close to zero while at high M it tends to the whirl angle. The transmission coefficient $\mathcal{T}^+_{mm}(\psi_\mathrm{p})$ has a main peak value of unity which falls at $\psi^{\mathcal{T}}_\mathrm{p} = \chi$, the rotor stagger angle.

It has been found that there is a significant transmission loss when the peaks in $\mathcal{D}(\psi_\mathrm{p})$ and $\mathcal{T}^+_{mm}(\psi_\mathrm{p})$ are misaligned, so that the majority of the sound power is incident with a

phase angle that is not efficiently transmitted. Both $\mathcal{D}(\psi_\mathrm{p})$ and $\mathcal{T}(\psi_\mathrm{p})$ become narrower as the relative Mach number $\hat{M}$ increases so that there is greater attenuation overall at high flow rates.

The whirl angle is related to χ by

$$\theta = \arctan\left(\tan\chi - \frac{M_{\Omega\mathrm{R}}}{\hat{M}\cos\chi}\right).$$

For stationary blades where $M_{\Omega\mathrm{R}} = 0$ this results in alignment of the flow whirl angle with the rotor stagger angle $\theta = \chi$ and thus for any given $\hat{M}$ the misalignment of the peaks is minimal. Increasing the value of $M_{\Omega\mathrm{R}}$ results in an increase in peak separation and an increase in transmission loss.

Chapter 6

Investigation of self-preservation for rotor wakes

In Chapter 7 techniques will be presented for the processing of rotor wake velocity data in order to decompose instantaneous velocity data into steady and unsteady components with the following properties:

- The steady velocity profile component $\langle U \rangle$ is aligned with the mean flow while $\langle V \rangle$ and $\langle W \rangle$ are perpendicular to it. These velocity profiles are repeated for each blade passage and are referred to as 'mean wakes'.

- The unsteady velocity fluctuation component u is aligned with the mean flow and v and w are perpendicular to it. These fluctuating components are associated with turbulent velocity perturbations that are superposed upon the steady velocity profiles.

In Chapter 8 an analysis of the rotor wake velocity data is conducted with the objective of finding structure in the turbulent wakes arising from wake self-preservation as described by Townsend [8].

In this chapter, the concept of wake self-preservation is reviewed, defining the characteristics of a self-preserving wake in terms of the mean wakes and the unsteady velocity components. Following this description the direct implications of wake self-preservation on the measurement of rotor wakes are explored, with a particular emphasis on the observed wake behaviour when adjacent mean wakes overlap. The chapter commences by introducing the characteristic length and velocity scales used to describe a mean wake.

6.1 Characteristic scales of individual mean wakes

Figure 6.1 shows a sketch of the azimuthal variation (y_3) of the flow-aligned mean velocity component of an individual mean wake $\langle U \rangle$ due to a single wake generating body. The mean wake velocity is located so that its minimum $\min(\langle U \rangle)$ lies at $y_3 = 0$. Also marked are the characteristic velocity and length scales of the mean wake, described below:

- The width of the mean wake is denoted L_{WW}. A procedure for identifying the extent of the wake is described in Section 7.1.3.

- Far from the wake minimum the mean wake velocity plateaus to the 'free-stream' velocity U_∞.

- The maximum wake velocity deficit ΔU is the difference between U_∞ and $\min(\langle U \rangle)$.

- One-half the width of the wake deficit at the point that $\langle U \rangle$ has the value $U_\infty - \Delta U/2$ is defined as the half-width half-minimum L_0.

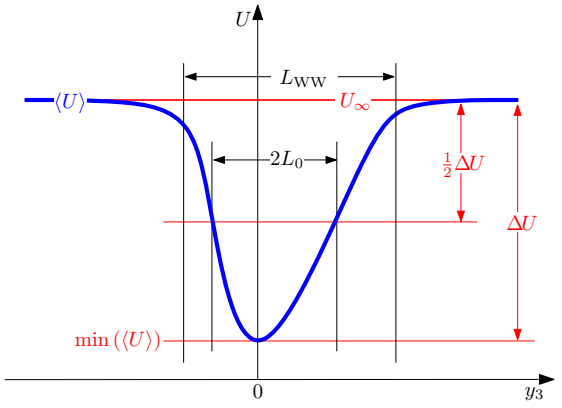

Figure 6.1 – Characteristic scales of an individual mean wake.

6.1.1 Normalised distance downstream of the wake generating body $\hat{x}$

In the forthcoming description of the effects on mean wake shape and length and velocity scales of self-preserving wakes in Section 6.2 the evolution of the wake due to an arbitrary body is described as a function of the distance downstream of the body. The distance is taken along the mean flow streamline which, in the case of rotor wakes, is a helical path of length x_{h}. Calculation of this length from experimental data is discussed in Section 7.2.

The normalised downstream distance is given by

$$\hat{x} = \frac{x_{\mathrm{h}}}{2\theta_{\mathrm{m}}}, \tag{6.1}$$

where θ_{m} is the momentum thickness of the wake. Calculation of θ_{m} is discussed in Section 7.3. This normalisation is chosen to match that used in several earlier studies such as those due to Wygnanski et al. [12] and Gliebe et al. [19].

6.2 Self-preserving wakes

In this section the concept of the self-preservation of a wake is reviewed.

6.2.1 Characteristics of self-preserving wakes.

Townsend [8] defines self-preservation of a wake as an asymptotic state in which wake flow changes in scale but has a similar shape at all stages of decay. Thus, a non-dimensional mean wake velocity profile function $f(\eta)$ can be defined that is independent of $\hat{x}$ such that the mean flow velocity $\langle U \rangle$ at any arbitrary distance $\hat{x}$ is given by

$$\langle U \rangle = U_\infty - \Delta U f(\eta), \tag{6.2}$$

where U_∞ is the free-stream velocity, ΔU is the maximum mean wake deficit and

$$\eta = \frac{y_3}{L_0}, \tag{6.3}$$

is the normalised azimuthal distance [11]. For self-preserving wakes the mean wake length and velocity scales L_0, U_∞ and ΔU defined in Section 6.1 should vary according to development relations of the form $f(\hat{x}) = a\hat{x} + b$. For ΔU and L_0 these relations are specifically [12, 14]

$$\left(\frac{L_0}{\theta_\mathrm{m}}\right)^2 = a\hat{x} + b, \tag{6.4a}$$

$$\left(\frac{U_\infty}{\Delta U}\right)^2 = c\hat{x} + d, \tag{6.4b}$$

for some constants a, b, c and d. Note that the constants b and d in Equations (6.4) account for the 'virtual origin' of the turbulence that can appear to originate upstream of the wake generating body's trailing edge [12]. In Chapter 8, data measured on a fan test rig are analysed in order to identify the constants in Equations (6.4).

The unsteady or mean-square velocity wakes that will be discussed in Section 7.4 are described by length and velocity scales L_u and $\langle \overline{u^2} \rangle$ that are defined in Section 7.4.2. In fully self-preserving wakes these parameters are assumed to scale with mean wake parameters so that constant ratios will be observed between, say, L_u and L_0

$$\frac{L_\mathrm{u}}{L_0} = g, \tag{6.5}$$

for some constant g. The values of these constants are also sought in Chapter 8.

6.2.2 Universality of self-preserving wake characteristics

In a comparison of the values of the constants in Equations (6.4) reported in the literature, Wygnanski et al. [12] found that the inflow turbulence in different test facilities greatly influenced the observed wake evolution. The wakes due to several different bodies were measured, including circular cylinders and a symmetric airfoil, all experiments being conducted in axial flows with no mean loading. The published results showed that the wake evolution was also dependent on the geometry of the different wake generating bodies.

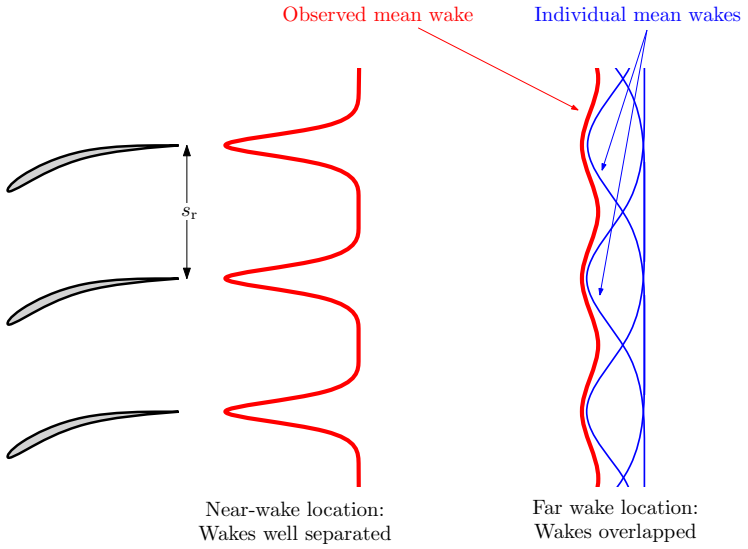

Figure 6.2 – Sketched mean wakes due to periodic distribution of bodies in a uniform flow.

The universality of self-preserving states has been investigated theoretically by George [14, 15]. George shows that the governing equations permit solutions where partial self-preservation is attained, i.e. where the wake profile function $f(\eta)$ is preserved but some or all of the wake parameters evolve in non-self-preserving manner. It is also shown that the self-preserving state is sensitive to the flow conditions at the wake generator: changing the geometry or operating condition will result in a different set of development relations.

Moser et al. [17] conducted a series of wake predictions using Direct Numerical Simulation (DNS) and demonstrated the sensitivity of the flows to the initial conditions. However, due to finite resources, their simulations were not able to show the final state of the wakes.

Sreenivasan and Narasimha [9] argue for a universal self-preserving state when measured sufficiently far downstream. They contend that differences observed in experiment are long-lived transients.

In the present context of rotor wakes in typical turbofan geometries, $\hat{x}$ will be shown to be relatively small and therefore it seems likely that significant variations in wake development with rotor geometry and operating conditions will be observed.

6.3 Wakes due to a periodic distribution of wake generating bodies

Consider the wakes generated by a periodic distribution of identical bodies separated by a distance s_r. The wake due to each body is assumed to be self-preserving so that the wake profile due to each body is described by Equation (6.2). In the near-wake the observed mean wake velocity is a train of isolated wakes, as sketched in Figure 6.2.

Equation (6.4a) shows that the half-width half-minimum L_0 is approximately proportional to $\hat{x}^{1/2}$ so that at some point in the far-wake the wake width L_{WW} becomes large with respect to s_r and the mean wakes become significantly overlapped, as shown on the right-hand side of Figure 6.2. When this occurs the observed mean wake velocity (shown in red) is assumed to be a superposition of the individual mean wakes (shown in blue) and

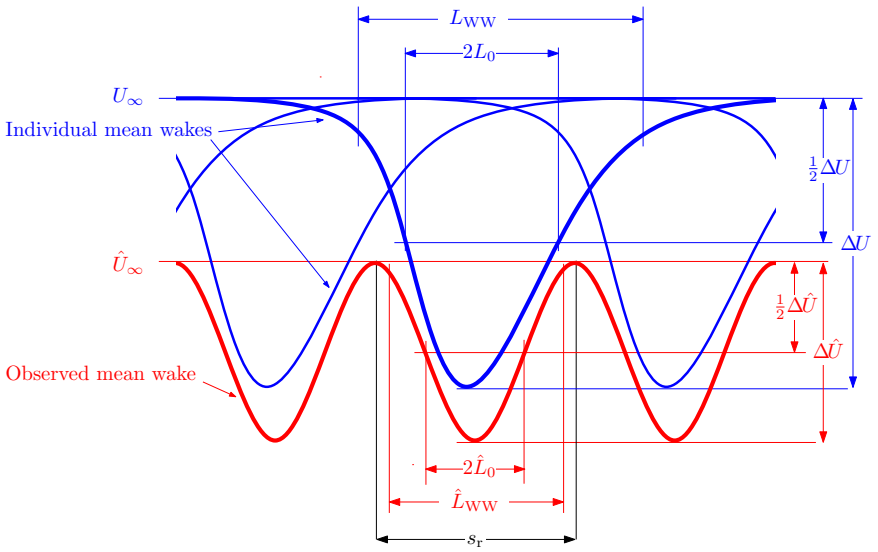

Figure 6.3 – Notation used for characteristics of individual and observed overlapped mean wakes.

the individual mean wake parameters U_∞, ΔU and L_0 can no longer be measured directly.

6.3.1 Characteristic scales of significantly overlapped mean wakes

Figure 6.3 shows a train of individual mean wakes separated by distance s_r in blue and the observed mean wake formed from their superposition in red. The individual mean wake parameters U_∞, ΔU, L_0 and L_{WW} defined in Section 6.1 are shown again along with the parameters for the observed overlapped wake, distinguished by the addition of the $\hat{}$ accent. Note that for mean wakes with negligible overlap the individual and observed mean wakes are identical.

The degree of mean wake overlap can be quantified by the relative width of the individual and observed mean wakes with respect to the rotor blade spacing s_r

$$\zeta = \frac{4L_0}{s_r}, \qquad \hat{\zeta} = \frac{4\hat{L}_0}{s_r}, \tag{6.6}$$

where all terms are defined in Figure 6.3. In Section 6.5 it will be shown that as wake overlap increases the observed mean wake becomes sinusoidal with a spatial period of s_r. The factor of 4 in Equation (6.6) is chosen so that $\hat{\zeta} \to 1$ as $\zeta \to \infty$.

6.4 Effects of isolated mean wake overlap on observed mean wakes

To illustrate the effects of mean wake superposition and overlap a periodic wake profile function is defined as

$$F(\eta) = \sum_{n=-\infty}^{\infty} f\left(\eta + \frac{n s_r}{L_0}\right), \tag{6.7}$$

which will subsequently be substituted into Equation (6.2) in place of the single wake profile function $f(\eta)$ to illustrate the effects of mean wake overlap.

Figure 6.4 shows plotted against y_3/s_r for several values of ζ to illustrate the effects on the shape of $F(\eta)$ due to varying degrees of mean wake overlap. In this example $f(\eta)$ is chosen to be the wake function defined in Equation (8.3) that is fitted to test rig hotwire data as described in Chapter 8. In the list below three values of ζ are identified, as shown in Figure 6.4, in order to illustrate different degrees of wake overlap:

- $\zeta = 1/2$: Negligible mean wake overlap. Observed mean wake resembles a train of isolated mean wakes separated by regions where $F(\eta) = 0$.

- $\zeta = 1$: Partial mean wake overlap. No regions of $F(\eta) = 0$ are seen as the gaps between individual mean wakes begin to 'fill in'.

- $\zeta > 1$: Significant mean wake overlap. Increasing ζ results in a progressive flattening of the response and increase in its mean value. The summed wake profile becomes increasingly sinusoidal.

Figure 6.5 shows a comparison of the mean wake relative width ζ and the observed wake relative width $\hat{\zeta}$ as defined in Equation (6.6). The effects of mean wake overlap on the observed values of wake deficit $\Delta\hat{U}$ and free stream velocity $\hat{U}_\infty$ are shown in Figures 6.6 and 6.7 respectively. The observed values of relative wake width, wake deficit and free stream velocity $\hat{\zeta}$, $\Delta\hat{U}$ and $\hat{U}_\infty$ are shown to be very close to their corresponding isolated wake values for $\zeta \lesssim \zeta_c = 2^{-1/2}$. Above this critical value wake overlap effects are significant on the parameters obtained if the observed wake parameters were measured directly.

When wakes are significantly overlapped the velocity gradient, and hence turbulence production, is reduced (see Figure 6.4). This suggests that turbulence measured in these downstream locations will be mostly convected from upstream locations.

Where rotor mean wakes are self-preserving but also significantly overlapped, the effects shown in Figures 6.5, 6.6 and 6.7 suggest that the development of the observed wake scales $\hat{\zeta}$, $\Delta\hat{U}$ and $\hat{U}_\infty$ will not be linear or constant, as for the mean wakes due to isolated wake generating bodies defined in Equations (6.4) and (6.5). In order to determine the mean wake velocity that will interact with the OGV the overlapped wake shape can be predicted using Equation (6.7) once the underlying evolution of the individual mean wakes is understood. It shall also be shown in Section 7.3.2 that the momentum thickness θ_m can only be calculated accurately from the isolated wake parameters L_0, ΔU and U_∞. It is therefore necessary to find a method to deduce isolated mean wake parameters when they are obscured by wake overlap. It is assumed that the evolution of the wakes due to individual rotor blades is unaffected by wake overlap. In Section 6.5 this assumption is used to develop a method for extracting estimates for the isolated mean wake parameters from overlapped mean wakes thus allowing the prediction of mean wake parameters at far-wake locations such as the leading edge of the OGV necessary for noise predictions.

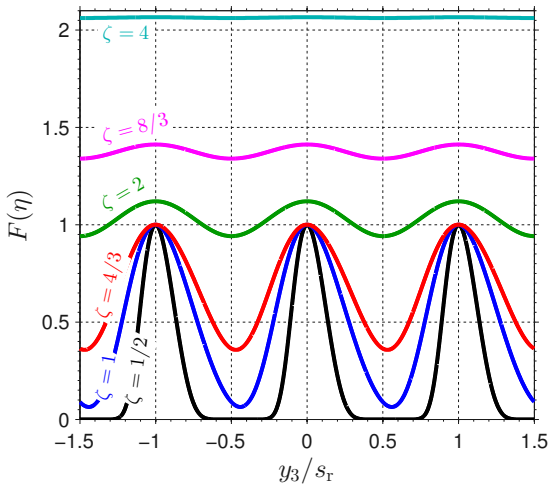

Figure 6.4 – Effect of wake overlap illustrated by summation of wake profiles of variable relative wake width ζ.

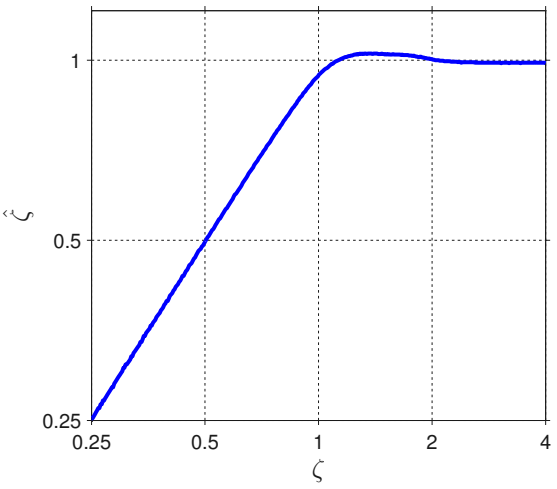

Figure 6.5 – Effects on observed relative wake width $\hat{\zeta}$ as the relative width of the individual wakes ζ is varied.

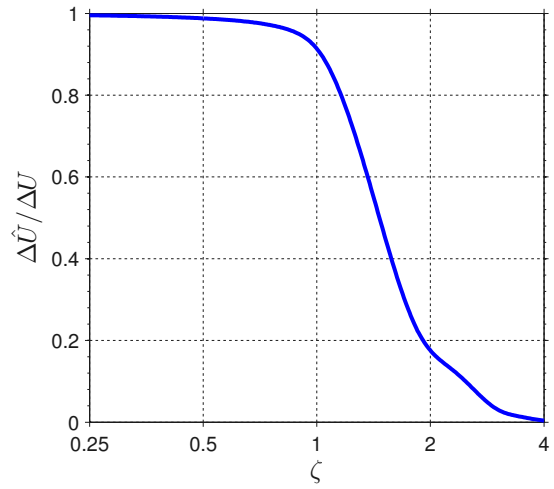

Figure 6.6 – Effects on observed wake deficit $\Delta\hat{U}$ as the relative width of the individual wakes ζ is varied.

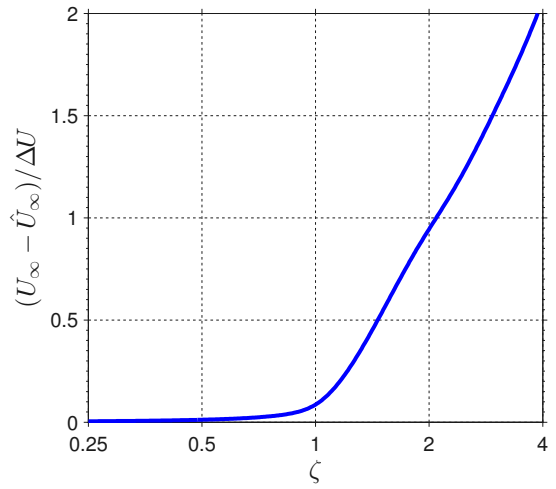

Figure 6.7 – Effects on observed free stream velocity $\hat{U}_\infty$ as the relative width of the individual wakes ζ is varied.

6.5 Determination of isolated mean wake maximum velocity deficit and relative width for overlapped mean wakes using Fourier decomposition

In this section a method is developed to allow the estimation of the individual mean wake parameters ζ and ΔU from measurements of significantly overlapped mean wakes.

The wakes due to all rotor blades are assumed to be identical so that the ensemble-averaged streamwise velocity component is a $2\pi/B_\mathrm{r}$ periodic function of the form

$$\langle U \rangle(\gamma) = U_\infty - \Delta U \sum_{n=-\infty}^{\infty} f\left(\gamma + \frac{2\pi n}{B_\mathrm{r}}\right), \tag{6.8}$$

where γ represents the azimuthal angle, U_∞ is the free stream velocity, ΔU is the maximum wake deficit and f is a non-dimensional wake profile function. The Poisson summation formula allows the periodic term in Equation (6.8) to be represented as

$$\sum_{n=-\infty}^{\infty} f\left(\gamma + \frac{2\pi n}{B_\mathrm{r}}\right) = \frac{B_\mathrm{r}}{2\pi} \sum_{m=-\infty}^{\infty} \hat{f}_m \mathrm{e}^{\mathrm{i}B_\mathrm{r} m\gamma}, \tag{6.9}$$

where $\hat{f}_m$ are Fourier coefficients, given by

$$\hat{f}_m = \int_{-\infty}^{\infty} f(\gamma) \mathrm{e}^{-\mathrm{i}B_\mathrm{r} m\gamma} \mathrm{d}\gamma. \tag{6.10}$$

For the purposes of this analysis the wake profile function $f(\gamma)$ will be assumed to be the Gaussian function

$$f_\mathrm{G}(\eta) = \exp\left[-\ln 2\, \eta^2\right], \tag{6.11}$$

using the identity

$$\eta = \frac{R\gamma}{L_0}, \tag{6.12}$$

where R is the radius of the point under consideration. It will be shown in Section 8.2.1 that the Gaussian wake profile is not a perfect match for the asymmetric individual mean wakes measured on a fan test rig. However, the Gaussian function has the advantage of simplicity and integrability which is necessary for this analysis. Note that in principle the skewed wake profile function f_S defined in Equation (8.3) and used in the examples shown in Figures 6.4–6.7 could be used in place of the Gaussian function, but this would present significant difficulties in performing the Fourier transformation required in the technique. Substitution of Equation (6.11) into Equation (6.10) gives

$$\hat{f}_m = \frac{L_0}{R} \sqrt{\frac{\pi}{\ln 2}} \exp\left[-\left(\frac{B_\mathrm{r} m L_0}{2\sqrt{\ln 2} R}\right)^2\right]. \tag{6.13}$$

Figure 6.8 is a plot of the Fourier coefficients obtained using Equation (6.13) for three values of the wake overlap parameter ζ. For values of $\zeta \gtrsim 1$ the zero-order term is dominant

with the only significant harmonic contributions coming from $|m| = 1$ terms. These $|m| = 1$ terms lead to the observed sinusoidal wake profiles where mean wakes are significantly overlapped. At high values of ζ where the mean wakes are highly overlapped, the $|m| = 1$ terms also become very small. This corresponds to the 'flattening' of $F(\eta)$ observed in Figure 6.4.

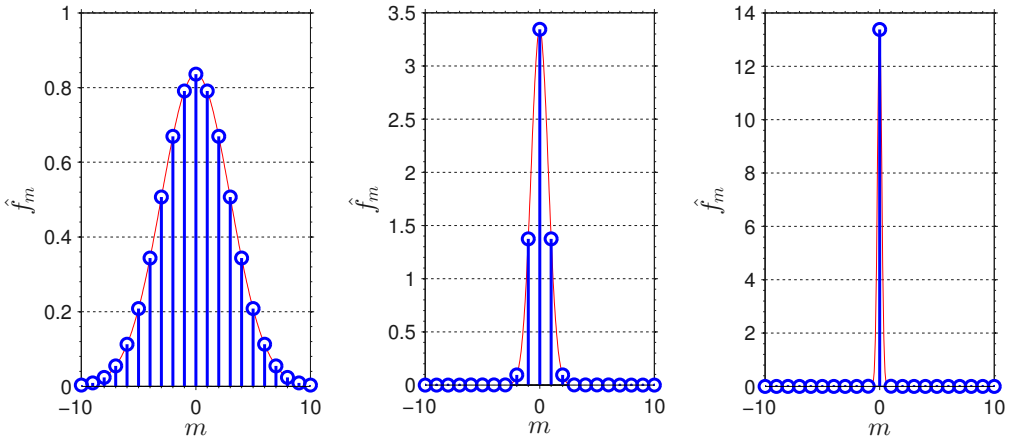

(a) $\zeta = 0.25$ **(b)** $\zeta = 1$ **(c)** $\zeta = 4$

Figure 6.8 – Fourier coefficients of overlapped Gaussian wakes with three relative wake widths ζ calculated using Equation (6.13).

The present study is concerned with mean wakes where there is significant overlap $\zeta > \zeta_c$. In this regime it has been shown that the observed wake is dominated by the order $m = 0$ and $|m| = 1$ Fourier coefficients. The $m = 0$ term gives the mean level and the $|m| = 1$ terms the sinusoidal oscillation. The sum of these three contributions is given by substitution of Equations (6.9) and (6.13) into Equation (6.8) giving

$$\langle U \rangle(\gamma) = U_\infty - \frac{\Delta U B_r}{2\pi} \sum_{m=-1}^{1} \frac{L_0}{R} \sqrt{\frac{\pi}{\ln 2}} \exp\left[-\left(\frac{B_r m L_0}{2\sqrt{\ln 2} R} \right)^2 \right] \exp\left[\mathrm{i} B_r m \gamma \right], \tag{6.14}$$

$$= \underbrace{\left\{ U_\infty - \Delta U \frac{B_r L_0}{2\pi R} \sqrt{\frac{\pi}{\ln 2}} \right\}}_{\text{Steady Term}} - \underbrace{\left\{ \Delta U \frac{B_r L_0}{2\pi R} \sqrt{\frac{\pi}{\ln 2}} \exp\left[-\left(\frac{B_r L_0}{2\sqrt{\ln 2} R} \right)^2 \right] \left[2 \cos B_r \gamma \right] \right\}}_{\text{Oscillating Term}}. \tag{6.15}$$

Recalling the definition $\zeta = 4L_0/s_r$ in Equation (6.6) this becomes

$$\langle U \rangle(\gamma) = \underbrace{\left\{ U_\infty - \frac{\Delta U \zeta}{4} \sqrt{\frac{\pi}{\ln 2}} \right\}}_{\text{Steady Term}} - \underbrace{\left\{ \frac{\Delta U \zeta}{2} \sqrt{\frac{\pi}{\ln 2}} \exp\left[-\left(\frac{\pi \zeta}{4\sqrt{\ln 2}} \right)^2 \right] \cos B_r \gamma \right\}}_{\text{Oscillating Term}}. \tag{6.16}$$

The overlapped wake profile described by Equation (6.16) may be used to determine $\overline{U}$ and $\Delta\hat{U}$ which form the input for the technique for deducing the parameters of individual wakes, as illustrated in Figure 6.9. The steady and oscillating terms of Equation (6.16)

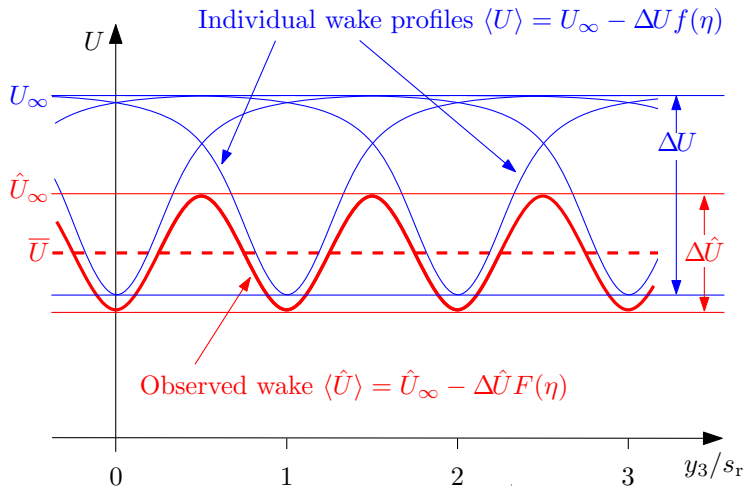

Figure 6.9 – Parameters of observed overlapped wake profile. Mean value $\overline{U}$ and peak-to-trough difference $\Delta\hat{U}$ are readily measured but the free stream velocity U_∞ is obscured.

can be related to the measured parameters $\overline{U}$ and $\Delta\hat{U}$ by

$$\overline{U} = U_\infty - \frac{\Delta U\,\zeta}{4}\sqrt{\frac{\pi}{\ln 2}}, \tag{6.17}$$

$$\Delta\hat{U} = \Delta U\,\zeta\sqrt{\frac{\pi}{\ln 2}}\exp\left[-\left(\frac{\pi\zeta}{4\sqrt{\ln 2}}\right)^2\right]. \tag{6.18}$$

Rearranging these expressions yields

$$\zeta = \frac{4\sqrt{\ln 2}}{\pi}\sqrt{\ln\left\{\frac{4[U_\infty - \overline{U}]}{\Delta\hat{U}}\right\}}, \tag{6.19}$$

$$\Delta U = \sqrt{\pi}\frac{U_\infty - \overline{U}}{\sqrt{\ln\left\{\dfrac{4[U_\infty - \overline{U}]}{\Delta\hat{U}}\right\}}}. \tag{6.20}$$

For substantially overlapped wakes the relative width of the individual mean wakes ζ and the maximum individual mean wake deficit ΔU may be estimated from parameters that are readily measurable if the free-stream flow speed U_∞ is known. In practice it will be necessary to use an estimate for U_∞, as discussed in Section 8.4.

6.6 Sensitivity of overlapped wake method to errors in U_∞

The extraction of isolated wake parameters from significantly overlapped wakes requires an estimate for the free stream velocity U_∞ that is subject to error. The sensitivity of the expressions Equations (6.19) and (6.20) to errors in U_∞ is now investigated.

It is assumed that the correct value of the free-stream velocity U_∞ is known and that the value used is subject to some error δU_∞. Errors in the expressions for ζ and ΔU are now obtained by taking partial derivatives of Equations (6.19) and (6.20) with respect to

U_∞. The resulting error sensitivity expressions are

$$\frac{\partial \zeta}{\partial U_\infty} = \frac{2\sqrt{\ln 2}}{\pi[U_\infty - \overline{U}]} \left(\ln \left\{ \frac{4[U_\infty - \overline{U}]}{\Delta \hat{U}} \right\} \right)^{-1/2}, \tag{6.21}$$

$$\frac{\partial (\Delta U)}{\partial U_\infty} = \sqrt{\pi} \left(\ln \left\{ \frac{4[U_\infty - \overline{U}]}{\Delta \hat{U}} \right\} - \frac{1}{2} \right) \cdot \left(\ln \left\{ \frac{4[U_\infty - \overline{U}]}{\Delta \hat{U}} \right\} \right)^{-3/2}. \tag{6.22}$$

Figure 6.10 shows two representations of the sensitivity of ζ to errors in U_∞ normalised with U_∞, plotted against $(U_\infty - \overline{U})/U_\infty$ which indicates the normalised difference between the mean of the observed wake and the actual free stream flow speed. The values of $(U_\infty - \overline{U})/U_\infty$ are linked to the degree of mean wake overlap so that small values are associated with partial overlap where the assumptions made in Section 6.5 are close to breakdown.

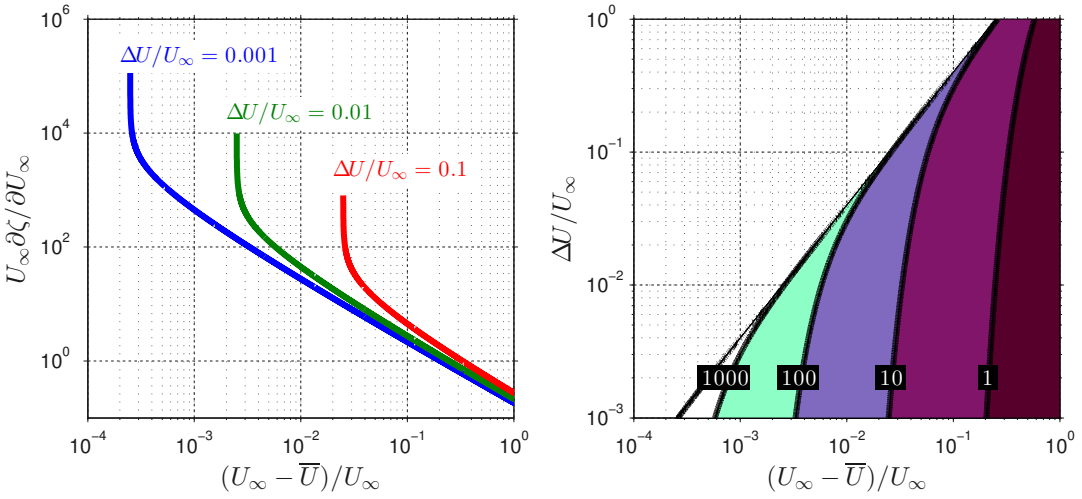

(a) Sensitivity for three values of $\Delta \hat{U}/U_\infty$ **(b)** Contours indicate value of $U_\infty \partial\zeta/\partial U_\infty$.

Figure 6.10 – Normalised sensitivity of ζ to errors in U_∞ over the domain $U_\infty - \overline{U} > \Delta \hat{U}/4$ obtained by evaluation of Equation (6.21).

Figure 6.10a shows $U_\infty \partial\zeta/\partial U_\infty$ plotted for three values of $\Delta \hat{U}/U_\infty$ — the size of the observed wake fluctuations relative to the free-stream flow speed. The sensitivity to errors in U_∞ is high for small values of $(U_\infty - \overline{U})/U_\infty$ but decreases as overlap increases.

Figure 6.10b shows contours of iso-sensitivity versus $\Delta \hat{U}/U_\infty$ and $(U_\infty - \overline{U})/U_\infty$. Contours of $U_\infty \partial\zeta/\partial U_\infty$ are plotted for $U_\infty - \overline{U} > \Delta \hat{U}/4$. Outside this domain, points on the observed wake exceed the free-stream velocity which is non-physical and in violation of the wake overlap model shown in Equation (6.8). The contours of $U_\infty \partial\zeta/\partial U_\infty$ indicate that the sensitivity to error increases towards the left, where the overlap condition is close to breakdown.

Figure 6.11 shows the modulus of the sensitivity of ΔU to errors in U_∞ plotted against $(U_\infty - \overline{U})/\Delta \hat{U}$. Large magnitude negative values of sensitivity are seen for $1/4 < (U_\infty - \overline{U})/\Delta \hat{U} < \sqrt{e}/4$, which correspond to cases where the assumptions made in Section 6.5 are

approaching or exceeding their limits. At all other points the magnitude of the sensitivity is less than unity.

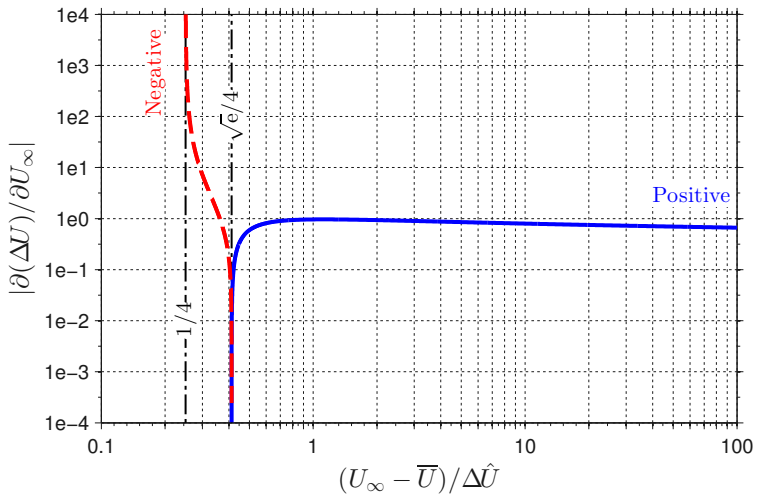

Figure 6.11 – Sensitivity of ΔU to errors in U_∞ over the domain $U_\infty > \Delta\hat{U}/4$ obtained using Equation (6.22).

The expressions in Equations (6.19) and (6.20) for the relative width and the velocity deficit of the isolated mean wake as derived from observed mean wake parameters have been shown to be sensitive to errors in the estimated free-stream velocity U_∞ when the mean wakes begin to overlap and the assumption of significant wake overlap is close to breaking down.

Chapter 7

Extraction of mean and turbulent wake data from hotwire and RANS CFD data for input to broadband noise models

This chapter will give a description of the general procedures applied in order to extract mean and turbulent flow data from hotwire anemometry velocity timeseries data and RANS CFD predictions with a simple turbulence model. In particular, this includes:

- Resolution of velocities in a duct-aligned coordinate system into a coordinate system aligned with the mean flow.
- Calculation of the mean wakes and extraction of mean wake parameters.
- Calculation of the momentum thickness θ_{m}.
- Obtaining the unsteady component of the wake velocity and extraction of the unsteady wake parameters.

The hotwire data are in the form of instantaneous timeseries that require ensemble-average processing. The RANS CFD simulation data are mean velocity profiles with turbulence velocity statistics so the ensemble-averaging steps are omitted.

All examples using hotwire data in this chapter are taken from the LSFR tests described in Section 8.1.

7.1 Resolution of velocities into a flow-oriented coordinate system

In Chapter 8 mean and turbulent wake data are used to predict the flow conditions at the OGV leading edge for broadband noise predictions. The analysis of this data is performed in terms of a coordinate system aligned with the mean flow. The measured data are, however, expressed in terms of a coordinate system aligned with the duct. This section will describe the processes required in order to resolve these velocities into components aligned with the mean flow and perpendicular to it.

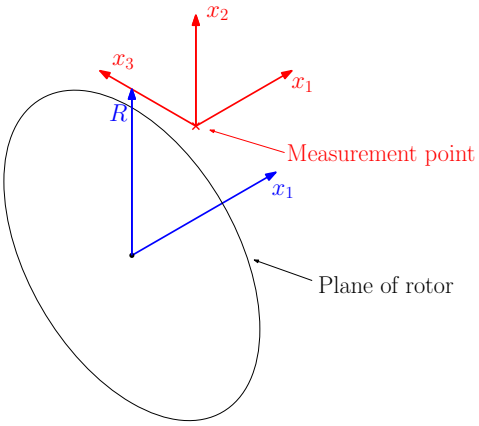

Figure 7.1 – Sketch of duct-aligned coordinate system **x** and its relation to the measurement location.

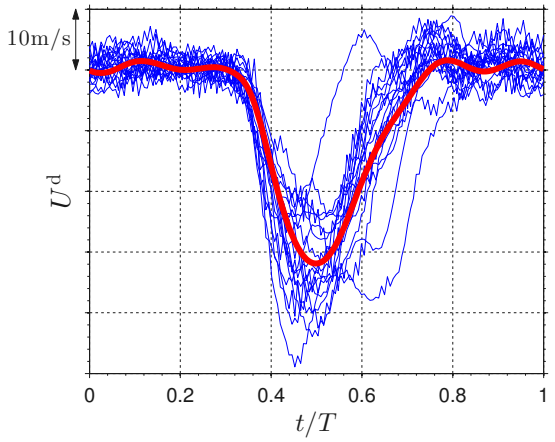

Figure 7.2 – Axial velocity data over 18 blade passages (blue lines) and the corresponding ensemble-average taken over 25,308 blade passages (red) plotted against t/T. These data taken from LSFR run at 50% fan speed and working line 5, from the hotwire measurement location at axial location Pos.1, radial location 7.

7.1.1 Duct-aligned coordinate system

Instantaneous hotwire velocity data are described in terms of duct-aligned coordinate component velocities U^{d}, V^{d} and W^{d}. U^{d} is aligned with the fan rig axis x_1. V^{d} and W^{d} are aligned with the azimuthal x_2 and radial x_3 directions respectively at the points of measurement as sketched in Figure 7.1.

7.1.2 Forming ensemble-average of hotwire timeseries

The hotwire data is in the form of instantaneous timeseries U^{d}, V^{d} and W^{d}. It is assumed that variations of geometry between rotor blades are insignificant so that the instantaneous velocities are a superposition of a mean velocity wake repeated for each blade passage and an unsteady random component representing the turbulence velocity perturbations. The steady flow component is obtained from an ensemble-average of the instantaneous data.

The hotwire velocity timeseries have a constant number of samples for each blade passage $N_{\mathrm{j}} \in \mathbb{N}$. A per-blade ensemble average for the U^{d} velocity component is deduced from

$$\langle U^{\mathrm{d}} \rangle (j) = \frac{1}{N_{\mathrm{b}}} \sum_{n=1}^{N_{\mathrm{b}}} U^{\mathrm{d}}(j + (n-1)N_{\mathrm{j}}), \tag{7.1}$$

where $N_{\mathrm{b}} \in \mathbb{N}$ is the number of blade passages included in the average. Similar calculations are performed for the V^{d} and W^{d} velocity components.

Figure 7.2 shows the instantaneous axial velocity data over 18 blade-passages in blue, plotted against t/T. An ensemble average taken over 25,308 blade passages from the same data set is also shown in red. The ensemble-averaged velocity profile exhibits a distinct velocity deficit. Away from the velocity minimum the velocity profile plateaus. The velocity in this 'flat region' is regarded as being free-stream and will be used to determine

the flow angles, as described in Section 7.1.

Several of the instantaneous timeseries shown in Figure 7.2 have wake minima that are not aligned with the mean wake. This 'wander' of the wake is not considered further in this thesis, but can be expected to lead to a broadening of the mean wake.

7.1.3 Identifying the extent of the rotor blade wake velocity deficit

In the subsequent sections it will be important to identify the extents of the mean wake so that the mean flow and wake can be considered separately. In this section a procedure is described for automatically determining the mean wake extents.

In the present study, the axial velocity component U^{d} is most closely aligned with the streamwise direction and is the only component to exhibit clear wake deficit-like behaviour, as shown in Figure 7.2. Care has been taken to define a procedure to automatically identify the mean wake extents from $\langle U^{\mathrm{d}} \rangle$ and hence to obtain the width of the observed mean wake $\hat{L}_{\mathrm{WW}}$. The procedure is described below and is illustrated in Figure 7.3.

1. The location of mean wake minimum in $\langle U^{\mathrm{d}} \rangle$ is identified (marked with red square).

2. The ensemble-average wake $\langle U^{\mathrm{d}} \rangle$ is a discrete signal and its gradient is approximately proportional to the difference between adjacent samples $\delta\langle U^{\mathrm{d}} \rangle$. This difference signal is shown as the blue dashed line. In practice, smoothing is generally applied to $\delta\langle U^{\mathrm{d}} \rangle$ in order to reduce the effects of noise in this 'derivative'.

3. The maximum and minimum of $\delta\langle U^{\mathrm{d}} \rangle$ are found either side of the minimum of the mean wake $\langle U^{\mathrm{d}} \rangle$ (blue triangles).

4. The location of the wake extents are supposed to correspond to the points at which the difference falls to $1/2.1$ of its maximum and minimum values (blue circles and red stars). The factor 2.1 has been chosen empirically in order to match the automatic results to those picked 'by eye' and improve robustness of the results in the face of contamination from probe vibrations (as compared with a value of 2).

7.1.4 Free-stream velocity

The free-stream velocity components U^{d}_{∞}, V^{d}_{∞} and W^{d}_{∞} resolved in the x_1, x_2 and x_3 directions respectively are now determined by taking the mean of the corresponding ensemble-averaged velocity outside the wake extent obtained in Section 7.1.3. Examples of the three ensemble-averaged velocity components and the corresponding free-stream velocities are shown in Figure 7.4 plotted against t/T.

7.1.5 Mean flow angles

The free-stream velocity component estimates U^{d}_{∞}, V^{d}_{∞} and W^{d}_{∞} are used to provide estimates for the mean flow whirl angle ψ_{w} and radial angle ψ_{r} relative to the local machine

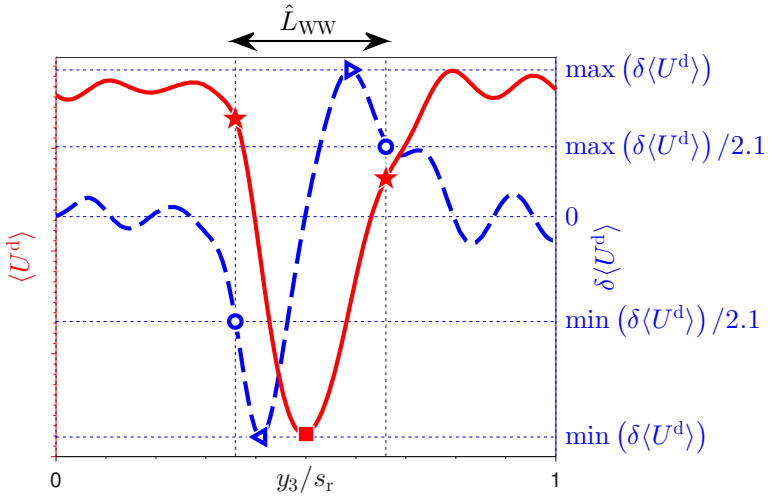

Figure 7.3 – Illustration of the procedure for identifying the extent of an ensemble-averaged wake. The red line and left-hand axis represent the ensemble-averaged wake. The blue dashed line and right-hand axis represent its smoothed difference. The various markers are referred to in the text.

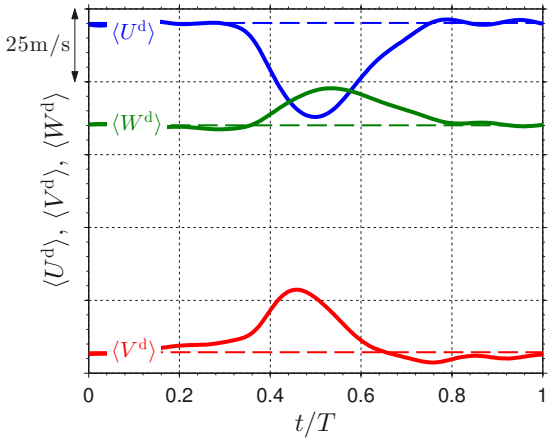

Figure 7.4 – Ensemble-averaged velocities resolved in the duct-aligned coordinate system plotted against t/T. The corresponding free-stream velocities are shown as dashed lines. These data taken from LSFR at 50% fan speed at working line 5 at axial location Pos.1, radial station 7.

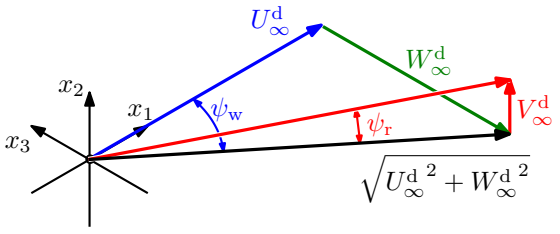

Figure 7.5 – Definition of the radial and whirl angles relative to the local machine coordinate system.

coordinate system, as illustrated in Figure 7.5 so that

$$\psi_{\mathrm{w}} = \arctan\left(\frac{W_{\infty}^{\mathrm{d}}}{U_{\infty}^{\mathrm{d}}}\right), \tag{7.2a}$$

$$\psi_{\mathrm{r}} = \arctan\left(\frac{V_{\infty}^{\mathrm{d}}}{\sqrt{{U_{\infty}^{\mathrm{d}}}^2 + {W_{\infty}^{\mathrm{d}}}^2}}\right). \tag{7.2b}$$

7.1.6 Rotation matrix for resolving velocity data

The flow angles ψ_{w} and ψ_{r} are used to assemble the rotation matrix

$$\mathbf{R} = \begin{bmatrix} \cos\psi_{\mathrm{r}}\cos\psi_{\mathrm{w}} & \sin\psi_{\mathrm{r}} & \cos\psi_{\mathrm{r}}\sin\psi_{\mathrm{w}} \\ -\sin\psi_{\mathrm{r}}\cos\psi_{\mathrm{w}} & \cos\psi_{\mathrm{r}} & -\sin\psi_{\mathrm{r}}\sin\psi_{\mathrm{w}} \\ -\sin\psi_{\mathrm{w}} & 0 & \cos\psi_{\mathrm{w}} \end{bmatrix}. \tag{7.3}$$

The matrix $\mathbf{R}$ may be used to resolve the duct coordinate velocity hotwire timeseries data into streamwise and stream-normal components

$$\begin{Bmatrix} U \\ V \\ W \end{Bmatrix} = \mathbf{R} \begin{Bmatrix} U^{\mathrm{d}} \\ V^{\mathrm{d}} \\ W^{\mathrm{d}} \end{Bmatrix}. \tag{7.4}$$

An identical operation is used to resolve the ensemble-averaged velocity components

$$\begin{Bmatrix} \langle U \rangle \\ \langle V \rangle \\ \langle W \rangle \end{Bmatrix} = \mathbf{R} \begin{Bmatrix} \langle U^{\mathrm{d}} \rangle \\ \langle V^{\mathrm{d}} \rangle \\ \langle W^{\mathrm{d}} \rangle \end{Bmatrix}. \tag{7.5}$$

Examples of the stream-resolved ensemble-averaged velocity components given by the application of Equation (7.5) are shown in Figure 7.6 plotted against t/T. Having performed this transformation, the streamwise component $\langle U \rangle$ can be used to extract the mean wake velocity and length scales U_{∞}, ΔU and L_0 as described in Chapter 6. Note that the velocities of the transverse components $\langle V \rangle$ and $\langle W \rangle$ are close to zero outside the wake region.

7.2 Non-dimensional downstream distance

The self-preserving wake development described in Section 6.2 is expressed in terms of the normalised distance between the rotor trailing edge and the measurement position $\hat{x}$. The radial and whirl angles obtained in Section 7.1.5 are now used to calculate $\hat{x}$.

The convection streamline from the rotor trailing edge to the measurement location is assumed to follow a helical path of length

$$x_{\mathrm{h}} = \sqrt{(\Delta x_1 \sec\psi_{\mathrm{w}})^2 + \Delta x_2^2}, \tag{7.6}$$

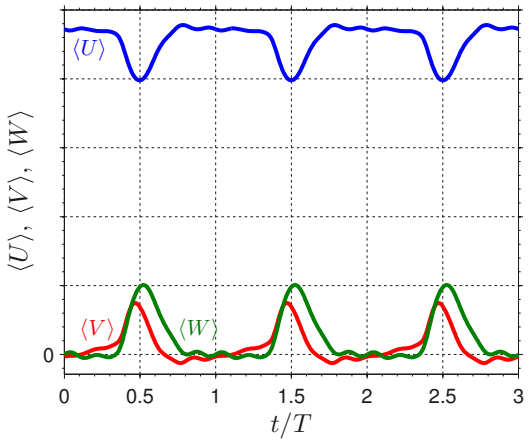

Figure 7.6 – Ensemble-averaged velocity resolved into streamwise and stream-normal components from radial station 7 of Case HW2 plotted against t/T.

where Δx_1 and Δx_2 are the axial and radial differences between a given point on the OGV leading edge and the intersection of the rotor trailing edge with straight lines projected back from that point with radial angle ψ_r, as illustrated in Figure 7.7. The flow angles ψ_w and ψ_r are obtained using Equation (7.2). The non-dimensional distance $\hat{x}$ is then given by $\hat{x} = x_\mathrm{h}/2\theta_\mathrm{m}$ as originally defined in Equation (6.1).

7.3 Momentum thickness θ_m

The momentum thickness θ_m is used as the main lengthscale in the subsequent analysis of the variation of the wake width L_0 and velocity deficit ΔU. Momentum thickness is a quantity closely related to the drag coefficient of a given body and as such should be only weakly dependent on the downstream location at which it is measured [12]. In this section the steps taken to calculate θ_m from experimental data are explained. It shall be shown that where the wakes due to individual rotor blades are significantly overlapped (see Chapter 6) the conventional method for evaluating θ_m causes significant errors. A method is proposed to obtain robust estimates of θ_m under mean wake overlap conditions which show little variation with the axial location at which the flow measurements were made. The section commences by reviewing the conventional calculation method, that is appropriate for use when individual mean wakes are well separated.

7.3.1 Calculation of θ_m for mean wakes with negligible overlap

The momentum thickness θ_m of the wake due to an isolated body may be calculated using [12]

$$\theta_\mathrm{m} = \int_{-\infty}^{\infty} \frac{\bar{U}(y_3)}{U_\infty}\left(1 - \frac{\bar{U}(y_3)}{U_\infty}\right) \mathrm{d}y_3, \tag{7.7}$$

where y_3 is the distance along a direction normal to the streamwise flow corresponding to the azimuthal direction, $\bar{U}(y_3)$ is the time-averaged streamwise velocity component which varies as a function of at y_3 and U_∞ is the streamwise free-stream velocity.

When working with rotor wake data Equation 7.7 is approximated by the finite integral

$$\theta_{\mathrm{m}} = \int_{-s_{\mathrm{r}}/2}^{s_{\mathrm{r}}/2} \frac{\langle U \rangle(y_3)}{U_\infty} \left(1 - \frac{\langle U \rangle(y_3)}{U_\infty}\right) \mathrm{d}y_3, \tag{7.8}$$

where s_{r} is the rotor blade separation distance and $\langle U \rangle$ is the ensemble-averaged mean wake profile, obtained as described in Section 7.1.2. This truncation of the domain relies on the fact that the contributions of the integrand fall to zero as $\langle U \rangle$ tends to U_∞, as is shown in Figure 7.8. If the rotor mean wakes are well separated then only the wake velocity deficit contributes significantly to the value of θ_{m} in Equation (7.8). Problems associated with calculation of θ_{m} when mean wakes are overlapped shall be discussed in Section 7.3.2.

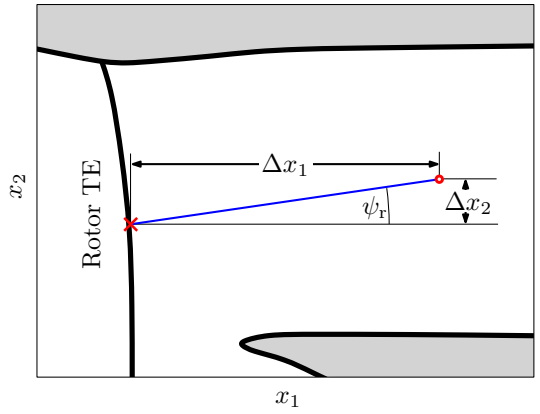

Figure 7.7 – Illustration of parameters used in calculation of helical distance.

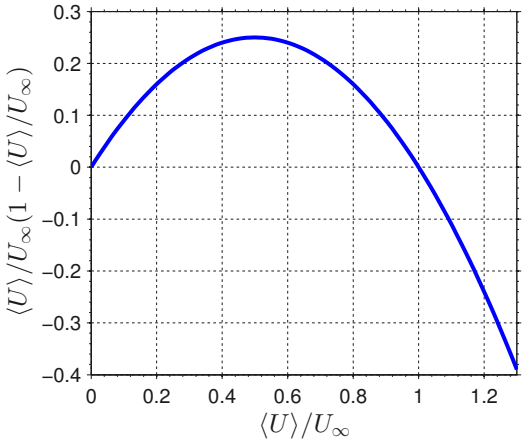

Figure 7.8 – Integrand of the momentum thickness calculation Equation (7.8) plotted against its independent variable $\langle U \rangle / U_\infty$.

7.3.2 Calculation of momentum thickness θ_{m} for significantly overlapped mean wakes

In Section 7.3.1 it was shown that Equation (7.8) can be applied to calculate the momentum thickness for non-overlapped mean wakes. This section will propose a method for the calculation of θ_{m} when the mean wakes are significantly overlapped.

When the mean wakes are non-overlapped the velocity deficit falls to near zero before the limits of integration in Equation (7.8) are reached. As the isolated wake profile broadens the wake extends beyond these limits and, because of the periodicity of the observed wake, the velocity deficits from adjacent blade passages are found to contribute to the observed mean wake profile. Now the maximum apparent mean wake velocity is smaller than the free-stream velocity (see the right hand side of Figure 6.2).

Two options for the calculation of the momentum thickness for overlapped mean wakes using Equation (7.8) exist:

- **Method 1** Calculate using the observed overlapped wake $\langle U \rangle$ and the observed free

stream velocity $\hat{U}_\infty$ in place of U_∞. This would be the calculation made if wake overlap had not been identified. The integrand of this calculation is illustrated by the shaded area in Figure 7.9a. It will be shown that this method consistently underestimates θ_m because of the reduction of $\Delta\hat{U}$ that occurs with increasing mean wake overlap.

- **Method 2** Calculate using the observed overlapped wake $\langle U \rangle$ and the isolated free stream velocity U_∞ (see Section 8.4). The integrand of this calculation is illustrated by the shaded area in Figure 7.9b. It will be shown that this method is highly sensitive to errors in the estimate of U_∞.

A third method, referred to as Method 3, is proposed that uses an individual mean wake profile that is 'reconstructed' using the mean wake parameters U_∞, ΔU and L_0 obtained using the methods developed in Chapter 6. Equation (6.2) for the isolated mean wake model is substituted into Equation (7.7) to give

$$\theta_\mathrm{m} = \int_{-\infty}^{\infty} \frac{U_\infty - \Delta U f(\eta)}{U_\infty} \left(1 - \frac{U_\infty - \Delta U f(\eta)}{U_\infty}\right) \mathrm{d}y_3. \tag{7.9}$$

where $\eta = y_3/L_0$ is the azimuthal distance normalised with the half-wake half-width of the individual mean wake. For the examples that follow, and for use in Equation (7.9) in Chapter 8, $f(\eta)$ is chosen to be the asymmetric mean wake shape of Equation (8.3) derived from the experimental data which is discussed in Section 8.2.1. The integrand of Equation (7.9) is illustrated by the shaded area in Figure 7.9c.

The accuracy of the three methods for calculating θ_m described above is assessed by observing their behaviour as the relative wake width ζ of a hypothetical mean wake is changed. Consider mean wakes separated by distance s_r in a flow with $U_\infty = 100\,\mathrm{m/s}$. The half-wake half-width L_0 is varied so that the relative mean wake width covers the range $0.25 \leq \zeta \leq 4$. It is assumed that the product $L_0\Delta U$ is constant so that ΔU is inversely proportional to L_0, consistent with the behaviour of a self-preserving wake [12]. The values of ΔU are chosen so that the largest is $10\,\mathrm{m/s}$ — one-tenth of the free-stream velocity. For each combination of L_0 and ΔU the individual mean wake and overlapped mean wake velocity profiles are calculated using Equations (6.2) and (6.7). The three momentum thickness calculation methods are then used to obtain estimates for θ_m. Note that as Method 3 uses an isolated wake and the conventional calculation method it perform the function of a 'control' in this exercise. The results obtained using each method are shown in Figure 7.10.

1. For $\hat{\zeta} > \zeta_\mathrm{c}$ Method 1 (black line) consistently underestimates θ_m when compared with Method 3. As wake overlap increases and $\Delta\hat{U}$ decreases the predicted value of θ_m rapidly tends to zero.

2. Method 2 (blue solid line) and Method 3 (red solid line) are in close agreement over the entire domain of calculation suggesting that both are accurate.

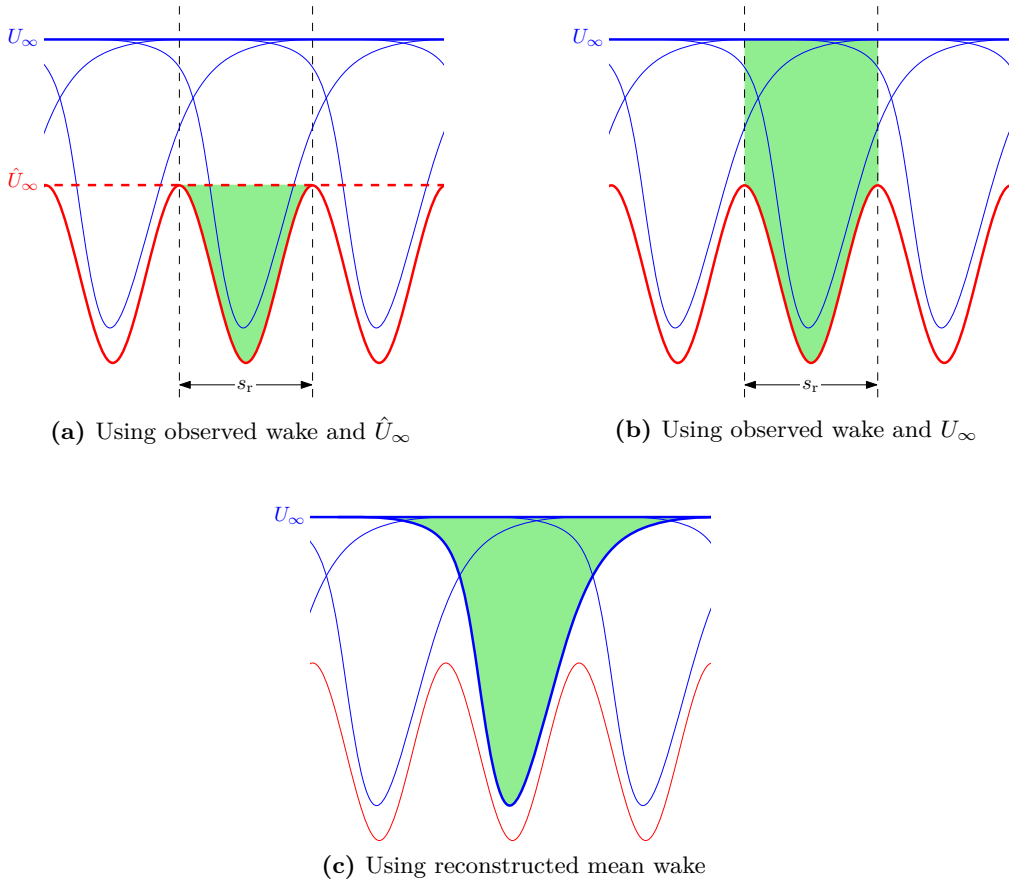

(a) Using observed wake and $\hat{U}_\infty$

(b) Using observed wake and U_∞

(c) Using reconstructed mean wake

Figure 7.9 – Calculation of momentum thickness from significantly overlapped mean wakes using three methods.

3. Also shown on Figure 7.10 as blue and red dashed lines are the results obtained using Methods 2 and 3 when a -0.5% 'error' is applied to the value of U_∞. The Method 2 result is changed by over one-third its original value indicating that it is highly sensitive to errors in U_∞. Bearing in mind that in practice this value will be estimated, the observed sensitivity is not acceptable. Conversely, the Method 3 results are nearly indistinguishable from those obtained when using the correct value of U_∞, indicating that this method is robust to errors in U_∞.

4. Also of note here is that the self-preserving nature of the flow, enforced by maintaining $L_0\,\Delta U = \text{const}$, do not result in a constant value of θ_m as ζ is changed. This is in contradiction to Wygnanski et al. [12]. The effect is observed to be sensitive to the ratio $\Delta U/U_\infty$, with larger variations seen for large ratios, and hence the applicability only to small-deficit wakes.

In this section several methods for the calculation of the momentum thickness θ_m for rotor wakes have been investigated. Where individual wake overlap is negligible the ensemble-average calculation of Equation 7.8 gives accurate results provided that the extracted value of $U_\infty = \hat{U}_\infty$ is accurate. However, where wakes are significantly overlapped with $\hat{\zeta} > \zeta_c$ this method leads to values of θ_m that rapidly approach zero. A similar

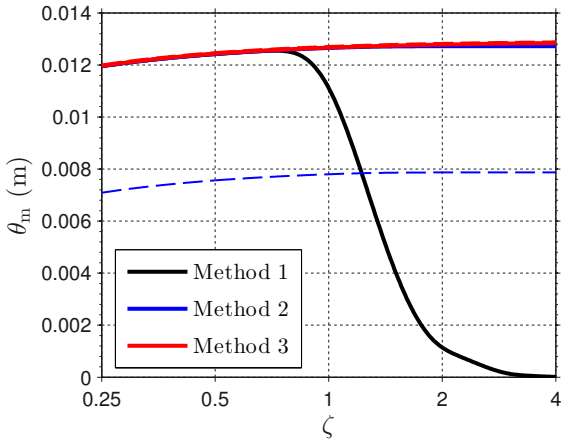

Figure 7.10 – Comparison of momentum thickness calculated for non-overlapped and overlapped mean wakes in a hypothetical self-preserving flow with $U_\infty = 100\,\mathrm{m/s}$. Three calculation methods are used; (black line) a single blade-passage calculation using Equation (7.8) with apparent free stream velocity $\hat{U}_\infty$, (blue line) a similar calculation using the isolated wake free stream velocity U_∞ and (red line) a method using a 'reconstructed' mean wake. The product of half-wake half-width to the wake velocity deficit is constant with the maximum wake velocity deficit being 10% of the free stream velocity. Dashed lines indicate the values obtained when a -0.5% perturbation is introduced into the value of U_∞, showing the sensitivity to errors of Methods 2 and 3.

approach using an estimate of U_∞ as discussed in Chapter 6 has been shown to yield accurate results but is extremely sensitive to errors in U_∞. A 'reconstructed wake' method developed here, shown in Equation (7.9), has been found to be robust to errors in the estimates of U_∞.

7.4 Extraction of turbulence data from unsteady wakes

So far the analysis of hotwire and RANS CFD data has been conducted on ensemble-averaged mean wake data. In this section the unsteady component of the rotor wakes shall be examined.

As noted in the introduction to this chapter the hotwire data are instantaneous velocity timeseries while the results of RANS CFD calculations are per-blade ensemble-average statistics. The RANS CFD calculations used in the present study were performed with a k-ω turbulence model. Here k represents the total turbulence kinetic energy and ω the specific dissipation. The procedures involved in producing turbulence statistics from these types of data are presented in this section.

7.4.1 Ensemble-averaged mean-square turbulent velocities

Ensemble-averages of the mean-square unsteady velocity components as resolved in the streamwise and transverse directions are assembled from the instantaneous hotwire time-

series using

$$\overline{u^2} = \frac{1}{N_\mathrm{b}} \sum_{n=1}^{N_\mathrm{b}} \left(U - \langle U \rangle\right)^2, \tag{7.10a}$$

$$\overline{v^2} = \frac{1}{N_\mathrm{b}} \sum_{n=1}^{N_\mathrm{b}} \left(V - \langle V \rangle\right)^2, \tag{7.10b}$$

$$\overline{w^2} = \frac{1}{N_\mathrm{b}} \sum_{n=1}^{N_\mathrm{b}} \left(W - \langle W \rangle\right)^2, \tag{7.10c}$$

where N_b is the number of blade passages included in the average and U, $\langle U \rangle$, V, $\langle V \rangle$, etc. are the flow-aligned and transverse components defined in Section 7.1.6.

The RANS CFD predictions express the unsteady velocity data in terms of a total turbulent kinetic energy [86]

$$k = \frac{1}{2}\left(\overline{u^2} + \overline{v^2} + \overline{w^2}\right). \tag{7.11}$$

The k-ω turbulence model has been adopted when performing these RANS calculations. This model assumes isotropy so that

$$\overline{u^2} = \overline{v^2} = \overline{w^2} = \frac{2k}{3}. \tag{7.12}$$

7.4.2 Mean-square unsteady wake parameters

By way of an example, a typical mean-square velocity wake profile is sketched in Figure 7.11. The wake profile and its characteristic parameters are described below, along with descriptions of the procedures used to obtain them. Identical methods are applied to the mean-square wake profiles $\overline{v^2}$ and $\overline{w^2}$ to obtain the corresponding parameters for these velocity components.

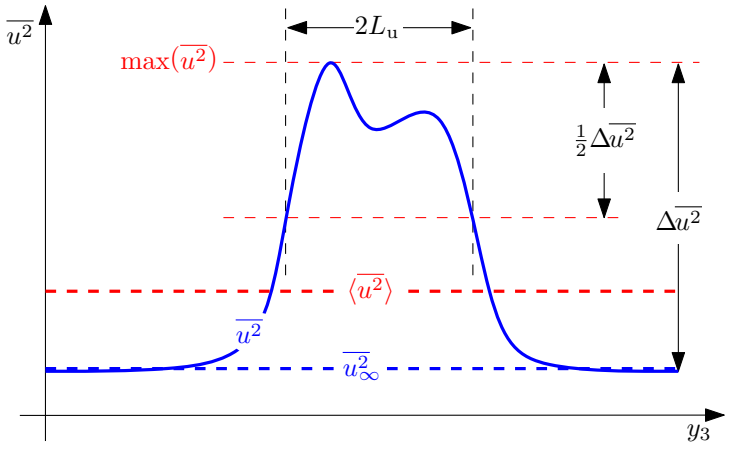

Figure 7.11 – Illustration of the characterising parameters for a mean-square turbulent velocity wake. The turbulent wake half-maximum half-width L_u is shown in relation to the peak and baseline mean-square velocities $\max(\overline{u^2})$ and $\overline{u^2_\infty}$. The circumferentially-averaged mean-square unsteady velocity $\langle\overline{u^2}\rangle$ is obtained from the mean over a blade passage.

- A two-peaked wake is shown with maximum value $\max(\overline{u^2})$. This value is obtained

by inspection of the turbulent wake profile.

- Outside the wake, the profile drops to a plateau associated with free-stream turbulence $\overline{u^2_\infty}$. This parameter is obtained by taking the mean of the values outside the extents of the turbulent wake. These extents are determined identically to the extents of the mean wake as described in Section 7.1.3.

- Half the width of the wake at the half-way point between $\overline{u^2_\infty}$ and $\max(\overline{u^2})$ is the turbulent half-wake half-width L_u.

- The circumferentially-averaged mean-square turbulence velocity $\langle\overline{u^2}\rangle$ is used as an input to the noise model described in Chapter 2. $\langle\overline{u^2}\rangle$ is obtained from the average of the turbulent wake profile over the entire blade passage.

7.5 Concluding remarks

Methods have been described for the processing of instantaneous timeseries from hotwire anemometry and ensemble-averaged mean and unsteady wake data from RANS CFD predictions. These methods allow the extraction of parameters relating to the characteristics of the mean wakes and turbulent wakes.

It is observed that for significantly overlapped mean wakes the computation of momentum thickness θ_m is subject to significant error if the effects of wake overlap are not taken into consideration. A new method for the calculation of θ_m for significantly overlapped mean wakes has been developed that has been shown to be accurate and robust to errors in the free-stream velocity U_∞.

Chapter 8

The use of hotwire anemometry and RANS CFD for the prediction of flow and turbulence characteristics

When developing a new engine it is important to be able to predict the noise it generates, preferably for several iterations of design. In the preceding chapters, models have been presented that allow the prediction of noise radiated from an OGV when a turbulent flow impinges on it from the rotor. The noise models require a description of the turbulent flow impinging on the OGV leading edge in the form of its mean flow Mach number M_s, circumferentially-averaged turbulence mean-square velocity $\langle\overline{w^2}\rangle$ and integral lengthscale Λ.

In this chapter turbulent wake parameters obtained from direct measurement on the Large Scale Fan Rig (LSFR) using hotwire anemometry and simulated using Reynolds-Averaged Navier-Stokes Computational Fluid Dynamics (RANS CFD) are compared.

Measurement of the turbulence offers the possibility of making measurements under exact operating conditions. However, it requires the construction and testing of a fan rig for each design which is time-consuming and expensive. The data in the present study are taken at a limited number of axial locations and operating points and so it is necessary to develop methods for predicting the turbulent flow parameters M_s, $\langle\overline{w^2}\rangle$ and Λ at the OGV leading edge. The measured mean wake and turbulence parameters are analysed in order to look for structure. The presence of structure relies on the wakes being in a 'self-preserving' state. The importance of such self-preserving wakes and how they are used in this analysis is discussed in Section 6.2.

RANS CFD modelling is a cheaper and faster way to obtain the required information but some degree of empiricism is needed to obtain a value for the turbulence integral lengthscale Λ. Comparison of the RANS CFD parameters with equivalent measurements allows consistent values of Λ to be obtained from RANS CFD.

The turbulent wake parameters predicted in this chapter will be used to predict forward-arc and rear-arc noise In Chapter 9.

Figure 8.1 – A test rig in the process of being installed in Test Bed III at AneCom AeroTest GmbH. This inlet-side anechoic chamber has a floor area of 1000 m^2 and is 10 m high. In the foreground an array of microphones that are used for sound power measurement may be seen (see Section 9.1).

8.1 The Large Scale Fan Rig (LSFR)

Hotwire measurements and RANS CFD simulations were performed on the Large Scale Fan Rig (LSFR). The LSFR was subjected to aerodynamic and acoustic testing on Test Bed III at AneCom AeroTest GmbH. This facility is equipped with a large anechoic chamber on the inlet side of the facility, shown in Figure 8.1, allowing forward-arc sound power measurements, that are described in Section 9.1.

The location of the rotor and OGV within the LSFR is sketched in Figure 8.2. The location of the rotor trailing edge is shown on the left hand side of the picture. Three OGV configurations are shown: a 44-vane OGV in 'forward' location with small interstage gap (red) and a 28-vane OGV in both a 'forward' (green) and 'rearward' (blue) axial location. These three OGV configurations shall be referred to as 44F, 28F and 28R. Note that the duct annulus reduces in area across the chord of the 28R OGV. This chord-wise annular contraction is common to all the OGV configurations but is only shown in the 28R axial location for the sake of clarity. The crosses show the location of the hotwire measurements, that are described in the following section.

8.1.1 Hotwire measurements on the LSFR

The axial and radial locations of downstream hotwire probes are marked in Figure 8.2 by black crosses. Groups of measurement locations were specified at three axial locations, referred to as Pos.1, Pos.2 and Pos.3. The radial measurement locations are indicated by R_i where i counts outwards from the hub. Hotwire measurements were confined to the 28-vane OGV in its rearward location (28R – blue). These tests were conducted over a range of fan speeds and working lines, as summarised in Table 8.1.

The hotwire data is in the form of instantaneous velocity timeseries recorded over many fan revolutions; each being approximately 25 s of data acquired at 192 kHz. These timeseries have been resampled so that an integral number of samples describes a single

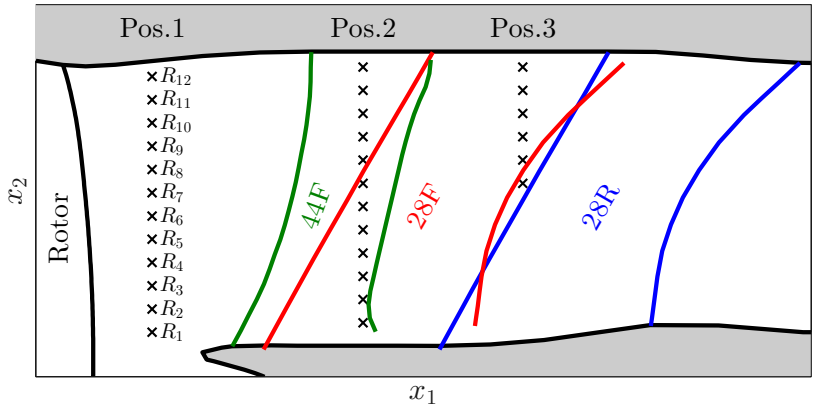

Figure 8.2 – Sketch of the LSFR in cross-section showing the rotor trailing edge, three OGV configurations and hotwire probe locations.

Table 8.1 – Configurations for which hotwire measurements were conducted.

Fan	Working	Axial location		
speed (%)	line	Pos.1	Pos.2	Pos.3
50	3	✓	✓	-
	5	✓	✓	✓
80	3	✓	-	-
	5	✓	-	-
90	3	✓	-	-
	5	✓	-	-

blade passage.

8.1.2 LSFR configurations predicted with RANS CFD

RANS CFD flow predictions for the LSFR were conducted for a range of fan speeds and working lines by John Coupland at Rolls-Royce. These predictions did not include the OGV but did include the annular contraction associated with two of the OGV configurations: 28R and 44F (see Section 8.1). A full description of the RANS CFD simulations, contributed by John Coupland, is given in Appendix B.

8.2 Comparison of normalised mean wake velocity profiles

In Section 6.2 it was noted that for wakes to be self-preserving the wake profile function $f(\eta)$ should be unchanging irrespective of where it is measured so that the mean wakes are exactly similar. In this section the level of self-similarity is assessed by the comparison of the normalised mean wake velocity profiles, defined by $(\hat{U}_\infty - \langle U \rangle)/\Delta\hat{U}$, measured at different positions using hotwire and predicted using RANS CFD.

Figure 8.3 shows comparisons between the normalised mean wake velocities derived from hotwire measurements (red lines) and equivalent RANS CFD predictions (blue lines)

plotted against $\hat{\eta}$ where (see Equation (6.3))

$$\hat{\eta} = y_3/\hat{L}_0, \tag{8.1}$$

and $\hat{L}_0$ is the half-minimum half-width of the observed mean wake, as discussed in Section 6.3.1. Similar plots are shown in Figure 8.4 for 50% and 80% fan speed over a range of radial locations. Observations with respect to these figures are given below:

1. The hotwire measurements (red lines) are seen to be affected by probe oscillations to varying degrees. Their effects are greater at 80% and 90% fan speed than at 50% and are particularly severe at 80% fan speed (Figures 8.3c, 8.4b, 8.4d and 8.4f). At these higher fan speeds the oscillations in the measured wakes leads to uncertainty over the observed mean wake parameters $\hat{U}_\infty$, $\Delta\hat{U}$ and $\hat{L}_0$ obtained using the methods described in Section 6.1. Self-preserving wake development relations, as discussed in Section 6.2, are therefore only sought for the 50% fan speed results.

2. At low fan speed the mean wake profiles predicted by RANS CFD (blue dashed lines) are similar to those measured using hotwire probes, particularly around the wake minimum (maximum in these normalised plots).

3. Similar levels of agreement at each of the two working lines are observed in Figures 8.3a and 8.3b.

4. The mean wakes profiles from Pos.1 (Figures 8.3a–8.3d) all exhibit some degree of asymmetry, with a shallower slope on their right hand side than their left. Mean loading on the rotor blades results in a favourable pressure gradient on the pressure surface that is associated with thin wakes (left hand side of wake as plotted). Adverse pressure gradients occur on the suction side of the blades resulting in greater wake thickness on the right hand side of the mean wake velocity profile.

5. The mean wakes at Pos.2 are more symmetric than the corresponding wakes at Pos.1 (compare Figure 8.3e with Figure 8.3a). At Pos.2 the measured and predicted wakes appear to be nearly sinusoidal. In these cases the observed relative wake width $\hat{\zeta} > \zeta_c$ indicates significant wake overlap as defined in Chapter 6.

6. At the outermost radial location, R_{12}, (Figure 8.4e) a significant slope is seen between adjacent wakes so that the predicted wake is almost sawtooth in shape. The slope corresponds to the ramp function identified by Majiggi and Gliebe [87] for rotor wake profiles and is due to pressure differences across the rotor blade surfaces caused by steady loading. At these outboard locations the rotor tip leakage and boundary flows lead to substantially different flows than are seen at inboard locations.

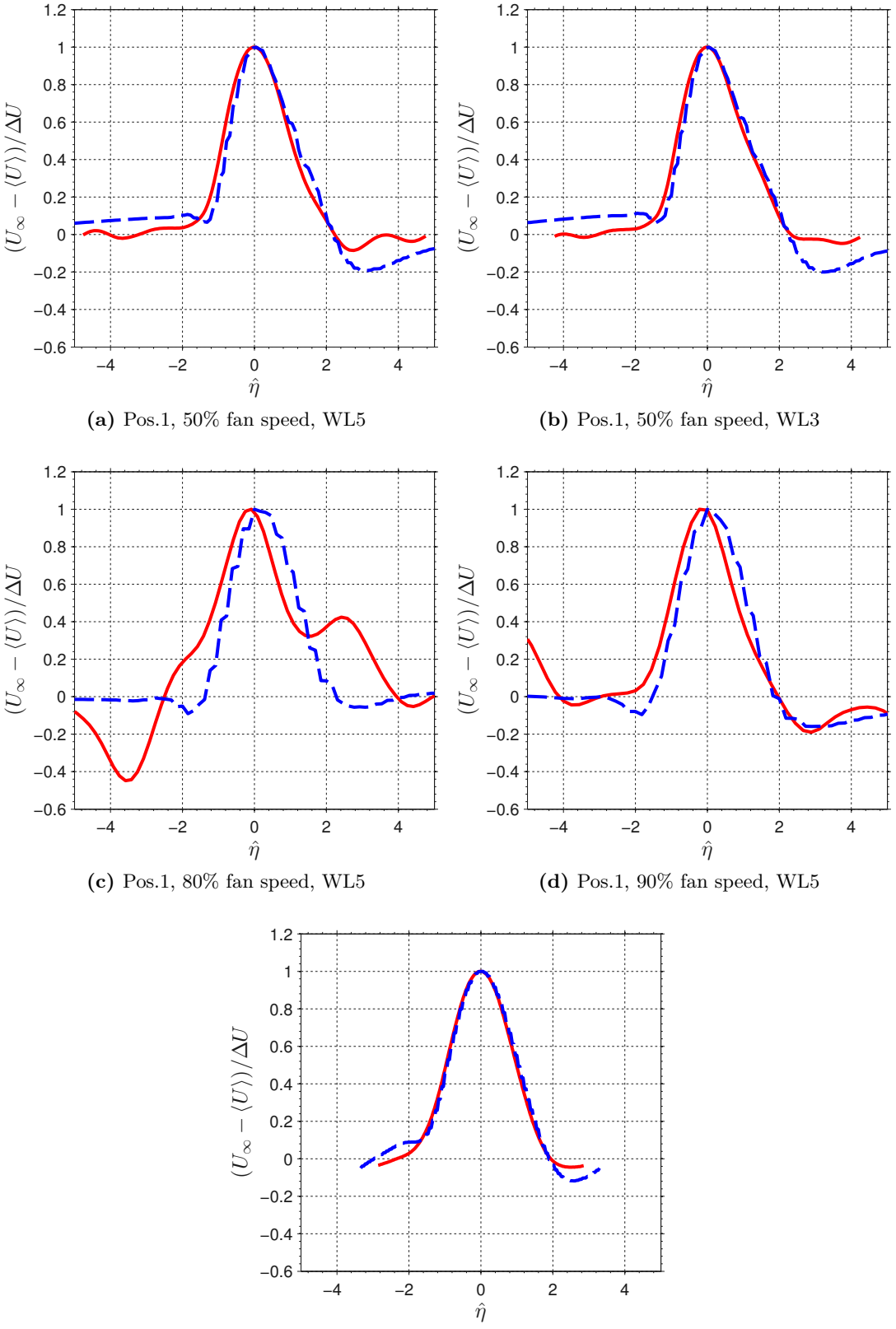

(a) Pos.1, 50% fan speed, WL5

(b) Pos.1, 50% fan speed, WL3

(c) Pos.1, 80% fan speed, WL5

(d) Pos.1, 90% fan speed, WL5

(e) Pos.2, 50% fan speed, WL5

Figure 8.3 – Comparison of normalised mean wake velocity from hotwire measurements (——) and RANS CFD extractions (– – –) at radial location R_7 showing similarity of wake profiles as axial position, fan speed and working line are altered.

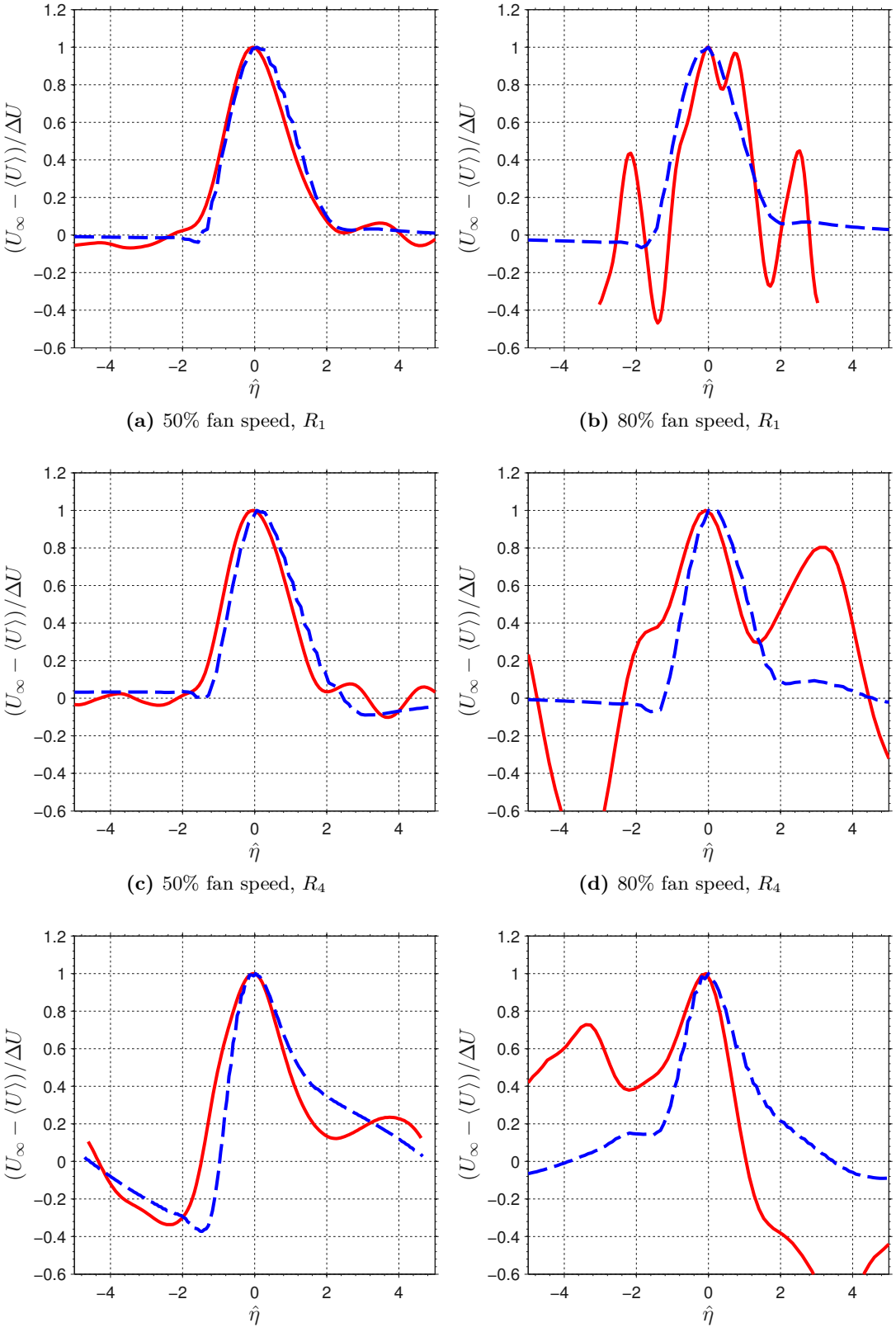

(a) 50% fan speed, R_1

(b) 80% fan speed, R_1

(c) 50% fan speed, R_4

(d) 80% fan speed, R_4

(e) 50% fan speed, R_{12}

(f) 80% fan speed, R_{12}

Figure 8.4 – Comparison of normalised mean wake velocity from hotwire measurements (—) and RANS CFD extractions (- - -) at Pos.1 at 50% and 80% fan speed at WL5 for a range of radial locations.

8.2.1 Modelling the mean wake profile function

In Section 8.2 it was observed that the RANS CFD and hotwire wake profiles measured at Pos.1 were very similar at 50% fan speed. In this section these near-wake low speed mean wake profiles are compared with the symmetric Gaussian function f_{G} and a new function f_{S} that attempts to model the observed asymmetry. The fitted wake profile function developed here is used to reconstruct individual mean wakes in order to robustly calculate momentum thickness θ_{m} in the cases where mean wakes are significantly overlapped, as described in Section 7.3.2.

Figure 8.5a shows the normalised mean wake profiles measured at Pos.1 at 50% fan speed and at both working lines plotted against normalised azimuthal distance $\hat{\eta}$ as defined in Equation (8.1). The results from all radial measurement locations are shown. Overlaid on these are non-dimensional mean wake profile functions $f(\eta)$ that may be used to model the mean wakes when used in Equation (6.2). The mean wake functions for individual blades are described below.

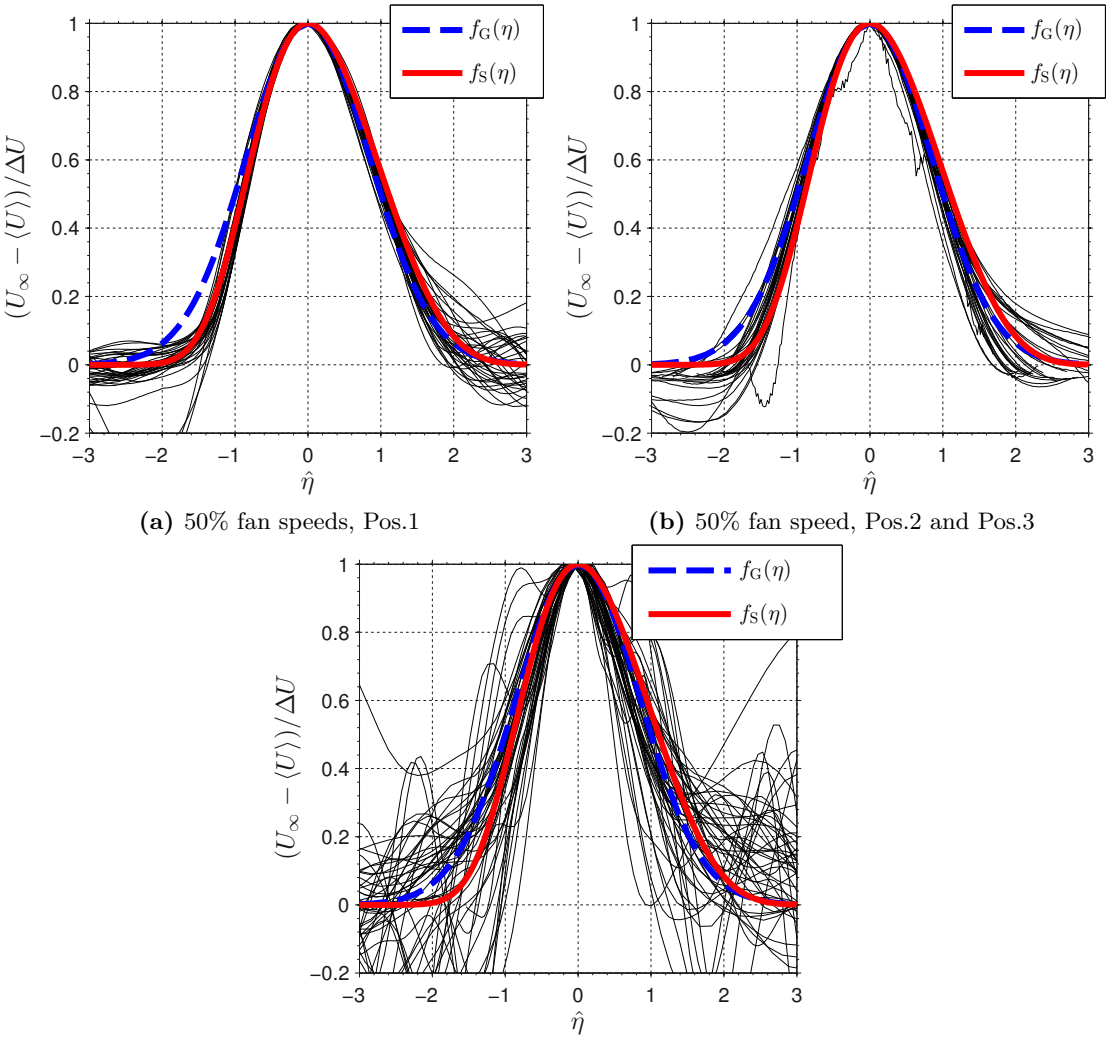

(a) 50% fan speeds, Pos.1

(b) 50% fan speed, Pos.2 and Pos.3

(c) 80% and 90% fan speeds, Pos.1

Figure 8.5 – Normalised ensemble-averaged wake profiles compared with Gaussian and skewed wake functions.

Gaussian wake profile The Gaussian function f_{G} defined in Equation (6.11) is often used to model wakes because of its simplicity and integrability and good approximation of the wake shape. For these reasons the Gaussian function is used to model the wake profile in the analysis of adjacent wake overlap in Section 6.5.

Proposed skewed wake profile Wygnanski et al. [12] measured the wakes due to symmetric wake generators in axial flows and found that the Gaussian function f_{G} overestimated the values they observed at the edges of the wake and so applied a fourth-order correction to obtain

$$f_{\mathrm{W}}(\eta) = \exp\left[-0.637\eta^2 - 0.056\eta^4\right]. \tag{8.2}$$

The wakes obtained from the LSFR hotwire data measured in near wake locations are not symmetric for the reasons noted in Item 4 on Page 130. In order to better fit to these data a skewed wake function is proposed with a third-order correction term of the form

$$f_{\mathrm{S}}(\eta) = \exp\left[-0.661\eta^2 + 0.165\eta^3 - 0.072\eta^4\right]. \tag{8.3}$$

The coefficients of the polynomial terms have been chosen to fit the shapes of the wakes measured at 50% fan speed at Pos.1, where the effects of wake overlap and probe oscillation are negligible. The fitting of these coefficients is explained in Appendix C.

Effect on observed wake profiles of axial location of hotwire probe Figure 8.5b shows a similar plot of wake profiles to Figure 8.5a at 50% fan speed but for the downstream locations Pos.2 and Pos.3 instead of Pos.1. The profiles seen at these downstream locations are more symmetric than those measured at Pos.1, being generally closer in shape to the Gaussian function f_{G} than the skewed wake profile f_{S}. This behaviour is consistent with the overlapping of adjacent wakes, as explored in Section 6.4. In Section 8.3 it will be shown that the observed relative wake width $\hat{\zeta} > \zeta_{\mathrm{c}}$ for the outer radial locations of measurements made at Pos.2 at 50% fan speed.

Effect on observed wake profiles of changing fan speeds Figure 8.5c shows the wake profiles measured at Pos.1 at 80% and 90% fan speeds. Significant disturbances associated with probe vibration are seen in the plotted normalised wakes so that they do not show collapse onto any wake profile.

8.3 Observed relative wake width $\hat{\zeta}$

Figure 8.6 shows the observed wake widths $\hat{\zeta}$ as defined in Equation (6.6) obtained from measurements at Pos.2 at 50% fan speed and both working lines shown against normalised radius $\hat{R}$ defined as

$$\hat{R} = \frac{R - R_{\mathrm{in}}}{R_{\mathrm{out}} - R_{\mathrm{in}}}, \tag{8.4}$$

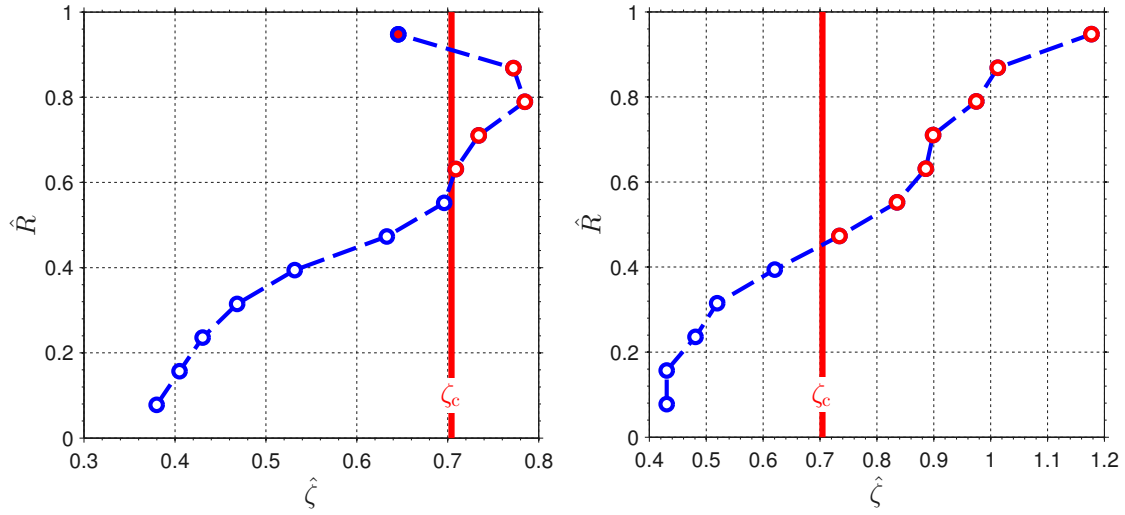

(a) Working line 5 **(b)** Working line 3

Figure 8.6 – Apparent wake width across the normalised span for mean wakes obtained at Pos.2 at two working lines. Non-overlapped measurements are indicated by blue markers while significant overlap occurs for $\zeta > \zeta_c$.

where R is the radius of the measurement point and R_{in} and R_{out} are the radii of the inner and outer casing at the axial location of the measurement point (see Figure 8.2). Note that for Pos.1 R_{hub} is assumed to lie on a line joining the radius of the splitter leading edge to the same normalised radius at the rotor trailing edge.

In each subplot the outer radial locations are seen to have $\hat{\zeta} > \zeta_c$ showing that they are significantly overlapped. The outermost radial measurement in Figure 8.6a has $\hat{\zeta} < \zeta_c$ but this measurement is affected by tip leakage and boundary layers associated with the outer casing, causing a significantly more complex mean wake shape, similar to that observed in the Pos.1 R_{12} measurement shown in Figure 8.4e.

8.4 Estimation of free-stream velocity U_∞ for significantly overlapped mean wakes

In Chapter 6 is was shown that the relative width and velocity deficit of the isolated mean wake can be inferred from measurements taken from wakes that are significantly overlapped. The method requires an estimate for the free stream velocity U_∞ that is obscured by the overlap of wakes.

Two methods for estimating U_∞ have been devised. The first attempts to use the apparent relative wake width $\hat{\zeta}$ as the basis of the prediction. This approach has been found to be too sensitive where the value of $\hat{\zeta}$ approaches unity. It is these precise conditions for which the predicted values of U_∞ are required, so that this approach of little use.

A second method applies a constant scaling factor to measurements of the free stream velocity U_∞ made at near-wake locations where mean wakes are non-overlapped and U_∞ is obtained directly.

8.4.1 Assessment of streamlines joining Pos.1 and Pos.2 measurement locations

By applying a single scaling factor to the Pos.1 values of U_∞ to estimate the Pos.2 values it is assumed that there is a 1:1 correspondence between the hotwire measurement locations in the two axial groups so that the streamline passing through, say, R_1 at Pos.1 also passes through R_1 at Pos.2. The validity of this assumption is assessed in this section.

Figure 8.7 shows streamlines obtained from hotwire measurements at 50% fan speed at the two working lines using Equation (7.2b). The working line 5 results are shown for three axial positions in Figure 8.7b while two axial locations are shown in Figure 8.7b. The streamlines originating from Pos.1 are generally found to be misaligned with the corresponding radial stations at Pos.2. The radial angles at Pos.2 and Pos.3 are small by comparison.

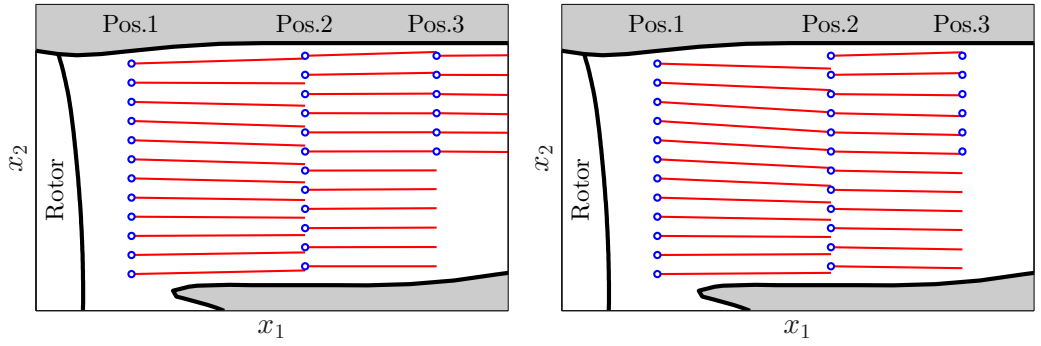

(a) Working line 5 **(b)** Working line 3

Figure 8.7 – Streamlines from measured radial flow components, fan speed 50%.

The radial flow angles ψ_r used to obtain these streamlines are 'snapshots' taken at discrete locations. The extrapolations of these angles are not likely to be representative of the streamlines over the inter-measurement distances, and may represent 'worst cases'. It shall be assumed that each radial location corresponds to its downstream counterpart.

8.4.2 Comparison of free-stream velocity U_∞ at two axial locations

In Section 8.3 it was shown that, for measurements made at Pos.2, the mean wakes are non-overlapped at inboard locations where the relative wake width is small $\zeta < \zeta_\mathrm{c}$. All mean wakes measured at Pos.1 are non-overlapped. Where the mean wakes are non-overlapped the free-stream velocity is obtained directly from the mean wake and $U_\infty = \hat{U}_\infty$.

In Figure 8.8 U_∞ obtained at the non-overlapped inboard radial locations of Pos.2 are plotted as blue circles against U_∞ obtained from the corresponding probe locations at Pos.1. These measurements were taken at 50% fan speed for two working lines, which are shown in separate sub-figures. The blue circles lie on a line of constant slope, indicating that when there is no mean wake overlap there is a constant ratio $\aleph = 0.984$ between U_∞ at the two axial measurement positions. This line is shown in red and labelled $\aleph U_\infty|_{\mathrm{Pos.1}}$.

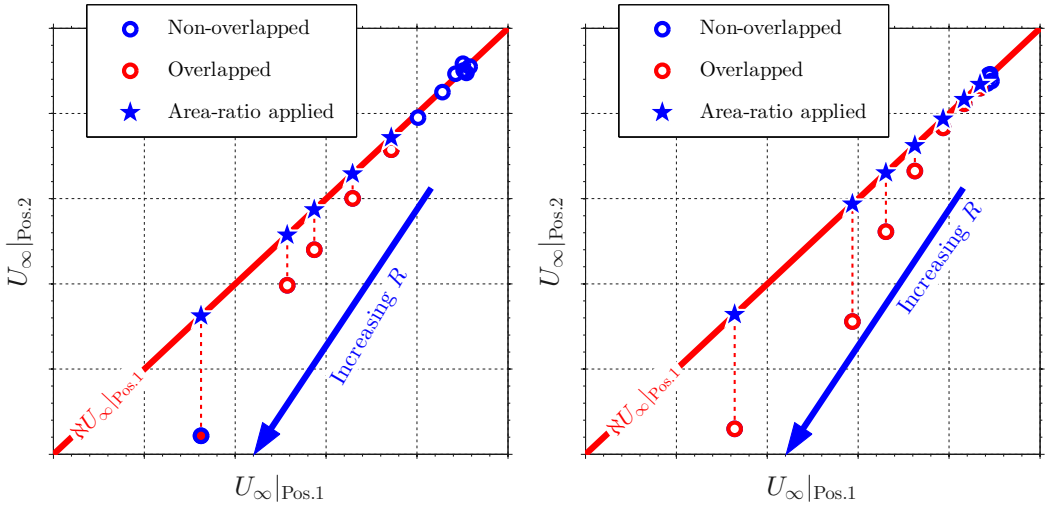

(a) Working line 5 **(b)** Working line 3

Figure 8.8 – Comparison of U_∞ as measured at Pos.1 and $\hat{U}_\infty$ at Pos.2 for fan speed 50%. Note that for the inner radii where mean wakes are non-overlapped there is good agreement between the plotted results and the fixed area-ratio line $\aleph U_\infty|_{\text{Pos.1}}$. At the outer radial positions where the Pos.2 mean wakes are significantly overlapped the values of $\hat{U}_\infty$ are reduced.

In Figure 8.8 the observed free-stream velocity $\hat{U}_\infty$ obtained at Pos.2 radial positions where the mean wakes are significantly overlapped $\zeta < \zeta_c$ are shown as red circles plotted against U_∞ obtained from the corresponding probe locations at Pos.1. These $\hat{U}_\infty$ lie below the line $\aleph U_\infty|_{\text{Pos.1}}$ which is consistent with the effect on $\hat{U}_\infty$ of significant wake overlap (see Section 6.4).

It is assumed that the flow is incompressible and that the change in U_∞ observed between Pos.1 and Pos.2 is due to the change in duct area upstream and downstream of the core/bypass splitter (see Figure 8.2). The area-ratio effect is assumed to be constant across the duct radius. Thus, the free-stream velocity U_∞ at a Pos.2 measurement point where the mean wakes are significantly overlapped is estimated by multiplying the value obtained from the equivalent Pos.1 measurement point by $\aleph$:

$$U_\infty|_{\text{Pos.2}} = \aleph U_\infty|_{\text{Pos.1}}. \tag{8.5}$$

The results obtained using Equation (8.5) are shown as black star markers in Figure 8.8. The use of Equation (8.5) yields improvements in parameter collapse and calculation of momentum thickness θ_m over the use of the $\hat{U}_\infty$.

The area of the duct is nearly constant downstream of the core/bypass splitter. It shall therefore be assumed that Equation (8.5) is applicable for all points downstream of the core/bypass splitter.

8.5 Momentum thickness θ_m from LSFR measurements

Section 7.3 examined methods for the calculation of the momentum thickness θ_m. Where the mean wakes are significantly overlapped it was shown that inaccurate values of θ_m were obtained if the mean wake overlap effects were not taken into consideration. In this section the reconstructed-wake method for the calculation of θ_m developed in Section 7.3.2 is applied to the LSFR measurements.

Figure 8.9 shows values of θ_m obtained from mean wake data measured on the LSFR at Pos.1, Pos.2 and Pos.3 at 50% fan speed and working line 5. For measurement locations where the relative wake width $\hat{\zeta} < \zeta_c$ and the mean wakes are non-overlapped Equation (7.8) was used. For measurement locations where $\hat{\zeta} \geq \zeta_c$ and the mean wakes are significantly overlapped the reconstructed-wake method given by Equation (7.9).

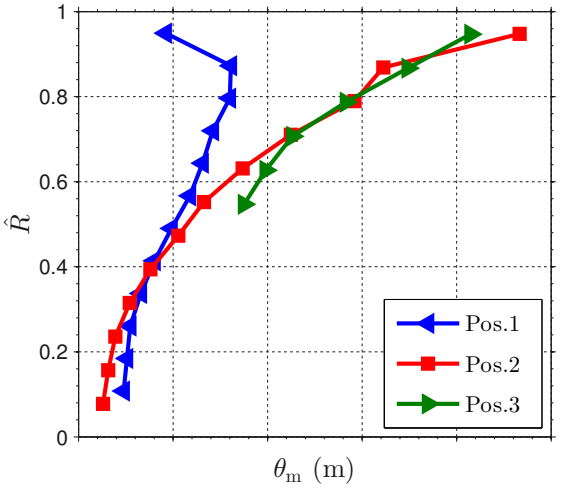

Figure 8.9 – Momentum thickness θ_m obtained from LSFR hotwire data at 50% fan speed and working line 5 at three axial locations.

1. At inboard locations ($\hat{R} < 0.5$) there is no overlap in any of the measured mean wakes. Differences between the values obtained at Pos.1 (blue) and Pos.2 (red) may be due to errors in the extracted values of U_∞, to which this method of calculation is sensitive (see Figure 7.10).

2. At outboard locations ($\hat{R} > 0.5$) mean wake overlap is seen in Pos.2 and Pos.3 axial positions but not at Pos.1. The two overlapped-wake results are in close agreement. Significant differences are seen between the Pos.1 values of θ_m and those at further downstream locations. This could be due to large wake velocity deficits in the near-wake measurement at Pos.1 as this tends to reduce θ_m for small ζ, as noted in Item 4 on Page 123.

The values of θ_m obtained at Pos.2 and Pos.3 using the reconstructed wake method of Section 7.3.2 are consistent with one another. In Section 8.11 the momentum thickness θ_m obtained using these methods is used as the normalising lengthscale allowing the self-preserving wake development relations for the LSFR to be determined.

8.6 Ensemble-averaged turbulence intensity

The ensemble-averaged mean-square turbulent velocities, $\overline{u^2}$, $\overline{v^2}$ and $\overline{w^2}$, calculated as described in Section 7.4.1 using Equation (7.10), are used to obtain the component turbulence intensities

$$T_{\mathrm{u}} = \frac{\sqrt{\overline{u^2}}}{U_\infty}, \quad T_{\mathrm{v}} = \frac{\sqrt{\overline{v^2}}}{U_\infty}, \quad T_{\mathrm{w}} = \frac{\sqrt{\overline{w^2}}}{U_\infty}, \tag{8.6}$$

where U_∞ is the free-stream velocity due to the isolated mean wake as discussed in Section 6.1. Note that T_{v} and T_{w} the transverse components are normalised with respect to U_∞ rather than their corresponding free stream velocity components which by the nature of the streamwise resolution are near zero (see Figure 7.6).

Figure 8.10 shows plots of ensemble-averaged turbulence intensity as measured at a range of axial and radial locations at working line 5 and 50% fan speed. These are normalised with the largest plotted value, the peak of Figure 8.10d. In this matrix of plots the axial position ranges from Pos.1 in the left hand column to Pos.3 in the right hand column while each row refers to a particular radial location. The colours of the lines indicate the direction of the velocity component in resolved coordinates; blue streamwise, red whirl and green radial. Also shown in black are the equivalent isotropic turbulence intensities derived from the RANS CFD data. These plots show that:

1. The shapes of T_{u}, T_{v} and T_{w} from the hotwire measurements (blue, red and green lines) are considerably different around the peaks, indicating some degree of anisotropy. This contradicts the isotropic assumption of the k-ω model adopted in RANS CFD calculations and in the noise model of Chapter 2.

2. The RANS CFD peak turbulence intensity is consistently overestimated, particularly at the upstream axial position 2. This may indicate some sensitivity of the k-ω turbulence model to flow anisotropy that a two-equation turbulence model cannot predict (see Item 1 above).

3. All axial position 2 plots, except radial location 12, show a distinct 'flat' baseline or free-stream turbulent intensity. In the RANS CFD modelling this baseline turbulence is an input parameter, which is smaller than the measured results.

4. Measurements made at radial location 12 (Figures 8.10a–8.10c) all show significant increases in turbulence intensity between wake regions, indicating that the boundary layer associated with the outer duct wall influences the measurements. Similar predictions are made by RANS CFD.

5. Measurements at the outer radial locations and axial positions 3 and 4 no longer have distinct free-stream regions. There appears to be an overlap of adjacent turbulent wakes as seen in the ensemble-averaged wakes (see Chapter 6), and the apparent free stream turbulence intensity is increased due to this overlap.

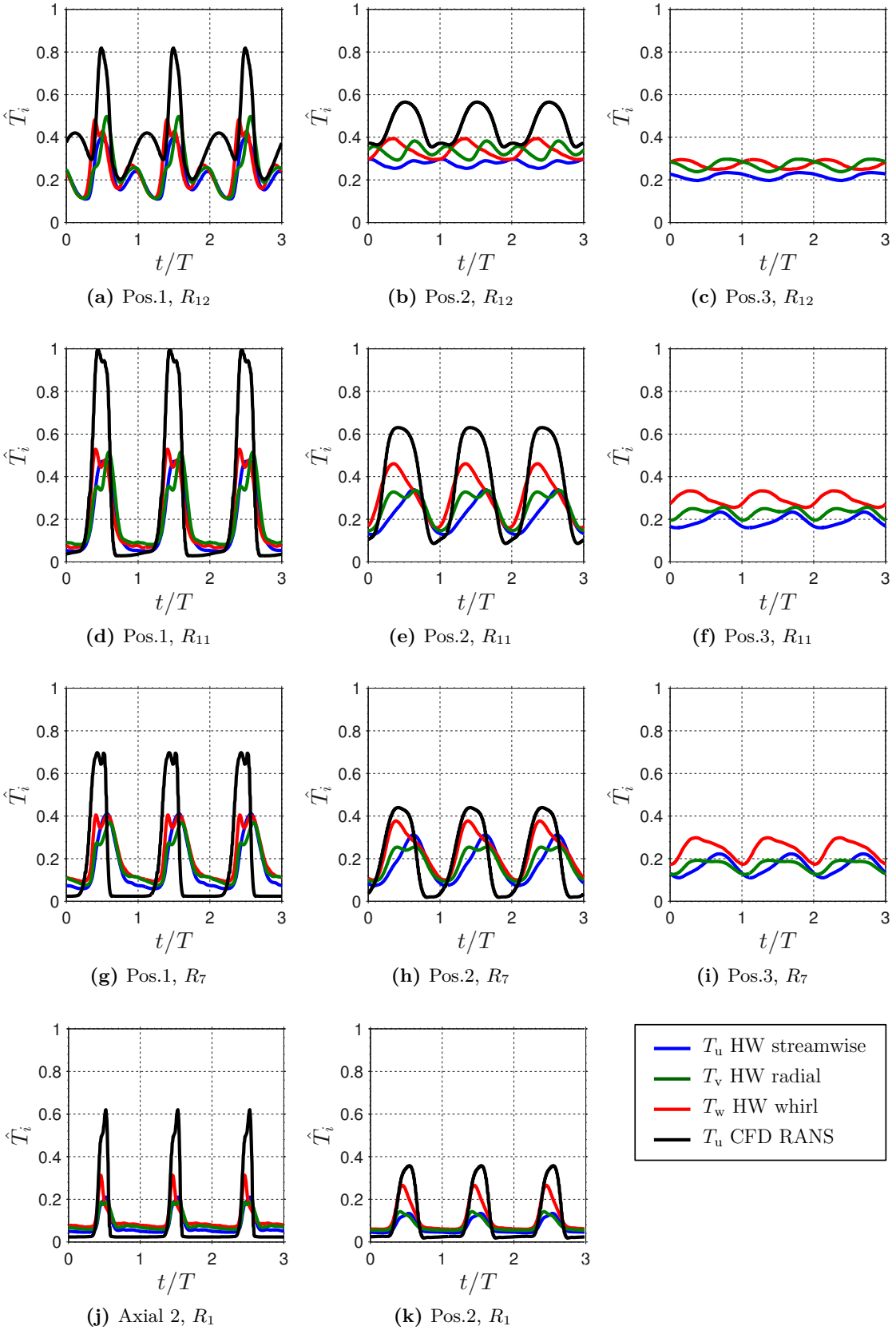

(a) Pos.1, R_{12} **(b)** Pos.2, R_{12} **(c)** Pos.3, R_{12}

(d) Pos.1, R_{11} **(e)** Pos.2, R_{11} **(f)** Pos.3, R_{11}

(g) Pos.1, R_7 **(h)** Pos.2, R_7 **(i)** Pos.3, R_7

(j) Axial 2, R_1 **(k)** Pos.2, R_1

Figure 8.10 – Plots of ensemble-averaged turbulence intensity representing a range of axial and radial locations at 50% fan speed and working line 5. Plotted value are normalised with respect to the peak value shown across the entire matrix of plots. The hotwire data have coloured lines indicating velocity component: blue streamwise, green radial and red whirl. Black lines show equivalent isotropic turbulence intensities derived from the RANS CFD data.

8.7 Turbulent velocity spectra

The velocity timeseries $U(n)$ taken from the hotwire measurements were processed to remove the ensemble-averaged velocity $\langle U \rangle$ to extract timeseries $u(n)$ relating to the unsteady components in the streamwise and transverse directions (only u component shown for the sake of brevity)

$$u(n) = U(n) - \langle U \rangle(\mathrm{mod}(n, N_j)), \tag{8.7}$$

where $\mathrm{mod}(n, N_j)$ denotes the remainder when dividing sample number n by the number of samples in a single blade passage N_j.

Figure 8.11 shows velocity PSD plots for the stream-aligned component u extracted at four radial locations. Two subplots are shown; Figure 8.11a has data measured at Pos.2, 50% fan speed and working line 5, Figure 8.11b has data measured at Pos.1, 80% fan speed and working line 3. The spectra plotted in Figure 8.11 are composites assembled from PSDs of various bandwidths in order to improve the visibility of the underlying shapes by optimising the sampling density in different frequency bands. These PSDs were obtained using Welch's method [88]. Observations are noted below.

1. The spectra shown for each fan speed and working line display a similar shape characterised by a flat section for $f \lesssim 1\,\mathrm{kHz}$ and a roll off with an approximate -2 slope for $1\,\mathrm{kHz} \lesssim f \lesssim 8\,\mathrm{kHz}$ (indicated by blue dashed line). This shape is consistent with the 1-dimensional Liepmann turbulence model used in the noise model described in Chapter 2 and defined in Equations (8.8a) and (8.8b).

2. For $8\,\mathrm{kHz} \lesssim f \lesssim 60\,\mathrm{kHz}$ a steeper roll-off with approximate -6 slope is observed (indicated by red dashed line). High frequency dissipation is characterised by exponential high frequency roll-off rather the constant gradient observed in these PSDs [89]. The observed roll-off is, however, consistent with a second order low pass filter (12 dB per octave, 40 dB per decade, -4 slope) superimposed on the existing -2 slope.

3. At very high frequencies, $f \gtrsim 60\,\mathrm{kHz}$, a large increase in level is seen in all spectra, associated with the noise floor of the rig.

4. Peaks are seen for both sets of spectra at $f \approx 7.5\,\mathrm{kHz}$, $f \approx 10.4\,\mathrm{kHz}$ and $f \approx 19.5\,\mathrm{kHz}$, their bandwidths suggesting significant damping. These peaks are greater in magnitude at 80% fan speed (Figure 8.11b). The frequency at which the tones appear is independent of the fan speed and they are believed to be associated with vibration of the hotwire probes.

5. The overall level increases with radius at low frequencies.

The results shown in Figure 8.11b indicate that parameters fitted to the spectra at higher fan speeds will be affected by hotwire probe vibration.

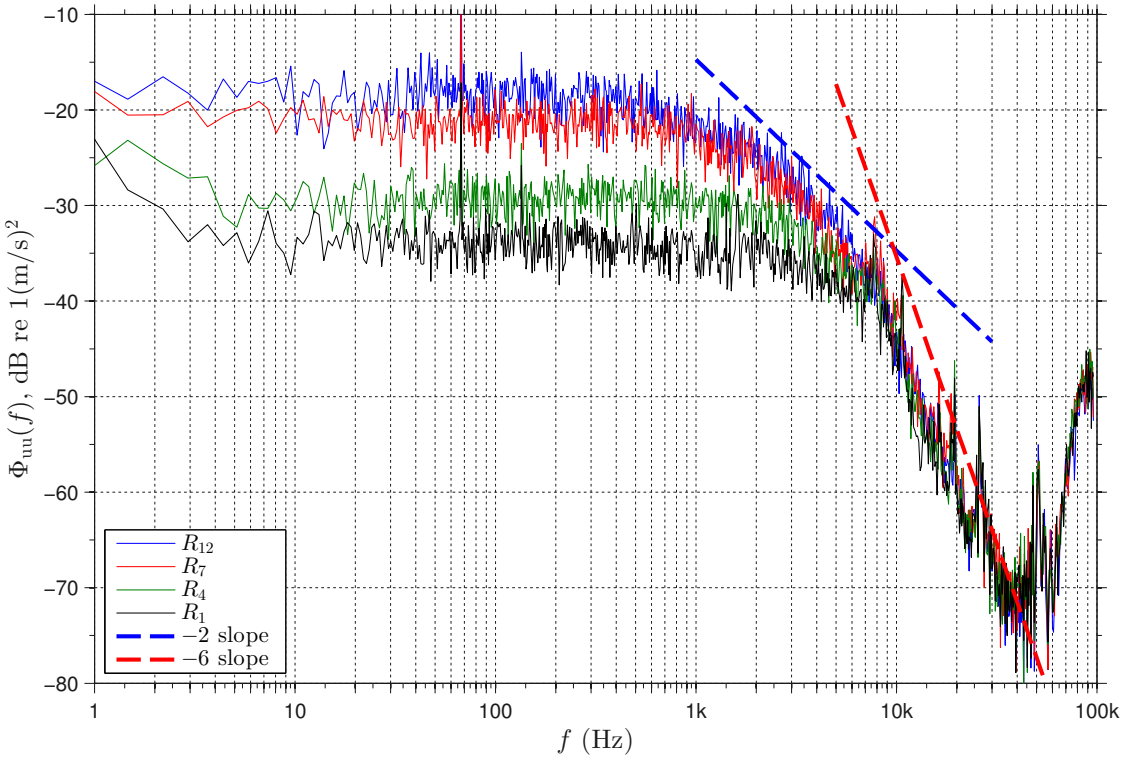

(a) Pos.2, 50% fan speed, working line 5

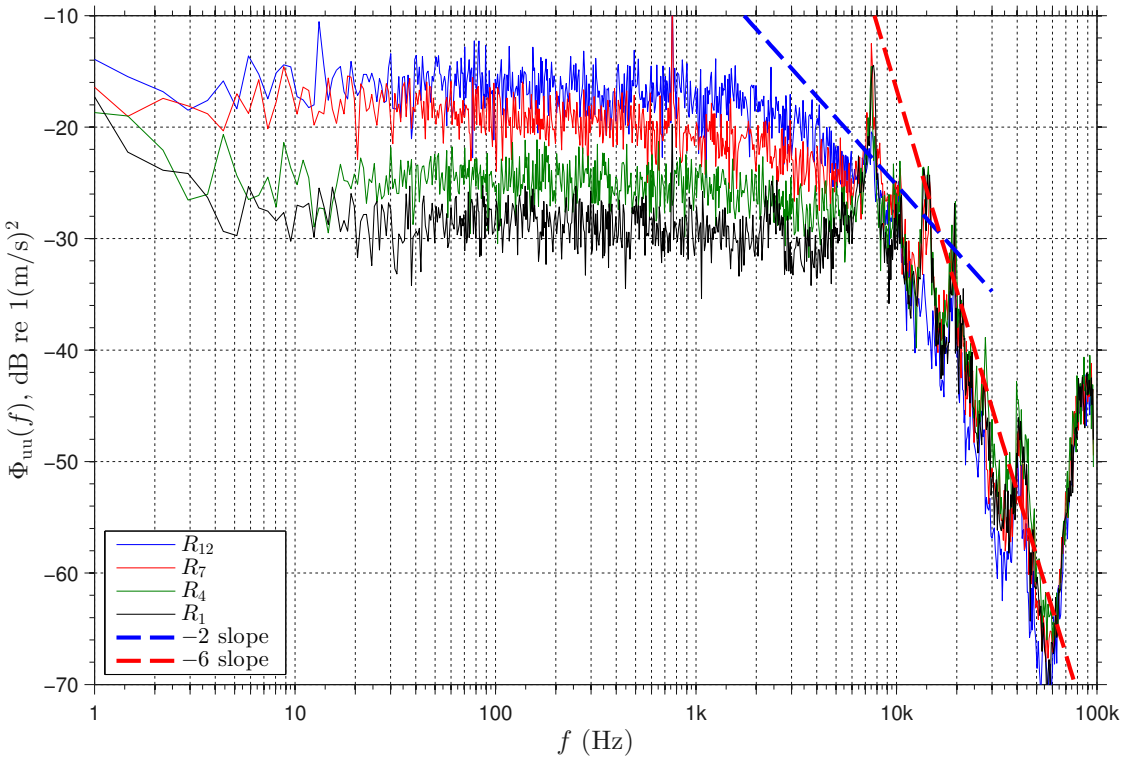

(b) Pos.1, 80% fan speed, working line 3

Figure 8.11 – Velocity PSD spectra extracted from LSFR hotwire measurements at different axial and radial positions, fan speeds and working lines. Displayed PSDs are composites assembled from a range of PSDs of differing length in order to optimise resolution and increase clarity over all frequencies. Dashed lines show the -2 slope high-frequency roll-off associated with 1-dimensional Liepmann spectrum and a -6 slope roll-off.

8.8 Assessment of the validity of the isotropic turbulence assumption

The noise model described in Chapter 2 assumes an isotropic model for the turbulence incident on the OGV. In Section 8.6 it was observed that the ensemble-averaged turbulence intensity profiles for the three velocity components exhibited different shapes, suggesting a possible lack of isotropy.

In this section, the isotropy of the turbulence in the measured wakes is assessed by deducing estimates of the turbulence integral lengthscale Λ from the component velocity PSD spectra. It will be shown that the isotropic assumption and the Liepmann model are appropriate for the rotor wake turbulence on the LSFR but that caution is required at low frequencies, where the whirl velocity component w is under-predicted by the turbulence model.

8.8.1 Turbulence integral lengthscale deduced from Liepmann isotropic turbulence model

In the noise model of Chapter 2 the turbulence impinging on the OGV is assumed to be isotropic so that the turbulence can be modelled using a single integral lengthscale Λ and component mean-square velocities $\langle\overline{u^2}\rangle$, $\langle\overline{v^2}\rangle$ and $\langle\overline{w^2}\rangle$. Equation (2.50) defines the two-dimensional Liepmann isotropic turbulence model for the blade-normal w component which has Λ and $\langle\overline{w^2}\rangle$ as inputs.

The one-dimensional Liepmann isotropic turbulence model defines the streamwise u component as

$$\Phi_{\mathrm{uu}}(f) = \frac{4\Lambda\langle\overline{u^2}\rangle}{U_\infty}\frac{1}{(1+(\Lambda k_1)^2)}, \tag{8.8a}$$

while the transverse components v and w are given by integration of Equation (2.50) over k_2 (only w shown for brevity)

$$\Phi_{\mathrm{ww}}(f) = \frac{2\Lambda\langle\overline{w^2}\rangle}{U_\infty}\frac{(1+3(\Lambda k_1)^2)}{(1+(\Lambda k_1)^2)^2}, \tag{8.8b}$$

where $k_1 = 2\pi f/U_\infty$ is the streamwise wavenumber of frozen harmonic turbulence. Note that in this thesis the isolated wake free stream velocity U_∞ is used rather than the value extracted from the observed wake $\hat{U}_\infty$ for significantly overlapped mean wakes. The length scales may be deduced by taking the low frequency limit of Equation (8.8)

$$\Lambda = \lim_{k_1\to 0}\Phi_{\mathrm{uu}}(f)\frac{U_\infty}{4\langle\overline{u^2}\rangle}, \tag{8.9a}$$

and

$$\Lambda = \lim_{k_1\to 0}\Phi_{\mathrm{ww}}(f)\frac{U_\infty}{2\langle\overline{w^2}\rangle}, \tag{8.9b}$$

where again the v component may be substituted for w without loss of generality. Due

to low frequency noise present in the measured spectra below 5 Hz (see Figure 8.11) the low-frequency limit shown in Equation (8.9) is replaced with the average of the spectrum over a significant portion of the low frequency 'flat' section, excluding any points for which $f < 5\,\mathrm{Hz}$.

At each measurement location Equation (8.9) is used to deduce a value of Λ from each velocity component timeseries u, v and w. These three lengthscales are denoted Λ_u, Λ_v and Λ_w respectively.

For isotropic turbulence the ratios $\Lambda_\mathrm{u}/\Lambda_\mathrm{v}$ and $\Lambda_\mathrm{u}/\Lambda_\mathrm{w}$ are unity. Figure 8.12 shows the ratios $\Lambda_\mathrm{u}/\Lambda_\mathrm{v}$ and $\Lambda_\mathrm{u}/\Lambda_\mathrm{w}$ plotted against the normalised radius of the measurement locations $\hat{R}$. These hotwire measurements were taken at Pos.2 at 50% fan speed. Results from working line 5 are shown as filled square markers and solid lines while working line 3 results are shown as circle markers with dashed lines.

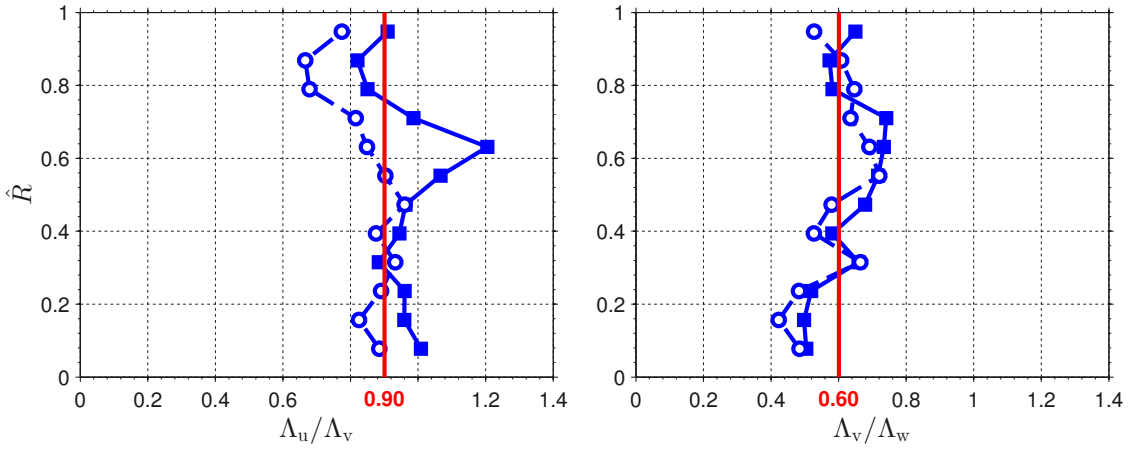

Figure 8.12 – Ratios of turbulence integral lengthscales fitted to streamwise velocity component Λ_u and transverse components Λ_v and Λ_w. For isotropic turbulence the ratios $\Lambda_\mathrm{u}/\Lambda_\mathrm{v}$ and $\Lambda_\mathrm{u}/\Lambda_\mathrm{w}$ are unity.

Across the span, the values of $\Lambda_\mathrm{u}/\Lambda_\mathrm{v}$ and $\Lambda_\mathrm{u}/\Lambda_\mathrm{w}$ do not deviate greatly from the average values of 0.9 in the case of $\Lambda_\mathrm{u}/\Lambda_\mathrm{v}$ and 0.6 in the case of $\Lambda_\mathrm{u}/\Lambda_\mathrm{w}$. The $\Lambda_\mathrm{u}/\Lambda_\mathrm{w}$ average ratio is significantly lower than the unity required for isotropy. For subsequent use the estimated value of Λ is taken to be the arithmetic mean of the three component-derived lengthscale estimates

$$\Lambda = \frac{1}{3}(\Lambda_\mathrm{u} + \Lambda_\mathrm{v} + \Lambda_\mathrm{w}). \tag{8.10}$$

In the following section the averaged value of Λ obtained from Equation (8.10) is used to assess the effect of the anisotropy observed in Figure 8.12 on the fit of the Liepmann isotropic turbulence model to the measured spectra.

8.8.2 Comparison of measured and modelled turbulence spectra

Figure 8.13 shows the three measured component velocity PSDs $\Phi_\mathrm{uu}(f)$, $\Phi_\mathrm{vv}(f)$ and $\Phi_\mathrm{ww}(f)$ normalised with respect to $\Lambda\langle\overline{u^2}\rangle/U_\infty$, $\Lambda\langle\overline{v^2}\rangle/U_\infty$ and $\Lambda\langle\overline{w^2}\rangle/U_\infty$ respectively.

These are plotted against frequency normalised with U_∞/Λ. Note that all calculations have been performed using a single power spectral density (PSD) obtained using Welch's method [88] with an FFT length of 2^{19} points but the displayed PSDs shown in Figure 8.13 are composites of several PSDs of differing resolutions to provide optimal clarity at all frequencies. Two sets of data are shown; Figure 8.13a is for data measured at Pos.2, and R_7 at 50% fan speed and working line 5, Figure 8.13b shows data from Pos.1 and R_7 at 80% fan speed and working line 3. Also shown in Figure 8.13 are the three Liepmann spectra $\Phi_{uu}(f)$, $\Phi_{vv}(f)$ and $\Phi_{ww}(f)$ (coincident with $\Phi_{vv}(f)$) generated using Equation (8.8) with the averaged value of Λ obtained from Equation (8.10).

1. At the 50% fan speed (Figure 8.13a) the streamwise and transverse Liepmann spectra are in good agreement with the measured streamwise (blue lines) and radial (red lines) spectra. The low frequency asymptotes of these components are 4 for streamwise u and 2 for radial v.

2. In Figure 8.13a the whirl component w (green line), used as the velocity spectrum in the noise model described in Chapter 2, is underestimated by a factor of nearly 2 by the Liepmann spectrum in the normalised frequency regime $\Lambda f/U_\infty < 0.1$. This underestimation of the turbulence velocity suggests that noise predictions may be underestimated by up to 3 dB for $f \lesssim 1$ kHz in rig scale.

3. At 80% fan speed (Figure 8.13b) the fit of the modelled spectra to the measured data is generally poor. The frequencies at which the high-frequency roll-off of the predicted spectra occur is too high for all three components. This is due to the broad 'tonal' peaks in the measured spectra that arise from probe vibration (see Item 4 on Page 141). These increase the calculated value of the component circumferentially-averaged mean-square velocities $\langle\overline{u^2}\rangle$, $\langle\overline{w^2}\rangle$ and $\langle\overline{w^2}\rangle$ and hence cause an underestimate of Λ (see Equation (8.9)).

4. Also in Figure 8.13b the fitted Liepmann spectrum is seen to overestimate the measured spectrum for $\Lambda f/U_\infty > 0.5$. In this frequency range the steeper -6 slope is seen in the measured spectra (see Item 2 on Page 141).

Measured turbulence velocity PSDs have been compared with isotropic turbulence spectra obtained using the Liepmann isotropic turbulence model. This comparison has shown that the Liepmann isotropic model provides a good fit to the measured spectra. However, it is observed that The Liepmann isotropic turbulence model underestimates the w component of measured turbulence at low normalised frequencies $\Lambda f/U_\infty < 0.01$ which may lead to underestimates of low-frequency noise in the noise model described in Chapter 2.

At higher fan speeds the measured spectra are contaminated by tone-like noise due to probe vibrations. These broad tonal contributions lead to an over-estimate of the

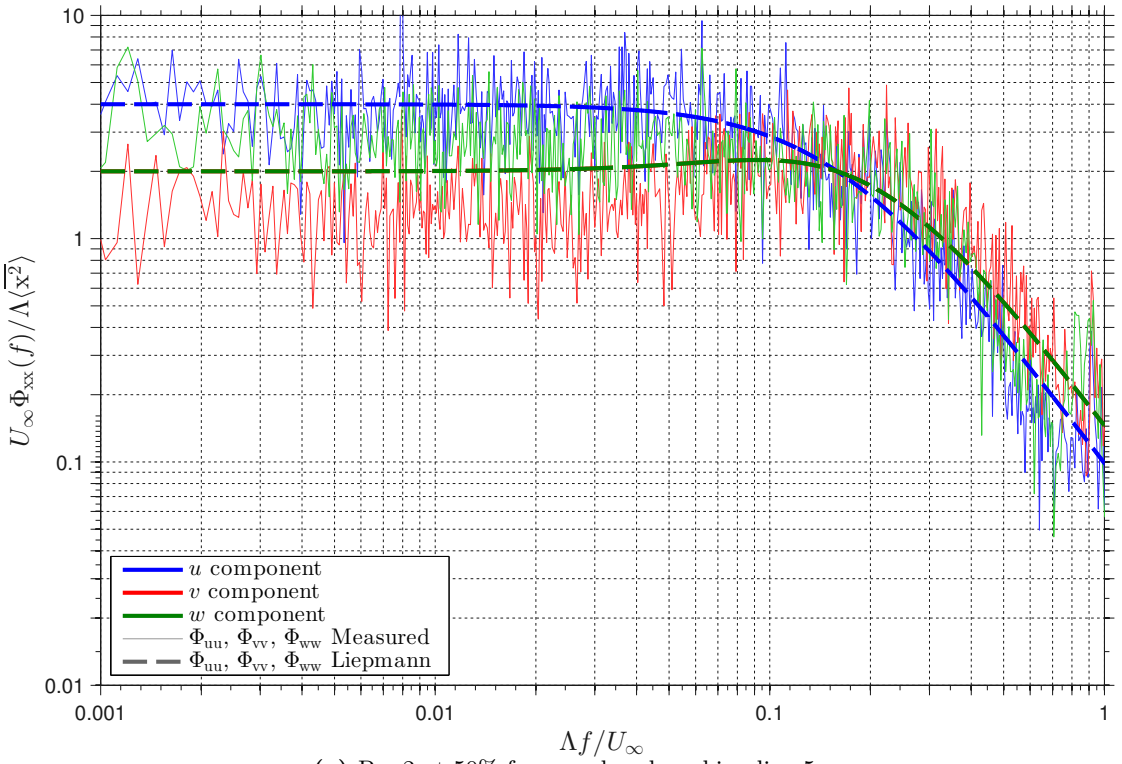

(a) Pos.2 at 50% fan speed and working line 5

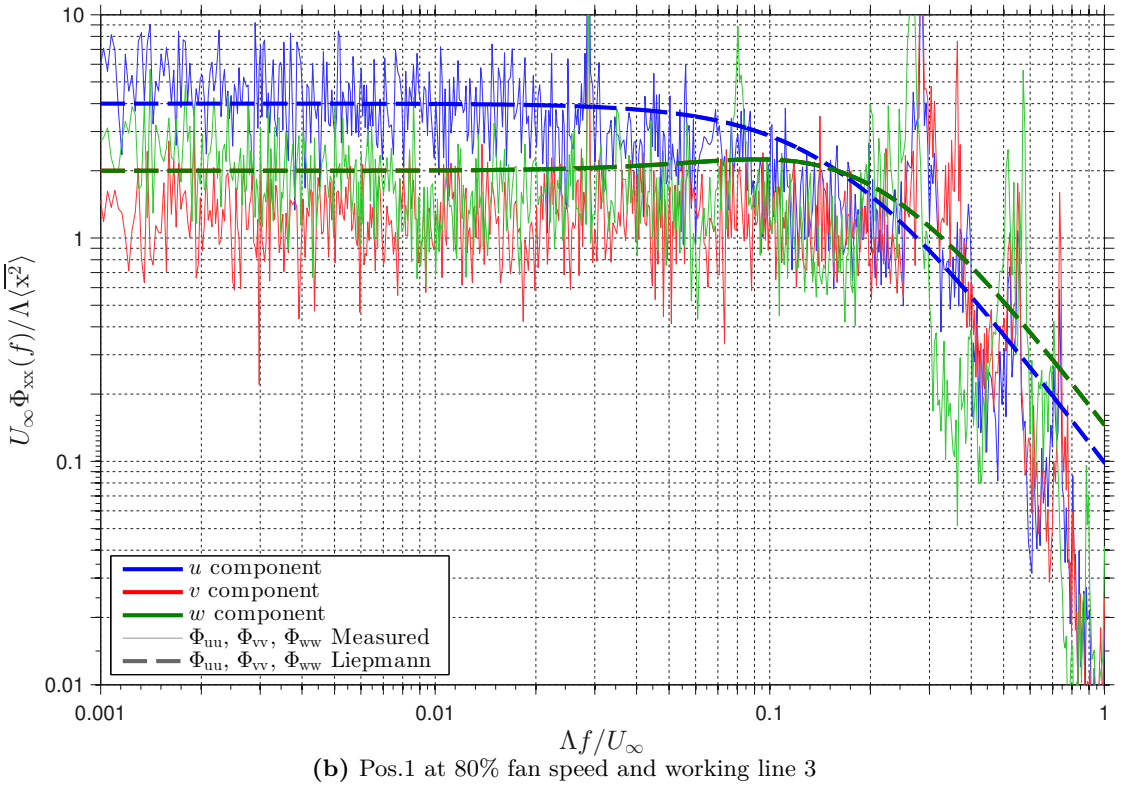

(b) Pos.1 at 80% fan speed and working line 3

Figure 8.13 – Normalised component velocity PSDs and Liepmann component velocity spectra. Hotwire data measured at different axial positions, fan speeds and working lines at R_7. Displayed PSDs are composites assembled from a range of PSDs of differing length in order to optimise resolution and increase clarity over all frequencies.

component circumferentially-averaged mean-square velocities $\langle\overline{u^2}\rangle$, $\langle\overline{v^2}\rangle$ and $\langle\overline{w^2}\rangle$ and cause underestimation of the values obtained for Λ.

8.8.3 Collapse of normalised w component velocity PSDs onto a common curve

The appropriateness of the Liepmann isotropic turbulence model is further illustrated in Figure 8.14 which shows normalised w component velocity PSDs collapsing onto a common curve. The 'shoulder' for the onset of the -2 slope is consistently located but the onset of the steeper -6 slope occurs at different normalised frequencies as the normalising frequency U_∞/Λ changes. This is consistent with low-pass filter set at a fixed frequency.

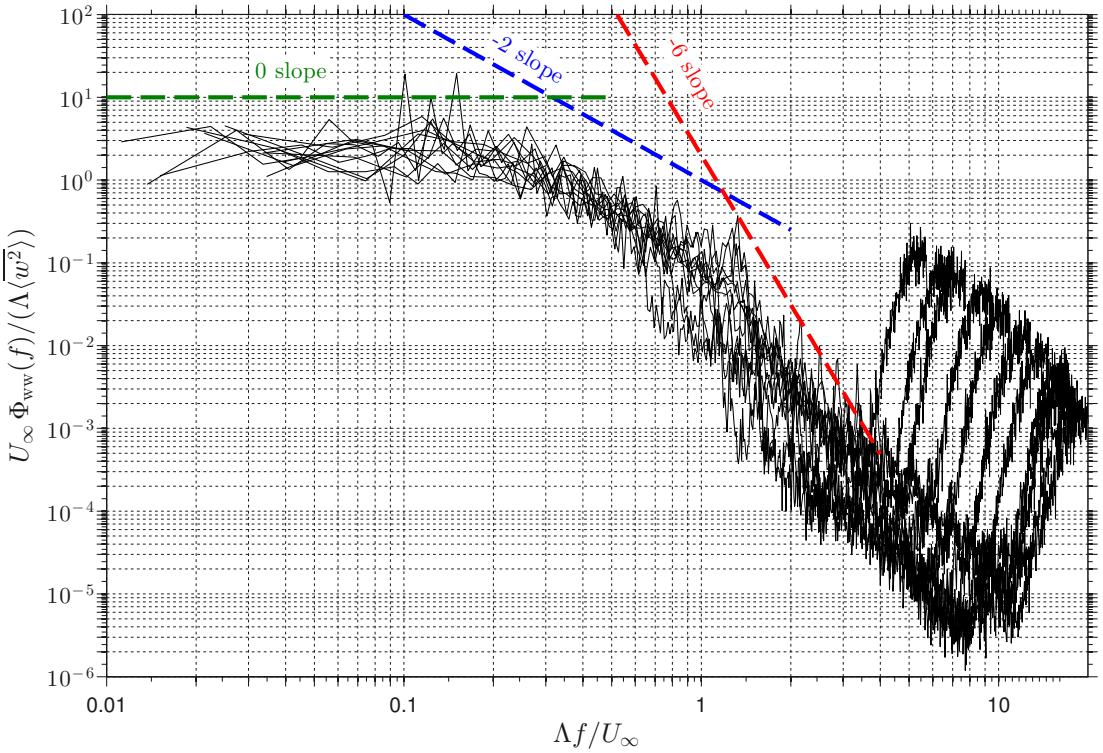

Figure 8.14 – Normalised PSDs extracted from the w velocity component at all 12 radial locations of Pos.2 at 50% fan speed and working line 3.

8.9 Determination of the natural lengthscale for wake turbulence integral lengthscale

Figure 8.15 shows values of Λ_u, Λ_v and Λ_w obtained from Equation (8.9) plotted against the normalised radius $\hat{R}$ defined in Equation (8.4). The values of Λ_u, Λ_v and Λ_w were obtained from hotwire measurements taken at Pos.2 and 50% fan speed at working lines 5 and 3. Each of the three subplots of Figure 8.15 shows Λ_u, Λ_v and Λ_w normalised with one of the three mean-wake parameters:

- The half-minimum half-width of the isolated mean wake L_0 (see Section 6.3.1),
- The half-minimum half-width derived from the observed mean wake $\hat{L}_0$,

- The width of the observed wake extent $\hat{L}_{\mathrm{WW}}$ as defined in Section 7.1.3.

The solid square markers indicate working line 5 while the white-faced circle markers and dashed lines indicate working line 3.

In Figure 8.15a the normalised values of Λ_u, Λ_v and Λ_w drop significantly towards the outer part of the span where adjacent wakes are significantly overlapped (see Chapter 6). In Figures 8.15b and 8.15c similar but smaller reductions occur in the streamwise aligned Λ_{u} and whirl components Λ_{w} when normalising with $\hat{L}_0$ and $\hat{L}_{\mathrm{WW}}$ respectively. However, in these cases the radial component Λ_{v} is seen to be reasonably constant across the span. In all cases the collapse is better when using the lengthscales $\hat{L}_0$ and $\hat{L}_{\mathrm{WW}}$ derived from the observed mean wake profile, suggesting that these characteristics of the observed mean wake are the natural lengthscales on which to scale the turbulence integral lengthscale.

8.10 Turbulence integral lengthscale from RANS CFD

In Section 8.8, turbulence lengthscales Λ were obtained from the unsteady component of the instantaneous hotwire velocity measurements from the LSFR. In this section turbulence lengthscales are defined, based on the RANS CFD solutions for the LSFR.

The RANS CFD solutions for the LSFR are based on a k-ω turbulence model where k denotes the total kinetic energy and ω represents specific dissipation (see Appendix B for a full description of the RANS CFD simulations conducted by John Coupland at Rolls-Royce). These parameters are expressed in terms of per-blade ensemble-averaged values and therefore no instantaneous velocity is available for processing as described in Section 8.8. Instead, estimates of Λ are obtained from the azimuthal average values of k and ω which are given by

$$\bar{k} = \frac{1}{N_{\mathrm{j}}} \sum_{j=1}^{N_{\mathrm{j}}} k_j, \tag{8.11a}$$

$$\overline{\omega} = \frac{1}{N_{\mathrm{j}}} \sum_{j=1}^{N_{\mathrm{j}}} \omega_j, \tag{8.11b}$$

where x_j denotes the jth sample of a parameter x and N_{j} is the number of samples representing a single blade passage. Dimensional analysis shows that the turbulence integral lengthscale can be estimated by

$$\Lambda = C_\Lambda \frac{\bar{k}^{1/2}}{\overline{\omega}}, \tag{8.12}$$

where $C_\Lambda = \mathcal{O}(1)$ is the constant of proportionality. In the following section estimates for the value of C_Λ are obtained by comparison of the results obtained using Equation (8.12) with those taken from the hotwire measurements, as described in Section 8.8.

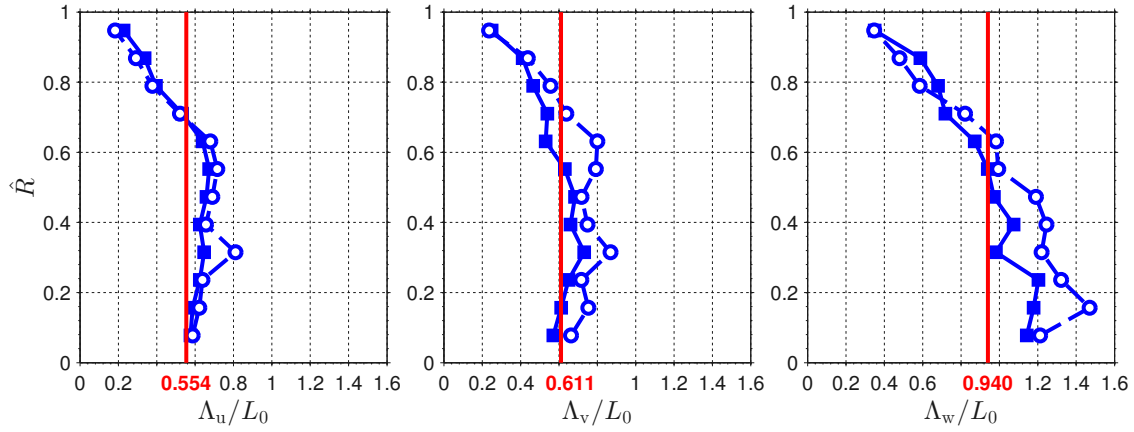

(a) Normalisation with half-minimum half-width of individual mean wake L_0

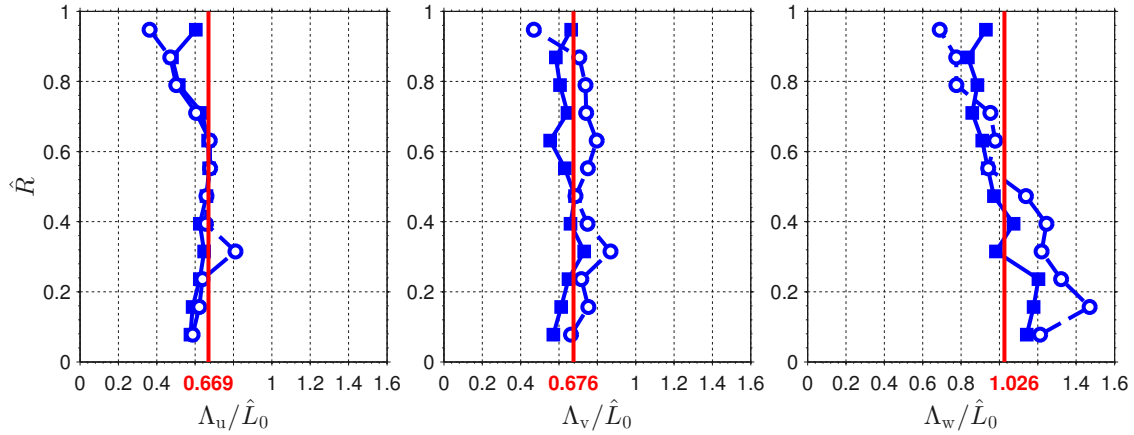

(b) Normalisation with half-minimum half-width of observed mean wake $\hat{L}_0$

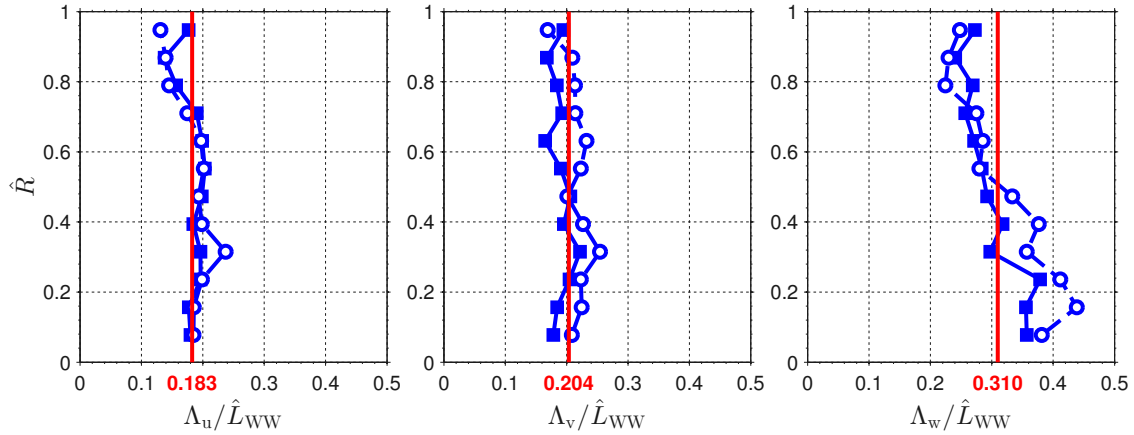

(c) Normalisation with width of observed mean wake extent $\hat{L}_{WW}$

Figure 8.15 – Comparison of measured component turbulence velocity integral lengthscales Λ_u, Λ_v and Λ_w normalised with three mean wake dimensions; L_0, $\hat{L}_0$ and $\hat{L}_{WW}$. These values of Λ_u, Λ_v and Λ_w are obtained from measurements taken at Pos.2 at 50% fan speed. Working line 5 results are shown as solid blue lines with filled square markers, working line 3 as dashed lines with white-faced circle markers. Span-wise average values are indicated by red lines.

8.10.1 Comparison of turbulence integral lengthscales and definition of RANS CFD lengthscale constant of proportionality C_Λ

In this section the turbulence integral lengthscale Λ obtained using Equation (8.12) is compared with estimates of Λ obtained using different methods. This comparison will allow the estimation of the constant of proportionality C_Λ used in Equation (8.12).

Values of Λ are compared by plotting its development against the normalised downstream distance $\hat{x}$, as defined in Section 6.1.1. In Section 8.9 it was shown that $\hat{L}_0$ was a natural lengthscale for normalisation of Λ. During the discussion of self-preserving wakes in Section 6.2 Equation (6.4a) stated that $(L_0/\theta_\mathrm{m})^2 = a\hat{x} + b$. Therefore, at least for non-overlapped mean wakes, the normalised integral lengthscale Λ should behave according to

$$\left(\frac{\Lambda}{\theta_\mathrm{m}}\right)^2 = a\hat{x} + b, \tag{8.13}$$

for some constants a and b. Note that the momentum thickness is calculated using the methods described in Section 7.3 so that the effects of mean wake overlap are accounted for.

Figure 8.16a shows a comparison between estimates of the turbulence integral lengthscale $(\Lambda/\theta_\mathrm{m})^2$ plotted against $\hat{x}$ in accord with Equation (8.13). The estimates of Λ are obtained using four methods:

1. Λ deduced from the low-frequency asymptote of the measured velocity spectrum, as described in Section 8.8.1, shown as red circle markers.

2. Λ deduced from the half-maximum half-width of the w component of the measured unsteady mean-square velocity L_w as defined in Section 7.4.2 using the relation $\Lambda = 0.42L_\mathrm{w}$ due to Jurdic et al. [22]. These values are shown as green square markers.

3. Λ deduced from the half-maximum half-width L_w due to the azimuthal profile of $\overline{w^2} = 2k/3$ predicted by RANS CFD (see Equation (7.12)) using the relation $\Lambda = 0.42L_\mathrm{w}$. These values are shown as black diamond markers.

4. Using the k-ω model with $C_\Lambda = 1$, as defined in Equation (8.12), shown as blue star markers.

Linear regression is used to fit lines $f(\hat{x}) = a\hat{x} + b$ to these data which are also shown on Figure 8.16a.

The values of Λ derived from the $k - \omega$ model used in Equation (8.12) are very small compared with those due to the other three methods, with $C_\Lambda = 6.47$ providing a good fit to the values at 50% fan speed at both working lines from axial locations Pos.1 and Pos.2, as is shown in Figure 8.16b. Λ obtained from measurements at higher fan speeds have been found to have poor linear fits and have significantly lower ratios (and hence C_Λ)

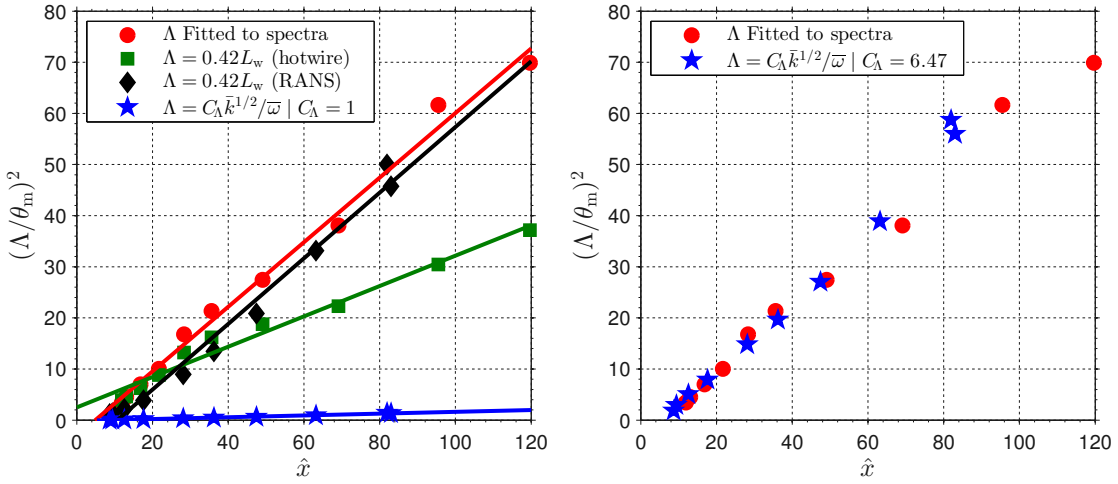

(a) Comparison of Λ obtained using various methods.

(b) Λ derived from measured spectra and using Equation (8.12) for $C_\Lambda = 6.47$.

Figure 8.16 – Comparison of turbulence integral lengthscales obtained using the methods described in Section 8.10.1. Result obtained using Equation (8.12) is in good agreement with values fitted to measured spectra for $C_\Lambda = 6.47$. Displayed data for Pos.2 at 50% fan speed and working line 5.

when compared with equivalent cases from RANS CFD. These results are consistent with the problems associated with significant probe vibrations, as observed in Section 8.8.1.

8.11 Extrapolation of mean flow and turbulent wake parameters to OGV leading edge locations

The purpose of this chapter is to obtain mean flow and turbulence parameters for the LSFR at the OGV leading edge locations for the prediction of rear-arc and forward-arc noise in Chapter 9. The RANS CFD solutions described in Section 8.1.2 have been sampled at the OGV leading-edge locations. By contrast, the hotwire measurement locations are not at the OGV leading edges (see Figure 8.2). A method must therefore be developed to predict the circumferentially-averaged mean-square turbulence velocity in the direction normal to the OGV surface $\langle\overline{w^2}\rangle$, the turbulence integral lengthscale Λ and the circumferentially-averaged mean flow Mach number M at arbitrary points downstream of the rotor. Problems with hotwire vibration mean that only the data for 50% fan speed collected at axial location Pos.2 are used for the development of this method.

8.11.1 Problems associated with the use of LSFR hotwire anemometry data and limitations of its use

Oscillations in the hotwire timeseries data and a lack of self-preserving flow at upstream measurement locations limit the scope of turbulence and flow parameter predictions made using them. These, and the impact they have on the subsequent processing of the hotwire data, are discussed below.

8.11.1.1 Oscillations in the hotwire timeseries data

The hotwire timeseries at the higher fan speeds of 80% and 90% are contaminated by oscillations due to vibration of the hotwire probe as observed in Section 8.2. Parameters extracted where oscillations are severe are too uncertain to be used. Therefore the higher fan speeds are not employed in subsequent analysis.

8.11.1.2 Lack of fully self-preserving flow at Pos.1

The rotor wakes must be fully self-preserving for there to be relationships of the form $f(\hat{x}) = a\hat{x} + b$ between each of the mean wake and mean-square wake parameters and their natural scales, such as in Equation 6.4. These development relations form the basis of the method for predicting the turbulent flow parameters at the OGV leading edge.

Figure 8.17 gives examples of the development of mean wake and mean-square wake parameters demonstrating that the mean wake parameters are self-preserving but that the mean-square parameters are not.

Figure 8.17a shows the mean wake characteristic $(U_\infty/\Delta U)^2$ plotted against $\hat{x}$. A linear response is observed, in accordance with Equation (6.4b). Close agreement is obtained between the trends in the data taken from both Pos.1 (red triangles) and Pos.2 (blue squares). It is also noted that these results are different from the results published by Wygnanski et al. [12] and Gliebe et al. [19] that are shown by magenta and cyan lines respectively. This indicates that the self-preserving flow behaviour is sensitive to the wake's initial conditions, as observed by George [14].

Figure 8.17b shows the circumferentially-averaged mean-square velocity $\langle\overline{w^2}\rangle$ normalised by the squared maximum wake deficit ΔU. For fully self-preserving flows this ratio is expected to be constant. For $\hat{x} > 40$ the Pos.2 data (blue squares) are consistent with a constant ratio. However, for $\hat{x} < 40$ the ratio is seen to increase while the Pos.1 points (red triangles) exhibit a strong dependence on $\hat{x}$ and a different overall trend to Pos.2. In the near wake this mean-square wake characteristic does not exhibit self-preservation. The rotor wakes from the LSFR are therefore only partially self-preserving for relatively small $\hat{x}$.

The Pos.3 measurements are significantly further downstream than Pos.2 and as such exhibit a greater degree of mean wake overlap. In the subsequent analysis of the rotor wakes the Pos.3 data will not be used due to the additional uncertainty associated with these measurements.

8.11.1.3 Implications of hotwire data problems

As a result of the problems with the hotwire data from the LSFR discussed earlier in Section 8.11.1 the analysis will be performed only on the 50% fan speed data recorded at the single axial location Pos.2. Thus, the variations in $\hat{x}$ are obtained through variation in

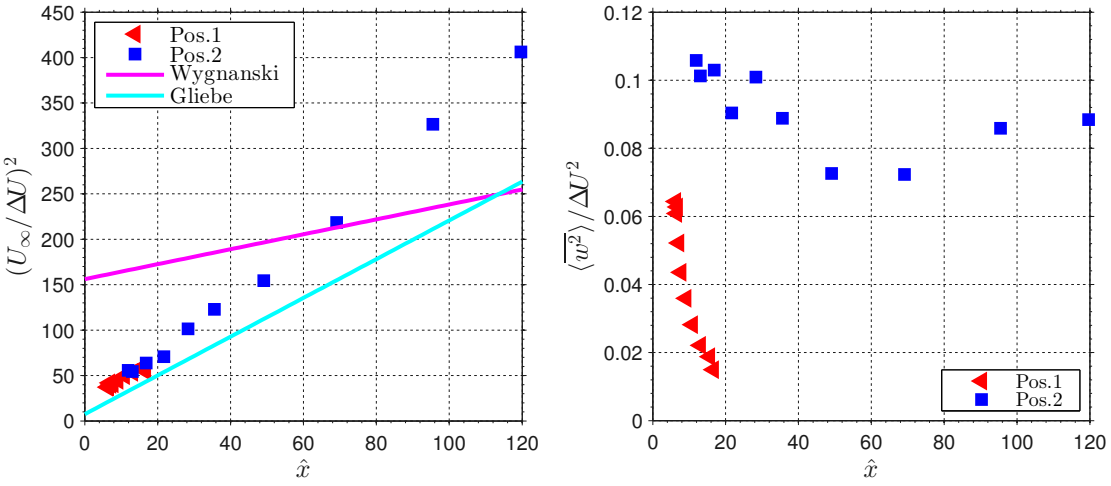

(a) Mean wake parameter: maximum wake deficit ΔU

(b) Mean-square wake parameter: circumferentially-averaged mean-square velocity $\langle\overline{w^2}\rangle$

Figure 8.17 – Examples of development of normalised mean wake and mean-square wake parameters obtained at Pos.1 and Pos.2. The mean wake parameters are consistent with self-preserving flow whilst the mean-square wake parameters are not. The flow has not become fully self-preserving at the upstream Pos.1 axial location.

θ_m rather than the dimensional downstream distance x_h. It is important to bear in mind that in the presented data $\hat{x}$ is derived from radial changes rather than axial.

Span-wise variations of the rotor geometry and flow conditions mean that it is not assured that the wakes will develop identically at all duct radii. Ideally measurements would be made at a large range of axial and radial locations downstream of the rotor, allowing the observation of wake development at different radii. In the present situation, where usable measurements are only available at a single axial location, it must be assumed that the rotor wakes develop in some universal sense. It will be shown that wake development across the span with respect to the normalised downstream distance $\hat{x}$ is consistent with that of self-preserving wakes at least at the level of mean wake parameters such as ΔU, shown in Figure 8.17a.

8.11.2 Wake development relations derived from LSFR hotwire measurements

In this section, the measurements made on the LSFR at Pos.2 are analysed to seek the self-preserving wake development relationships for the mean wake parameters L_0 and ΔU in the form $f(\hat{x}) = a\hat{x} + b$, as described in Section 6.2. The $\hat{x}$-independent ratios between the mean-square wake parameters L_u and $\langle\overline{w^2}\rangle$ and the turbulence integral lengthscale Λ and their natural scales are also sought.

Figures 8.18a–e show plots of $(L_0/\theta_\mathrm{m})^2$, $(U_\infty/\Delta U)^2$, L_u/L_0, $\langle\overline{w^2}\rangle/\Delta U^2$ and Λ/L_u against $\hat{x}$ with the individual data points for working lines 5 and 3 shown by blue squares and white-faced circles respectively. Lines of best fit, shown in red, have been obtained

from all measurements except those from R_{12} that are influenced by boundary flows from the outer casing.

The results for the mean wake parameters $(L_0/\theta_\mathrm{m})^2$ and $(U_\infty/\Delta U)^2$ (Figures 8.18a and 8.18b) collapse well onto their respective lines of best fit $f(\hat{x}) = a\hat{x} + b$ for all $\hat{x}$. This indicates both the success of the procedures developed in Section 6.5 for extraction of individual mean wake parameters from overlapped mean wakes and that the mean wakes are self-preserving.

The results for the mean-square velocity wake parameters L_u/L_0 and $\langle\overline{w^2}\rangle/\Delta U^2$ (Figures 8.18c and 8.18d) and the turbulence integral lengthscale Λ/L_u (Figure 8.18e) exhibit behaviour that is not consistent with fully self-preserving wakes, with strong $\hat{x}$ dependency observed at relatively small $\hat{x}$. Furthermore, the behaviour at the two measured working lines is seen to differ in these ranges of $\hat{x}$ so that there is a lack of universality. The wakes measured at the higher-loaded working line 3 operating condition are further from full self-preservation.

In Sections 8.11.3 and 8.11.4 the lines of best fit shown in Figures 8.18a–e are combined to allow the prediction of $\langle\overline{w^2}\rangle$ and Λ at the OGV leading edge locations, as required for inputs to the noise model described in Chapter 2.

8.11.3 Predicting circumferentially-averaged mean-square turbulence velocity $\langle\overline{w^2}\rangle$ at arbitrary $\hat{x}$

The circumferentially-averaged mean-square turbulence velocity is related to the maximum mean wake deficit by

$$\frac{\langle\overline{w^2}\rangle}{\Delta U^2} = \begin{cases} -0.00424\hat{x} + 0.252 & \text{(Working line 3 AND } \hat{x} \leq 40\text{)} \\ 0.0902 & \text{(Working line 5 OR } \hat{x} > 40\text{)} \end{cases}, \tag{8.14}$$

whilst the maximum mean wake deficit is given by

$$\left(\frac{U_\infty}{\Delta U}\right)^2 = 3.195\hat{x} + 11.95. \tag{8.15}$$

8.11.4 Predicting turbulence integral lengthscale Λ at arbitrary $\hat{x}$

The turbulence integral lengthscale Λ is related to the half-maximum half-width of the streamwise velocity component of the unsteady wake L_u by

$$\frac{\Lambda}{L_\mathrm{u}} = \begin{cases} -0.00151\hat{x} + 0.749 & \text{(Working line 3 AND } \hat{x} \leq 100\text{)} \\ 0.571 & \text{(Working line 5 OR } \hat{x} > 100\text{)} \end{cases}. \tag{8.16}$$

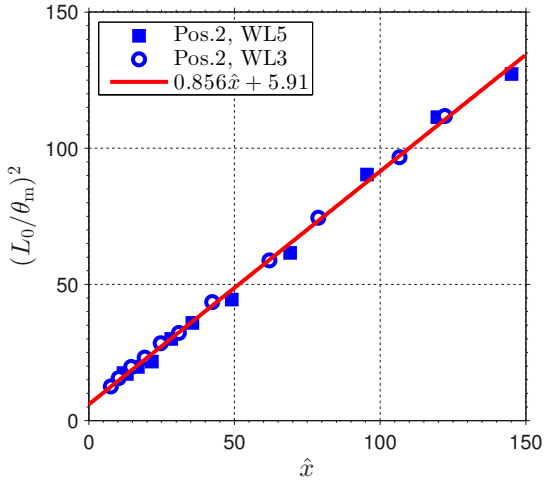

(a) Half-minimum half-width of mean wake

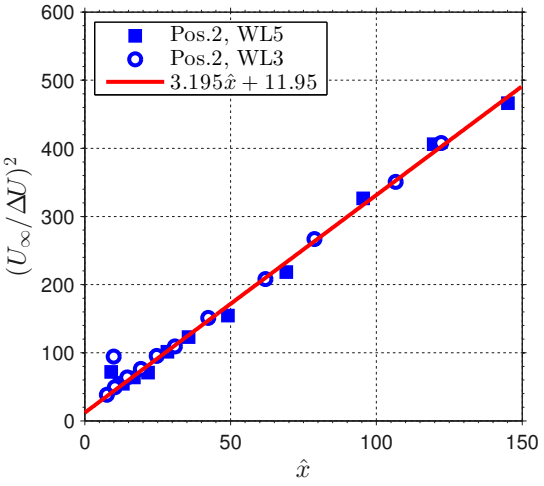

(b) Maximum wake velocity deficit

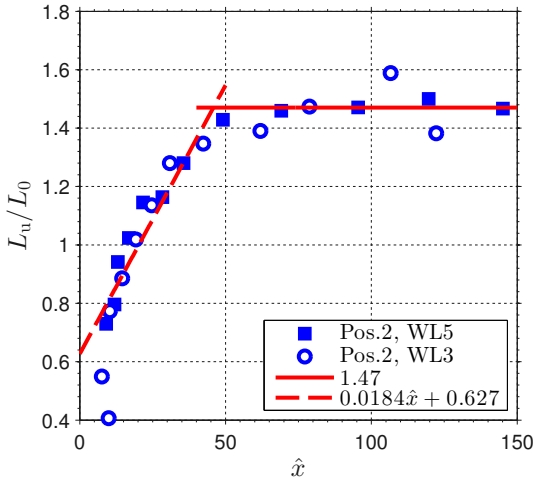

(c) Ratio of streamwise component of unsteady wake and mean wake half-wake half-widths

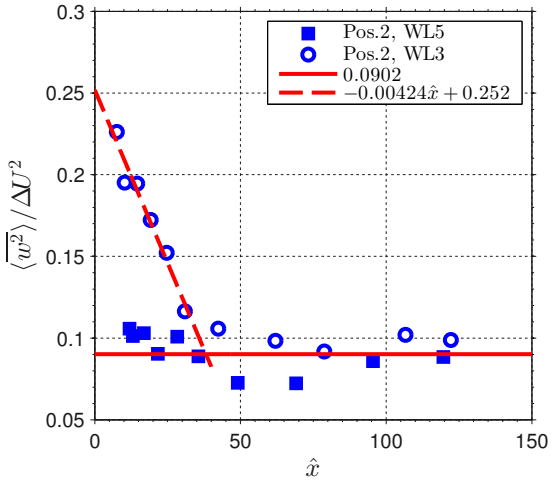

(d) Ratio of mean-square turbulence velocity and squared maximum velocity deficit

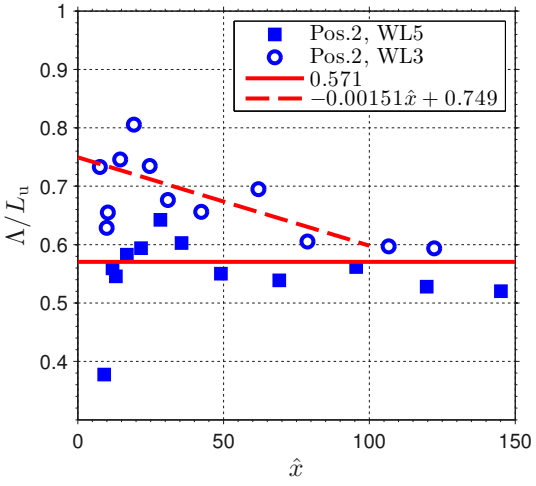

(e) Ratio of integral turbulence lengthscale and streamwise component of unsteady wake half-maximum half-width

Figure 8.18 – Relations between the wake moments used to define wake development rules.

L_u is related to the half-minimum half-width of the mean wake by

$$\frac{L_u}{L_0} = \begin{cases} 0.0184\hat{x} + 0.627 & (\hat{x} \leq 50) \\ 1.47 & (\hat{x} > 50) \end{cases}, \tag{8.17}$$

which develops according to

$$\left(\frac{L_0}{\theta_m}\right)^2 = 0.856\hat{x} + 5.91, \tag{8.18}$$

for all values of $\hat{x}$.

8.11.5 Non-dimensional downstream locations of OGV leading edges

Figure 8.19 shows the non-dimensional downstream distance $\hat{x}$ of the three OGV configurations tested during the LSFR programme against the normalised span $\hat{R}$. These values of $\hat{x}$ are obtained using Equation (6.1) for 50% fan speed. Working line 5 is indicated by solid markers and lines while working line 3 has white faced markers and dashed lines. The values of $\hat{x}$ at the hotwire locations Pos.1 and Pos.2 are also shown as black crosses. The flow angles ψ_w and ψ_r and the momentum thicknesses used in these calculations were taken from the measurements at Pos.2. Note that $\hat{x}$ generally decreases with increasing $\hat{R}$ as the momentum thickness θ_m increases at a faster rate than the helical distance x_h.

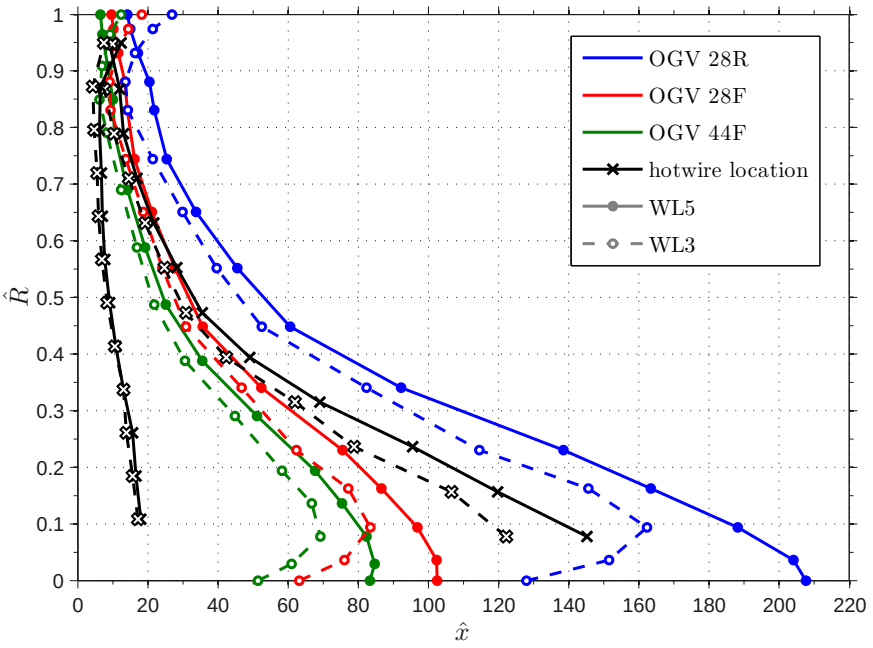

Figure 8.19 – Non-dimensional distance downstream of the three LSFR OGV configurations and hotwire locations at 50% fan speed, working lines 5 and 3.

8.11.6 Turbulent wake parameters $\langle\overline{w^2}\rangle$ and Λ predicted at OGV leading edges

The results of applying the methods shown in Sections 8.11.3 and 8.11.4 for the calculation of the turbulent wake parameters $\langle\overline{w^2}\rangle$ and Λ at the LSFR OGV leading edge locations are shown in Figures 8.20a and 8.20b. In these plots the colour of the line indicates the OGV configuration; blue for 28-vane OGV in rearward location, red for the 28-vane OGV in forward location and green for the 44-vane OGV in forward location. The solid lines with filled markers show the results for working line 5 while the white-faced markers and dashed lines denote working line 3. The values of $\langle\overline{w^2}\rangle$ and Λ measured at Pos.2 are marked by crosses, black for working line 5 and white on black for working line 3.

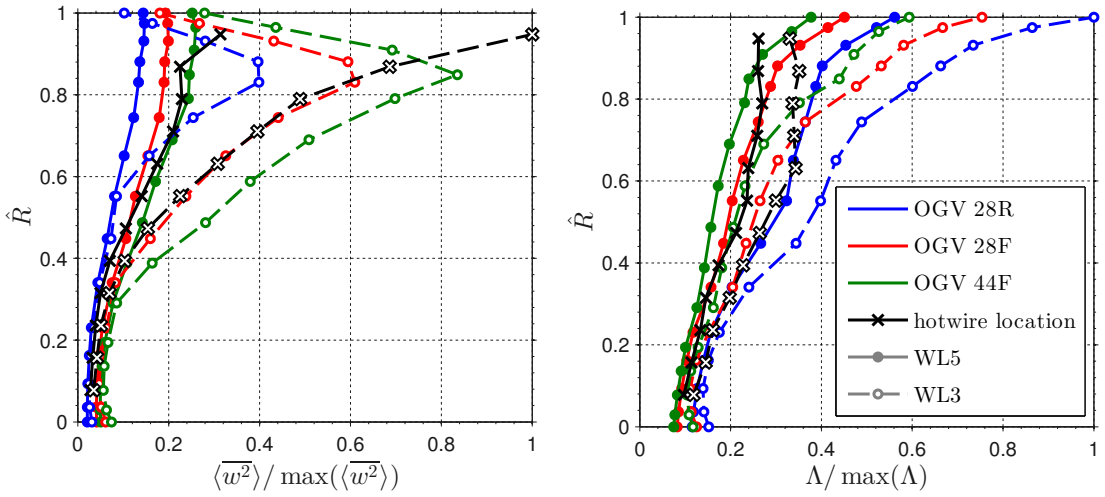

(a) Circumferentially-averaged mean-square velocity

(b) Turbulence integral lengthscale

Figure 8.20 – Turbulent wake parameters $\langle\overline{w^2}\rangle$ and Λ extrapolated to the leading edge of the three LSFR OGV configurations using the prediction rules defined in Sections 8.11.3 and 8.11.4. Values at the hotwire measurements positions are shown by black lines with cross markers.

8.11.7 Mean flow Mach number M

The circumferentially-averaged mean flow Mach number M is derived from the mean flow velocity onto the OGV

$$M = \overline{U}/c_0, \tag{8.19}$$

where c_0 is the local speed of sound. Here $\overline{U}$ is the circumferentially-averaged velocity of the observed mean wake resolved in the streamwise direction, as described in Section 6.5. This quantity is related to the individual mean wake parameters as defined in Equation (6.17) so that $M = M(\overline{U}, \Delta U, L_0)$. Assuming that at positions downstream of the core/bypass splitter the free-stream velocity U_∞ is axially invariant, (as stated in Section 8.4) M can be estimated using Equations (6.17), (8.15), (8.18) and (8.19).

Figure 8.21 shows a comparison of $\overline{U}$ obtained using this method (red) with corre-

sponding values of the apparent free stream velocity $\hat{U}_\infty$ (green) and the isolated wake free stream velocity U_∞ (blue).

- For inner radial locations $\overline{U} \approx U_\infty$. Here the mean wakes are non-overlapped and the wake deficits are relatively narrow ($\zeta << 1$), thus contributing little to the circumferentially-averaged wake velocity.
- At outer radial locations $\overline{U} \approx \hat{U}_\infty$. Here the mean wake overlap is significant and observed peak-to-trough difference $\Delta\hat{U}$ becomes small.

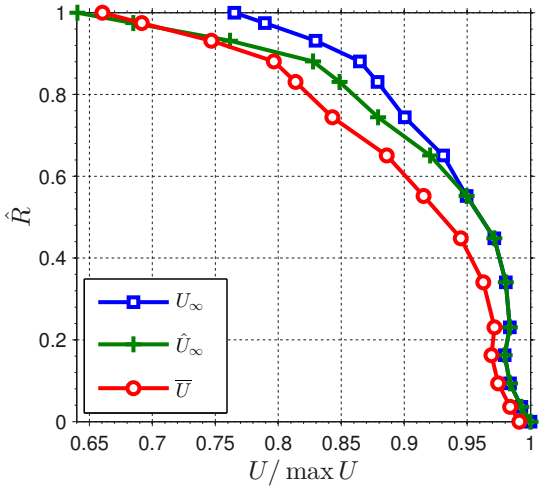

Figure 8.21 – Comparison of the values of U_∞ and $\overline{U}$ obtained from the observed and isolated mean wakes at 28R OGV leading edge at 50% fan speed and working line 5.

8.12 Verifying wake development rules by prediction of wake parameters at hotwire probe locations

In Section 8.11.2 rules were developed that allow the estimation of mean flow and turbulent wake parameters M, $\langle\overline{w^2}\rangle$ and Λ necessary as inputs for the noise model of Chapter 2. In this section these rules are verified by using them to predict the turbulent wake parameters at the hotwire measurement locations, where they can be directly verified. The effect of the observed errors on noise estimates is then estimated.

Comparisons between the predicted values and those measured are shown in Figure 8.22. The measured parameters are indicated by solid lines and markers whilst the predicted values are represented by dashed lines with white-faced markers. Working line 5 is shown in blue while working line 3 is in red.

Normalised errors are calculated using

$$\varepsilon = \frac{(x_{\text{pred}} - x_{\text{meas}})}{x_{\text{meas}}}, \tag{8.20}$$

where x_{pred} and x_{meas} indicate the predicted and measured values of parameters respectively. Statistics have been extracted from the normalised errors for these predictions and

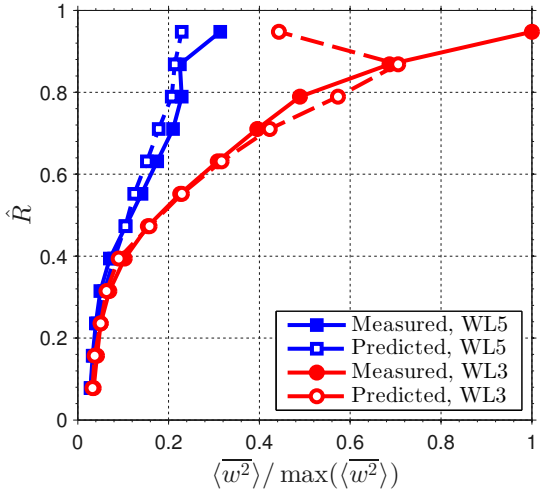

(a) Circumferentially-averaged mean square upwash velocity $\langle\overline{w^2}\rangle$, Pos.2

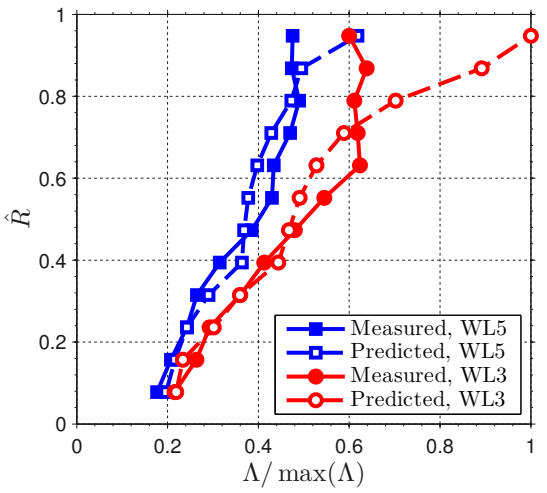

(b) Turbulence integral lengthscale Λ, Pos.2

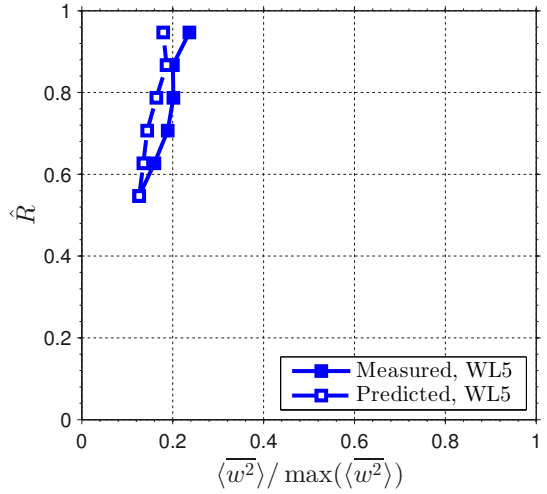

(c) Circumferentially-averaged mean square upwash velocity $\langle\overline{w^2}\rangle$, Pos.3

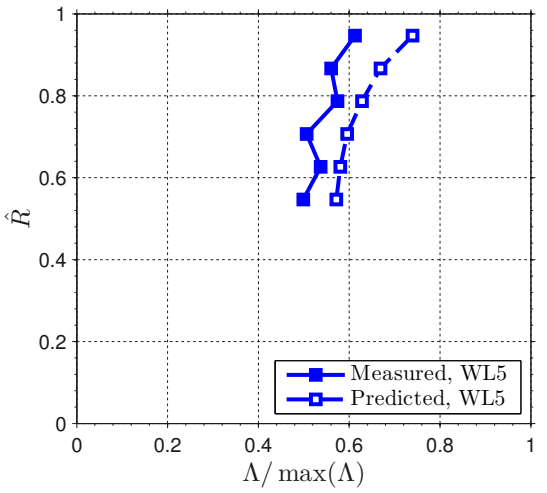

(d) Turbulence integral lengthscale Λ, Pos.3

Figure 8.22 – Comparison of measured turbulence and values predicted at hotwire axial locations Pos.2 and Pos.3 using the rules defined in Section 8.11.2. Note that the scales of Pos.2 and Pos.3 plots are normalised with the maximum values shown for both Pos.2 and Pos.3.

Table 8.2 – Statistics of the normalised prediction errors.

Location	Working line	max $\lvert\varepsilon\rvert$		$\overline{\varepsilon}$		σ_ε	
		$\langle\overline{w^2}\rangle$	Λ	$\langle\overline{w^2}\rangle$	Λ	$\langle\overline{w^2}\rangle$	Λ
Pos.2	5	(-)0.270	0.301	-0.0298	0.0318	0.124	0.116
	3	(-)0.557	0.667	-0.0532	0.0743	0.173	0.226
Pos.3	5	(-)0.242	0.207	-0.148	0.150	0.0879	0.0480

are listed in Table 8.2.

- The circumferentially-averaged mean-square velocity $\langle\overline{w^2}\rangle$ is generally under-predicted while the integral lengthscale Λ is generally over-predicted.
- Significantly smaller errors are observed at Pos.2 than at Pos.3. The Pos.2 measurement data were used to define the prediction rules (see Section 8.11.2) and therefore errors in the Pos.2 values represent the goodness of fit of the rules applied to the predictions. However predictions at Pos.3 require a significant extrapolation of the data and larger errors are to be expected.

The accuracy of the predicted values of $\langle\overline{w^2}\rangle$ and Λ is critical to the subsequent noise predictions in which the parameters are used as input quantities. The effects on noise predictions of the mean errors $\bar{\varepsilon}$ at Pos.3 recorded in Table 8.2 are estimated below:

- The mean error $\bar{\varepsilon} = -0.148$ in $\langle\overline{w^2}\rangle$ represents a change of $\approx -0.7\,\mathrm{dB}$ with respect to the measured values. A change of $\approx -0.7\,\mathrm{dB}$ is expected in the noise spectrum.
- The mean error $\bar{\varepsilon} = 0.150$ in Λ will increase low-frequency sound power by $\approx 0.7\,\mathrm{dB}$ and decrease high frequency sound power by $\approx -0.7\,\mathrm{dB}$ (see Section 3.2.6).

The combined effect of the mean errors in $\langle\overline{w^2}\rangle$ and Λ is to decrease high frequency sound power by $\approx -1.4\,\mathrm{dB}$. The distinction between low and high frequency is the 'shoulder' of the turbulence spectrum, which at rig scale is approximately 1 kHz.

8.13 Comparison of parameters predicted using hotwire prediction method and using RANS CFD

In this section comparison will be made between the mean flow and turbulent wake parameters obtained using the rules defined in Section 8.11 and from RANS CFD extractions.

Figures 8.23 and 8.24 show radial variations of $\overline{U}$, Λ and $\langle\overline{w^2}\rangle$ at 50% fan speed. Figure 8.23 shows predictions made at the leading edge of the 44F OGV at working line 3 and Figure 8.24 shows predictions made at the leading edge of the 28R OGV at working line 5. The predictions made using the hotwire-based method described in Section 8.11 are shown in red with cross markers, the predictions made using RANS CFD are shown in blue with circle markers.

In Figure 8.23 all three parameters $\overline{U}$, Λ and $\langle\overline{w^2}\rangle$ are in good agreement across the span. At the tip the estimates of Λ diverge but they are closely matched inboard. The RANS prediction of $\langle\overline{w^2}\rangle$ is larger than that from the hotwire method but the shapes of the two span-wise predictions are similar.

In Figure 8.24 the circumferentially-averaged velocity $\overline{U}$ is closely matched from RANS and hotwire data but larger differences are observed between the prediction methods in Λ and $\langle\overline{w^2}\rangle$. In particular, the predicted span-wise shapes are less similar than were seen in Figure 8.23.

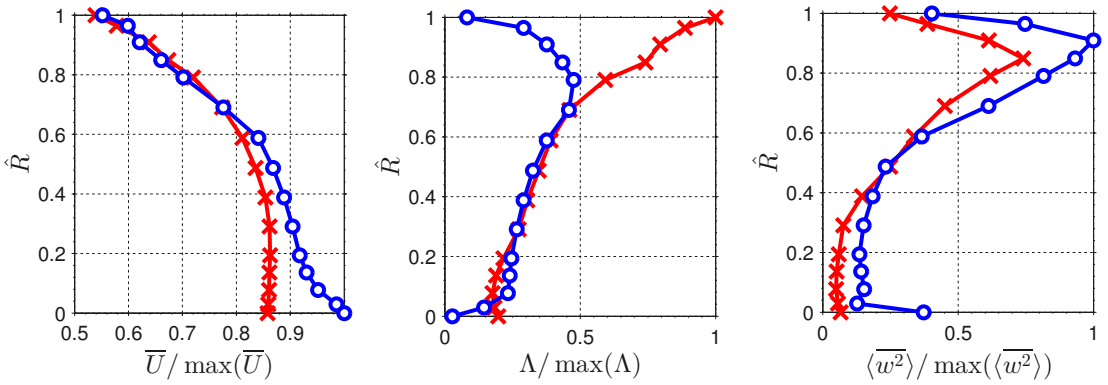

(a) Mean velocity onto OGV **(b)** Turbulence lengthscale **(c)** Mean-square velocity

Figure 8.23 – Noise model input parameters from RANS CFD and hotwire prediction method compared. Predictions for 44F OGV at 50% fan speed and working line 3. Line types indicate data source: Hotwire (—×—), RANS CFD (—○—).

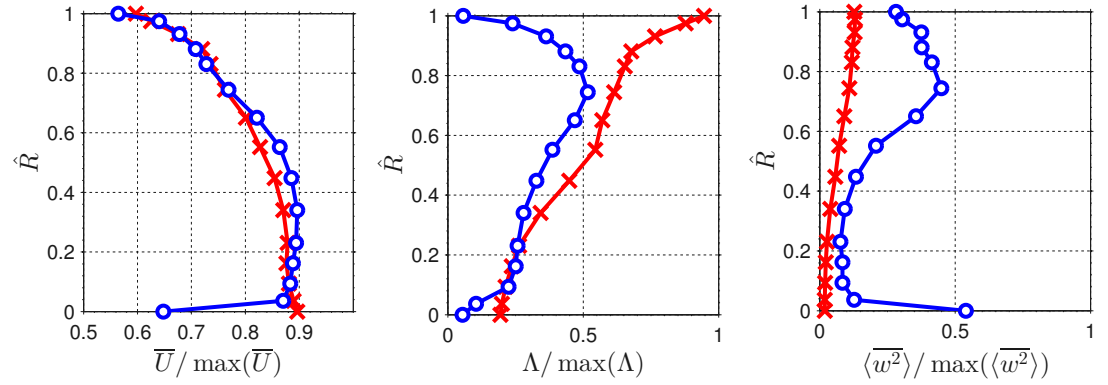

(a) Mean velocity onto OGV **(b)** Turbulence lengthscale **(c)** Mean-square velocity

Figure 8.24 – Noise model input parameters from RANS CFD and hotwire prediction method compared. Predictions for 28R OGV at 50% fan speed and working line 5. Line types indicate data source: Hotwire (—×—), RANS CFD (—○—).

8.14 Concluding remarks

The main conclusions arising from this chapter are summarised below:

- An analysis of hotwire anemometry data recorded on the Large Scale Fan Rig (LSFR) has been performed and comparisons are made with RANS CFD solutions based on the LSFR geometry.
- Large amplitude oscillations are present in the data recorded at higher fan speeds (80% and 90%), believed to be associated with vibrations of the hotwire probes. Mean wake parameters and parameters fitted to spectra extracted from these data are subject to uncertainty.
- Measurements taken at Pos.2 and Pos.3 exhibit characteristics consistent with the overlapping of adjacent mean wakes. Wake overlap obscures the development of the individual mean wakes, which has been assumed to be unaffected by the phenomenon. A method has been developed to deduce the individual wake maximum wake deficit ΔU and relative wake width ζ where the relative wake width is large: $\hat{\zeta} > \zeta_c = 2^{-1/2}$.
- Measured and RANS-predicted mean wakes are asymmetric and a mean wake profile function has been suggested which provides a good fit to the measured data.
- Data measured at Pos.1 show that the flow is not fully self-preserving at such near-wake locations. Collapse of the Pos.1 data with those from Pos.2 is not possible except for the mean wake parameters. Data measured at Pos.2 and Pos.3 show some collapse of mean-squared wake parameters, but only for $\hat{x} \gtrsim 80$, indicating that the wakes are partially self-preserving. The onset of self-preservation is delayed by the increased loading at working line 3.
- The isolated wake data extracted from Pos.2 measurements taken at 50% fan speed have been analysed to determine the self-preserving wake development relations. These relations been used to predict the turbulence parameters at OGV leading edge locations.
- A large range of $\hat{x}$ values are required to capture the full range of helical distances between rotor trailing edge and OGV leading edge.
- The observed wake development for the LSFR differs significantly from that published by Gliebe et al. [19]. This indicates that the evolution of the rotor wakes is sensitive to the initial conditions and that there is not 'universal' wake rule, supporting the findings of Wygnanski et al. [12] and George [14].
- Turbulence lengthscales have been found to be nearly proportional to the width of the mean wake profile, which is consistent with the findings of Ganz et al. [5](p.98). However, Gliebe et al. [19] found that the ratio of lengthscale to mean wake width tended to decrease with normalised downstream distance ([19](Figures 36–38)).

- RANS CFD solutions have been compared with hotwire data and predictions of flow and turbulence characteristics at OGV locations.
- RANS predictions of the maximum velocity deficit ΔU are over-predicted by as much as 100% in the near wake region but improves for measurements made further downstream.
- RANS predictions of the free-stream velocity U_∞ are within 10% of the measured values.
- Predictions of turbulence lengthscale Λ obtained using RANS CFD by the use of an k-ω model agree with the values obtained from hotwire measurements at 50% fan speed measured within a factor of $C_\Lambda = 6.47$ which appears to be reasonably constant across different working lines and measurement locations.

Chapter 9

Application of noise models to the prediction of experimental noise

Earlier chapters have presented methods for the prediction of the noise resulting from turbulence interactions with downstream stator vanes, the acoustic transmission through a spinning rotor and rotor wake turbulence parameters at the OGV leading edge. This chapter shall describe the application of these methods to predict the sound power generated by the Large Scale Fan Rig (LSFR) introduced in Chapter 8. The resulting sound power predictions will be validated against experimental noise measurements taken on the same rig. The chapter shall commence with a description of the methods used to combine the models.

9.1 Experimental sound power measurements on LSFR

Noise measurements were taken on the LSFR using two arrays of microphones, one set located in an anechoic chamber forward of the rig and a second set embedded in the hard-walled bypass duct as illustrated in Figure 9.1.

The anechoic chamber and forward arc array have been used to provide sound power spectral measurements with a 100 EO bandwidth at 1/4 EO resolution for a number of combinations of fan speed and OGV configuration at a single working line. The inlet was lined and so a correction must be applied to the predicted sound power to include the reduction is sound power due to the duct liner. The details of this correction are described in Section 9.2.8.

Insufficient microphones are used in the duct by pass to perform a full modal decomposition and hence accurately deduce the sound power. The sound power level is inferred from the mean square pressure at the duct wall by assuming that each of the propagating duct modes has equal sound power. Details of this procedure for deducing sound power are given in Appendix D.

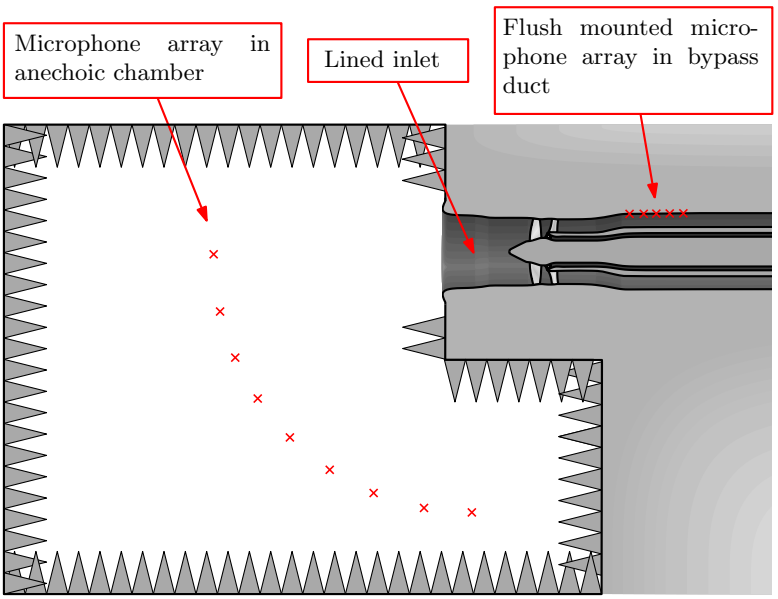

Figure 9.1 – Sketch in planform of the microphone arrays used to measure noise on the LSFR. Note that this is not drawn to scale.

9.2 Overview of simulation methodology

In this section a description is given of the steps taken to produce rear-arc and forward-arc noise predictions using the noise radiation and rotor transmission models introduced in Chapters 2–5, along with the flow and turbulence parameters derived from hotwire and RANS CFD analyses of Chapter 8.

9.2.1 Input parameters

Geometric, mean flow and turbulence parameters are needed to perform the noise predictions. Their estimation for input to the noise model are described later in this section.

Of note here are the intake and exhaust flows into which sound radiates, as the flow Mach number and whirl angle directly affect the modal power factor $\mathcal{H}^{\pm}$ (see Section 9.2.3 for definition). A discussion of the choice of flow regime at the rotor and OGV is given below.

Downstream of OGV Due to the assumption of zero steady loading (Assumption 6 in Section 2.1) there is no turning of the flow at the OGV so that the whirl angle is maintained as the blade row is crossed. However, in a physical engine the exhaust flow is substantively axial. There is no information available for the un-swirled flow downstream of the OGV. Sound is therefore assumed to radiate into the whirling flow at the OGV leading edge, defined using hotwire and RANS CFD as described in Chapter 7.

Upstream of rotor Information regarding the axial flow upstream of the rotor was extracted from mass flow predictions performed by Rolls-Royce. However, all rotor transmission calculations were performed with the whirling-flow parameters at the

rotor as observed in the stationary reference frame. Radiation calculations may be performed with either set of flow parameters. These two alternative flow assumptions are sketched in Figures 9.2a and 9.2b respectively. However, it shall be shown in Section 9.3.1 that the assumption of axial inlet flow for sound power radiation calculations, with the associated radiation across the inlet-rotor flow discontinuity, leads to non-physical transmission loss values across the rotor.

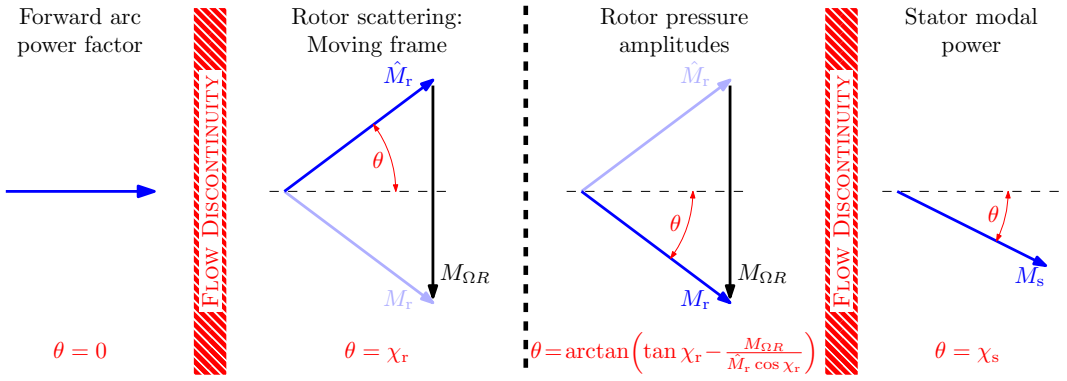

(a) Radiation into inlet flow

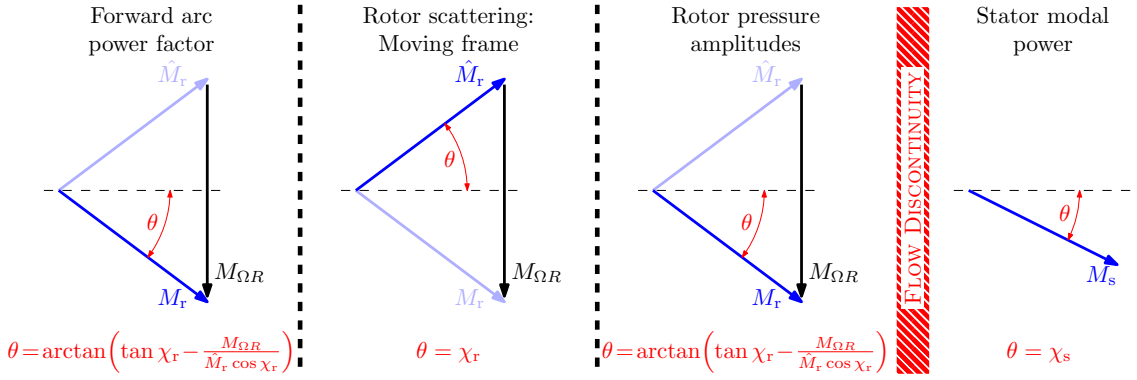

(b) Radiation into flow at rotor position

Figure 9.2 – Illustration of the calculation regions in which different flow parameters are used.

9.2.1.1 Geometric parameters

The rotor and OGV geometric parameters: B_r, B_s, R, s_r, s_s, c_r, c_s, χ_r, χ_s and x are assumed to be constant and independent of flow conditions. The rotor geometry is taken from the case of 90% fan speed, 28F-OGV at working line 5, as this was assumed to be the closest to on-design. The 28F and 28R-OGV geometries are selected from the same case as the rotor geometry, with an axial displacement applied to the 28R cases. The 44F-OGV geometry is taken from its 90% working line 5 case for the same reasons.

9.2.1.2 Flow parameters: inlet

The flow parameters U and c_0 are regarded as being dependent only on the fan speed and working line. The required values of U and c_0 are extracted from the Rolls-Royce mass

flow prediction code Q263. The whirl angle at the inlet θ is assumed to be zero for the axial flow assumption. These parameters are used for the calculation of radiated sound power described in Section 9.2.7.

9.2.1.3 Flow parameters: rotor

The flow parameters U, θ and c_0 at the rotor are taken as being dependent on the fan speed and working line but independent of the OGV configuration. Only six combinations of fan speed and working line are therefore required to perform the transmission calculations for all cases under investigation here. These mean flow parameters are extracted from Q263.

9.2.1.4 Flow parameters: stator

The flow parameters U, θ and c_0 at the stator are taken as being dependent on the fan speed, working line and OGV configuration. The sound speed c_0 is taken from Q263 but velocity U and whirl angle θ are derived from RANS CFD or hotwire measurements.

In general the interstage flow angle does not match the metal angle of the OGV. The magnitude of the average difference angle is 1.82° while the peak is 6.14°.

9.2.1.5 Turbulence parameters

The turbulence parameters of mean square velocity $\overline{w^2}$ and integral length scale Λ are derived from the appropriate RANS CFD or hotwire measurements as described in Chapter 8.

9.2.2 Choice of frequencies

The rotor transmission model presented in Chapter 5 predicts frequency scattering of incident sound power such that sound power incident in a mode order m at source frequency ω scatters into modes $n = m + B_{\mathrm{r}}r$ for scattering orders $r \in \mathbb{Z}$. The computation of the sound field incident on the rotor as a function of frequency needs to be evaluated on a grid of discrete frequencies so that scattered sound power falls on the same frequency grid. It shall be shown in Section 9.2.6.2 that this approach affords significant computational efficiencies.

In the results presented in this chapter the band-limited source spectrum is defined at single engine order points up to 100 EO so that $\omega = j\Omega$ for $j \in [1, 2, 3, \cdots 100]$. These frequency points ω constitute a set of frequencies at which modes are radiated from the OGV and shall be denoted $\boldsymbol{\omega}$. There is no problem in principle associated with finer division of the bandwidth (e.g. $\omega = j(\Omega/4)$ for 1/4 EO resolution).

9.2.3 Power spectral density radiated from OGV

In this chapter the upstream and downstream propagating power spectral density per unit span $\mathcal{P}^{\pm}$ is obtained for a given set of geometric, flow and turbulence parameters

using either the exact cascade model of Chapter 2 or the single airfoil model described in Chapter 4. The sound power spectral density per unit span radiated upstream and downstream from the stator cascade across the source frequencies shall be denoted by $\mathcal{P}^{s\pm}(\omega)$, where $+$ and $-$ indicate upstream and downstream propagation respectively.

Of the two sound power radiation models used in the current study only the cascade model yields a modal power distribution for upstream propagating modes $\mathcal{P}_m^+$. These are required for rotor transmission calculations as described in Chapter 5. The single airfoil noise model assumes radiation into free-field and is therefore not suitable for transmission calculations.

9.2.4 Acoustic mode cut-on ranges

The rotor scattering calculations of the rotor transmission are formulated in terms of the scattering of modal pressure amplitudes. Therefore pressure amplitudes are required for all modes cut-on at the rotor for a given source frequency ω.

The range of modal orders m cut-on at a given frequency ω are defined by Equation (5.5). The range of m is dependent on the radius $R = Bs/2\pi$, flow angle θ, Mach number M and sound speed c_0. The values of these parameters generally differ at the rotor and OGV locations so that the range of cut-on modes at the rotor is not generally the same as that at the OGV (see Figure 9.2). An example of the range of cut-on mode orders m at the rotor and the OGV is shown in Figure 9.3 versus engine order and mode order m. In this figure the overlap between the modal orders is indicated by the white region.

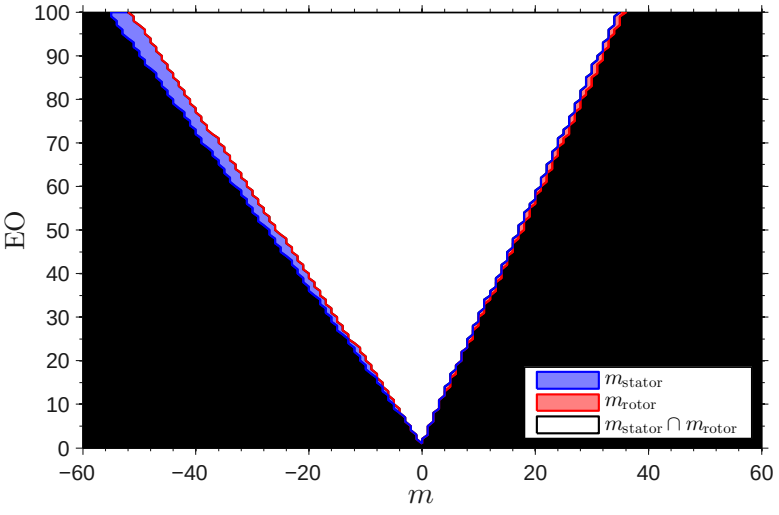

Figure 9.3 – Differences in mean flow at stator and rotor locations resulting in different sets of cut-on acoustic modes. The intersection of these sets is used when performing rotor transmission calculations. Power in modes falling outside this intersection is excluded. These sets correspond to the case: 50% fan speed, working line 5 with 28F OGV at radial strip 7 using hotwire-derived flow parameters.

Sound power that is radiated upstream from the OGV into a mode that is cut-off at

the rotor is not included, while a mode cut-on at the rotor that is cut-off at the OGV is assumed to carry no power. The effect of the exclusion of sound power in modes cut-off at the rotor is illustrated by comparison of the span-wise sum of modal sound power PSDs per unit EO at the OGV and rotor, denoted by $\mathcal{P}^{\mathrm{s}+}(\omega)$ and $\mathcal{P}^{\mathrm{inc}}(\omega)$ respectively. The PWL spectra can be derived from sound power PSDs using

$$\mathrm{PWL}(\omega) = 10 \log_{10} \frac{\mathcal{P}^{\mathrm{s}+}(\omega)}{10^{-12}}, \tag{9.1}$$

where $\mathcal{P}^{\mathrm{s}+}(\omega)$ is shown without loss of generality.

Figure 9.4 shows a comparison of the PWL spectra derived from $\mathcal{P}^{\mathrm{s}+}(\omega)$ and $\mathcal{P}^{\mathrm{inc}}(\omega)$ to illustrate the effect of the modal power not included on the overall power at the rotor compared with the power at the stator. Here it can be seen that the total effect of excluding sound power in cut-off modes is approximately 1 dB at 50% fan speed, becoming increasingly negligible at higher fan speeds.

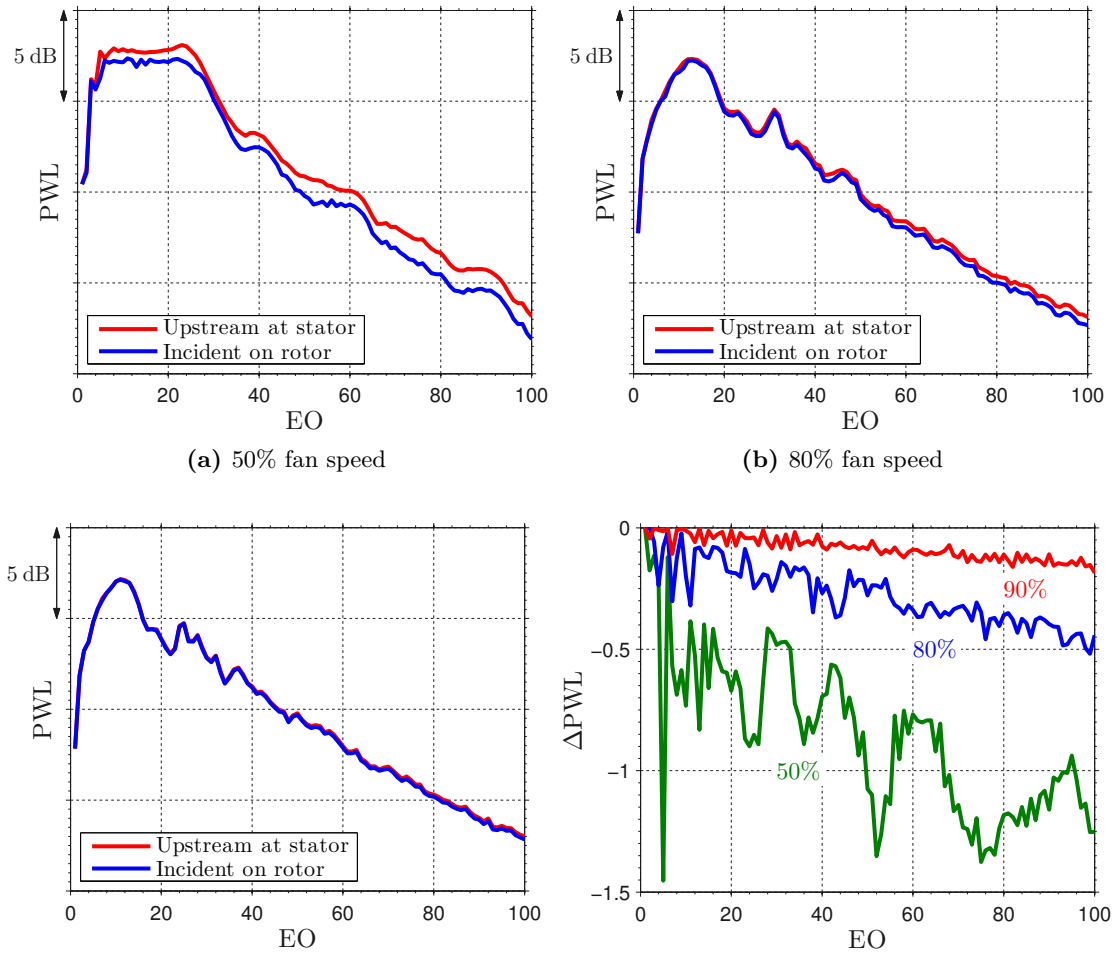

(a) 50% fan speed

(b) 80% fan speed

(c) 90% fan speed

(d) Differences of PWL due to changing modal cut-on ranges

Figure 9.4 – Spectra of span-wise sum of sound power level incident on the rotor compared with the source sound power level showing the sound power reduction between stator and rotor through removal of cut-off modes. Effect at three fan speeds is shown individually and the change associated with these is summarised in subplot (d).

9.2.5 Modal pressure amplitudes at the rotor

Calculations of the scattered sound by the rotor are expressed in terms of the scattered modal pressure amplitudes P_m at each source frequency (see Equation (5.32)). These values are derived from the sound power incident on the rotor in each mode order m.

The modal power per unit span per unit radian frequency at the rotor $\mathcal{P}_m^{\mathrm{r}+}$ is obtained from the modal power per unit span per unit radian frequency at the OGV $\mathcal{P}_m^{\mathrm{s}+}$ using

$$\mathcal{P}_m^{\mathrm{r}+}(\omega) = \mathcal{P}_m^{\mathrm{s}+}(\omega)\frac{\Delta R_{\mathrm{r}}}{\Delta R_{\mathrm{s}}}, \tag{9.2}$$

where ΔR_{r} and ΔR_{s} are the widths of the annular strips at the rotor and OGV respectively.

The squared pressure amplitude of each mode m at the rotor is given by rearranging Equation (5.32) whilst assuming that the non-dimensional pressure scattering coefficient $\mathcal{G}_{mn}^{\pm} = 1$ as no scattering has yet taken place

$$|P_m|^2(\omega) = \frac{\rho_0}{B_{\mathrm{r}} s_{\mathrm{r}}}\frac{\mathcal{P}_m^{\mathrm{r}+}(\omega)}{\mathcal{H}^+(\omega, M_{\mathrm{r}}, \theta_{\mathrm{r}}, m)}, \tag{9.3}$$

where $\mathcal{H}^+$ is the upstream power factor evaluated using Equation (2.49) with parameters ω, M_{r}, θ_{r} from the rotor location in the stationary frame of reference. Note that the sound power calculations are not sensitive to the phase of the pressure amplitude.

9.2.6 Calculation of rotor transmission loss

9.2.6.1 Frequency indexing

Calculations of the modal scattering due to each mode m by the rotor are required to obtain the overall sound power transmitted through the rotor. These are performed in the moving rotor-fixed frame of reference by changing to a coordinate system rotating with the rotor. Recalling Equation (5.14), each cut-on mode order m incident on the rotor at frequency $\omega = j\Omega$ appears in the rotor-fixed reference frame at the Doppler-shifted frequency $\omega_m = (j - m)\Omega$. The apparent rotor-frame frequency can be identified by the index

$$q = j - m. \tag{9.4}$$

Note that the cut-on condition shown in Equation (2.58) ensures that the value of q is always positive. In the calculation of sound transmission through the rotor the range of modes cut-on in the rotor-fixed reference frame at the apparent frequency

$$\omega_m = q\Omega \tag{9.5}$$

is calculated and any modes m that fall outside the cut-on range are discarded.

9.2.6.2 Identifying unique rotor kernel matrices

The calculation of sound power transmission through the rotor requires the calculation of non-dimensional pressure scattering coefficients $\mathcal{G}^{\pm}_{mn}$ (see Equation (5.32)). The calculation of $\mathcal{G}^{\pm}_{mn}$ is dependent on the evaluation of kernel matrices $\mathbf{K}$, as discussed in Section 2.4.9, for each mode incident at the reduced frequency λ, defined using Equation (9.5) as [46]

$$\lambda = q\Omega \frac{c_\mathrm{r}}{\hat{M}_\mathrm{r} c_0}. \tag{9.6}$$

λ represents the total phase change of the incident mode along the cascade chord. Periodicity in the geometry coupled with periodicity in the incident wavenumbers and the m-dependence of λ leads to the periodicity relation for $\mathbf{K}$ in the rotor-fixed reference frame

$$\mathbf{K}(\lambda, m) = \mathbf{K}(\,\lambda(j + rB_\mathrm{r}, m + rB_\mathrm{r}),\; m + rB_\mathrm{r}\,) : r \in \mathbb{Z}. \tag{9.7}$$

This means that $\mathbf{K}$ is uniquely identified by the indices q and $m' = \mathrm{mod}(m, B_\mathrm{r})$. Calculation of q and m' for a range of source frequencies $\omega = j\Omega$ results in a duplication of certain values of these indices and hence a duplication of $\mathbf{K}$, obtained using LINSUB which is computationally demanding. It is possible to identify the unique combinations of q and m' in advance of the transmission calculation and avoid the generation of redundant kernel matrices, thus saving significant amounts of time and storage space.

Figure 9.5 shows a grid plotted against q and m' in which combinations of q and m' for which kernel matrices are required for a set of rotor sound power transmission calculations are indicated by the presence of coloured squares. The contributions due to the cut-on modes incident on the rotor at $j = 100$ are marked in red and are located on the 'wrapped' diagonal that passes through $q = 100$, $m' = 0$.

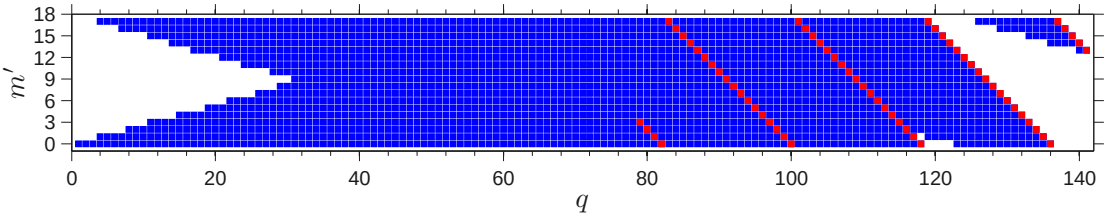

Figure 9.5 – Grid showing the combinations of q and m' for which kernel matrices are required for a set of rotor sound power transmission calculations. This corresponds to the case: 50% fan speed, working line 5, 28F OGV radial strip 1 using hotwire-derived flow parameters. Contributions due to modes cut-on at $j = 100$ are marked in red.

9.2.6.3 Rotor pressure amplitude calculation from modal power

The pressure amplitudes of scattered mode orders $n = m + rB_\mathrm{r}$ are obtained in this chapter either using the exact formulation of cascade scattering with the kernel matrices described above using LINSUB, or using the $n = m$ plane-wave formulation due to Kaji and Okazaki

[67] by way of an approximation. All scattering calculations are performed in the rotor frame of reference with the local flow parameters.

9.2.7 Calculation of sound power upstream of the rotor

The PSD of the sound power transmitted through the rotor is obtained from the scattered pressure amplitudes P_n using Equation (5.32). In the calculation of the power factor $\mathcal{H}^+$ necessary to evaluate Equation (5.32) is undertaken using the flow parameters M_r, θ_r and c_0 as defined at either the inlet or the rotor, as described in Section 9.2.1.2.

Recalling Equations (5.9) and (5.22), an incident mode m is scattered into modes

$$n = m + rB_\mathrm{r}$$

at frequencies in the stationary observer frame

$$\omega_{mn} = (j - (m - n))\Omega = \omega + rB_\mathrm{r}\Omega.$$

For $r \leq 0$ these frequencies ω_{mn} all overlap with the source frequency band $\boldsymbol{\omega}$ defined in Section 9.2.2 (assuming that the source is band-limited, as in the results shown here). However, for $r > 0$ some sound power is scattered into higher frequencies $\omega_{mn} \notin \boldsymbol{\omega}$.

Typical examples of the power spectral density versus modes m incident on the rotor and the scattered modes n and the normalised radiation frequency ω/Ω are shown in Figures 9.6a and 9.6b respectively. In Figure 9.6a the triangle of values corresponds to the impinging modes in the source frequency band $1 \leq \omega/\Omega \leq 100$. Scattering of the incident modes in accordance with Equations (5.9) and (5.22) leads to the translated 'images' of the incident mode triangle seen in Figure 9.6b.

Recalling Section 5.3.2.1, the semi-actuator disk model due to Kaji and Okazaki employs a mode-matching approach such that the gap-wise wavenumber component ν is identical for rotor incident and transmitted modes. This restriction prevents scattering of the incident modes so that the non-dimensional pressure scattering coefficients are $\mathcal{G}^+_{mn} = \mathcal{G}^+_{mm}\delta_{mn}$

Sound power PSDs per unit span upstream of the rotor are obtained by summation over all scattered mode indices n, with the resulting upstream spectrum denoted $\mathcal{P}^{\mathrm{r}+}(\omega)$. The PWL spectrum for the upstream-transmitted sound power is calculated using Equation (9.1) as discussed in Section 9.2.4.

Figure 9.7 shows PWL spectra of upstream-propagating sound power per unit engine order. The sound power incident on the rotor is shown in black and is compared with three spectra of rotor-transmitted sound power level:

- **Blue line** Exact cascade scattering formulation radiating into axial inlet flow.
- **Red line** Exact cascade scattering formulation radiating into whirling rotor flow.

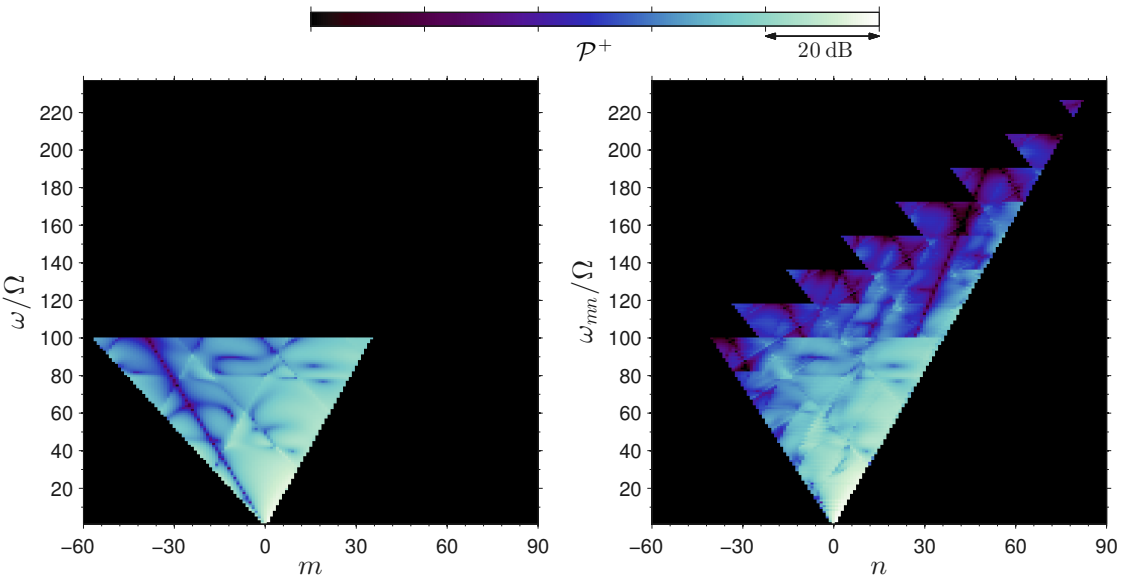

(a) Incident modes **(b)** Scattered modes

Figure 9.6 – Power spectral density of modes incident on the rotor (a) and scattered values (b) shown against modal orders m, n and normalised frequency ω/Ω. The majority of scattered power is concentrated in the source frequency band $1 \leq \omega/\Omega \leq 100$ but some power is scattered out of band.

- **Green line** Kaji-Okazaki scattering formulation into whirling rotor flow.

9.2.8 Correction for intake liner

The LSFR includes a sound absorbing liner that is not included in the noise models described in preceding chapters. The insertion loss associated with this liner must be determined and accounted for before forward-arc predictions can be compared with experimental measurements.

Figure 9.8 shows the estimated insertion loss plotted against engine order at 50% fan speed. This insertion loss has been estimated using a generic PWL attenuation spectrum derived from a composite of Rolls-Royce proprietary rig tests. The attenuation data are derived from measurements taken at 0° to the duct axis and will therefore underestimate the sound power insertion loss by neglecting the greater attenuation associated with larger measurement angles. When applying the insertion loss to forward arc noise estimates it is done with respect to absolute frequency rather than the engine order shown in Figure 9.8.

9.3 Analysis of predicted rotor sound power transmission and its effect on forward arc noise

The methods described in Section 9.2 have been applied to predict the rear-arc and forward-arc noise for the LSFR geometry and flows. In this section, the predicted rotor sound power transmission shall be analysed, considering the span-wise variations of block-

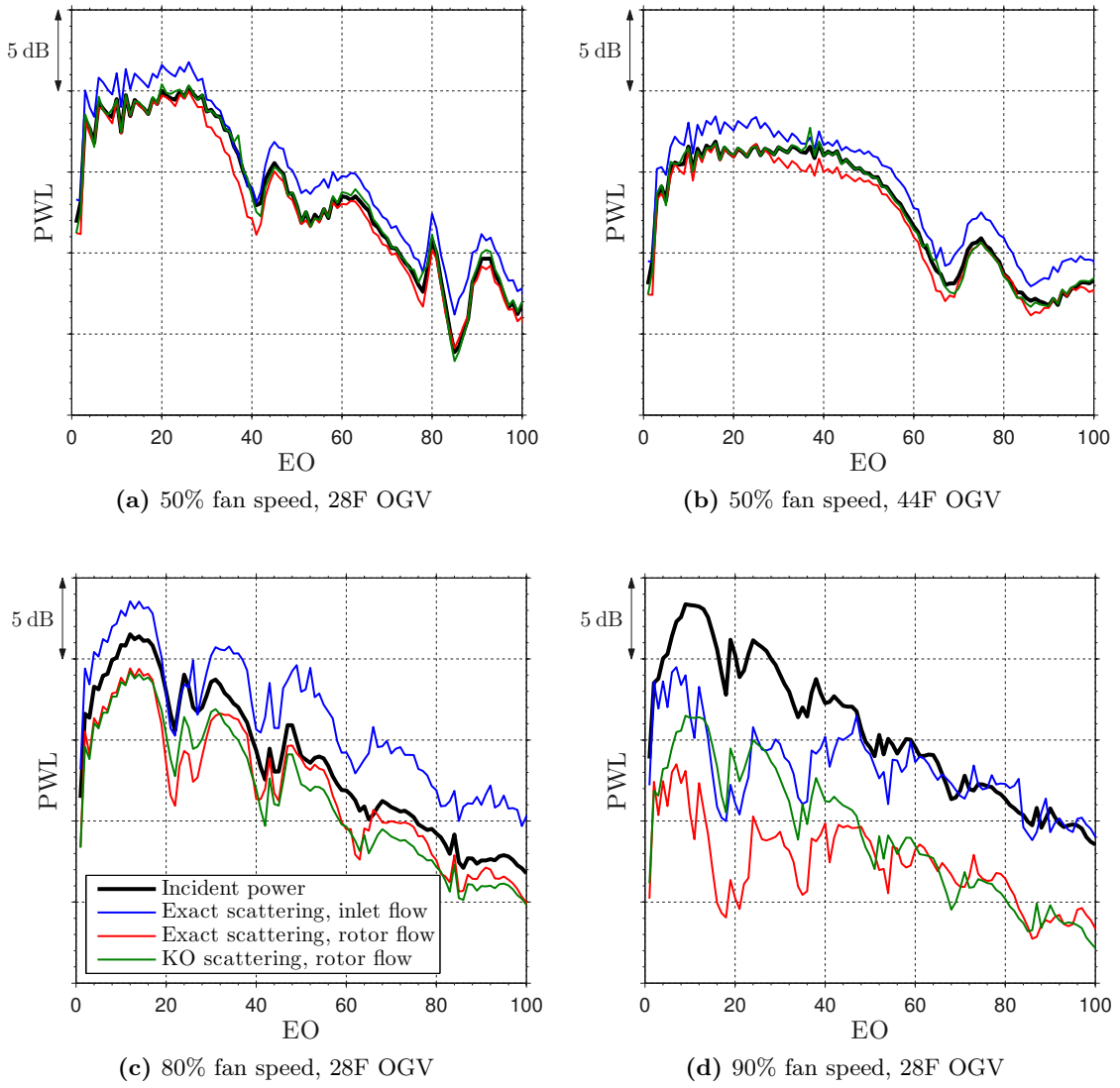

(a) 50% fan speed, 28F OGV

(b) 50% fan speed, 44F OGV

(c) 80% fan speed, 28F OGV

(d) 90% fan speed, 28F OGV

Figure 9.7 – PWL spectra for rotor-incident sound power level per unit engine order and corresponding transmission calculated using two methods and radiation into two flows. Four configurations are shown, each for a single radial strip at a single working line.

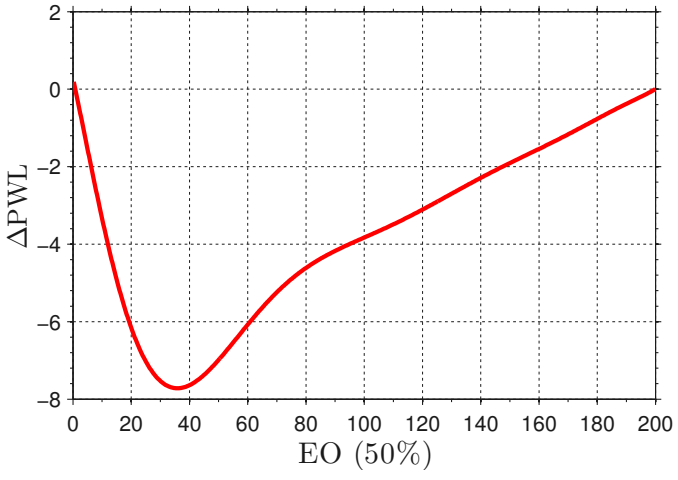

Figure 9.8 – Inlet liner insertion loss spectrum based on data from 0 EO–100 EO at 50% fan speed.

age and changes due to fan speed, working line and OGV configuration. The combined effect of changing fan speed on OGV turbulence interaction noise and rotor transmission loss is also considered.

9.3.1 Strip transmission spectra

Having calculated the acoustic power spectral density $\mathcal{P}^{\text{inc}}(\omega)$ incident on the rotor in each strip and the corresponding power upstream of the rotor $\mathcal{P}^{\text{r}+}(\omega)$ a strip sound power level spectrum in dB for transmission across the rotor for frequencies in the source frequency band $\boldsymbol{\omega}$ is defined in Equation (5.39), reproduced below:

$$L_\tau(\omega) = 10\log_{10}\frac{\mathcal{P}^{\text{r}+}(\omega)}{\mathcal{P}^{\text{inc}}(\omega)},$$

where $\omega \in \boldsymbol{\omega}$. Figure 9.9 shows transmission spectral levels plotted against engine order (EO $= \omega/\Omega$) corresponding to the power spectra shown in Figure 9.7. Observations are listed below.

1. Rotor transmission predicted using inlet flow parameters (blue lines) results in positive values, suggesting increasing noise through the rotor. Clearly this is non-physical and arises because the scattered pressure amplitudes P_n and corresponding power factors $\mathcal{H}^+_{mn}$ are calculated with different flow parameters, either side of a flow discontinuity (see Figure 9.2a). Henceforth all stages in calculation of the rotor transmission shall be performed using flow parameters as defined at the rotor.

2. Some small positive values of L_τ are observed over short frequency ranges in the exact cascade spectrum using rotor flow parameters. These are associated with frequencies where $\mathcal{P}^{\text{inc}}(\omega)$ is small and frequency scattered contributions have 'overfilled' the transmission spectrum $\mathcal{P}^{\text{r}+}(\omega)$. As such these features are physically valid as the sound power is accounted for.

3. The frequency-averaged value of value of L_τ decreases with increasing fan speed.

4. A band of reduced transmission is seen in all strip transmission spectra calculated using the exact cascade transmission model; for $\omega/\Omega \approx 40\,\text{EO}$ in the 50% fan speed cases and $\omega/\Omega \approx 20\,\text{EO}$ at the higher fan speeds. For frequencies higher than this 'enhanced blockage band' (particularly at the higher fan speeds) L_τ appears to reach a plateau at similar level to the transmission predicted using the Kaji-Okazaki model (green line) that is seen to be frequency-insensitive, as observed in Section 5.2.3. A similar 'enhanced blockage' feature was observed in Chapter 5 for stationary fans for $0.7 \lesssim \omega/\Delta\omega \lesssim 3$, where a few higher order cascade modes are cut-on or close to cut-on (see Figure 5.10). Figure 9.10 shows the three strip transmission spectra calculated with rotor flow parameters and the exact cascade model plotted against frequency normalised with $\Delta\,\omega$. Here it can be seen that the normalised

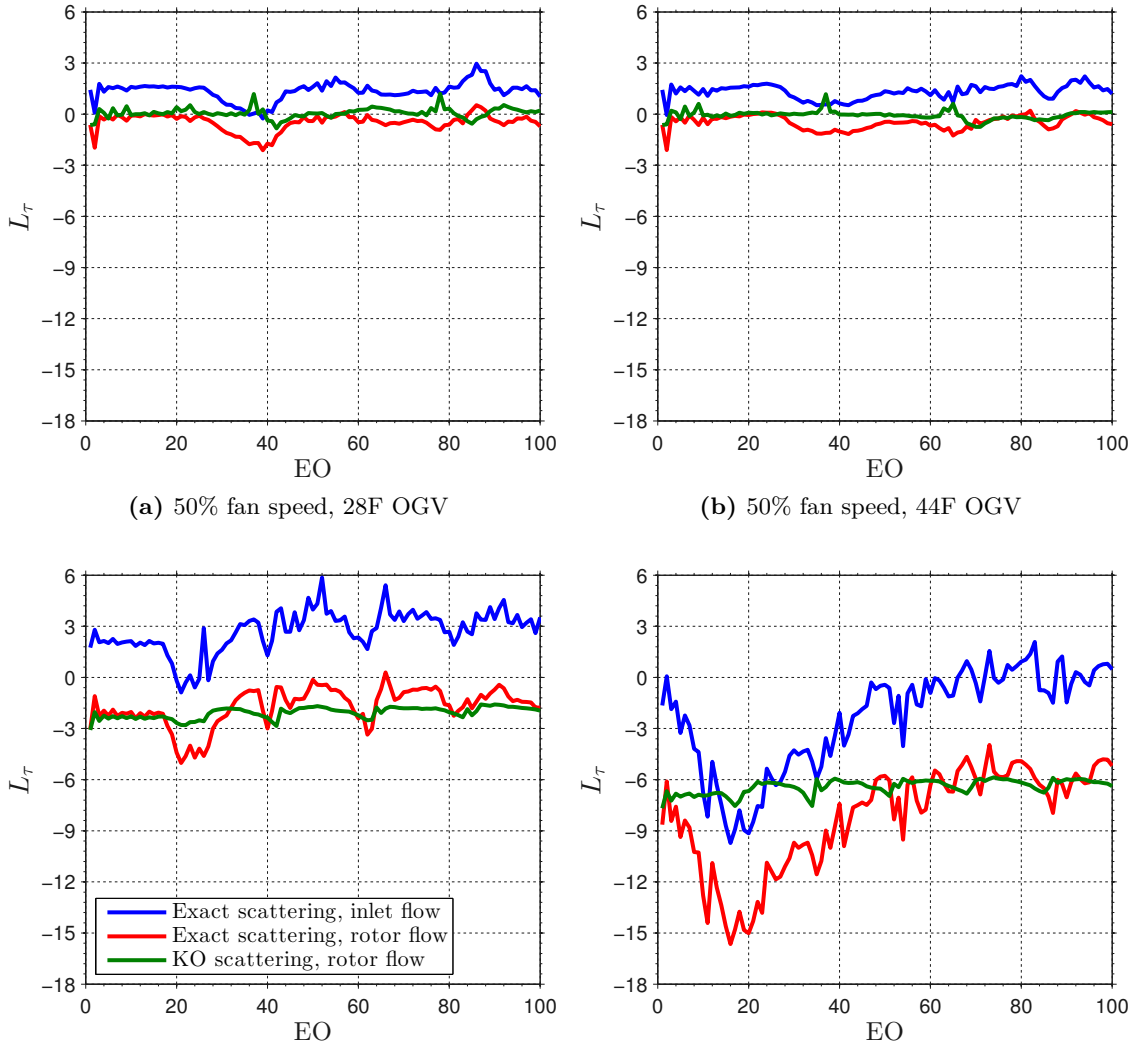

(a) 50% fan speed, 28F OGV

(b) 50% fan speed, 44F OGV

(c) 80% fan speed, 28F OGV

(d) 90% fan speed, 28F OGV

Figure 9.9 – Comparison of individual strip transmission spectra calculated using two methods and radiation into two flows. Four configurations are shown, each for a single radial strip at a single working line.

frequency at which the 'enhanced blockage band' occurs increases with fan speed. In all cases the band appears at higher normalised frequencies than for the stationary case (Figure 5.10). Further work is required to explain this phenomenon, which is important for understanding the low frequency behaviour of acoustic transmission through the rotor.

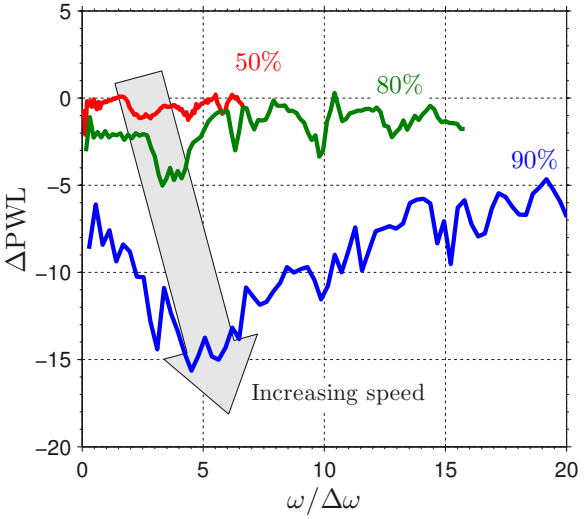

Figure 9.10 – Individual strip transmission spectra calculated using exact scattering formulation into mean flow at rotor plotted against frequency normalised with cut-on frequency of the first higher order mode between the rotor blades $\Delta\omega$.

Having considered the spectrum of rotor transmission in individual strips the overall frequency-averaged behaviour shall be examined in the following section, with particular attention being paid to the variation of transmission level across the rotor span.

9.3.2 Radial variation of frequency-averaged rotor transmission

As discussed in the preceding section and Section 5.2.3, the rotor transmission loss calculated in a single strip may be represented by the frequency-averaged transmission loss coefficient L_τ owing to the 'flatness' of the predicted transmission spectrum. The frequency-averaged transmission loss coefficient is defined in Equation (5.41) and reproduced below:

$$L_\tau = \frac{\sum_{\omega\in\boldsymbol{\omega}} \mathcal{P}^{\mathrm{r}+}(\omega)}{\sum_{\omega\in\boldsymbol{\omega}} \mathcal{P}^{\mathrm{inc}}(\omega)}.$$

Radial variations of L_τ are shown in Figure 9.11 against normalised radius $\hat{R}$. The minimum and maximum transmission loss values in each radial strip are also indicated by triangle markers and dashed lines. In all cases greater transmission loss is seen towards the tip of the rotor. This effect is more pronounced at the higher fan speeds and suggests that the transmission loss level is linked to the rotor-relative Mach number $\hat{M}_\mathrm{r}$ that increases with radius, as discussed in Section 5.3.3.1.

The strip transmission coefficients L_τ discussed above are plotted against $\log_{10} M_{\mathrm{r},1}\beta_\mathrm{r}^2$ in Figure 9.12, where $M_{\mathrm{r},1}$ is the axial component of the mean flow at the rotor and

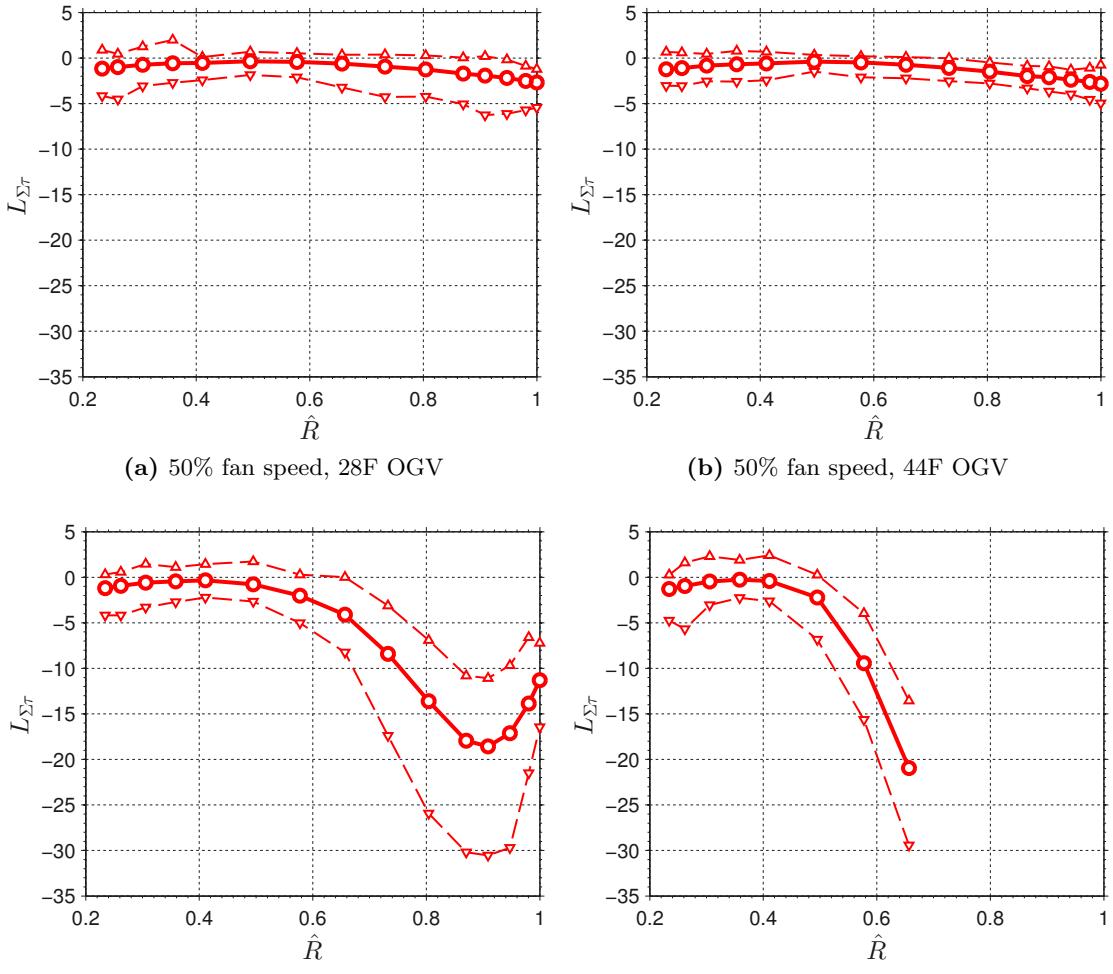

(a) 50% fan speed, 28F OGV

(b) 50% fan speed, 44F OGV

(c) 80% fan speed, 28F OGV

(d) 90% fan speed, 28F OGV

Figure 9.11 – Radial variation of frequency-averaged rotor transmission spectra.

$\beta_r^2 = 1 - M_r^2$ is the squared Prandtl-Glauert number with respect to the rotor-relative Mach number. This representation of the data now shows reasonable collapse of the data onto the black line representing $30 \log_{10} M_{r,1} \beta_r^2 + 19\,\text{dB}$. At the present time the physical reason behind this observation is unclear. Application of the high frequency 'continuum' model of Section 5.3 based on Kaji-Okazaki plane-wave theory shows a considerably weaker dependence on β_r, suggesting that the assumptions underlying the Kaji-Okazaki model are unrealistic or that the span-wise variation of the LSFR geometry contributes significantly to the observed trend.

9.3.2.1 Interpretation of rotor transmission effects using modal phase velocity angle ψ_p

In this section the rotor sound power transmission coefficient is estimated using the Kaji-Okazaki power transmission model averaged over frequency as presented in Section 5.3. This will allow the rotor transmission loss to be assessed in terms of the phase velocity angle sound power density. It will be shown that the smallest transmission loss across the span is associated with the point at which the greatest incident sound power density is aligned with the maximum sound power transmission coefficient predicted using the Kaji-Okazaki model. It will also be shown that the increased transmission loss at higher fan speeds corresponds to a narrowing of both the incident sound power and transmission coefficient distributions with respect to ψ_p, so that misalignment effects close to the rotor tip are enhanced.

Figure 9.13 shows a grid of plots similar to those in Figure 5.19 where the approximate sound power phase velocity angle density, calculated from noise predictions as described in Section 3.1.1 and normalised with the peak value in each subplot, is plotted against phase velocity angle ψ_p. Also plotted is the Kaji-Okazaki power transmission coefficient $\mathcal{T}_{mm}^+$ as a function of ψ_p, obtained by solving the system in Equation (5.54), and the product of the incident sound power with $\mathcal{T}_{mm}^+$. The results for three fan speeds and a range of radial locations are shown. Note that the outer two radial locations at 90% fan speed (Figures 9.13c and f) are assumed to be completely blocked due to supersonic $\hat{M}_r$.

1. At $\hat{R} = 0.5$ the centre of the incident power distribution is nearly aligned with the nil-shielding angle ($\mathcal{T}_{mm}^+ = 1$). This corresponds to the location of the maximum transmission seen in Figure 9.11.

2. Increases in fan speed and radius result in narrowing of both $\mathcal{T}_{mm}^+$ and incident power distributions. This causes an increase in sensitivity to alignment effects.

9.3.3 Total rotor incident and transmitted sound power spectra Π^{inc} and Π^{r+}

The procedures described in the preceding sections are applied to individual radial strips. The total sound power is also of interest, both in terms of noise prediction and in under-

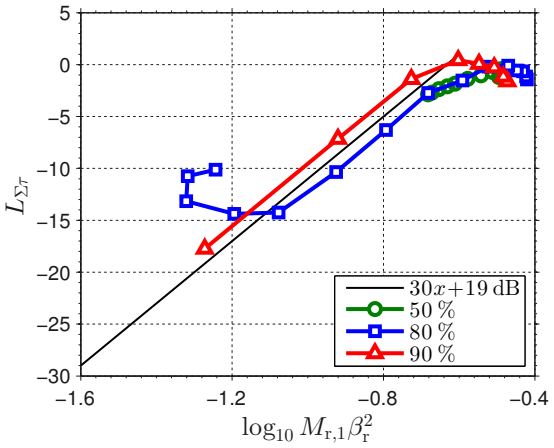

(a) 28R OGV, working line 5

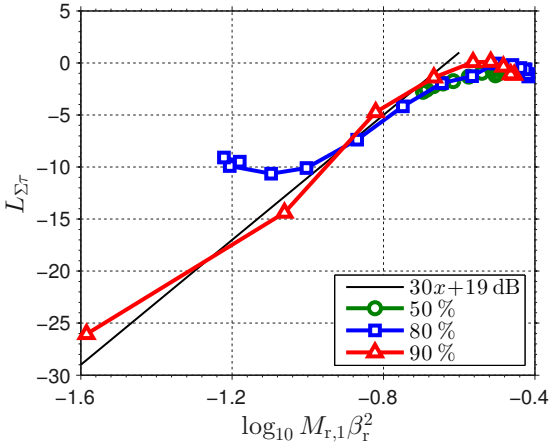

(b) 28R OGV, working line 3

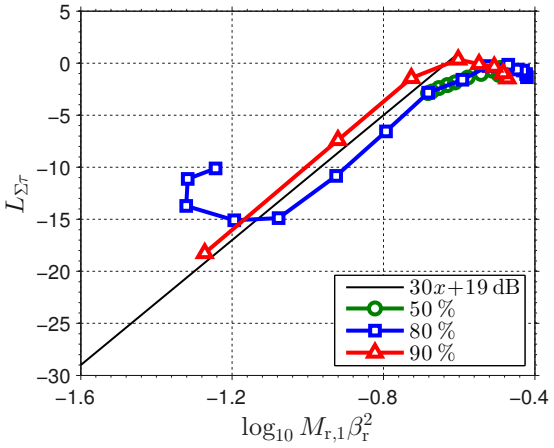

(c) 28F OGV, working line 5

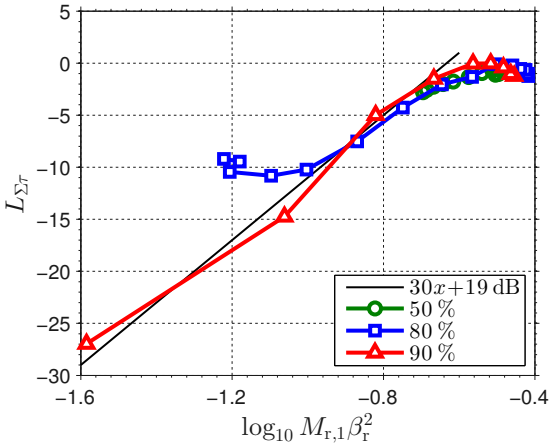

(d) 28F OGV, working line 3

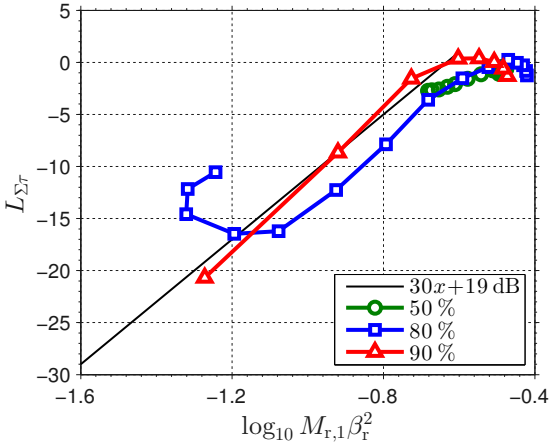

(e) 44F OGV, working line 5

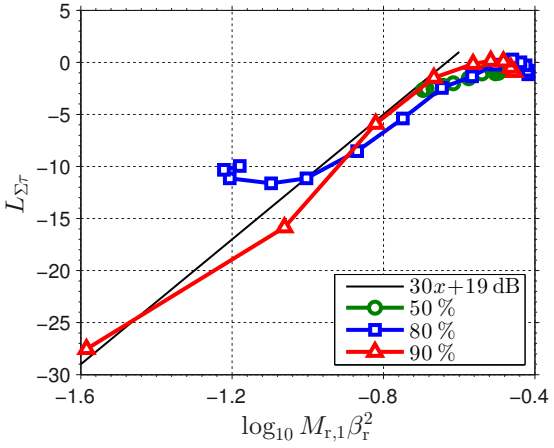

(f) 44F OGV, working line 3

Figure 9.12 – Frequency-averaged rotor transmission level collapsing onto $30\log_{10} M_{\mathrm{r},1}\beta_{\mathrm{r}}^2 + 19\,\mathrm{dB}$.

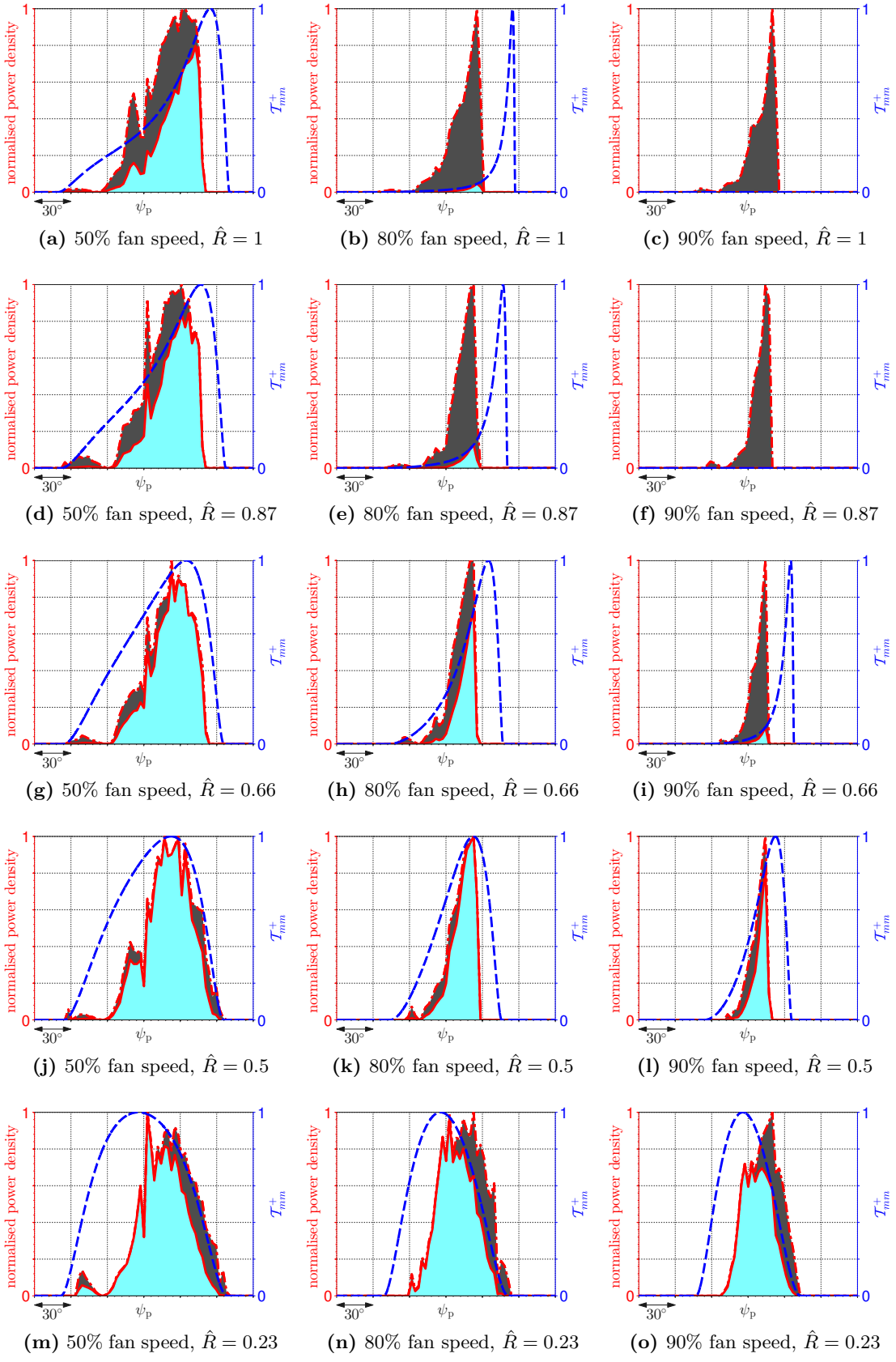

(a) 50% fan speed, $\hat{R} = 1$ **(b)** 80% fan speed, $\hat{R} = 1$ **(c)** 90% fan speed, $\hat{R} = 1$

(d) 50% fan speed, $\hat{R} = 0.87$ **(e)** 80% fan speed, $\hat{R} = 0.87$ **(f)** 90% fan speed, $\hat{R} = 0.87$

(g) 50% fan speed, $\hat{R} = 0.66$ **(h)** 80% fan speed, $\hat{R} = 0.66$ **(i)** 90% fan speed, $\hat{R} = 0.66$

(j) 50% fan speed, $\hat{R} = 0.5$ **(k)** 80% fan speed, $\hat{R} = 0.5$ **(l)** 90% fan speed, $\hat{R} = 0.5$

(m) 50% fan speed, $\hat{R} = 0.23$ **(n)** 80% fan speed, $\hat{R} = 0.23$ **(o)** 90% fan speed, $\hat{R} = 0.23$

Figure 9.13 – Rotor-incident sound power normalised with peak value (– · –), the Kaji-Okazaki power transmission coefficient $\mathcal{T}^+_{mm}$ (– – –) and their product (—) for variations of fan speed and radial location. All configurations use the 28F OGV and working line 5. Incident sound power contributions summed over 2-octave band 26 EO–100 EO

standing rotor blockage.

The span-wise total sound power per unit engine order that is incident on and radiated forward from the rotor is calculated from the contributions in each strip annular strip $\mathcal{P}^{\mathrm{inc}}(\omega)$ and $\mathcal{P}^{\mathrm{r+}}(\omega)$ respectively.

$$\Pi^{\mathrm{inc}}(\omega) = \sum_{i=1}^{N_{\mathrm{R}}} \Omega\, \Delta R_i\, \mathcal{P}_i^{\mathrm{inc}}(\omega), \qquad \Pi^{\mathrm{r+}}(\omega) = \sum_{i=1}^{N_{\mathrm{R}}} \Omega\, \Delta R_i\, \mathcal{P}_i^{\mathrm{r+}}(\omega), \tag{9.8}$$

where N_{R} is the number of radial strips, Ω is the shaft rotation frequency, ΔR_i is the span-wise width of the ith strip and $\mathcal{P}_i^{\mathrm{inc}}(\omega)$ and $\mathcal{P}_i^{\mathrm{r+}}(\omega)$ are the corresponding rotor scattered sound power PSDs per unit span per unit angular frequency. PWL spectra are derived from $\Pi^{\mathrm{inc}}(\omega)$ and $\Pi^{\mathrm{r+}}(\omega)$ using Equation (9.1).

9.3.4 Total rotor transmission level spectra L_τ^{tot}

The total rotor transmission level spectrum L_τ^{tot} is obtained from the total rotor incident and transmitted sound power spectra Π^{inc} and $\Pi^{\mathrm{r+}}$ using

$$L_\tau^{\mathrm{tot}}(\omega) = 10 \log_{10} \frac{\Pi^{\mathrm{r+}}(\omega)}{\Pi^{\mathrm{inc}}(\omega)} \tag{9.9}$$

Figure 9.14 shows the effects on overall spectral transmission level due to OGV configuration change at three fan speeds (increasing from top to bottom) and two working lines (arranged in left and right hand columns). Different line colours indicate the OGV configuration, as indicated in the legend. All plotted results are obtained using RANS-derived turbulence parameters. No significant differences exist when using the hotwire-derived parameters as flow conditions at the rotor are identical is either case.

1. For fixed fan speed and working line (within each subplot) the changes in OGV cause the rotor transmission spectra to alter in detail but the underlying levels remain consistent.

2. At higher fan speeds (Figures 9.14c–9.14f) the rotor transmission level L_τ^{tot} is reduced at frequencies EO$\lesssim$30 relative to higher frequencies. The decreased transmission at low frequencies is due to the 'enhanced blockage bands' observed in individual strip transmission spectra in Section 9.3.1 (see Item 4 on Page 178). The frequency at which the 'enhanced blockage bands' appear is not yet understood but as a low frequency phenomenon is probably related to cascade interaction effects. These effects diminish as rotor blades are decoupled by the cut-on of higher order modes in the inter-blade gap. The predicted transmission levels in bands either side of 30 EO are summarised in Table 9.1.

3. Predicted transmission levels are observed to be insensitive to working line except at 80% fan speed (compare Figures 9.14c and 9.14d). At this fan speed the RANS CFD analysis predicts a significant increase in mean-square turbulence velocity $\overline{w^2}$

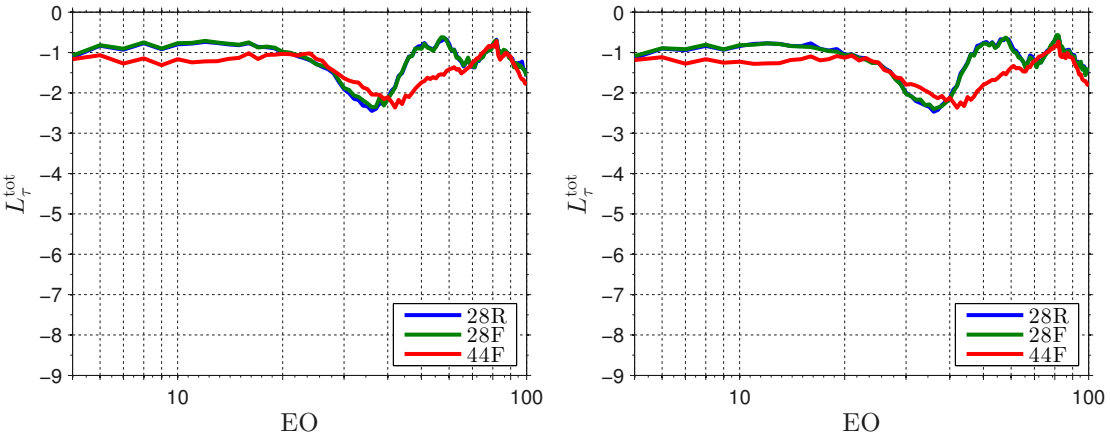

(a) 50% fan speed, working line 5

(b) 50% fan speed, working line 3

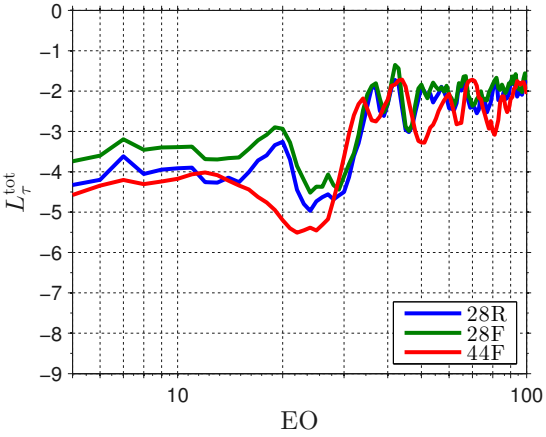

(c) 80% fan speed, working line 5

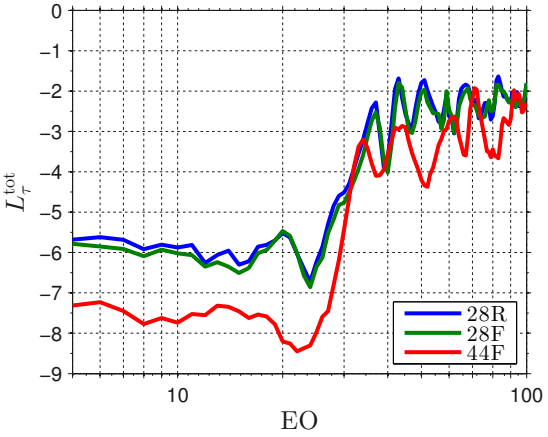

(d) 80% fan speed, working line 3

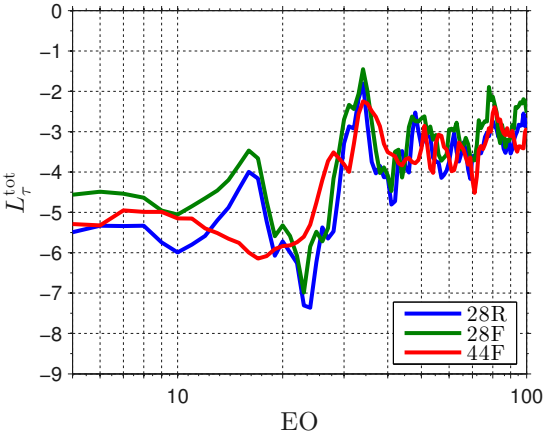

(e) 90% fan speed, working line 5

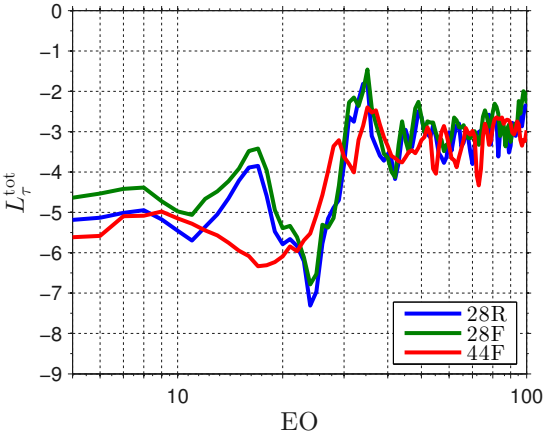

(f) 90% fan speed, working line 3

Figure 9.14 – Total transmission level spectral changes due to variation of fan speed, working line and OGV configuration.

in the outer span when changing from working line 5 to working line 3. The spanwise sums of sound power incident on and transmitted through the rotor at working line 3 are consequently weighted towards the outer span. In this location the overall transmission is reduced, as observed in Section 9.3.2, especially for EO$\lesssim$30 as noted in Item 2 above.

4. Comparing the same working line as fan speed is changed, the low and high frequency transmission level tends to decrease with increasing fan speed. The exception to this is the 80% fan speed working line 3 result noted in Item 3 above.

Table 9.1 – Summary of overall rotor transmission levels L_τ^{tot} for low frequency band LF 6 EO–13 EO and high frequency band HF 50 EO–100 EO. Results obtained using hotwire-derived turbulence and flow parameters are shown in parentheses.

		28R		28F		44F	
FS (%)	WL	LF	HF	LF	HF	LF	HF
50	5	-0.8 (-0.9)	-1.1 (-0.9)	-0.8 (-0.9)	-1.1 (-0.9)	-1.2 (-1.3)	-1.3 (-1.2)
	3	-0.9 (-0.9)	-1.0 (-0.9)	-0.8 (-0.9)	-1.0 (-0.8)	-1.2 (-1.4)	-1.3 (-1.2)
80	5	-4.0	-2.1	-3.5	-1.9	-4.2	-2.3
	3	-5.9	-2.2	-6.1	-2.3	-7.5	-2.9
90	5	-5.5	-3.3	-4.7	-2.9	-5.2	-3.3
	3	-5.2	-3.1	-4.6	-2.8	-5.3	-3.1

The rotor transmission behaviour shown in Figure 9.14 is dominated by the rotor speed with overall transmission coefficient reducing as the rotor speed increases. The differences due to the three available OGV configurations are negligible at working line 5. At high fan speeds the predicted transmission level can be separated into two distinct frequency bands either side of $\approx$ 30 EO. In the low frequency band increased transmission loss is observed compared with the high frequency band. In the following section the effects of fan speed and incident sound power are investigated.

9.3.5 Effects of fan speed on rotor transmission behaviour and forward-arc power

In Section 9.3.4 it was observed that the overall transmission loss was characterised by two distinct frequency bands, within each the frequency sensitivity is low (see Item 2 on Page 183).

The total incident sound power, transmitted sound power and transmission level are compared at three fan speeds for a single OGV configuration. Two working lines are considered. For the purposes of this investigation the low frequency band covers 6 EO–13 EO while the high frequency band is 50 EO–100 EO.

Figure 9.15 shows a comparison between the predicted power incident on the rotor and the power transmitted through the rotor. The corresponding band-averaged transmission loss is shown in blue on the same plot against the right hand vertical axis.

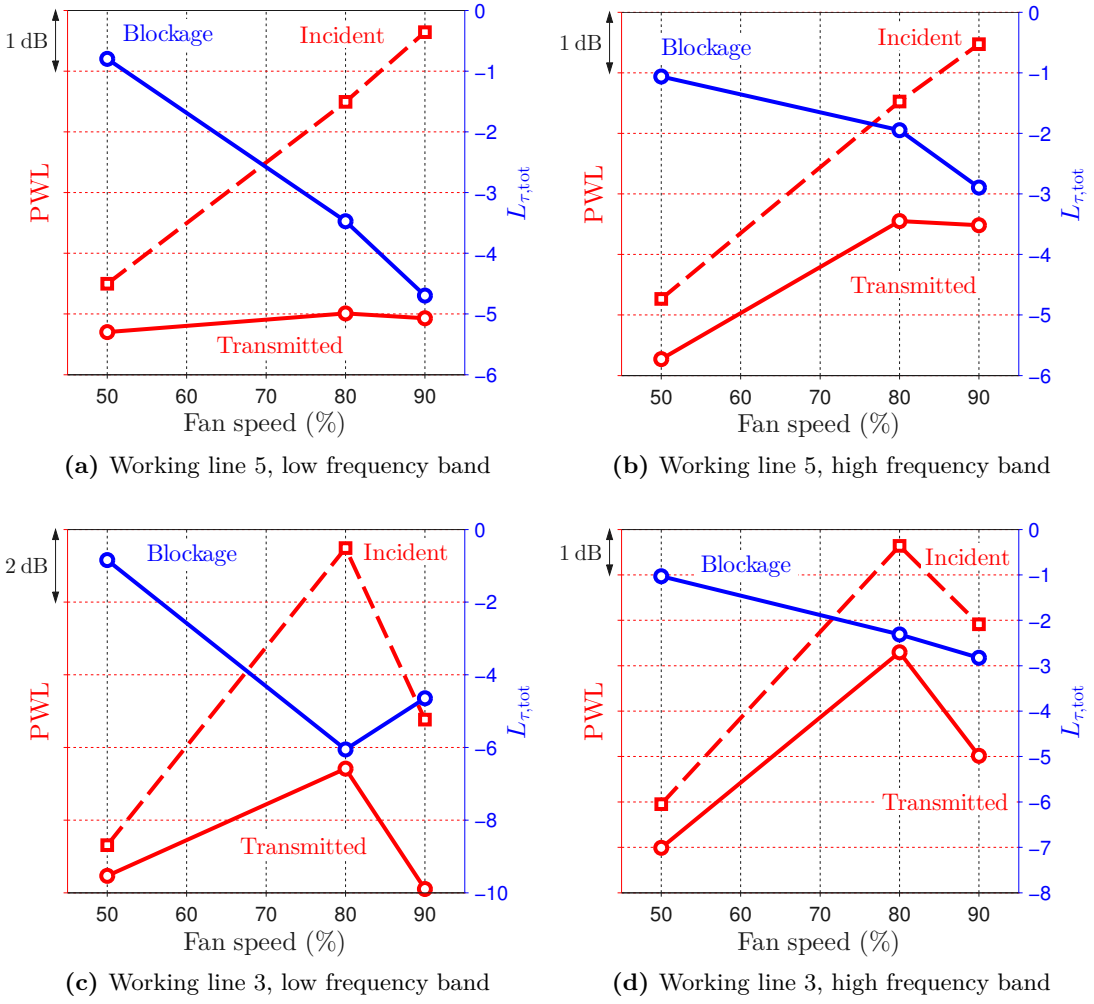

(a) Working line 5, low frequency band

(b) Working line 5, high frequency band

(c) Working line 3, low frequency band

(d) Working line 3, high frequency band

Figure 9.15 – Overall sound power incident on and transmitted through rotor in low and high frequency bands shown with corresponding band averaged transmission level. Results in each sub plot show the effect of changing fan speed with constant working line and OGV configuration, which is 28F in all cases.

The balance between increased fan speed, increased source noise and decreased transmission versus fan speed is particularly marked in the low frequency band at working line 5 (Figure 9.15a). Here the transmitted power is observed to be almost constant at all fan speeds. The corresponding high frequency band result in Figure 9.15b shows that whilst the sound power onto the rotor increases by 4 dB the rotor transmission decreases by 2 dB over the same increase in fan speed. The overall increase in power transmitted through the rotor is therefore limited to just 2 dB.

Of the three fan speeds considered the predicted forward-arc power is greatest at 80%. The sound power incident on the rotor generally increases with fan speed in agreement with the stator-incident Mach number power law observed in Section 3.2.4 (except for the 80% fan speed at working line 3 where significant differences are seen in the turbulence

parameters obtained from RANS CFD analysis). However, as the fan speed increases above 80% the rotor-relative Mach number $\hat{M}_{\mathrm{r}}$ becomes supersonic in the outer strips so that no sound is transmitted through the rotor in these strips. At these high speeds the rotor-incident sound power increases are more than balanced by the decreases in rotor transmission due to rotor flow effects.

9.4 Comparison of predictions with measured rig noise

In this section simulated broadband noise PWL spectra will be compared with measurements taken from the LSFR. The rear and forward arc sound power level spectra shall be presented in Sections 9.4.1 and 9.4.2.

9.4.1 Rear-arc PWL spectra

Figure 9.16 shows plots at three fan speeds of the rear arc sound power level spectra with 1 EO bandwidth deduced from the in-duct sound pressure measurements made on the LSFR with the 44F OGV configuration using the procedure described in Appendix D. The measured spectra have been processed by Rolls-Royce to remove tonal components. Also shown on these figures are the predicted sound power radiated downstream of the OGV obtained using the exact cascade noise model of Chapter 2 and the single airfoil model described in Chapter 4. The flow and turbulence parameters for the predictions are derived from RANS CFD solutions in all cases and hotwire data at 50% fan speed. The spectral differences between the predictions and the experimental measurements are shown in Figure 9.17.

1. The overall level and shape of the predicted noise spectrum performed using the exact model with hotwire flow data (solid red line in Figure 9.16a, only available for 50% fan speed) is seen to match the measured data reasonably well at low frequencies (<40 EO) with the difference between the prediction and measurement being of less than 2 dB magnitude (see Figure 9.17a). This level of agreement is within the uncertainty introduced by the equal power per mode assumption employed in the sound pressure-sound power conversion applied to the measured data (see Appendix D).

2. In Figure 9.16a the shape of the spectrum predicted using the exact cascade noise model with RANS-derived turbulence parameters (solid blue line) matches well with that of the prediction using hotwire-derived parameters (solid red line). They differ in level by ≈3.5 dB. A similar effect is observed in the forward arc predictions shown in Section 9.4.2 (see Item 2 on Page 193). This suggests that the RANS CFD techniques applied are over-predicting the turbulence velocity amplitudes by a factor of approximately 1.5. These effects are considered further in Section 9.4.3.

3. Above 40 EO the predicted spectra diverge from the measured data. The roll-off in frequency exhibited by the predictions is predominantly due to the combined effect

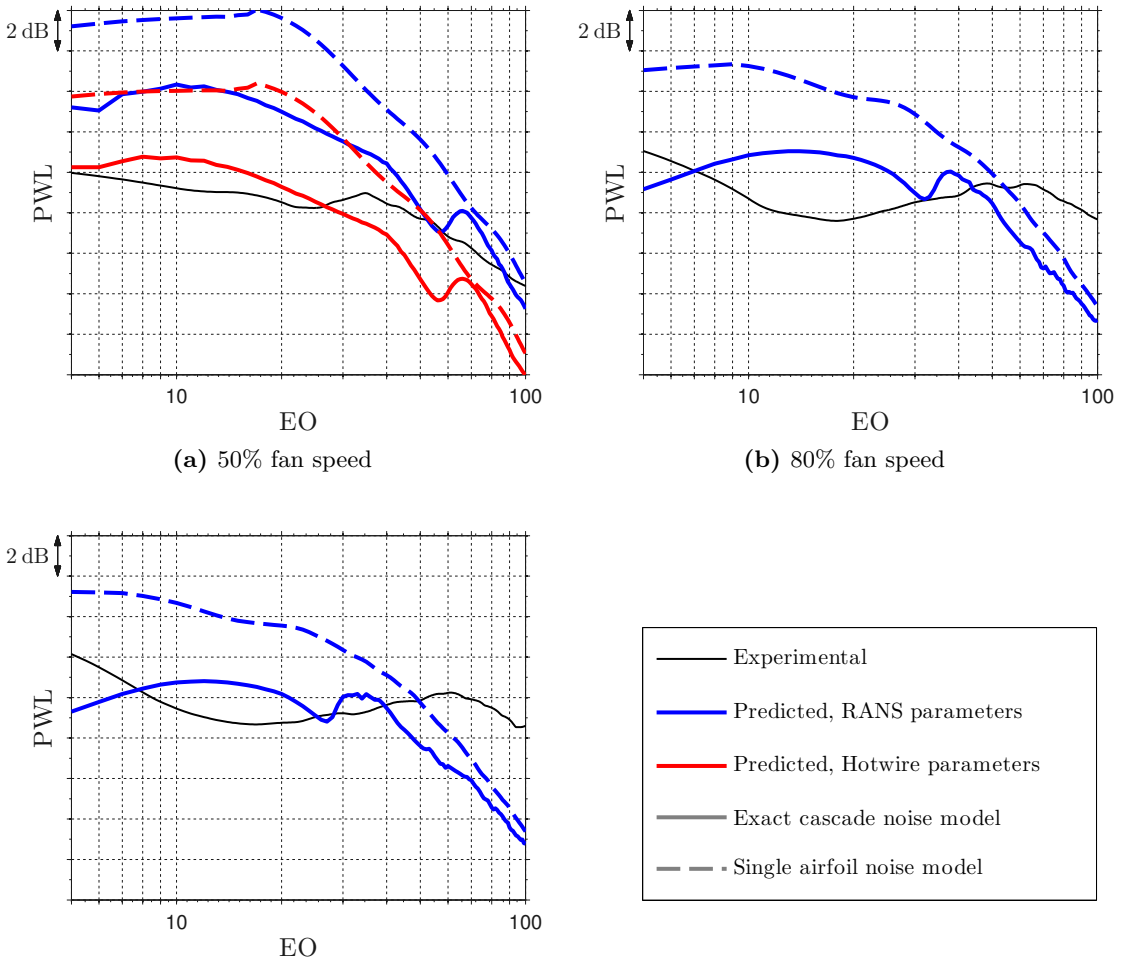

(a) 50% fan speed

(b) 80% fan speed

(c) 90% fan speed

Figure 9.16 – Rear-arc spectra: three fan speeds at working line 5 for the 44F OGV configuration. Black lines represent rear arc sound power spectra per unit EO from experiment while coloured lines indicate predicted noise. Blue lines obtained using turbulence and OGV flow data derived using RANS CFD while red lines indicate hotwire derived results. Hotwire data was not available at the higher fan speeds. Solid coloured lines indicate exact solution whilst the dashed lines indicate equivalent noise estimates obtained using the single airfoil model.

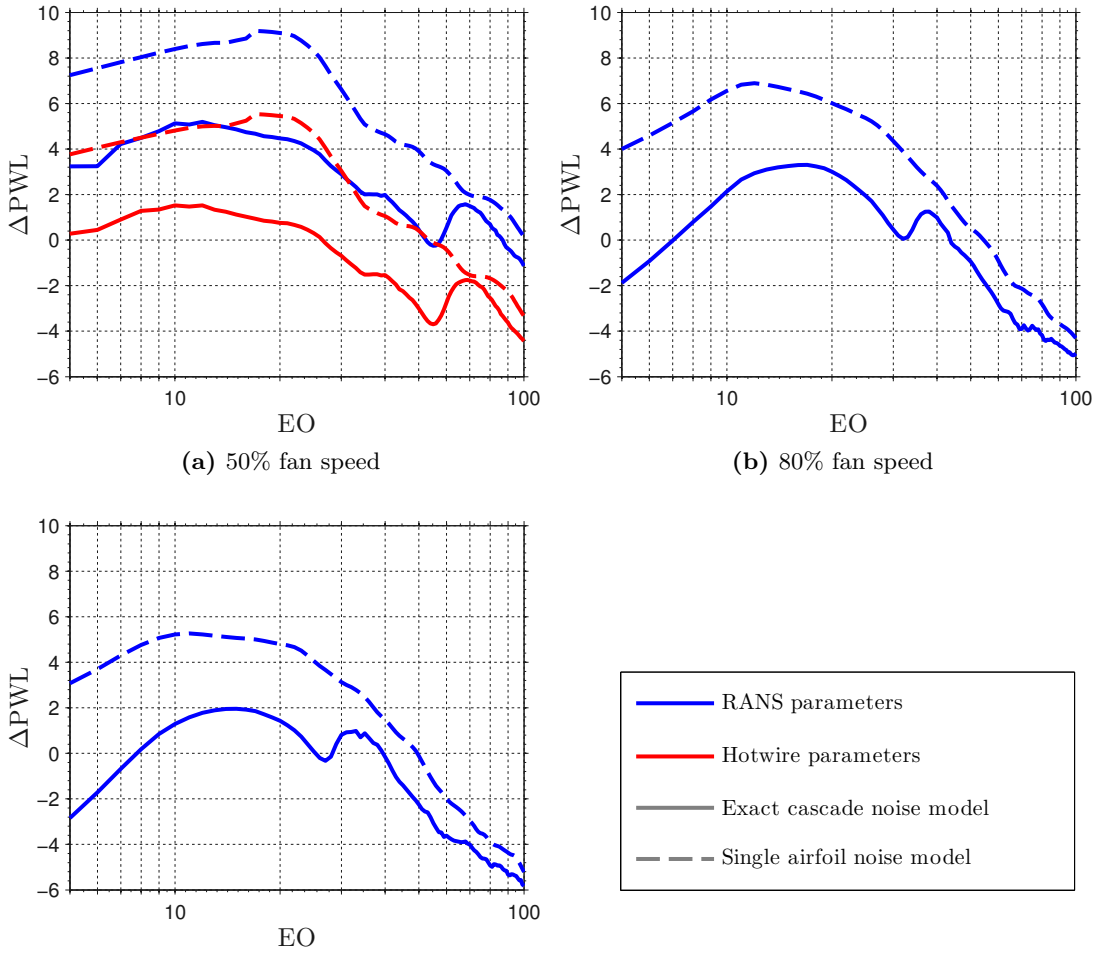

(a) 50% fan speed

(b) 80% fan speed

(c) 90% fan speed

Figure 9.17 – Difference between experimental and predicted rear-arc PWL spectra shown in Figure 9.16 for three fan speeds at working line 5 with the 44F OGV configuration. Blue lines show predictions obtained using turbulence and OGV flow data derived using RANS CFD solutions while red lines indicate hotwire derived results. Hotwire data was not available at the higher fan speeds. Solid lines indicate exact solution whilst the dashed lines indicate equivalent noise estimates obtained using the single airfoil model.

of the -2 law in the one-dimensional Liepmann turbulence velocity spectrum (see Equation (8.8b)) that is approximated by the summation of the two-dimensional spectrum over k_2 (Equation (2.54)) and the high frequency cascade response. The predicted roll-off is weakly dependent on fan speed, ranging from ≈23 dB/decade at 50% to ≈18 dB/decade at 80% and 90%. The corresponding rates of decay in the measured spectra are ≈11 dB/decade at 50% and ≈10 dB/decade at 80% and 90%. That the measured rates of decay are significantly lower than predictions cannot be readily explained by the incident turbulence velocity spectra and possibly suggests the presence of another high frequency source such as rotor self noise or rotor tip noise.

4. The predictions obtained using the single airfoil model differ from the exact solutions by approximately 4 dB for EO $\lesssim$ 20. Above this frequency the predictions from the two models to converge to within 1 dB at 80% and 90% fan speeds and within 1.5 dB at 50%. Convergence of the noise predicted by the two models at frequencies above the inter-blade cut-on frequency $\Delta\omega$ was demonstrated in Chapter 4. The values of $\Delta\omega$ in EO across the normalised OGV span for these three fan speeds are shown in Figure 9.18. The frequencies at which these predictions are made are too low relative to $\Delta\omega$ to get better agreement than is observed.

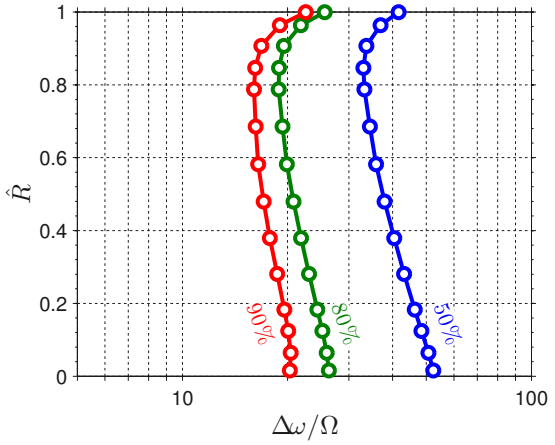

Figure 9.18 – Inter-blade cut-on frequency $\Delta\omega$ for the 44F-OGV at three fan speeds expressed in engine order across the normalised span.

The combination of a possible high-frequency noise source other than the turbulence-OGV interaction and the relatively high frequencies associated with $\Delta\,\omega$ for this OGV design and set of operating conditions means that the single airfoil model is of limited use in the prediction of accurate rear-arc noise spectra, despite the computational advantages that it offers.

At low frequencies EO$\lesssim$40 the exact cascade model predicts the measured spectrum to within 2 dB when the hotwire-derived turbulence and flow parameters are employed. A systematic difference is observed when using the RANS CFD solutions for these parameters,

suggesting that modification of the RANS analysis would allow significant improvement in these results.

In the following section the forward arc noise predictions are compared with experimental measurements in a similar manner to this section.

9.4.2 Forward-arc PWL spectra

Plots of the forward arc sound power measured on the LSFR are shown in Figure 9.19 where they are compared with predictions, taking into account the intake liner insertion loss described in Section 9.2.8. The differences between the predictions and the experimental measurements are shown in Figure 9.20. Note that the measured spectra have been processed by Rolls-Royce to remove tonal components.

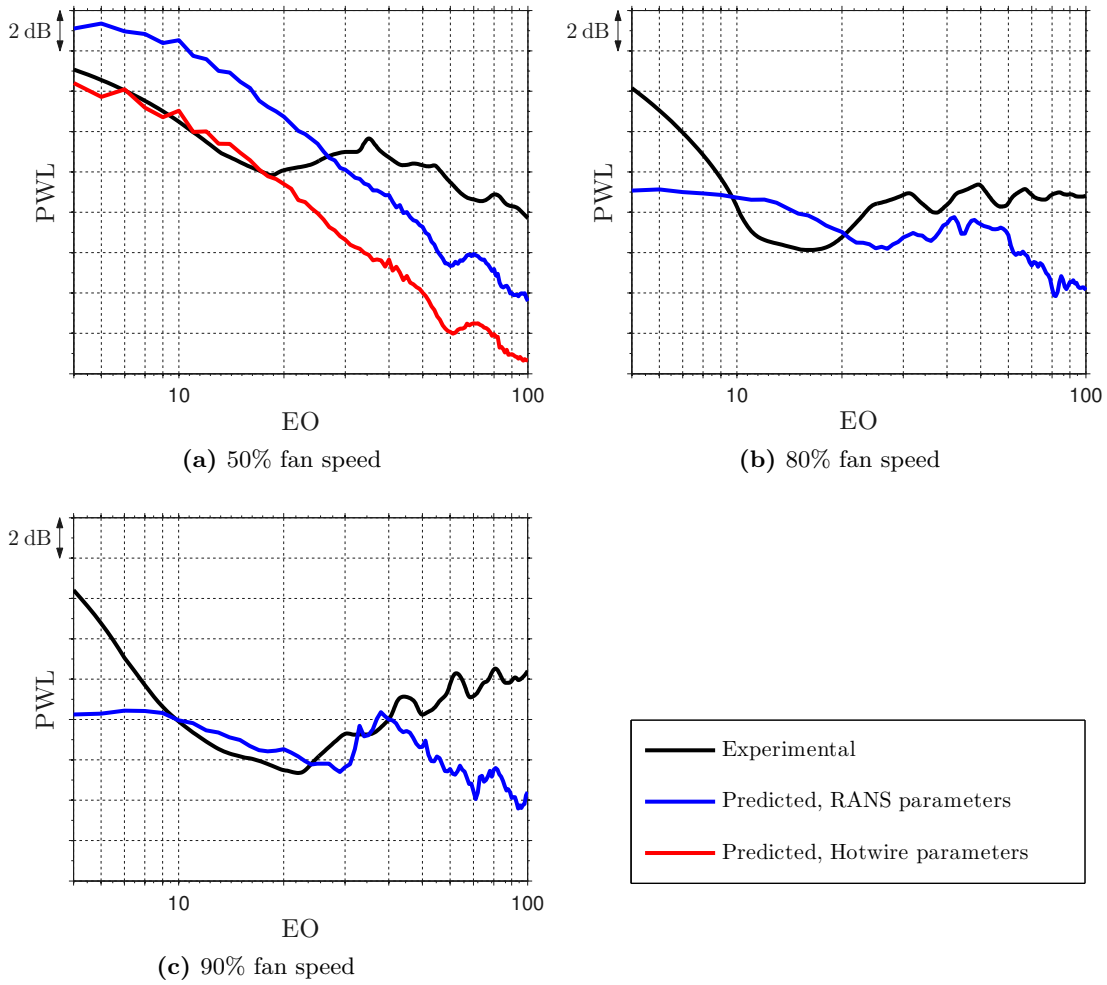

(a) 50% fan speed

(b) 80% fan speed

(c) 90% fan speed

Figure 9.19 – Forward-arc spectra: three fan speeds at working line 5 for the 44F OGV configuration. Black lines represent rear arc sound power spectra per unit EO from experiment while coloured lines indicate predicted noise. Blue lines show predictions obtained using turbulence and OGV flow data derived using RANS CFD solutions while red line indicates hotwire derived results. Hotwire data was not available at the higher fan speeds.

1. The prediction made using the hotwire-derived turbulence parameters (red line in Figure 9.19a) closely follows the measurements at low frequency. Figure 9.20a shows

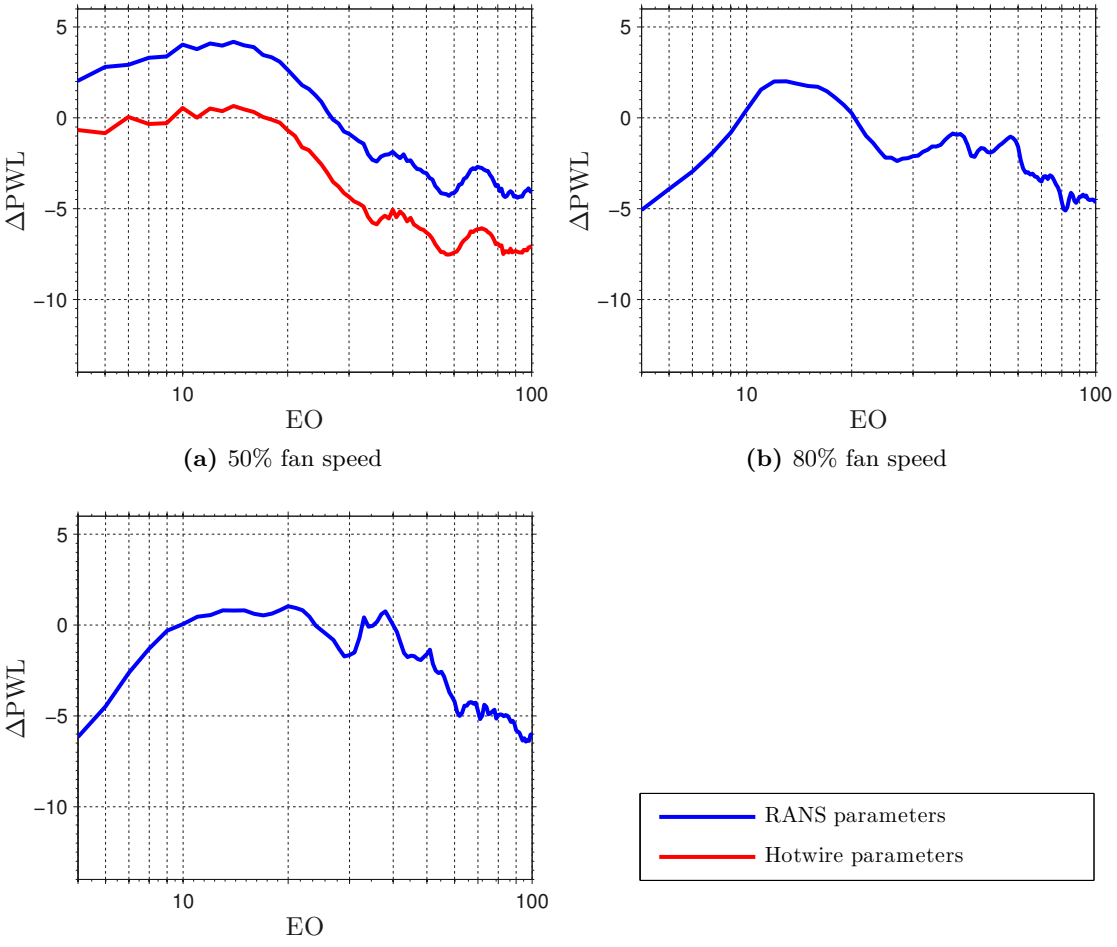

(a) 50% fan speed

(b) 80% fan speed

(c) 90% fan speed

Figure 9.20 – The difference between experimental and the predicted forward-arc PWL spectra shown in Figure 9.19 for three fan speeds at working line 5 with the 44F OGV configuration. Blue lines show predictions obtained using turbulence and OGV flow data derived using RANS CFD solutions while red lines indicate hotwire derived results. Hotwire data was not available at the higher fan speeds.

that difference is less than 1 dB for EO$<$ 20.

2. In Figure 9.19a the shape of the predictions obtained using the RANS-derived turbulence parameters is very similar to that obtained with hotwire-derived parameters. The two predictions are separated by $\approx$ 3.5 dB at all calculated frequencies. The same behaviour was observed in the rear-arc predictions discussed in Section 9.4.1 (see Item 2 on Page 187). These effects are considered further in Section 9.4.3.

3. Agreement between the predictions made at 80% and 90% fan speed (Figures 9.19b and 9.19c) are within $\pm$3 dB of the measurement for $7 \lesssim$ EO $\lesssim 60$ (see also Figures 9.20b and 9.20c). At frequencies EO$\lesssim$7 the measured noise increases considerably, suggesting contributions from a noise generation mechanism not accounted for in the present model.

4. At high frequencies EO$>$40 the measured spectra exhibit fan speed-dependent behaviour. At 50% fan speed a decay rate of $\approx$8 dB per decade is observed, at 80% fan speed the spectrum is flat whilst at 90% fan speed the noise level increases by $\approx$5 dB per decade. As mentioned in Section 9.4.1 this suggests that another noise source may be contributing to the measurements, possibly rotor self-noise or noise due to interactions between the rotor and the turbulent inlet boundary layer.

9.4.3 Sensitivity of noise predictions to input parameters

This section investigates the sensitivity of the noise predictions to using input turbulence data obtained from either RANS CFD or directly from hotwire data. It has been shown in Figures 9.16a and 9.19a that these two sets of parameters yield differences in predicted spectra of approximately 3.5 dB for the 44F-OGV. The differences calculated from the spectra shown in Figures 9.16a and 9.19a and from similar predictions made for the 28R and 28F-OGV configurations are summarised in Figure 9.21. The rear-arc and forward-arc data are indicated by solid and dashed lines respectively.

Very similar behaviour is observed in rear-arc and forward-arc predictions as the turbulence parameters are changed, differing by less than 1 dB. This suggests that variations in the lengthscale and mean-square turbulence velocity are the cause of the variations in predicted noise spectra: the mean flow being very similar in both cases (see Section 8.13).

9.4.4 Forward arc 'decel' noise comparison

Forward arc PWL data have been extracted at discrete engine orders over a range of fan speeds as the LSFR underwent a 'decel'; sweeping from high to low speed. Figure 9.22 shows the recorded experimental noise data at four normalised frequencies, EO $<$ 50. Noise predictions at three fan speeds, taken as the average sound power predicted at frequencies either side of the experimental engine order, are also shown for comparison. Higher frequencies are not shown as the match is poor for $\omega/\Omega \gtrsim 50$ EO, as observed in

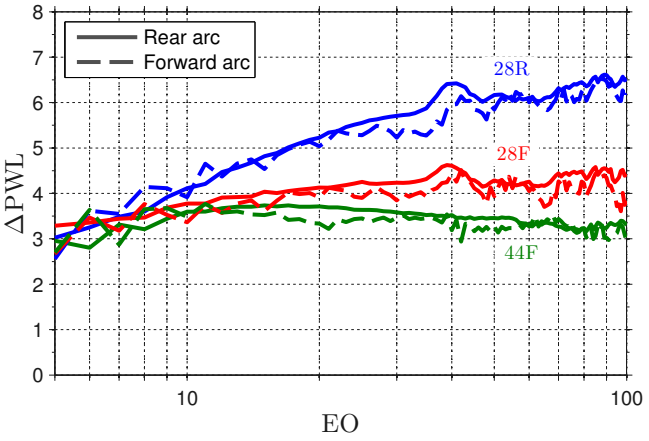

Figure 9.21 – Effects on predicted noise levels of changing input turbulence parameters obtained from hotwire data to parameters from RANS CFD using exact noise model. Solid lines indicate rear-arc and dashed lines show corresponding forward-arc results that are seen to be within 1 dB at all frequencies.

Section 9.4.2. The fifth plot, on the right hand side of each subfigure, shows the sum of the four single engine-order contributions.

1. Simulations predict the trends very well at discrete frequencies but absolute levels tend to be high at 12.5 EO, and decreasing relative to measurement as frequencies increase. This trend in absolute value was noted in Section 9.4.2.

2. When taking the sum of the four discrete normalised frequency data the predictions collapse onto the measured data to within 1.5 dB. The largest differences are observed at 50% fan speed.

9.5 Concluding remarks

This chapter has shown the results of predictions of rear-arc and forward-arc sound power for the Large Scale Fan Rig (LSFR) described in Chapter 8 with three OGV configurations at a range of operating conditions have been performed using the exact cascade and single airfoil noise models described in Chapters 2 and 4 and the rotor transmission models developed in Chapter 5. Input flow and turbulence parameters for these models have been obtained from the Rolls-Royce plc. mass flow prediction code Q263 in combination with analysis of hotwire data and RANS CFD solutions as described in Chapter 8. These predictions have been compared with noise measurements taken from the LSFR. The findings of this chapter are summarised below.

1. The rear-arc prediction made using the exact cascade noise model with hotwire-derived turbulence parameters (only available at 50% fan speed) is in agreement with LSFR measurement to within 2 dB for EO $<$ 40. The corresponding forward-arc prediction using the exact cascade rotor transmission model is within 1 dB of measurement for EO $<$ 20.

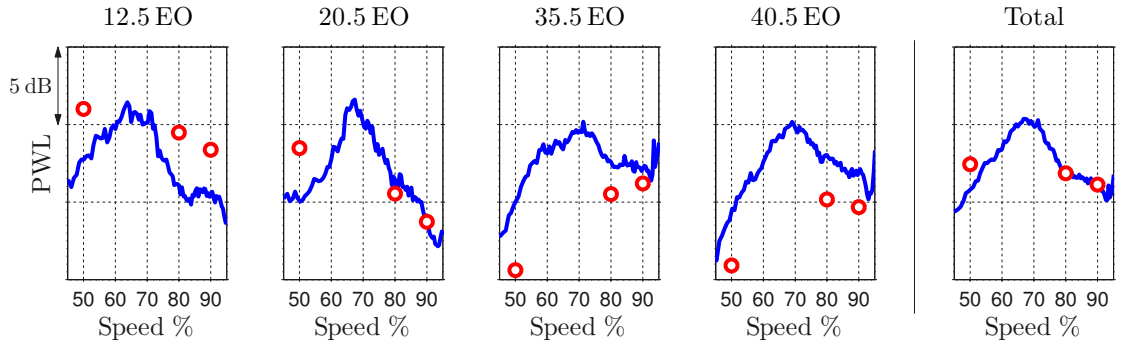

(a) 28R OGV

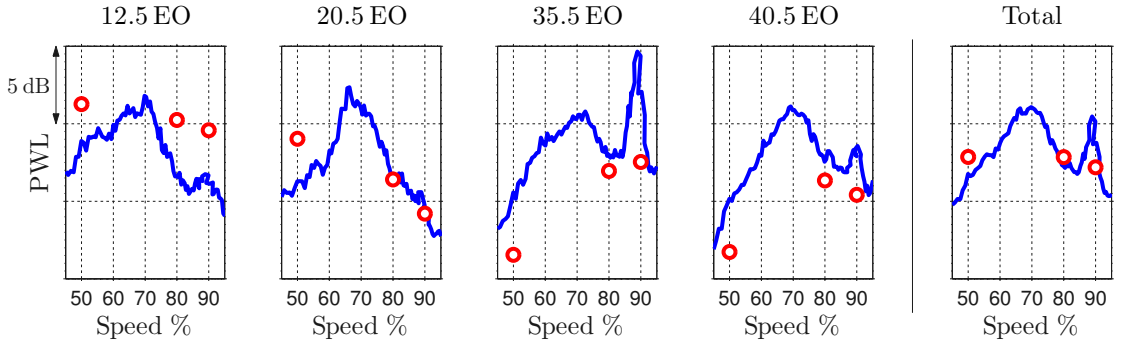

(b) 28F OGV

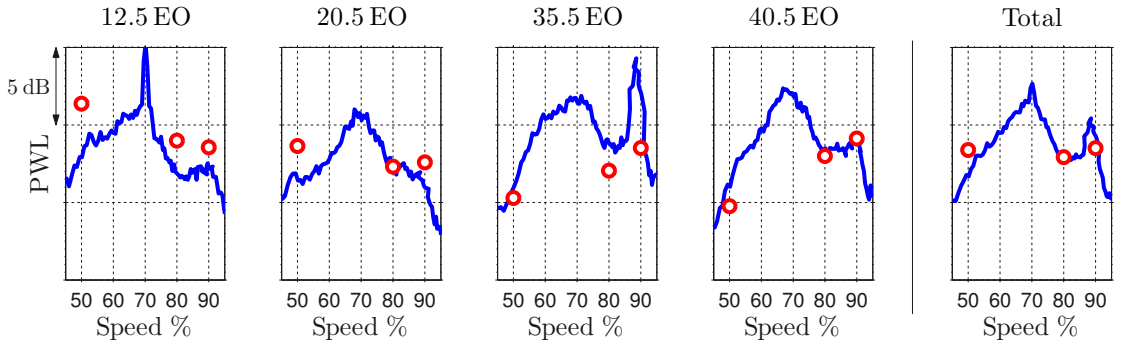

(c) 44F OGV

Figure 9.22 – Forward arc 'decel'. Comparison of predicted sound power level and experimental values at noted discrete normalised frequencies. Plots on the right hand side, marked 'Total', show the PWL associated with the sum of power in the four single-frequency sets of data. All predictions derived using RANS input data.

2. Predictions made using exact cascade noise and rotor transmission models with turbulence parameters obtained from RANS CFD solutions are higher than those predicted using hotwire-derived parameters, suggesting that the RANS CFD solutions are over-predicting the mean-square turbulence velocity.

3. All exact noise and rotor transmission model predictions differ from measurements at high frequencies EO$\gtrsim$40. Additional noise sources are suspected of contributing to the observed differences.

4. Rear-arc predictions made using the single-airfoil noise model show signs of convergence with the exact cascade model results for EO>20 as observed in Chapter 4. Convergence is to within 1.5 dB at 50% fan speed and 1 dB at the higher fan speeds. Relatively high values of the stator inter-vane modal cut-on frequency $\Delta\omega$ mean that significant cascade interactions effects are observed at the highest frequencies calculated. The values of $\Delta\omega$ are lower for the 28-vane OGV designs due to the reduction in vane count.

5. Non-physical values of rotor transmission are predicted when radiation power factors $\mathcal{H}$ are calculated using inlet (axial) flow values. Radiation is instead calculated using mean flow at the rotor as defined in the stationary frame of reference.

6. Frequency-averaged rotor transmission is typically at its span-wise maximum at $\hat{R} \approx 0.45$. At this location the incident modal sound power is concentrated around the nil-shielding angle, as predicted using the simplified plane-wave transmission model due to Kaji and Okazaki. Transmission levels greater than -2 dB are observed inboard of this location at all calculated fan speeds. For $\hat{R} \gtrsim 0.45$ transmission is found to be strongly dependent on fan speed. At high fan speeds the range of phase velocity angles over which the majority of sound power is incident becomes narrower whilst the frequency-averaged Kaji-Okazaki model shows that the range of phase velocity angles that have large rotor transmission coefficients also becomes narrower. Furthermore, the span-wise increase of rotor stagger angles leads to a misalignment of these two distributions that results in reduced transmission.

7. Overall rotor transmission spectral levels obtained from the ratio of total power transmitted to total power incident show distinct split into low and high frequency regions. At higher fan speeds the transmission level is reduced for $\omega/\Omega \lesssim 30$ EO. The predicted transmission level in the high frequency band shows little sensitivity to frequency.

8. Overall rotor transmission tends to reduce with increasing fan speed, although predictions show that the span-wise variation of the turbulence parameters can have a strong influence on the obtained values. This effect tends to counteract increases in interaction noise at higher fan speeds due to increasing Mach number onto the

OGV. The resulting forward-arc noise is weakly dependent on fan speed and is at its maximum for the 80% fan speed predictions.

Chapter 10

Conclusions

This thesis has presented a comprehensive framework for the prediction of broadband sound power radiated from a turbofan engine due to the interaction of the turbulent rotor wakes with the OGVs. This study has taken into consideration the development of turbulence in the rotor wakes, the nature of the OGV response to the incident turbulence and the transmission loss associated with the path through the rotor to the forward arc.

10.1 Prediction of broadband noise generation

It has been demonstrated that the blade-to-blade interactions in significantly overlapped cascades become weak at frequencies where several high-order modes are cut-on between the cascade vanes. The sound power radiated from a cascade under these multi-mode conditions is equivalent to the sound power radiated from the identical number of isolated airfoils in an identical flow. At high frequencies this allows the computationally intensive cascade formulation to be replaced by analytic single-airfoil calculations. Where cascades are non-overlapped the blade-to-blade interactions are universally weak and the limitation on agreement between the cascade formulation and the single airfoil formulation results from the periodicity condition imposed on cascade radiation.

10.2 Broadband rotor transmission loss

A model has been presented for the prediction of the broadband sound power transmission loss applied to noise incident on the rotor from the downstream OGV. Scattering coefficients calculated using the exact cascade formulation due to Smith [46], Whitehead [47] are time consuming to obtain, but excellent agreement is observed when the analytic semi-actuator disk scattering model due to Kaji and Okazaki [67] is applied. A simplified sound power scattering model has also been developed that allows simple interpretation of rotor blockage effects.

It has been found that significant transmission loss occurs where sound power incident on the rotor is concentrated at phase velocity angles that are not efficiently transmitted. The distributions of incident sound power and sound power transmission are both shown

to become narrow at high flow rates, so that misalignment of the two distributions is more likely although the rotor and OGV stagger angles are also significant in influencing this behaviour. This results in greater rotor blockage at high fan speeds where the relative flow rates approach and exceed sonic speeds towards the fan tip.

10.3 Analysis of rotor wakes

Parameters describing the characteristics of the turbulence incident on the OGV are required as inputs for the noise models. Such information as there is in the literature with regard to rotor wakes has been measured on small scale fan rigs at low speed. Turbulent wake measurements made on the Large Scale Fan Rig (LSFR) have been analysed in order to determine the turbulence parameters from a large scale fan rig at operational speeds.

10.3.1 Self-preserving mean wakes and mean wake overlap

A mean wake overlap model has been developed and analysis of the wake overlap behaviour has yielded a new method to determine parameters describing the relative width L_0 and maximum wake deficit ΔU of the individual mean wakes from a significantly overlapped ensemble-averaged wake profile, given an estimate of the individual mean wake free-stream velocity U_∞. The mean wake overlap model also allows the robust calculation of θ_m for significantly overlapped mean wakes, the calculation of which is subject to significant errors when the wake overlap effects are not taken into consideration.

Analysis of wake velocity data measured on the LSFR has shown that the flow at 50% fan speed is partially self-preserving when measured at axial locations sufficiently far downstream of the rotor. The self-preserving state is sensitive to the mean loading of the rotor blades (working line) and differs significantly from the findings of Gliebe et al. [19], suggesting a lack of universality in the self preserving state.

10.3.2 Anisotropy in measured turbulent wakes

The analysis of the rotor wake measurements has allowed the prediction of the mean-square turbulence velocity $\langle\overline{u^2}\rangle$ and turbulence integral lengthscale Λ at the OGV leading edge for inputs to the broadband noise model. In the noise model, the whirl component of assumed isotropic turbulence is used to predict the upwash velocity on the cascade surfaces. Component integral lengthscales from the LSFR data exhibit strong evidence of anisotropy, where the ratio of the streamwise to whirl component values is 1.2 rather than 2 in the isotropic model. Consequently, the input to the noise model may be underestimated by up to 3 dB at low frequencies.

10.3.3 RANS predictions of rotor wakes

RANS predictions of the rotor flows have been found to accurately predict the measured mean wake profiles. However, RANS over-predicts the maximum velocity deficit ΔU by

as much as 100% in the near wake region and typically over-predicts the mean-square turbulence velocity. It is not known whether the RANS prediction errors are influenced by the use of isotropic k-ω modelling for the prediction of flows that have since been found to exhibit anisotropy.

Predictions of turbulence lengthscale Λ obtained using RANS CFD by the use of an k-ω model agree with the values obtained from hotwire measurements at 50% fan speed measured within a factor of $C_\Lambda = 6.47$, which appears to be reasonably constant across different working lines and measurement locations. The applicability of this coefficient to different fan speeds is not known due to the lack of suitable measured data at higher fan speeds.

10.4 Prediction of rotor-stator broadband interaction noise

Noise predictions for LSFR have been made using the turbulence parameters derived from hotwire measurements and from RANS simulations. Comparison between the predictions and experimental rig measurement shows agreement to within 2 dB at low frequencies. At higher frequencies it appears that other noise sources may contribute to the measured spectra.

Noise predictions made using parameters derived from RANS solutions are higher in level than those from hotwire-derived turbulence parameters due to the increased mean-square velocity predicted by the RANS method. Larger differences are observed for the 28F and 28R OGVs that are situated progressively further downstream of the rotor.

It has been shown that the single airfoil noise model can be used to accurately predict high density cascade noise levels at frequencies where several high order modes are cut on between the vanes of the OGV. In practice, relatively high values of the stator inter-vane modal cut-on frequency $\Delta\omega$ mean that significant cascade interactions effects are observed at the highest frequencies required for audible frequency range calculations. The value of $\Delta\omega$ reduces as the vane separation increases and so single airfoil noise predictions may prove useful when applied to ultra-low count OGVs.

10.5 Rotor transmission loss predictions

Overall rotor transmission reduces with increasing fan speed, although predictions show that the span-wise variation of the turbulence parameters can have a strong influence on the obtained values. This effect tends to counteract increases in interaction noise at higher fan speeds due to increasing Mach number onto the OGV. The resulting forward-arc noise is weakly dependent on fan speed and is at its maximum for the 80% fan speed predictions.

Overall rotor transmission spectral levels obtained from the ratio of total power transmitted to total power incident show distinct split into low and high frequency regions. At higher fan speeds (80% and 90%) the rotor transmission loss increases at low frequencies.

The predicted transmission level in the high frequency band shows little sensitivity to frequency.

Frequency-averaged rotor transmission loss is typically at its span-wise minimum at $\hat{R} \approx 0.45$. At this location the incident modal sound power is concentrated around the nil-shielding angle. For $\hat{R} \gtrsim 0.45$ transmission is found to be strongly dependent on fan speed.

10.6 Recommendations for future work

Investigation of 'enhanced blockage' effects predicted by exact cascade transmission model

The location and depth of the 'enhanced blockage band' observed in L_τ spectra calculated using exact cascade rotor transmission model is not understood. For stationary fans this feature is located at $\omega/\Delta\omega = 1$. For rotating fans the observed normalised frequency is increased and the transmission loss in the band is increased.

Anisotropic turbulence modelling

Strong evidence of anisotropy has been identified in the turbulent rotor wakes measured on the LSFR, resulting in an underestimate of low frequency sound power in the noise model. An investigation of anisotropic turbulence models to account for the measured turbulence characteristics would increase the accuracy of the modelling.

Oscillation of hotwire probes

Large amplitude oscillations observed in the hotwire timeseries at high fan speeds, associated with vibrations of the hotwire probe, have caused difficulties in the analysis such that data derived from these high fan speeds have not been included. Further measurements with probes that do not exhibit this behaviour are required. Techniques may also be developed to assist in processing the present data.

Universality of RANS integral lengthscale fitting parameter C_Λ

It would be extremely useful to investigate the applicability to different fan speeds and geometries of the RANS CFD turbulence integral lengthscale scaling factor C_Λ defined in Section 8.10.1. This investigation will require hotwire wake velocity data and RANS flow predictions at a range of fan speeds and downstream locations.

Re-analysis of rotor wake hotwire velocity data

In the present study, the hotwire data have been analysed on the basis of using the maximum possible number of wake passages to assemble the ensemble-averages. To this end,

the ensemble averaging has been performed on all complete blade passages with an assumption that there are no inter-blade differences. This approach leads to the possibility that several important phenomena are masked. These include but are not limited to:

- Blade-to-blade differences.
- 'Wander' of the wake: In the present study the wake data have been resampled in a rotor-locked sense. However, the azimuthal distance between the rotor trailing edge and the wake centreline is not constant (see Figure 7.2). Low frequency perturbation of the azimuthal wake location can also lead to many of the phenomena that have here been attributed to mean wake overlap.

Further research of these effects would be useful. This will require a modification of the ensemble-averaging method (see Section 7.1.2) so that the changes to the mean wake behaviour may be seen as the number of ensembles included is altered and so that the averaging is performed over an entire revolution as opposed to a single passage.

Alternative prediction scheme for the turbulence integral lengthscale from hotwire data

It is noted that the turbulence integral lengthscales fitted to the component spectra are nearly proportional to the apparent wake width $\hat{L}_0$, as shown in Figure 8.15b. $\hat{L}_0$ can be determined from L_0 which can be predicted robustly. It is possible that this relation could used as the basis of a prediction method for Λ which avoids the use of unsteady wake parameters and is therefore more robust that the method shown in Section 8.11.2. A study of the accuracy of these models would be informative.

Sound power propagation in the interstage region

Construct a model for modal power propagation from stator upstream to rotor that properly accounts for changing mean flow and cross-sectional geometry so that sound power is not lost as modes become cut-off. This effect is particularly important at lower fan speeds and flow rates.

Effects of large turbulence lengthscales $\Lambda/s_\mathrm{s} \gtrsim 0.25$ on low frequency noise predictions

During the course of the present studies it has been observed that for large turbulence lengthscales $\Lambda/s_\mathrm{s} \gtrsim 0.25$ the low frequency response of the cascade increases relative to that predicted by the single airfoil model. This behaviour is of particular interest when designing low noise OGVs. Further investigation is suggested by considering the effect of the normalised turbulence integral lengthscale Λ/s_s on the frequencies at which agreement is observed between the single airfoil and cascade noise predictions.

Appendix A

Derivation of cut-on condition for cascade modes

The overlap of adjacent flat plate airfoils in a rectilinear cascade causes the formation of a rectangular duct, as illustrated in Figure A.1. The mean flow through the duct is parallel to the blades and has velocity $\mathbf{U}$ of magnitude U with components U_i in the x_i direction. The secondary coordinate system y_j is rotated by an angle θ with respect to the x_i axes and the mean flow is aligned with the y_1 axis, having velocity U in that direction.

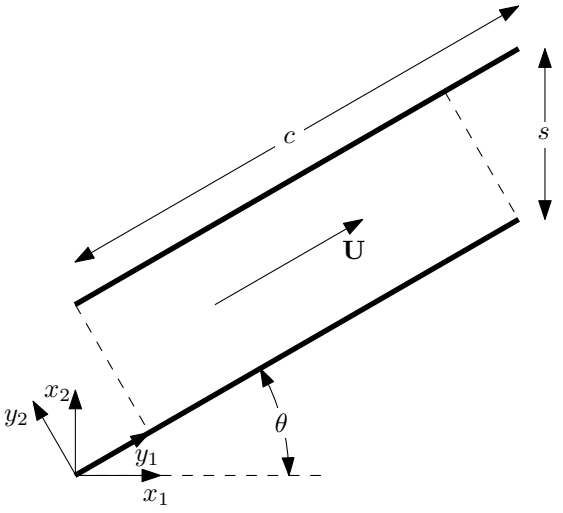

Figure A.1 – Geometry of the duct formed between adjacent fan blades.

The wave equation with one-dimensional convection is

$$\left[\frac{1}{c_0^2}\left(\frac{\partial}{\partial t}+U\frac{\partial}{\partial y_1}\right)^2-\nabla^2\right]p(\mathbf{x},t)=0, \tag{A.1}$$

where c_0 is the speed of sound propagation and p is the pressure perturbation. Assuming that p takes the form

$$p(\mathbf{x},t)=p(\mathbf{x})e^{\mathrm{i}\omega t}, \tag{A.2}$$

where ω is the angular frequency then Equation (A.1) gives

$$\left[\left(\mathrm{i}k + M\frac{\partial}{\partial y_1}\right)^2 - \nabla^2\right] p(\mathbf{x}) = 0, \tag{A.3}$$

where $k = \omega/c_0$ is the wavenumber and M is the Mach number. If it is also assumed that $p(\mathbf{x}) = Y_1(y_1)Y_2(y_2)$ then

$$\frac{-\beta^2 Y_1''}{Y_1} + \frac{2\mathrm{i}kMY_1'}{Y_1} - k^2 = \frac{Y_2''}{Y_2}, \tag{A.4}$$

where $'$ denotes a partial derivative. Both sides of this equation must be constant so it is possible to define

$$\frac{Y_2''}{Y_2} = -k_2^2, \tag{A.5}$$

$$\implies Y_2'' + k^2 Y_2 = 0. \tag{A.6}$$

Assuming a solution of the form $Y_2 = Ae^{\mathrm{i}k_2 y_2} + Be^{-\mathrm{i}k_2 y_2}$ and applying hard-walled boundary conditions $Y_2' = 0$ at $y_2 = 0$;

$$\mathrm{i}k_2 (A - B) = 0 \iff A = B. \tag{A.7}$$

So now

$$Y_2 = A\left(e^{\mathrm{i}k_2 y_2} + e^{-\mathrm{i}k_2 y_2}\right) = \hat{A}\cos k_2 y_2. \tag{A.8}$$

At $y_2 = s\cos\theta$ the boundary condition yields

$$-k_2\hat{A}\sin k_2 s\cos\theta = 0, \tag{A.9}$$

which is satisfied when

$$k_2 s\cos\theta = n\pi, \quad n \in \mathbb{Z}. \tag{A.10}$$

Therefore there are an infinite number of possible modes of order n, having components $k_{1,n}$ and $k_{2,n}$ in the y_1 and y_2 directions respectively.

Equations (A.4) and (A.5) give

$$\beta^2 Y_1'' - 2\mathrm{i}kMY_1' + \left(k^2 - k_{2,n}^2\right) Y_1 = 0. \tag{A.11}$$

Assuming that $Y_1 = De^{\mathrm{i}k_{1,n}y_1}$ this yields

$$-\beta^2 k_{1,n}^2 + 2kMk_{1,n} + \left(k^2 - k_{2,n}^2\right) = 0, \tag{A.12}$$

and so

$$k_{1,n} = \frac{kM \pm \sqrt{k^2 - \beta^2 k_{2,n}^2}}{\beta^2}. \tag{A.13}$$

For a mode to be cut-on its axial wavenumber component must be purely real. This condition requires that

$$k^2 - \beta^2 k_{2,n}^2 > 0, \tag{A.14}$$

so Equation (A.10) yields the following condition for the wavenumber magnitude in order for a mode of order n to be cut-on

$$\frac{ks\cos\theta}{\beta} > n\pi. \tag{A.15}$$

Appendix B

RANS CFD calculations

This appendix was contributed by John Coupland at Rolls-Royce who conducted the RANS CFD predictions of the LSFR that are discussed in Chapter 8.

RANS CFD calculations were conducted of the LSFR to provide a prediction of the turbulent rotor wake characteristics. The RANS CFD employed the Rolls-Royce plc. code, HYDRA, which is a general purpose CFD code for hybrid unstructured meshes and uses an efficient edge based data structure. The flow equations are integrated around a median-dual control volume using a MUSCL based flux-differencing algorithm. The discrete flow equations are iterated towards a steady state using a 5-stage Runge-Kutta scheme. Convergence to a steady state is further accelerated through use of an element collapsing multi-grid algorithm. The solver runs in parallel on both shared and distributed memory machines using domain decomposition.

For RANS modelling the Reynolds stresses are modelled using the Boussinesq hypothesis based on an isotropic turbulent viscosity. Note that the normal Reynolds stresses themselves are not isotropic in this model.

For these RANS calculations the k-ω/SST turbulence model is used to determine the turbulent viscosity, from

$$\mu_{\mathrm{T}} = \frac{\rho k}{\omega}, \tag{B.1}$$

where ρ is the mean flow density, k is the specific turbulence energy

$$k = \tfrac{1}{2}\left(\overline{u'^2} + \overline{v'^2} + \overline{w'^2}\right), \tag{B.2}$$

and ω is related to the turbulence dissipation rate ϵ through

$$\omega = \frac{\epsilon}{C_\mu k}, \tag{B.3}$$

where $C_\mu = 0.09$ is a standard empirical constant for this form of turbulence model determined from the ratio of turbulent shear stress to turbulence energy in the logarithmic region of a turbulent wall boundary layer. In the k-ω/SST turbulence model two additional transport equations, for k and ω, in addition to the RANS transport equations for mass,

momentum and energy, are solved.

For comparison with turbulent length scales derived from the LSFR hot-wire measurements then a turbulent mixing length scale can be derived from

$$L_{\text{mix}} = \frac{k^{1/2}}{C_\mu^{1/4}\omega}, \tag{B.4}$$

and a larger length scale, more representative of an integral length scale, using

$$\Lambda_{\text{RANS}} = \frac{k^{1/2}}{C_\mu\omega}. \tag{B.5}$$

Note that the values given by Equations (B.4) and (B.5) differ by a factor of 6.1. In general, the relationship between the turbulence parameters k and ω and the integral length scale Λ is not well defined and some degree of empiricism will be required to determine the best scaling of the two parameters. Nallasamy and Envia [80] use the length scale Λ_{RANS} above (although based on use of a k-ϵ turbulence model) as input to a broadband noise model. In Section 8.10.1 it shall be shown that adequate agreement with Λ obtained from hotwire data at 50% fan speed using an isotropic turbulence model assumption is given using Equation (8.12), reproduced below

$$\Lambda = C_\Lambda \frac{k^{1/2}}{\omega}.$$

where $C_\Lambda = 6.47$ is a constant factor. The value of Λ obtained using Equation (8.12) falls between the values given by Equations (B.4) and (B.5) and gives a lengthscale that is approximately half that used by Nallasamy and Envia [80].

Some investigation of the sensitivity of the RANS predictions to the turbulence model used were done using other models available in HYDRA

- k-ϵ CMOTT two equation model
- Spalart-Allmaras one equation model

In terms of overall fan performance there was little difference between the three turbulence models for the LSFR, except at lower flow rates than those on the working lines considered here. There were some small differences in wake turbulence parameters from the k-ϵ and k-ω turbulence models, with the k-ϵ model used here giving lower wake turbulence intensity than k-ω by around 10%. (The Spalart-Allmaras model does not give a direct prediction of turbulence intensity or length scale.)

To determine the wake properties of the fan in the LSFR rig the RANS computations covered a domain including the fan and the bypass duct, splitter and core duct. The bypass duct OGV and the engine section stator (ESS) are *n*ot included in the CFD domain. Including these blades would of course make the RANS CFD a fully unsteady calculation, and a sliding plane would be needed between the fan and the OGV/ESS. Rather the

approach here is to extend the bypass duct beyond the location of the OGV and then to extract turbulent wake parameters at the OGV leading edge location (or indeed at hotwire measurement locations) by interpolation of the CFD solution. This approach neglects the upstream influence of the OGV on the fan aerodynamics, which does cause some radial redistribution of the flow across the fan, and on the wake evolution. The more important influence of the splitter geometry on the fan flow is though represented in the current model. Figure B.1 illustrates the extent of the CFD domain.

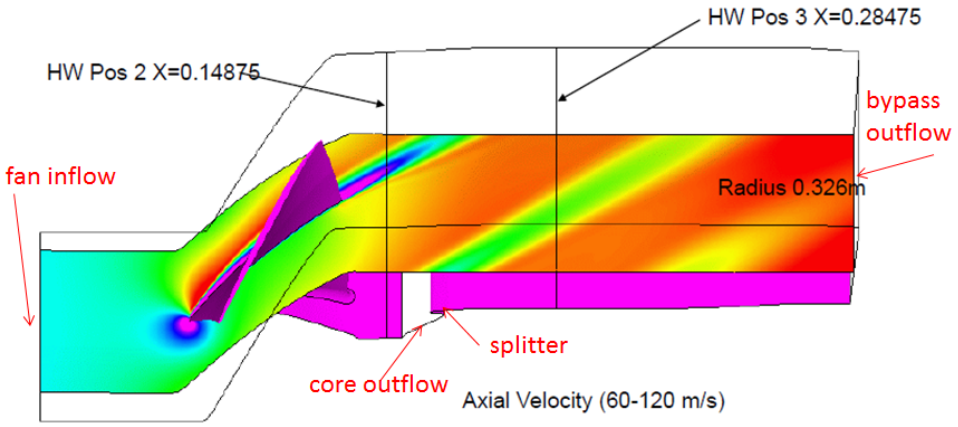

Figure B.1 – RANS CFD Fan and Bypass Duct Arrangement.

For the LSFR system there were some differences in bypass duct geometry with different OGV number and position. These differences were reflected in different RANS CFD computations done for the 28F and 28R OGV configurations.

A hexahedral mesh of around 3 million cells, generated using the Rolls-Royce in-house software PADRAM [90], was used for the fan calculations. The blade surface mesh and near wall resolution was typical of that used for fan aerodynamics predictions in HYDRA, but the stream-wise mesh downstream of the fan was much finer than standard to limit the numerical mixing of the wake along the bypass duct. With the long bypass duct of these configurations this led to the large total mesh size.

The RANS problem was solved in the frame of reference rotating with the fan, but all walls were set as stationary in the absolute frame except for the spinner and fan hub which move with the fan. The rotor tip gap was modelled using the standard tip gap size recommended for rig rotor blades.

Boundary conditions for the RANS CFD were

- Prescribed total pressure (including the casing boundary layer), total temperature, and whirl and radial flow angles at the inflow plane.
- Radial equilibrium static pressure profile at the bypass duct outflow.
- Radial equilibrium static pressure profile at the core duct outflow, scaled to achieve a prescribed mass flow split (bypass ratio) between the bypass flow and core flow.

- An inflow turbulent intensity of 0.5% of the mean inflow axial velocity. This is used to define the inflow turbulent kinetic energy

$$k_{\text{inflow}} = \left(0.005\overline{U_x}\right)^2. \tag{B.6}$$

- An inflow dissipation rate calculated by setting

$$\left(\frac{\mu_{\text{T}}}{\mu}\right)_{\text{inflow}} = 10. \tag{B.7}$$

The bypass duct static pressure is scaled to achieve a specific operating point of the fan system. In general a range of operating points are calculated to give a prediction of the fan characteristics, and the solution for a particular working line is defined at the operating point where the fan pressure ratio characteristic coincided with the working line itself.

Note that the hotwire measurements of the fan inflow free-stream turbulence discussed later actually suggest an inflow turbulence intensity of around 1%. This difference is not though expected to have any significant effect on the overall fan performance and wake turbulence prediction.

Appendix C

Fitting skewed wake function to mean wakes

In Section 8.2.1 an asymmetric wake function was proposed to describe the measured ensemble averaged rotor wakes. The coefficients of its polynomial terms have been determined from the LSFR mean wake data. This appendix describes the process employed to choose their values.

For each hotwire measurement coefficients a_i were used to fit the function

$$f(\eta) = \exp\left[a_1\eta^2 + a_2\eta^3 + a_3\eta^4\right] \tag{C.1}$$

to the experimental data using a least-squares method. Example values, plotted against normalised measurement radius $\hat{R}$, are shown in Figure C.1 for measurements made at 50% fan speed, working line 5, at Pos.1. Also shown are the mean values for each a_i and a 95% confidence interval. No strong radial variations are seen in the fitted values of a_i.

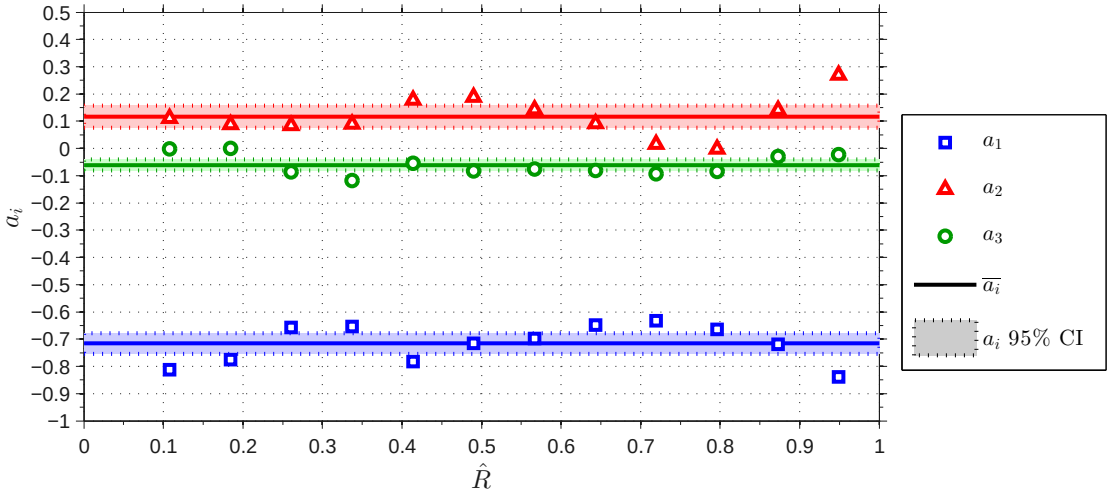

Figure C.1 – Values of the fitting coefficients a_i plotted against normalised radius $\hat{R}$ for measurements at 50% fan speed, working line 5, at Pos.1. Also marked are the mean values and 95% confidence intervals for each measurement i.

The fitted mean values and 95% confidence intervals for all cases are shown in Fig-

ure C.2. All Pos.1 values at 35% and 50% fan speed are in reasonable agreement, but considerable differences are seen as either the axial distance or fan speed is increased. In particular, the large confidence intervals associated with the higher fan speeds indicate a large spread of the fitted values due to probe vibration, whilst the Pos.2 and Pos.3 results are internally consistent but show a tendency towards a more symmetric sinusoidal shape, as noted in Section 8.2.1. Working line appears to have no systematic effect on wake profile shape.

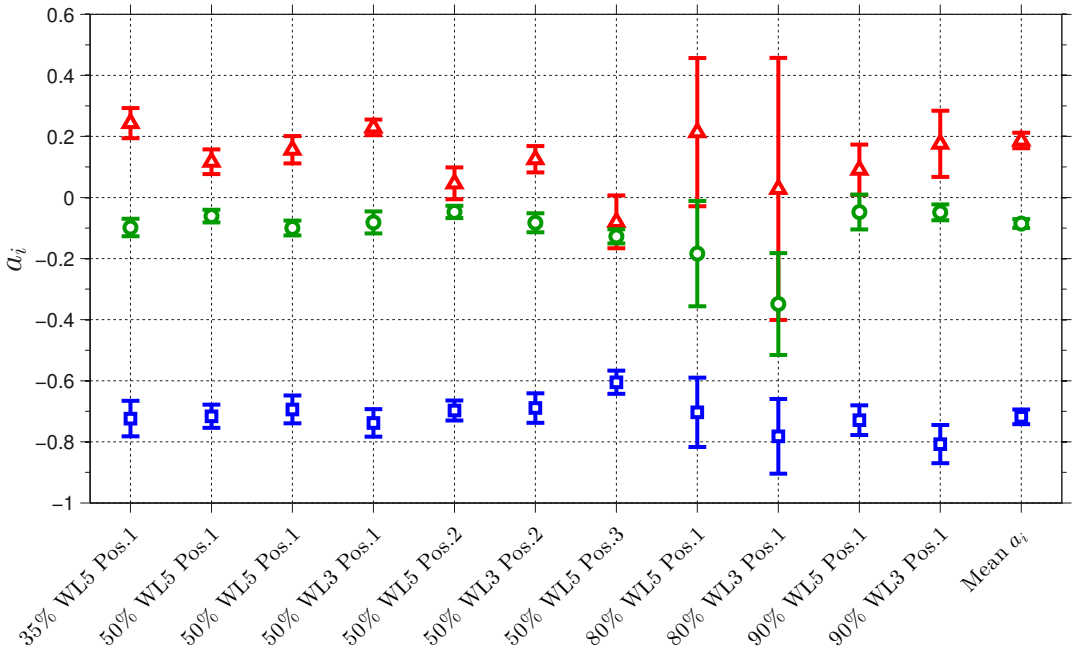

Figure C.2 – Mean values and 95% confidence intervals for fitting coefficients a_i for all hotwire measurements.

In light of the consistency in shape of the low fan speed cases at Pos.1, the mean derived from these four cases is used for the polynomial coefficients. These values and the corresponding 95% confidence interval are shown on the far right hand side of Figure C.2.

The values of a_i produced using this method result in an incorrect value of $L_0 = 0.96$ for the new wake function in Equation (C.1). The width of the wake function was corrected by scaling η by 0.96 to give the function given in Equation (8.3), reproduced below:

$$f_{\mathrm{S}}(\eta) = \exp\left[-0.661\eta^2 + 0.165\eta^3 - 0.072\eta^4\right].$$

Appendix D

Deducing sound power from in-duct sound pressure measurements

The rear-arc noise measurements taken on the Large Scale Fan Rig (LSFR) are records of sound pressure rather than the sound power predictions obtained from the cascade and single airfoil noise models. In order that the simulation data can be validated it is necessary to infer sound power from the sound pressure measurements.

The bypass duct is assumed to be a hemi-diffuse field where all cut-on modes carry equal power. In such a field the intensity is given by

$$I = \frac{\langle \bar{p}^2 \rangle}{2\rho_0 c_0}, \tag{D.1}$$

where $\langle \bar{p}^2 \rangle$ is the spatially averaged mean-square pressure, ρ_0 is the density and c_0 is the sound speed. The mean-square pressure at the duct wall is given to be

$$\bar{p}_w^2 = 2 \left\langle \bar{p}^2 \right\rangle. \tag{D.2}$$

Combining Equations (D.1) and (D.2) and integrating across the entire duct area results in the following expression for the total sound power

$$W = S \frac{\bar{p}_w^2}{4\rho_0 c_0}, \tag{D.3}$$

where S is the area of the duct. Recalling the relation between the reference pressure and power

$$p_{\text{ref}}^2 = \rho_0 c_0 W_{\text{ref}}, \tag{D.4}$$

substitution of Equation (D.3) into the definition of the sound power level yields

$$\text{PWL} = 10 \log_{10} \left(\frac{\bar{p}_w^2}{p_{\text{ref}}^2} \right) + 10 \log_{10} \left(\frac{S}{4} \right). \tag{D.5}$$

The annular are of the LSFR downstream measurement section is $S = 0.4\,\text{m}^2$. The last 'correction' term in Equation (D.5) therefore has the value -10 dB.

References

[1] Advisory Council for Aeronautics Research in Europe (ACARE). Aeronautics and Air Transport: Beyond Vision 2020 (Towards 2050). Technical report, European Comission, 2010.

[2] EUROCONTROL. EUROCONTROL Medium-Term Forecast: IFR Flight Movements 2013 - 2019. Technical report, EUROCONTROL, February 2013.

[3] H.A. Kumasaka, M.M. Martinez, and D.S. Weir. Definition of 1992 Technology Aircraft Noise Levels and the Methodology for Assessing Airplane Noise Impact of Component Noise Reduction Concepts. NASA Contractor Report CR-198298, NASA, Langley Research Center Hampton, Virginia 23681-0001, June 1996.

[4] N. Cumpsty. *Jet Propulsion: A simple guide to the aerodynamic and thermodynamic design and performance of jet engines*. Cambridge Univ Press, 2nd edition, 2003.

[5] U.W. Ganz, P.D. Joppa, T.J. Patten, and D.F. Scharpf. Boeing 18-inch Fan Rig Broadband Noise Test. Contractor Report NASA/CR-1998-208704, NASA, 1998.

[6] H. Blasius. *Grenzschichten in Flüssigkeiten mit kleiner Reibung*. Druck von BG Teubner, 1907.

[7] Y.B. Zel'dovich. Limiting laws for turbulent flows in free convection. *Zhurnal Eksperimental'noi Teoreticheskoi Fiziki (Journal of Experimental and Theoretical Physics)*, 7(12):1463, 1937.

[8] A.A. Townsend. *The Structure of Turbulent Shear Flow*. Cambridge Monographs on Mechanics. Cambridge University Press, 2nd edition, 1976.

[9] K.R. Sreenivasan and R. Narasimha. Equilibrium parameters for two-dimensional turbulent wakes. *Journal of Fluids Engineering*, 104(2):167–169, 1982.

[10] P.R. Louchez, J.G. Kawall, and J.F. Keffer. Investigation of the detailed spread characteristics of plane turbulent wakes. In *Turbulent Shear Flows 5*, pages 98–109. Springer, 1987.

[11] P.M. Bevilaqua and P.S. Lykoudis. Turbulence memory in self-preserving wakes. *Journal of Fluid Mechanics*, 89(3):589–606, 1978.

[12] I. Wygnanski, F. Champagne, and B. Marasli. On the large-scale structures in two-dimensional, small-deficit, turbulent wakes. *Journal of Fluid Mechanics*, 168:31–71, 1986.

[13] B. Marasli, F.H. Champagne, and I. Wygnanski. Effect of travelling waves on the growth of a plane turbulent wake. *Journal of Fluid Mechanics*, 235:511–528, 1992.

[14] W.K. George. The self-preservation of turbulent flows and its relations to initial conditions and coherent structures. In *Advances in Turbulence*, pages 39–73. Hemisphere, NY, 1989.

[15] W.K. George. The decay of homogeneous isotropic turbulence. *Physics of Fluids*, 4: 1492–1509, July 1992. doi: 10.1063/1.858423.

[16] S. Ghosal and M.M. Rogers. A numerical study of self-similarity in a turbulent plane wake using large-eddy simulation. *Physics of Fluids*, 9:1729, 1997.

[17] R.D. Moser, M.M. Rogers, and D.W. Ewing. Self-similarity of time-evolving plane wakes. *Journal of Fluid Mechanics*, 367(1):255–289, 1998.

[18] R.L. Evans. Turbulence and unsteadiness measurements downstream of a moving blade row. *Journal of Engineering for Power*, 97:131, 1975.

[19] P. Gliebe, R. Mani, H. Shin, B. Mitchell, G. Ashford, S. Salamah, and S. Connell. Aeroacoustic Prediction Codes. Contract Report NASA/CR-2000-210244, NASA, NASA Glenn Reasearch Centre, Cleveland, OH 44135, 2000.

[20] M. Nallasamy, E. Envia, S.A. Thorp, and A. Shabbir. Fan noise source diagnostic test computation of rotor wake turbulence noise. *NASA STI/Recon Technical Report N*, 3:03693, 2002.

[21] E. Envia, A.G. Wilson, and D.L. Huff. Fan noise: A challenge to CAA. *International Journal of Computational Fluid Dynamics*, 18(6):471–480, 2004.

[22] V. Jurdic, P.F. Joseph, and J. Antoni. Investigation of rotor wake turbulence through cyclostationary spectral analysis. *AIAA Journal*, 47(9):2022–2030, September 2009.

[23] V. Jurdic. *An Investigation into broadband noise due to rotor-stator interaction*. PhD thesis, Institute of Sound and Vibration Research, Southampton, UK, 2009.

[24] T. von Kármán and W.R. Sears. Airfoil theory for non-uniform motion. *Journal of the Aeronautical Sciences (Institute of the Aeronautical Sciences)*, 5(10), 1938.

[25] T. Theodorsen. General theory of aerodynamic instability and the mechanism of flutter. Technical Report NACA-TR-496, NACA, 1935.

[26] H.G. Küssner. Zusammenfassender bericht über den instationären auftrieb von flügeln. *Luftfahrtforschung*, 13(12):410–424, 1936.

[27] W.R. Sears. Some aspects of non-stationary airfoil theory and its practical applications. *Journal of Aeronautical Sciences*, 8(3):104–108, 1941.

[28] N. Curle. The influence of solid boundaries upon aerodymanic sound. *Proceedings of the Royal Society A*, 231:505–514, 1955.

[29] M.J. Lighthill. On sound generated aerodynamically. 1. General theory. *Proceedings of the Royal Society A*, 211:564–587, 1952.

[30] L.T. Filotas. Response of an Infinite Wing to an Oblique Sinusoidal Gust: A Generalization of Sears' Problem. *NASA Special Publication*, 207:231, 1969.

[31] J.M.R. Graham. Lifting surface theory for the problem of an arbitrarily yawed sinusoidal gust incident on a thin aerofoil in incompressible flow. *Aeronautical Quarterly*, 21:182–198, 1970.

[32] C. Osborne. Unsteady thin-airfoil theory for subsonic flow. *AIAA Journal*, 11(2): 205–209, 1973.

[33] R.K. Amiet. Compressibility effects in unsteady thin-airfoil theory. *AIAA Journal*, 12(2):252–255, 1974.

[34] J.M.R. Graham. Similarity rules for thin aerofoils in non-stationary subsonic flows. *Journal of Fluid Mechanics*, 43(4):753–766, 1970.

[35] J.J. Adamczyk. Passage of a swept airfoil through an oblique gust. *Journal of Aircraft*, 11(5):281–287, 1974.

[36] R.K. Amiet. Acoustic radiation from an airfoil in a turbulent stream. *Journal of Sound and Vibration*, 41(4):407–420, 1975.

[37] R.W. Paterson and R.K. Amiet. Noise and surface pressure response of an airfoil to incident turbulence. *Journal of aircraft*, 14(8):729–736, 1977.

[38] M. Roger, S. Moreau, and A. Guedel. Broadband fan noise prediction using single airfoil theory. *Noise Control Engineering Journal*, 54(1):5–14, 2006.

[39] S. Moreau and M. Roger. Competing broadband noise mechanisms in low-speed axial fans. *AIAA Journal*, 45(1):48–57, 2007.

[40] A. Pagano, M. Barbarino, D. Casalino, and L. Federico. Tonal and broadband noise calculations for aeroacoustic optimization of pusher propeller. *Journal of Aircraft*, 47 (3):835–848, 2010.

[41] V.P. Blandeau, P.F. Joseph, and G. Gabard. Sound power radiation due to an isolated airfoil in a turbulent stream. In *ICA2010*, 2010.

[42] R.K. Amiet. High frequency thin-airfoil theory for subsonic flow. *AIAA Journal*, 14 (8):1076–1082, 1976.

[43] F. Lane and M. Friedman. Unsteady aerodynamics of vortical flows: early and recent developments. Technical Note NACA-TN-4136, NACA, 1958.

[44] D.S. Whitehead. Bending Flutter of Unstalled Cascade Blades at Finite Deflection. Reports and Memoranda R. & M. No. 3386, Ministry of Aviation, Aeronautical Reseach Council, London, 1965.

[45] S. Kaji and T. Okazaki. Generation of sound by rotor stator interaction. *Journal of Sound and Vibration*, 13:281–307, 1970.

[46] S.N. Smith. Discrete Frequency Sound Generation in Axial Flow Turbomachines. Technical report, University Engineering Department, Cambridge, 1973.

[47] D.S. Whitehead. Classical two-dimensional methods. In M.F. Platzer and Carta F.O., editors, *AGARD Manual on Aeroelasticity in Axial-Flow Turbomachines Volume 1 Unsteady Turbomachinery Aerodynamics*, chapter III Classical two-dimensional methods, pages 3.1–3.30. AGARD, Neuilly sur Seine, 1987.

[48] R. Mani and G. Horvay. Sound transmission through blade rows. *Journal of Sound and Vibration*, 12(1):59–83, 1970.

[49] N. Peake. The interaction between a high-frequency gust and a blade row. *Journal of Fluid Mechanics*, 241:261–289, 1992.

[50] N. Peake. The scattering of vorticity waves by an infinite cascade of flat plates in subsonic flow. *Wave Motion*, 18:255–271, 1993.

[51] N. Peake and E.J. Kerschen. Influence of mean loading on noise generated by the interction of gusts with a flat-plate cascade: upstream radiation. *Journal of Fluid Mechanics*, 347:315–346, 1997.

[52] I. Evers and N. Peake. On sound generation by the interaction between turbulence and a cascade of airfoils with non-uniform mean flow. *Journal of Fluid Mechanics*, 463:25–52, 2002.

[53] D.B. Hanson and K.P. Horan. Turbulence / cascade interaction: spectra of inflow, cascade response and noise. In *4th AIAA/CEAS Aeroacoustics Conference 1998*, Toulouse, France, 1998. American Institute of Aeronautics and Astronautics. Have printed copy of paper.

[54] S.A.L. Glegg. The response of a swept blade row to a three-dimensional gust. *Journal of Sound and Vibration*, 227(1):29–64, 1999.

[55] D.B. Hanson. Acoustic reflection and transmission of 2-dimensional rotors and stators, including mode and frequency scattering effects. Technical Report CR—1999-208880, NASA, 1999.

[56] D.B. Hanson. Theory for Broadband Noise of Rotor and Stator Cascades With Inhomogeneous Inflow Turbulence Including Effects of Lean and Sweep. Contractor report NASA/CR–2001-210762, NASA, Glenn Research Center, 2001.

[57] D.B. Hanson. Broadband noise of fans - with unsteady coupling theory to account for rotor and stator reflection/transmission effects. Technical report, NASA, 2001.

[58] D.B. Hanson. Broadband theory for coupled fan stages including blade row reflection/transmission effects. In *8th AIAA/CEAS Aeroacoustics Conference & Exhibit*, number AIAA-2002-2488, Brekenridge, CO, USA, 2002. American Institute of Aeronautics and Astronautics.

[59] C. Cheong, P.F. Joseph, and S. Lee. High frequency formulation for the acoustic power spectrum due to cascade-turbulence interaction. *Journal of the Acoustical Society of America*, 119(1):108–122, January 2006.

[60] M.E. Goldstein. *Aeroacoustics*. McGraw-Hill, New York, first edition, 1976.

[61] H. Atassi and G. Hamad. Sound generated in a cascade by three-dimensional disturbances convected in a subsonic flow. In *7th AIAA Aero-Acoustics Conference*, Palo Alto, CA, USA, 1981. American Institute of Aeronautics and Astronautics.

[62] H. Posson, S. Moreau, and M. Roger. On the use of a uniformly valid analytical cascade response function for fan broadband noise predictions. *Journal of Sound and Vibration*, 329(18):3721–3743, 2010.

[63] H. Posson, M. Roger, and S. Moreau. On a uniformly valid analytical rectilinear cascade response function. *Journal of Fluid Mechanics*, 663:22–52, 11 2010. ISSN 1469-7645. doi: 10.1017/S0022112010003368.

[64] A.E.D. Lloyd and N. Peake. Rotor - Stator Broadband Noise Prediction. In *14th AIAA/CEAS Aeroacoustics Conference*, number AIAA-2008-2840, Vancouver, British Columbia, Canada, 2008. American Institute of Aeronautics and Astronautics.

[65] B. El Hadidi and H.M. Atassi. High Frequency Sound Radiation From an Annular Cascade in Swirling Flows. In *8th AIAA/CEAS Aeroacoustics Conference and Exhibit*, number AIAA-2002-2560, Breckenridge, CO, USA, 2002. American Institute of Aeronautics and Astronautics.

[66] H.M. Atassi, A.A. Ali, O.V. Atassi, and I.V. Vinogradov. Scattering of incident disturbances by an annular cascade in a swirling flow. *Journal of Fluid Mechanics*, 499:111–138, 2004.

[67] S. Kaji and T. Okazaki. Propagation of sound waves through a blade row. I. Analysis based on semi-actuator disk theory. *Journal of Sound and Vibration*, 11(3):339–353, 1970.

[68] S. Kaji and T. Okazaki. Propagation of sound waves through a blade row. II. Analysis based on the acceleration potential method. *Journal of Sound and Vibration*, 11(3): 355–75, 1970.

[69] W. Koch. On the transmission of sound waves through a blade row. *Journal of Sound and Vibration*, 18(1):111–128, 1971.

[70] H. Posson and M. Roger. Parametric study of gust scattering and sound transmission through a blade row. In *13th AIAA/CEAS Aeroacoustics Conference(28th AIAA Aeroacoustics Conference)*, Rome, Italy, 2007. American Institute of Aeronautics and Astronautics.

[71] H. Posson, S.H.B. Moreau, Y. Buot de l'Epine, and C. Schram. Prediction of sound transmission through an annular cascade using an analytical cascade response function. In *16th AIAA/CEAS Aeroacoustics Conference*, Stockholm, Sweden, 2010. American Institute of Aeronautics and Astronautics.

[72] H. Posson and S. Moreau. Rotor-shielding effect on fan-OGV broadband noise prediction. In *17th AIAA/CEAS Aeroacoustics Conference (32nd AIAA Aeroacoustics Conference)*, number AIAA 2011-2878, Portland, OR, USA, 2011. American Institute of Aeronautics and Astronautics.

[73] H. Posson, H. Bériot, and S. Moreau. On the use of an analytical cascade response function to predict sound transmission through an annular cascade. *Journal of Sound and Vibration*, 2013.

[74] H. Posson and S. Moreau. Effect of rotor shielding on fan-outlet guide vanes broadband noise prediction. *AIAA Journal*, pages 1–17, 2013.

[75] V.P. Blandeau, P.F. Joseph, G. Jenkins, and C.J. Powles. Comparison of sound power radiation from isolated airfoils and cascades in a turbulent flow. *The Journal of the Acoustical Society of America*, 129(6):3521–3530, 2011. doi: 10.1121/1.3569706.

[76] V.P. Blandeau, P.F. Joseph, G. Jenkins, and C.J. Powles. Sound power due to an airfoil of arbitrary stagger angle in a turbulent flow. In *17th AIAA/CEAS Aeroacoustics Conference. Portland, OR, USA*, number AIAA-2011-2828, Portland, OR, USA, 2011. American Institute of Aeronautics and Astronautics.

[77] G. Jenkins, C.J. Powles, V.P. Blandeau, and P.F. Joseph. Low and high frequency models for the prediction of noise due to cascade-turbulence interaction. In *17th AIAA/CEAS Aeroacoustics Conference*, number AIAA 2011-2826, Portland, OR, USA, 2011. American Institute of Aeronautics and Astronautics.

[78] G. Jenkins, P.F. Joseph, and C.J. Powles. Multimode blockage due to rotors and application to turbomachinery broadband noise. In *18th AIAA/CEAS Aeroacoustics Conference*, number AIAA-2012-2130, Colorado Springs, CO, USA, 2012. American Institute of Aeronautics and Astronautics.

[79] C.S. Ventres, M.A. Theobald, and W.D. Mark. Turbofan noise generation. volume 1: Analysis. Contractor Report NASA-CR-167951, NAS 1.26:167951, REPT-4770, NASA Lewis Research Center, 1982.

[80] M. Nallasamy and E. Envia. Computation of rotor wake turbulence noise. *Journal of Sound and Vibration*, 282(3):649–678, 2005.

[81] V. Jurdic, A. Moreau, P.F. Joseph, L. Enghardt, and J. Coupland. A comparison between measured and predicted fan broadband noise due to rotor-stator interaction. In *13th AIAA/CEAS Aeroacoustics Conference(28th AIAA Aeroacoustics Conference)*, Rome, Italy, 2007. American Institute of Aeronautics and Astronautics.

[82] H. Posson, S. Moreau, and M. Roger. Fan-OGV broadband noise prediction using a cascade response. In *15th AIAA/CEAS Aeroacoustics Conference (30th AIAA Aeroacoustics Conference)*, number AIAA 2009-3150, Miami, FL, USA, 2009. American Institute of Aeronautics and Astronautics.

[83] V. Jurdic and P.F. Joseph. Turbulence cascade interaction noise. In *Institute of Acoustics Spring Conference 2006: Futures in Acoustics: Today's Research - Tomorrow's Careers*, pages 205–225, 2006.

[84] H.M. Atassi and M.M. Logue. Effect of turbulence structure on broadband fan noise. In *29th AIAA Aeroacoustics Conference*, Vancouver, British Columbia, Canada, 2008. American Institute of Aeronautics and Astronautics.

[85] S.A.L. Glegg and C. Jochault. Broadband self-noise from a ducted fan. *AIAA Journal*, 36(8):1387–1395, 1998.

[86] B.E. Launder and D.B. Spalding. The numerical computation of turbulent flows. *Computer methods in applied mechanics and engineering*, 3(2):269–289, 1974.

[87] R.K. Majiggi and P.R. Gliebe. Development of a rotor wake-vortex model, volume 1. Technical Report NASA CR-174849, NASA, 1984.

[88] P. Welch. The use of fast fourier transform for the estimation of power spectra: a method based on time averaging over short, modified periodograms. *Audio and Electroacoustics, IEEE Transactions on*, 15(2):70–73, 1967.

[89] M. Kamruzzaman, T. Lutz, W. Würz, and E. Krämer. On the length scales of turbulence for aeroacoustic applications. In *17th AIAA/CEAS Aeroacoustics Conference*, Portland, OR, USA, 2011. American Institute of Aeronautics and Astronautics.

[90] S. Shahpar and L. Lapworth. PADRAM: parametric design and rapid meshing system for turbomachinery optimisation. In *ASME Turbo Expo 2003, collocated with the 2003 International Joint Power Generation Conference*, volume Volume 6: Turbo Expo 2003, Parts A and B, pages 579–590, Atlanta, GA, USA, 2003. ASME. doi: 10.1115/GT2003-38698.